A FULLY AUTOMATIC GENETIC APPROACH FOR GRAYSCALE IMAGE COLORIZATION

Dr. Bara'a Ali Attea **Sana'a Khudayer Jaddwa Al-Janaby**
University of Baghdad \ College of Science \ Computer Science

ABSTRACT
Colorization is a computer assisted process of adding color to a monochrome (grayscale) image or movie. **T**he early published methods to perform the image colorizing rely on heuristic techniques for choosing RGB colors from a global palette and applying them to regions of the target gray-scaled image. The main improvement of the proposed technique is the adoption in a fully automatic way the genetic algorithm as an efficient search method to find best match for each pixel in the target image. The proposed genetic algorithm evolves a population of randomly selected individuals (that represents a possible color setting for target image using a reference colored source image toward solution that could resemble natural or real colors to the objects of the target scene). Moreover this study proposes new crossover operator, called Spread out Uniform Crossover (SUX) that turns the recombination scheme of uniform crossover over spreading vital genes at the expense of lethal genes rather than exchanging genes between mating parents to the generated offspring. The results of the proposed colorization techniques are good and plausible.

الخلاصة

التلوين هو عملية مساعدة الحاسبة بإضافة اللون إلى الصورة أو الأفلام الأحادية اللون (الرمادية). تعول الطرق المنشورة سابقا لأداء عملية التلوين على التقنيات الحدسية لاختيار الالوان الأساسية (RGB colors) من لوحة ألوان الرسام وتطبيقها على مناطق الصورة الرمادية الهدف. التحسين الرئيسي للتقنية الجديدة هو اختيار الخوارزمية الجينية بشكل أوتوماتيكي كامل كطريقة بحث كفوءة لا يجاد التماثل الأحسن لكل عنصر صورة للصورة الهدف . تنشأ الطريقة الجينية المقترحة سكان لإفراد مختارون بشكل عشوائي(الذي يمثل تهيئة أو وضع اللون الممكن للصورة الهدف باستخدام مصدر– صورة ملونة – كمرجع نحو الحل الذي يمكن إن يشابه الألوان الطبيعية أو الحقيقية لكائنات المنظر الهدف) . بالإضافة لذلك فان هذه الدراسة تقترح عامل تهجين جديد يسمى تهجين النشر المنتظم (SUX) الذي يحول أسلوب التناسل للتهجين المنتظم عبر نشر الجينات الحيوية على حساب الجينات الميتة , بدل إن يبادل الجينات بين الآباء المتزوجون إلى الذرية المتولدة .أن نتائج تقنية التلوين المقترحة جيدة وقابلة للتصديق ظاهريا.

INTRODUCTION

Colorization is a term introduced by Wilson Markle in 1970 to describe the computer assisted process for adding color to black and white movies [Lev04]. His company Colorization, Inc. released the first full-length colorized movie in August 1985. Nowadays, the colorization term is used to describe the process of adding color to monochrome still images and movies [Sap04].

Colorization, in general, is an active and challenging area of research with a lot of interest in the image editing and compression community. With the luminance information and just some samples of the color (much less than the ordinary sub-sampling in common compression schemes) , the color components of the data can be faithfully recovered .This has implications also in wireless image transmission, where lost image blocks can be recovered from the available channels [Sap04].

Additionally, colorization helps in scientific illustration by exploiting variations in chromaticity as well as luminance. Further, color can be added to a range of scientific images for illustrative and educational purposes. In medicine, image modalities which only acquire grayscale images such Magnetic Resonance Imaging (MRI), X-ray and Computerized Tomography (CT) images can be enhanced with color for presentations and demonstrations [Wel02].

Moreover, more "mundane" applications can benefit from colorization techniques. For instance, consider a scenario where two people that chat regularly through the Internet decide to enhance their virtual meetings with live video. If colorization software, inexpensive and fully automatic one, was available to them, they might buy less expensive monochromatic web-cams instead of color ones, use limited bandwidth by transmitting monochromatic video, but still be able to view fully colored video streams [Vie03].

PREVIOUS WORK

Work interest in grayscale image colorization problem are pointed out:

- E. Reinhard, M. Ashikhmin, B. Gooch, and P. Shirley [Rei01], describe a method for a general color correction that borrows one image's color characteristics from another using mean and standard deviation statistical analysis with $\ell\alpha\beta$ color space to make a synthetic image take on another image's look and feel. The transfer of statistics can fail in case that source and target images don't work well together. To remedy this, the user selects separate swatches, the algorithm then computes their statistics. Then, scales and shifts each pixel in the input image according to the statistics associated with each of the cluster pairs.
- T**.** Welsh, M. Ashikhmin, and K. Muller [Wel02], introduce a general semi-automatic t color transfer between a source color image and a destination grayscale image. They choose to transfer only chromatic information and retain the original luminance values of the target image. Further, their procedure is enhanced by allowing the user to match areas of the two images with rectangular swatches. Colors are then transferred but between the corresponding swatches.
- G.Di. Blasi, and R. D. Recupero [Bla03], propose a semi-automatic colorization method. In this approach, image pixels are grouped into clusters of bounded radius by the Antipolee Tree Clustering. This clustering algorithm works in such a way that "far" elements lie in different clusters. The RGB source image is first converted to YUV space and the Antipole tree is constructed, in which each vector contains the information necessary to perform the Antipole search and the UV components of the pixel color. Then, for each grayscale pixel, in scan-line order, construct its vector and perform the Antipole search to select the best matching vector in the Antipole tree and transfer its UV components to the Y component (luminance) of that gray pixel.
- L.F.M. Vieira, R. D. Vilela, and E. R. do Nascimento [Vie03], introduce a methodology for adding color to grayscale images from a database of color images. Initially the database is semantically indexed. The color transfer process then takes the grayscale image and the color one that has the most similar feature vector as inputs, and adds to each scalar pixel of the

former, the chromatic components of an automatically chosen pixel of the later. The colorization proceeds by scanning the target image in scan-line order so that, for everyone of its pixels, the source image pixel that is closest in terms of intensity value and intensity standard deviation is selected as a match.

- Levin, D. Lischinski, and Y. Weiss [Lev04], present a method based on the simple premise: neighboring pixels in space-time that have similar intensities should have similar colors. This premise is formalized by using a quadratic cost function and obtain an optimization problem that can be solved efficiently using standard techniques.
- Z. Pan, Z. Dong, and M. Zhang [Pan04], present a method to transfer color from a reference image to the whole video. This method take advantage of the correlation between two conjoint frames of video, by tracking the object and assigning the color of it in the preceding frame to that of the posterior one. In many cases, the background will keep unchanged while an object is moving. Rather than choosing RGB colors from a palette to color individual components, they choose $\ell\alpha\beta$ color space that minimize correlation between channels for many natural scenes.
- D. Sỳkorå, J. Buriånek, and J. Žåra [Sỳk04], present a novel color-by example technique which combines image segmentation, patch-based sampling and probabilistic reasoning .This method is able to automatic colorization ofblack and –white cartoon. They state the problem as: having two segmented frames. First frame serves as a color example where each region has one color index assigned from the user-defined palette. The second frame contains unlabelled target regions. The colorization task, then, is to assign color indices to target regions similarly to as they are assigned in the example frame.
- G.Sapiro [Sap04], presented an approach for adding color to a monochrome image or movie, based on considering the geometry and structure of the monochrome luminance input, given by its gradient information. The luminance channel in YC_bC_r color space faithfully represents the geometry of the whole (vectorial) color image. In addition to having the monochrome (luminance) channel, the user provides a few strokes of color, that need to be propagated to the whole color channels. The color is then obtained by solving a partial differential equation that propagates the user selected colors while considering the gradient information brought in by the monochrome data.

THE COLORIZATION PROBLEM COMPLEXITY

The problem of coloring a grayscale image involves assigning three-dimensional (RGB) pixel values to an image whose elements (pixels) are characterized only by one feature (luminance). Since different colors may carry the same luminance in spite of differences in hue and/or saturation, the problem of colorizing gray-scaled images has no inherently "correct" solution [Bla03]. Thus , this in general a severely under-constrained and ambiguous problem for which it makes no sense to try to find an " optimum " solution , and for which even the obtainment of "reasonable " solution requires some combination of strong prior knowledge about the scene depicted and decisive human intervention [Vie03]. Even in the case of pseudo coloring, where the mapping of luminance values to color values is automatic, the choice of the color map is commonly determined by human decision [Bla03].

A major difficulty with colorization lies in the fact that it is an expensive and time-consuming process. For example, classically colorization is done by first segmenting the image into regions, and then proceeds to assign colors to each segment [Sap04]. Unfortunately, automatic segmentation algorithms often fail to correctly identify fuzzy or complex region boundaries [Lev04]. Colorization of movies requires, in addition, tracking regions across the frames of a shot. Existing tracking algorithms typically fail to robustly track non-rigid regions, again requiring massive user intervention in the process [Lev04].

THE PROPOSED COLORIZATION SYSTEM

The general procedure for coloring grayscale image requires as input a pair of images. The source colored image, S, and the target grayscale image, T. The source image could be selected to have similar semantic features to that of the target image (e.g., one can choose pair of faces, sunsets, trees , cars , etc.). Next, both source (colored) and target (grayscale) RGB images are converted to a de-correlated color space. The color space provides three de-correlated, principal channels corresponding to an achromatic luminance L channel, and two chromatic channels $C1$ and $C2$ in which changes made in one color channel should minimally affect values in the other channels. Examples of de-correlated color spaces are YIQ, YUV, ℓ α β, and $CIECAM97s$. The remaining (main) steps of the proposed colorization system are presented in what follows.

INDIVIDUAL REPRESENTATION AND INITIALIZATION

First, a population of P_{size} random chromosomes is generated. Each chromosome in the population is coded as a two-dimensional $m_T * n_T$ formation where m_T and n_T are respectively height and width of the target grayscale image. Each gene in the chromosome can hold an integer value, I, refers to a colored pixel in the source image. Hence, $1 \le I \le m_S * n_S$ where m_S and n_S are respectively height and width of the source colored image. **Fig. (1)** depicts this chromosome representation:

	1	2	3	…	n_T
1	20	315	1	…	511
2	5	16	900	…	100
3	512	322	262	…	104
.	.	.	.	…	.
.	.	.	.		.
.	.	.	.		.
m_T	70	83	69	…	2

$m_T * n_T$

Fig. (1) The chromosome of height m_T and width n_T equal to the size of the grayscale image. Gene no. $(1,1)$ in the figure, e.g., hold an integer 20 which refer to the colored pixel number 20 (from left-to-right and top-to bottom counting) in the source image .

FITNESS EVALUATION

A GA must qualify its population individuals through fitness measure to let evolution to those favorite individuals at the expense of weaker ones.

A similarity metric can be calculated for each GA individual to determine luminance differences between the GA selected pixels and the target pixels. Objective function, here, is calculated in three different variations. In the first approach (named objective 1), luminance values difference is used as the similarity measure between target and source images in which small difference gets better similarity measure than large differences. As a whole, objective1 is calculated as the sum of (achromatic) luminance differences between target gray pixels (indicated by the gene numbers) and source colored pixels (indicated by the gene contents) :

$$\text{Objective 1} = \sum_{i=1}^{n_t}\sum_{j=1}^{m_T} \left| L_T(i,j) - L_S(I(i,j)) \right| \qquad (1)$$

where:

n_T, and m_T are respectively width and height of T image .

L_T , L_S are respectively luminance values of T and S images.

i, j are indices of a gene in row i and column j .

$I(i,j)$ an indirect index to a pixel in S .

In the second and third Objective calculation approaches, the texture similarity or match is also compared. Objective2 sums differences between luminance average of surrounding neighborhood N_T in T image and surrounding neighborhood N_S in S image:

$$\text{Objective2} = \sum_{i=1}^{n_t}\sum_{j=1}^{m_T} \left| L_T(N_T(i,j)) - L_S(N_S(I(i,j))) \right| \qquad (2)$$

where :

n_T, m_T i, j and $I(i,j)$ are as defined previously in (1) .

N is the surrounding $3*3$, $5*5$,or $7*7$ neighborhood .

L_T is the luminance average of N_T neighborhood gray pixels .

L_S is the luminance average of N_S neighborhood colored pixels .

Finally , Objective3 uses matches luminance differences in term of weighted average (50% weight) and weighted standard deviation(50% weight) of neighborhood pixels :

$$\text{Objective 3} = \sum_{i=1}^{n_T}\sum_{j=1}^{m_T} \left| L_T(N_T(i,j)) - L_S(N_S(I(i,j))) \right| \qquad (3)$$

where :

n_T and m_T , i , j , $I(i,j)$, and N are as defined previously in (1) and (2) .

L_T is the sum of 50% luminance average and 50% standard deviation of N_T neighborhood gray pixels .

L_S is the sum of 50% luminance average and 50% standard deviation of N_S neighborhood colored pixels .

In Objective2 and Objective3, different colored regions give rise to distinct luminance clusters, or possess distinct regions. In other words, we expect pixels which are similar in texture to the source colored image regions to be colorized similarly. As high fitness values can represent good solutions to the problem at hand , the fitness then can be computed as inverse of objective function, i.e. ,

$$Fitness = \frac{1}{Objective} \qquad (4)$$

SELECTION OPERATOR

Once fitness is evaluated for each individual, we can form the mating pool that is a collection of individuals who will have the right to reproduce themselves into future generations. This selection is random, not deterministic. The most common selection operator used in GA is tournament selection. In tournament selection with size two, pair of chromosomes is compared. The string with highest fitness is copied into the mating pool. Repeating this process until the mating pool is filled with probably better chromosomes of p_{size} parents.

CROSSOVER OPERATOR

After the mating pool is formed, pairs of chromosomes (parents) are randomly chosen to be manipulated by the crossover operator before releasing them into the offspring. There are various crossover operators (e.g., one-point, two-point, and uniform crossovers), but all aim at recombining the genetic material of the two selected parents in an efficient manner.

However, a modification to the uniform crossover is proposed here. The new crossover operator (as we called Spread-out Uniform Crossover SUX) modifies the uniform crossover to spread out vital genes at the expense of lethal genes rather than exchanging genes between mating parents.

A gene can be classified as vital or lethal according to a predetermined threshold value. The threshold value determines whether luminance difference between a gray pixel and the GA selected colored pixel is accepted or not. If difference is less than or equal threshold value, then we can regard this gene as vital and a copy of it can be propagated to both offspring, otherwise the gene is lethal and is insufficient to be propagated next. Fig. (3).6 below depicts the scheme of **SUX** operator.

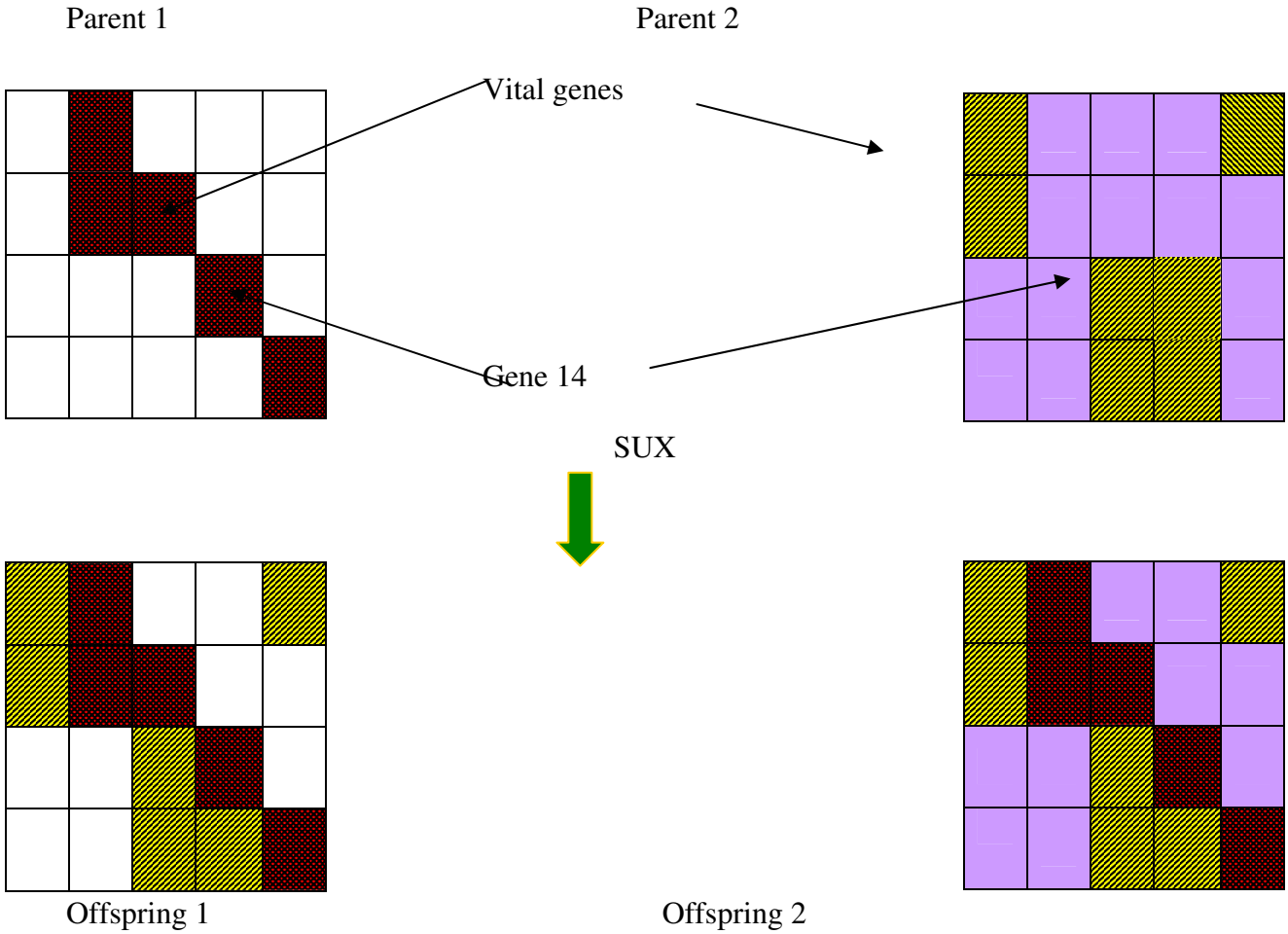

Fig. (2) SUX operator.

As can be seen from the figure, the vital genes of parent1 and parent2 are spread out over the generated offsprings. Moreover, SUX operator allows competition between two vital genes of one location to propagate the winner. However, lethal genes remain in their chromosome to its offspring without propagating to the second offspring. Additionally, for crossover operator there is a very important parameter that is crossover probability Pc. The normal range for Pc is between 0.5 to 0.8.

MUTATION OPERATOR

The second perturbation operator that manipulates the genetic material of individuals is mutation, which traditionally in GA plays as background operator. It randomly alters the genes of a population with a predetermined (normally low) probability, p_m from 0.005 to 0.05 to avoid the algorithm from becoming a purely random search. A gene in the chromosome may be altered to any value (from 1 to the $m_S * n_S$, full size of source colored image) if the condition of mutation is satisfied .

ELITISM STRATEGY AND STOPPING CONDITION

Elitist selection is the idea of preserving the best individual of a population in future generations. Elitist GAs copy the individual with the best fitness encountered so far into the next generation.

Different stopping conditions are used in GA literatures. However, we use the most common one. The GA is allowed to run to a maximum number gen-max, of generations [Gol89].

CONVERGENCE OF THE PROPOSED COLORIZATION SYSTEM

The genetic algorithm introduced in the previous section employs exhaustive searching (or explore the luminance search space of the source colored image), which makes it slow. To compensate the lack of human intervention and at the same time accelerate GA speed, an acceleration approach is proposed here. Acceleration works by considering neighborhoods *Ns* source colored pixels with their luminance values given the luminance setting selected by the genetic algorithm for a given individual. The proposed acceleration can be formulated as:

1. Determine the size of the neighborhood N_S, e.g., $3*3$, $5 * 5$, etc.
2. Select the best GA individual to be modified.

For each gene content of the selected GA individual, the acceleration searches over those *Ns* neighborhood of the colored pixel indexed by the gene content, I , and replace it with the index, J , of the neighborhood pixel that has luminance value close to the luminance value of the gray pixel indicated by that gene.

By this way, the search technique imposed by the proposed colorization system has two forms. A global search ability manifested by the genetic algorithm to explore the luminance search space of the source colored image to locate suitable regions (or swatches) to that of the luminance regions of the target grayscale image. This global search is hybrid with a local search that exploit the selected GA swatches for most suitable pixels luminances to that of the corresponding pixels in the target grayscale image. In short, there is a collaboration between the explorative power of the GA and exploitative power of the acceleration search.

RECOVER COLOR INFORMATION

The last step to do is that how to display the target image on the screen as a colored RGB one. This step represent how to extract phenotype of a GA individual and displaying it in RGB space on the screen. Figure 3.9 illustrates the color recovering sequences.

Recall that the target and the source images are represented in RGB color model. After processing (by GA and local accelerator) in luminance space, we can recover the color at each gray pixel by copying the two chromatic channels ($C1_S$ and $C2_S$) of the genetically chosen selected source colored image pixels into the output target image, combining them with the target luminance channel L_T , and then followed by a conversion back to RGB color space.

RESULTS

The experiments have been performed on a database of different image classes with a total of 30 images of colored and grayscale natural scenes. Both source colored and target grayscale images of a colorization query are taken from this database. In general, database images can be divided into

two groups: homogeneous and heterogeneous. Images that include a single object in the foreground and this object is clearly discernible from a mostly homogeneous background is said to be homogeneous (e.g. Apple, sunset1, and tiger1). On the other hand, an image that has multiple objects on the foreground, or has a cluttered background, or is illuminated in an uneven way is said to be a heterogeneous image (e.g., Trees, White Rose, and yellow Roses). Note that some images may not conform to this loose definition of the homogeneous or heterogeneous group. In other words, they could be semi- homogeneous or semi- heterogeneous images. Intuitively, for the colorization problem, a heterogeneous image is more complex than a homogeneous one. A colorization query requires two images, one source colored image, and one target grayscale image. Although input images can be taken from different classes, and one can just to see how this colorization technique work, we select input source and target images to be of the same semantic meaning. For example, the input to the colorization query can be a pair of cats, a pair of sunsets, etc.

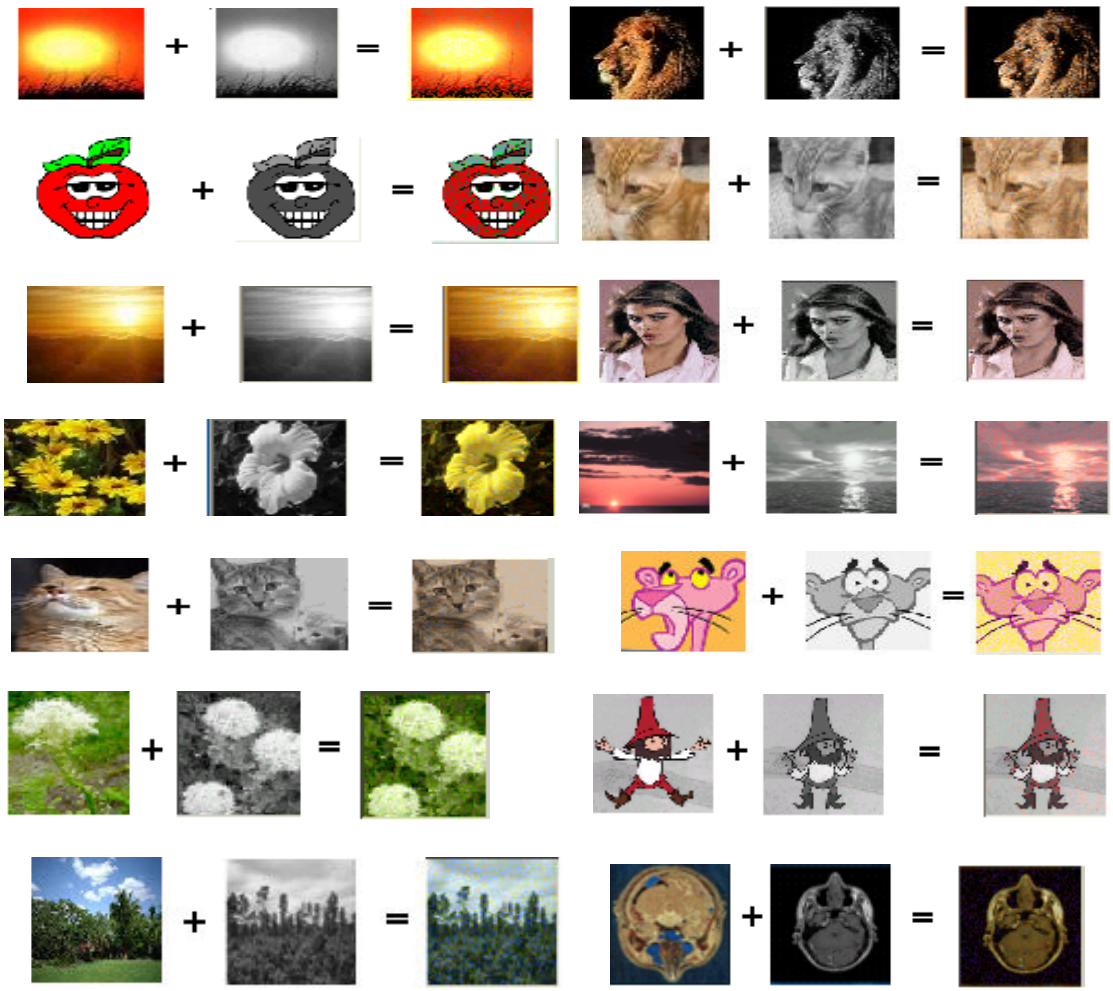

Fig. (3) Results (source colored image + target grayscale image = target colored image).

CONCLUSIONS

The presented results analyze the behavior of the genetic algorithm for grayscale image colorization problem experimentally. The core of the proposed colorization technique consists of searching luminance in a high dimensional space using genetic algorithm. The genetic algorithm searches for each target pixel, the most suitable source pixel that matches in luminance value. Take a simple example the case in which the source and target images are both of size $32*32$ pixels. Then for each target pixel of the 1024 $(32*32)$ pixels, the genetic algorithm explores the 1024 candidate

source pixels for best possible luminance match. This leads to a huge search space size of 1024^{1024} potential solutions. Taking this problem complexity into account, it can be argued that the proposed colorization technique achieves convergence to suitable and near realistic results in a fully automatic way (without human intervention) and without adding excessive iterations.
The results of the proposed colorization system, as a whole, demonstrate that it is possible to color many grayscale images (including natural scenes, cartoons, and scientific data) in a way that is completely automatic and look, reasonably well using a GA of small population size and a few generations evolution. Further, this technique works well on scenes where the image is divided into distinct luminance clusters. More images can be colorized using this technique with better results but at the expense of increasing the GA population size and/or generations number. The satisfactory quality of the technique is established by collaborating the exploration power of the genetic algorithm with the exploitation power of the local acceleration search operator. One can imagine that the GA can locate the most suitable clusters (in luminance and / or texture) to those of target image while the local accelerator searches the located GA clusters for most suitable pixel (in luminance) to transfer its color to the corresponding grayscale pixels.

REFERENCES

DiB, G., Reforgiato,R.D., (2003), Fast Colorization of Gray Images, Eurographics, Italian Chapter.

Goldberg, D. L., (1989), Genetic Algorithms in Search Optimization, and Machine learning,, Addison-Wesley, USA.

Hertzmann, A., Jacobs, C. E., Oliver, N., Curless, B., and Salesin, D. H., (2001), Image Analogies, In Proceeding of ACM SIGGRAPH ,pp. 327-340.

Levin, A., Lischinski, D. and Weiss, Y., (2004), Colorization using Optimization, ACM Transactions on Graphics.

Pan, Z. Dong, Z. and Zhang, M., (2004), A new Algorithm for Adding Color to Video or Animation Clips, In Proceedings of WSCG-International Conference in Central Europe on Computer Graphics, Visualization and Computer Vision, pp. 515-519.

Reinhard, E., (2001), Statistical approaches to image and scene manipulation, ACM SIGGRAPH/EUROGRAPHICS Campfire, Snowbird Utah.

Sapiro, G., (2004), Inpainting The Colors, IMA Preprint Series #1979 ,May.

Sýkora, D., Buriānek, J. and Žăra, J., (2004), Unsupervised Colorization of Black-and-White Cartoons, Proceedings of NPAR, Annecy,
ACM SIGGRAPH .

Vieira, L.F.M, Vilela, R.D., Nascimento, E.R., (2003), Automatically choosing source color images for coloring grayscale images.

Welsh, T., Ashikhmin, M., and Mueller, K., (2002), Transferring Color to Greyscale Images, In Proceeding of ACM SIGGRAPH , pp.277-280.

AEROTRIANGULATION BY COPLANARITY

Miss Fanar Mansour
Surveying Engineering Department/Engineering Collage/Baghdad University

ABSTRACT
Before corresponding points in photos taken with two cameras can be used to recover distances to objects in a scene, one has to determine the position and orientation of one camera relative to the other. This is the classic photogrammetric problem of aerotriangulation. Iterative methods for determining X,Y,Z ground positions for unknown points using aerotriangulation process, were developed long ago; without them we would not have most of the topographic maps we do today.
Described here in this research a simple iterative scheme for recovering relative orientation process then applying intersection problem (vector method) using the condition of coplanarity, out of the usual for photogrammetrists in using the familiar condition of collinearity. The data required is a pair of bundles of corresponding rays from the two projection centers to points in the scene. It is well known that at least five pairs of rays are needed, because, each object point gives only one equation. The results were amazing according to the variances that have been obtained for the angular orientation elements. The programs have been written using Matlab software ver. 5.3.

الخلاصة

قبل أن يكون بامكان زوج النقاط الصورية المتناظرة والملتقطة بكامرتين جويتين ان تستخدم لحساب المواقع الارضية والمسافات الحقيقية بين نقاط مجهولة الموقع الارضي الحقيقي في المشهد المصور ، يجب ان يحسب موقع وتوجيه احدى الكامرتين في الفضاء نسبة الى الاخرى ، هذه الخطوتين المتلاحقتين تعرف بعملية التثليث الجوي. هناك العديد من الطرق المستخدمة لحساب المواقع الارضية للنقاط المجهولة باستخدام عملية التثليث الجوي والتي استخدمت منذ فترات طويلة والتي لولاها لما كنا قد حصلنا على معظم الخرائط الطوبوغرافية التي نمتلكها ونتداولها اليوم.

في هذا البحث تم وصف وتطبيق طريقة بسيطة لحساب عناصر التوجيه الخارجي لاحدى الكامرتين نسبة الى الاخرى ثم تطبيق معادلات التقاطع الامامي (طريقة الـvectors) لحساب المواقع الارضية للنقاط المجهولة في المنطقة المراد تكثيفها وذلك باستخدام معادلات الـcoplanarity condition equations بدل استخدام الطريقة المألوفة والمستخدمة من قبل معظم باحثي وعلماء المسح التصويري وهي معادلات الـcollinearity condition equations وذلك لغرض اختبار النتائج المستحصلة باستخدام هذه المعادلات (coplanarity) ومقارنتها مع النتائج المستحصلة من معادلات الـ(collinearity). المدخلات المطلوبة لاستخدام هذه المعادلات تتطلب زوج من حزم الاشعة المتناظرة والقادمة من مركزي الاسقاط الى النقاط المعنية في المشهد المصور. وكما هو معلوم فانه على الاقل لابد من ان يتوفر خمسة ازواج من هذه الاشعة

واللازمة لايجاد قيمة المجاهيل وذلك لان كل هدف من هذه النقاط الارضية المختارة يعطينا معادلة واحـــدة فقط. النتائج التي تم الحصول عليها في هذا البحث كانت مذهلة نسبة الى الاختلافات التي تم الحصول عليها لعناصر التوجيه الزاوي. البرامج المستخدمة في هذا البحث تم اعدادها باستخدام لغة الـــــMatlab المرنـــة والتي توفر تصور واضح للقارئْ عن نجاح تجربة البحث.

KEY WORDS
Photogrammetry, Analytical Photogrammetry, Analytical Aerotriangulation, Coplanarity Condition

INTRODUCTION

Aerotriangulation is the term most frequently applied to the process of determining X,Y & Z ground coordinates of individual points based on measurements from photographs. Aerotriangulation process can be applied using different techniques, such as analogue, semianalytical, analytical and of course digital techniques. Analytical aerotriangulation tends to be more accurate than analogue or semi analytical aerotriangulation, largely because analytic techniques can more effectively eliminate systematic errors. Several different variations in analytical aerotriangulation techniques have evolved. Basically, however, all methods consist of writing condition equations, which express the unknown elements of exterior orientation of each photo. The equations are solved to determine the unknown orientation parameters and the ground coordinates of unknown points. The most commonly used methods enforce one of two conditions: collinearity or coplanarity. In coplanarity method (that used in this research), one equation may be written for each object point whose images appear on both photos of the stereopair. The coplanarity equations do not contain object space coordinates as unknown; rather, they contain only the elements of exterior orientation of the two photos of the stereopair. Therefore; after solving for the elements of exterior orientation, object point coordinates are calculated, by solving the space intersection problem by colliniarity,or using the vectors method that have been used in this research.

COPLANARITY CONDITION

The coplanarity condition equation illustrated in **Fig (1)** is fundamental to relative orientation. When relative orientation is achieved, the vector $\vec{R}_{1i}$ from O_i to P_i will interest the vector $\vec{R}_{2i}$ from O_2 to P_i , and these two vectors together with air base vector, $\vec{b}$, will be coplanar.

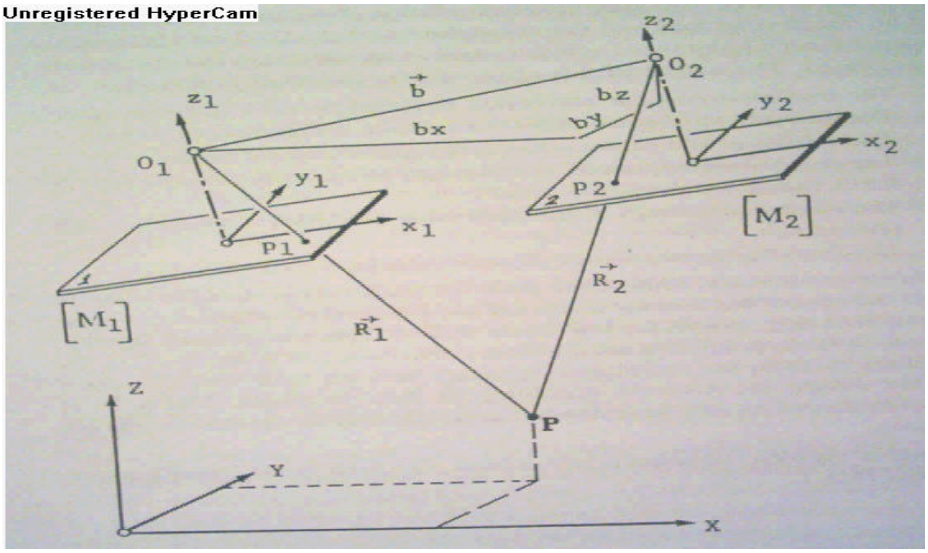

Fig. (1) The coplanarity condition

Hence, their scalar triple product is zero. That is

$$F_1 = \vec{b} \cdot \vec{R}_{1i} \times \vec{R}_{2i} = 0 \qquad (1)$$

Where F_1 is the mathematical model. Furthermore,

$$\vec{b} = \begin{bmatrix} b_X \\ b_Y \\ b_Z \end{bmatrix} = \begin{bmatrix} X_{O2} - X_{O1} \\ Y_{O2} - Y_{O1} \\ Z_{O2} - Z_{O1} \end{bmatrix}$$

$$\vec{R}_{1i} = \begin{bmatrix} X_{1i} \\ Y_{1i} \\ Z_{ii} \end{bmatrix} = K_1 M_1^T \begin{bmatrix} x_{1i} - x_{c1} \\ y_{1i} - y_{c1} \\ -f \end{bmatrix} = K_1 M_1^T \cdot \vec{r}_1$$

$$\vec{R}_{2i} = \begin{bmatrix} X_{2i} \\ Y_{2i} \\ Z_{2i} \end{bmatrix} = K_2 M_2^T \begin{bmatrix} x_{2i} - x_{c2} \\ y_{2i} - y_{c2} \\ -f \end{bmatrix} = K_2 M_2^T \cdot \vec{r}_2$$

K_1 and K_2 are scale factors, $\vec{r}_1$ and $\vec{r}_2$ are the corresponding location vectors in camera space.

$$M^T = \begin{bmatrix} m_{11} & m_{21} & m_{31} \\ m_{12} & m_{22} & m_{32} \\ m_{13} & m_{23} & m_{33} \end{bmatrix}$$

$$= \begin{bmatrix} \cos\phi\cos\kappa & -\cos\phi\sin\kappa & \sin\phi \\ \cos\omega\sin\kappa + \sin\omega\sin\phi\cos\kappa & \cos\omega\cos\kappa - \sin\omega\sin\phi\sin\kappa & -\sin\omega\cos\phi \\ \sin\omega\sin\kappa - \cos\omega\sin\phi\cos\kappa & \sin\omega\cos\kappa + \cos\omega\sin\phi\sin\kappa & \cos\omega\cos\phi \end{bmatrix}$$

The assumptions made about the rotation matrix M are:

- ❖ The rotations are in a right-handed system.
- ❖ The rotations, proceedings from the ground (or model) system to the photo system of coordinates are ω primary, ϕ secondary, and κ tertiary.

Equation (1) may be written in determinant form as,

$$F_1 = \begin{bmatrix} b_X & b_Y & b_Z \\ X_{1i} & Y_{1i} & Z_{1i} \\ X_{2i} & Y_{2i} & Z_{2i} \end{bmatrix} = 0 \qquad (2)$$

Now, let $K_1 = K_2 = 1$ and $x_c = y_c = 0$. Then, using photo 2 for the dependent method of relative orientation,

$$\omega_1 = \phi_1 = \kappa_1 = b_{y1} = b_{z1} = 0$$

Here

$$b_Y = b_{y2} - b_{y1} \quad \text{and} \quad b_Z = b_{z2} - b_{z1}$$

The vectors $\vec{R}_{1i}$ and $\vec{R}_{2i}$ are then reduced to

$$\vec{R}_{1i} = \begin{bmatrix} X_{1i} \\ Y_{1i} \\ Z_{1i} \end{bmatrix} = \begin{bmatrix} 1 & 0 & 0 \\ 0 & 1 & 0 \\ 0 & 0 & 1 \end{bmatrix} \begin{bmatrix} x_{1i} \\ y_{1i} \\ -f \end{bmatrix} = \begin{bmatrix} x_{1i} \\ y_{1i} \\ -f \end{bmatrix} \quad (3)$$

$$\vec{R}_{2i} = \begin{bmatrix} X_{2i} \\ Y_{2i} \\ Z_{2i} \end{bmatrix} = \begin{bmatrix} x_{2i}\cos\phi\cos\kappa - y_{2i}\cos\phi\sin\kappa - f\cdot\sin\phi \\ x_{2i}(\cos\omega\sin\kappa + \sin\omega\sin\phi\cos\kappa) + y_{2i}(\cos\omega\cos\kappa - \sin\omega\sin\phi\sin\kappa) + f\cdot\sin\omega\cos\phi \\ x_{2i}(\sin\omega\sin\kappa - \cos\omega\sin\phi\cos\kappa) + y_{2i}(\sin\omega\cos\kappa + \cos\omega\sin\phi\sin\kappa) - f\cdot\cos\omega\cos\phi \end{bmatrix} \quad (4)$$

Note here that $\omega, \phi,$ and κ are for camera 2.

Substituting Eqs (3) and (4) in Eq (1) and then expanding and rearranging, the mathematical model, F_1 is given by:

$$F_1 = [b_x y_{1i} - b_{y2} x_{1i}][x_{2i}(\sin\omega\sin\kappa - \cos\omega\sin\phi\cos\kappa) + y_{2i}(\sin\omega\cos\kappa + \cos\omega\sin\phi\sin\kappa) - f\cdot\cos\omega\cos\phi]$$
$$+ [b_x f + b_{z2} x_{1i}][x_{2i}(\cos\omega\sin\kappa + \sin\omega\sin\phi\cos\kappa) + y_{2i}(\cos\omega\cos\kappa - \sin\omega\sin\phi\sin\kappa) + f\cdot\sin\omega\cos\phi]$$
$$+ [b_{y2} f + b_{z2} y_{1i}][y_{2i}\cos\phi\sin\kappa - x_{2i}\cos\phi\cos\kappa + f\cdot\sin\phi] = 0 \text{.....(5)}$$

LINEARIZATION OF THE COPLANARITY CONDITION EQUATION

The coplanarity condition equation (eq. (5)), is linearized into the general form:

$$[A_i](V_i) + [B_i](\Delta) + (F_{Oi}) = 0 \quad (6)$$

Where

$[A_i] = \partial(F_i)/\partial$ (observed quantities)
$[B_i] = \partial(F_i)/\partial$ (parameters)
$(F_{Oi}) = F_i$ (evaluated with observations and approximate parameters)
$(V_i) =$ (a vector of residuals)
$(\Delta) =$ (a vector of corrections to approximate parameters)

Here:-

$$[A_i] = \begin{bmatrix} \frac{\partial F_i}{\partial x_{1i}} & \frac{\partial F_i}{\partial y_{1i}} & \frac{\partial F_i}{\partial x_{2i}} & \frac{\partial F_i}{\partial y_{2i}} \end{bmatrix} \quad (7)$$

$$\frac{\partial F_1}{\partial x_{1i}} = \begin{bmatrix} b_x & b_y & b_z \\ m_{11}^1 & m_{12}^1 & m_{13}^1 \\ X_{2i} & Y_{2i} & Z_{2i} \end{bmatrix}$$

$$= \begin{bmatrix} b_x & b_y & b_z \\ 1 & 0 & 0 \\ X_{2i} & Y_{2i} & Z_{2i} \end{bmatrix}$$

$$= (b_z \cdot Y_{2i} - b_y \cdot Z_{2i}) \quad (8)$$

Substituting from Eq.(4):-

$$\frac{\partial F_i}{\partial x_{1i}} = b_z\left[X_{2i}(\cos\omega\sin\kappa+\sin\omega\sin\phi\cos\kappa)+y_{2i}(\cos\omega\cos\kappa-\sin\omega\sin\phi\sin\kappa)+f\sin\omega\cos\phi\right]-$$
$$b_y\left[X_{2i}(\sin\omega\sin\kappa-\cos\omega\sin\phi\cos\kappa)+y_{2i}(\sin\omega\cos\kappa+\cos\omega\sin\phi\sin\kappa)-f\cos\omega\cos\phi\right].....(9)$$

Similarly,

$$\frac{\partial F_i}{\partial y_{1i}} = \begin{bmatrix} b_x & b_y & b_z \\ m_{21}^1 & m_{22}^1 & m_{23}^1 \\ X_{2i} & Y_{2i} & Z_{2i} \end{bmatrix}$$
$$= \begin{bmatrix} b_x & b_y & b_z \\ 0 & 1 & 0 \\ X_{2i} & Y_{2i} & Z_{2i} \end{bmatrix}$$

$$= (b_x\cdot Z_{2i}-b_z\cdot X_{2i}) \quad (10)$$
$$= b_x\left[x_{2i}(\sin\omega\sin\kappa-\cos\omega\sin\phi\cos\kappa)+y_{2i}(\sin\omega\cos\kappa+\cos\omega\sin\phi\sin\kappa)-f\cos\omega\cos\phi\right]$$
$$-b_z\left[x_{2i}\cos\phi\cos\kappa-y_{2i}\cos\phi\sin\kappa-f\sin\phi\right].....(11)$$

Furthermore,

$$\frac{\partial F_i}{\partial x_{2i}} = \begin{bmatrix} b_x & b_y & b_z \\ X_{1i} & Y_{1i} & Z_{1i} \\ m_{11}^1 & m_{12}^1 & m_{13}^1 \end{bmatrix}$$
$$= \begin{bmatrix} b_x & b_y & b_z \\ x_{1i} & y_{1i} & -f \\ \cos\phi\cos\kappa & \cos\omega\sin\kappa+\sin\omega\sin\phi\cos\kappa & \sin\omega\sin\kappa-\cos\omega\sin\phi\cos\kappa \end{bmatrix}.....(12)$$

$$= (b_x\cdot y_{1i}-b_y\cdot x_{1i})(\sin\omega\sin\kappa-\cos\omega\sin\phi\cos\kappa)+(b_x\cdot f+b_y\cdot x_{1i})(\cos\omega\sin\kappa+\sin\omega\sin\phi\cos\kappa)$$
$$-(b_y\cdot f+b_z\cdot y_{1i})\cos\phi\cos\kappa.....(13)$$

$$\frac{\partial F_i}{\partial y_{2i}} = \begin{bmatrix} b_x & b_y & b_z \\ X_{1i} & Y_{1i} & Z_{1i} \\ m_{21}^2 & m_{22}^2 & m_{23}^2 \end{bmatrix}$$
$$= \begin{bmatrix} b_x & b_y & b_z \\ x_{1i} & y_{1i} & -f \\ -\cos\phi\cos\kappa & \cos\omega\sin\kappa-\sin\omega\sin\phi\sin\kappa & \sin\omega\sin\kappa+\cos\omega\sin\phi\sin\kappa \end{bmatrix}.....(14)$$

$$= (b_x\cdot y_{1i}-b_y\cdot x_{1i})(\sin\omega\cos\kappa+\cos\omega\sin\phi\sin\kappa)+(b_x\cdot f+b_z\cdot x_{1i})(\cos\omega\cos\kappa-\sin\omega\sin\phi\sin\kappa)$$
$$+(b_y\cdot f+b_z\cdot y_{1i})\cos\phi\sin\kappa.....(15)$$

And:-

$$[B_i] = \begin{bmatrix} \frac{\partial F_i}{\partial b_{y2}} & \frac{\partial F_i}{\partial b_{z2}} & \frac{\partial F_i}{\partial \omega_2} & \frac{\partial F_i}{\partial \phi_2} & \frac{\partial F_i}{\partial \kappa_2} \end{bmatrix} \quad (16)$$

$$\frac{\partial F_i}{\partial b_{y2}} = -\begin{bmatrix} X_{1i} & Z_{1i} \\ X_{2i} & Z_{2i} \end{bmatrix} \quad .(17)$$

From equation (4):-

$$\frac{\partial F_i}{\partial b_{y2}} = x_{1i}\left[x_{2i}(\cos\omega\sin\phi\cos\kappa - \sin\omega\sin\kappa) - y_{2i}(\sin\omega\cos\kappa + \cos\omega\sin\phi\sin\kappa) + f\cdot\cos\omega\cos\phi\right]$$
$$- f\cdot\left[x_{2i}\cos\phi\cos\kappa - y_{2i}\cos\phi\sin\kappa - f\cdot\sin\phi\right] \quad .....(18)$$

Similarly,

$$\frac{\partial F_i}{\partial b_{z2}} = \begin{bmatrix} X_{1i} & Y_{1i} \\ X_{2i} & Y_{2i} \end{bmatrix}$$
$$= x_{1i}\left[x_{2i}(\cos\omega\sin\kappa + \sin\omega\sin\phi\cos\kappa) + y_{2i}(\cos\omega\cos\kappa - \sin\omega\sin\phi\sin\kappa) + f\cdot\sin\omega\cos\phi\right]$$
$$- y_{1i}\left[x_{2i}\cos\phi\cos\kappa - y_{2i}\cos\phi\sin\kappa - f\cdot\sin\phi\right] \quad .....(19)$$

$$\frac{\partial F_i}{\partial \omega_2} = \begin{bmatrix} b_x & b_y & b_z \\ X_{1i} & Y_{1i} & Z_{1i} \\ \frac{\partial X_{2i}}{\partial \omega_2} & \frac{\partial Y_{2i}}{\partial \omega_2} & \frac{\partial Z_{2i}}{\partial \omega_2} \end{bmatrix}$$
$$= \begin{bmatrix} b_x & b_y & b_z \\ x_{1i} & y_{1i} & -f \\ \frac{\partial X_{2i}}{\partial \omega_2} & \frac{\partial Y_{2i}}{\partial \omega_2} & \frac{\partial Z_{2i}}{\partial \omega_2} \end{bmatrix} \quad .(20)$$

From equation (4):

$$\frac{\partial X_{2i}}{\partial \omega_2} = 0$$

$$\frac{\partial Y_{2i}}{\partial \omega_2} = x_{2i}(\cos\omega\sin\phi\cos\kappa - \sin\omega\sin\kappa) - y_{2i}(\sin\omega\cos\kappa + \cos\omega\sin\phi\sin\kappa) + f\cdot\cos\omega\cos\phi$$

And

$$\frac{\partial Z_{2i}}{\partial \omega_2} = x_{2i}(\cos\omega\sin\kappa + \sin\omega\sin\phi\cos\kappa) + y_{2i}(\cos\omega\cos\kappa - \sin\omega\sin\phi\sin\kappa) + f\cdot\sin\omega\cos\phi$$

Now, substituting values in eq. (20):

$$\frac{\partial F_i}{\partial \omega_2} = \left(b_x \cdot y_{1i} - b_y \cdot x_{2i}\right)\left(x_{2i}\left(\cos\omega\sin\kappa + \sin\omega\sin\phi\cos\kappa\right) + y_{2i}\left(\cos\omega\cos\kappa - \sin\omega\sin\phi\sin\kappa\right) + f\cdot\sin\omega\cos\phi\right)$$
$$+\left(b_x \cdot f + b_z \cdot x_{1i}\right)\left(f\cdot\cos\omega\cos\phi + x_{2i}\left(\cos\omega\sin\phi\cos\kappa - \sin\omega\sin\kappa\right) - y_{2i}\left(\sin\omega\cos\kappa + \cos\omega\sin\phi\sin\kappa\right)\right)$$
.....(21)

$$\frac{\partial F_i}{\partial \phi_2} = \begin{bmatrix} b_x & b_y & b_z \\ X_{1i} & Y_{1i} & Z_{1i} \\ \dfrac{\partial X_{2i}}{\partial \phi_2} & \dfrac{\partial Y_{2i}}{\partial \phi_2} & \dfrac{\partial Z_{2i}}{\partial \phi_2} \end{bmatrix}$$
$$= \begin{bmatrix} b_x & b_y & b_z \\ x_{1i} & y_{1i} & -f \\ \dfrac{\partial X_{2i}}{\partial \phi_2} & \dfrac{\partial Y_{2i}}{\partial \phi_2} & \dfrac{\partial Z_{2i}}{\partial \phi_2} \end{bmatrix} \qquad (22)$$

From eq. (4)

$$\frac{\partial X_{2i}}{\partial \phi_2} = -x_{2i}\sin\phi\cos\kappa + y_{2i}\sin\phi\sin\kappa - f\cdot\cos\phi$$
$$\frac{\partial Y_{2i}}{\partial \phi_2} = x_{2i}\sin\omega\cos\phi\cos\kappa - y_{2i}\sin\omega\cos\phi\sin\kappa - f\cdot\sin\omega\sin\phi$$
$$\frac{\partial Z_{2i}}{\partial \phi_2} = -x_{2i}\cos\omega\cos\phi\cos\kappa + y_{2i}\cos\omega\cos\phi\sin\kappa + f\cdot\cos\omega\sin\phi$$

Substituting, values into eq. (22):

$$\frac{\partial F_i}{\partial \phi_2} = \left(b_x \cdot y_{1i} - b_y \cdot x_{1i}\right)\left(f\cdot\cos\omega\sin\phi + y_{2i}\cos\omega\cos\phi\sin\kappa - x_{2i}\cos\omega\cos\phi\cos\kappa\right) + \left(b_x \cdot f + b_z \cdot x_{1i}\right)\cdot$$
$$\left(x_{2i}\sin\omega\cos\phi\cos\kappa - y_{2i}\sin\omega\cos\phi\sin\kappa - f\cdot\sin\omega\sin\phi\right) + \left(b_y \cdot f + b_z \cdot y_{1i}\right)\cdot$$
$$\left(x_{2i}\sin\phi\cos\kappa - y_{2i}\sin\phi\sin\kappa + f\cdot\cos\phi\right).....(23)$$

$$\frac{\partial F_i}{\partial \kappa_2} = \begin{bmatrix} b_x & b_y & b_z \\ X_{1i} & Y_{1i} & Z_{1i} \\ \dfrac{\partial X_{2i}}{\partial \kappa_2} & \dfrac{\partial Y_{2i}}{\partial \kappa_2} & \dfrac{\partial Z_{2i}}{\partial \kappa_2} \end{bmatrix}$$

$$= \begin{bmatrix} b_x & b_y & b_z \\ x_{1i} & y_{1i} & -f \\ \frac{\partial X_{2i}}{\partial \kappa_2} & \frac{\partial Y_{2i}}{\partial \kappa_2} & \frac{\partial Z_{2i}}{\partial \kappa_2} \end{bmatrix} \quad .(24)$$

From eq. (4):

$$\frac{\partial X_{2i}}{\partial \kappa_2} = -x_{2i}\cos\phi\sin\kappa - y_{2i}\cos\phi\cos\kappa$$
$$\frac{\partial Y_{2i}}{\partial \kappa_2} = x_{2i}(\cos\omega\cos\kappa - \sin\omega\sin\phi\sin\kappa) - y_{2i}(\cos\omega\sin\kappa + \sin\omega\sin\phi\cos\kappa)$$
$$\frac{\partial Z_{2i}}{\partial \kappa_2} = x_{2i}(\sin\omega\cos\kappa + \cos\omega\sin\phi\sin\kappa) - y_{2i}(\sin\omega\sin\kappa - \cos\omega\sin\phi\cos\kappa)$$

Now, substituting the values into eq. (24):

$$\frac{\partial F_i}{\partial \kappa_2} = (b_x \cdot y_{1i} - b_y \cdot x_{1i})(x_{2i}(\sin\omega\cos\kappa + \cos\omega\sin\phi\sin\kappa) - y_{2i}(\sin\omega\sin\kappa - \cos\omega\sin\phi\cos\kappa)) +$$
$$(b_x \cdot f + b_z \cdot x_{1i}) \cdot (x_{2i}(\cos\omega\cos\kappa - \sin\omega\sin\phi\sin\kappa) - y_{2i}(\cos\omega\sin\kappa + \sin\omega\sin\phi\cos\kappa)) +$$
$$(b_y \cdot f + b_z \cdot y_{1i})(x_{2i}\cos\phi\sin\kappa + y_{2i}\cos\phi\cos\kappa) \quad .....(25)$$

Here in our case, we use two overlapped photos with six points appear on each one, so the dimensions of the matrices will be:

$$A_{(6\times24)} = \begin{bmatrix} [A_1]_{(1\times4)} & 0 & 0 & 0 & 0 & 0 \\ 0 & [A_2]_{(1\times4)} & 0 & 0 & 0 & 0 \\ 0 & 0 & [A_3]_{(1\times4)} & 0 & 0 & 0 \\ 0 & 0 & 0 & [A_4]_{(1\times4)} & 0 & 0 \\ 0 & 0 & 0 & 0 & [A_5]_{(1\times4)} & 0 \\ 0 & 0 & 0 & 0 & 0 & [A_6]_{(1\times4)} \end{bmatrix}$$

$$B_{(6\times5)} = \begin{bmatrix} [B_1]_{(1\times5)} \\ [B_2]_{(1\times5)} \\ [B_3]_{(1\times5)} \\ [B_4]_{(1\times5)} \\ [B_5]_{(1\times5)} \\ [B_6]_{(1\times5)} \end{bmatrix}$$

$$F_{O(6\times1)} = \begin{bmatrix} F_{O1} \\ F_{O2} \\ F_{O3} \\ F_{O4} \\ F_{O5} \\ F_{O6} \end{bmatrix}$$

$$\Delta_{(5\times1)} = \begin{bmatrix} \Delta b_y \\ \Delta b_z \\ \Delta\omega \\ \Delta\phi \\ \Delta\kappa \end{bmatrix}$$

$$V_{(24\times1)} = \begin{bmatrix} [V_1]_{(4\times1)} \\ [V_2]_{(4\times1)} \\ [V_3]_{(4\times1)} \\ [V_4]_{(4\times1)} \\ [V_5]_{(4\times1)} \\ [V_6]_{(4\times1)} \end{bmatrix}$$

Here

The numbers, (24) refers to the number of observed quantities, (6) refers to the number of condition equations where observed quantities and unknown quantities are present, and (5) refers to the number of unknown quantities.

LEAST SQUARE SOLUTION OF THE COPLANARITY CONDITION EQUATION

Coordinate observations at five selected points give a unique solution of the parameters ($b_{y2}, b_{z2}, \omega_2, \phi_2$ and κ_2). However, when redundant observations are made, an adjustment situation arises, and the principles of least squares is applied to minimize the sum of the squares of the residuals.

The solution vector (Δ) is given by

$$\Delta = -\left(B^T M^{-1} B\right)^{-1} B^T M^{-1} F_O \qquad (26)$$

Where

$M =$ $AW^{-1}A^T$

$W =$ weight matrix associated with the observations

$$V^T WV = -KL^T F_O \qquad .(27)$$

Where

$$KL = -M^{-1}\left(B\Delta + F_O\right)$$

The unit variance m_o^2 is given by

$$m_o^2 = \frac{V^T WV}{r-u} \qquad .(28)$$

Where

$r =$ number of condition equations
$u =$ number of unknown quantities
$(r-u) =$ the degree of freedom
The weight coefficient matrix of Δ can be written as

$$Q_{\Delta} = \left(B^T M^{-1} B\right)^{-1} \qquad (29)$$

The variance-covariance matrix of unknown parameters is

$$\sum \Delta = m_o^2 Q_{\Delta} \qquad .(30)$$

The corrections Δ are added to the approximate values of the parameters which were used in computing the coefficients of $F_i, [A_i]$, and $[B_i]$. It is sometimes necessary to iterate the solution until the corrections are negligible. Quantities related to both the parameters and the observations, should be updated for each iteration. The number of required iterations depends on the initial approximations, the total number of parameters, and the geometric strength of the model. Here, we used 6 iterations depending on the conditions above. There are several criteria, one of which may be used to terminate the iteration in a particular case, e.g., minimum variances of 0.00001rad for the angular orientation elements (as used by NOAA).

INTERSECTION BY VECTORS

The intersection of five pairs of rays $\vec{R}_1$ and $\vec{R}_2$ is the condition for relative orientation. After the relative orientation one may find, however, that the rays fail to intersect, i.e., there may be residual parallaxes. Therefore, one must define a point which will represent the location of intersection (acceptable for model point coordinates). A suitable point is one mid way along the vector $\vec{D}$ between vectors $\vec{R}_1$ and $\vec{R}_2$ (see **Fig. (2)**) in the region where the rays come closest together.

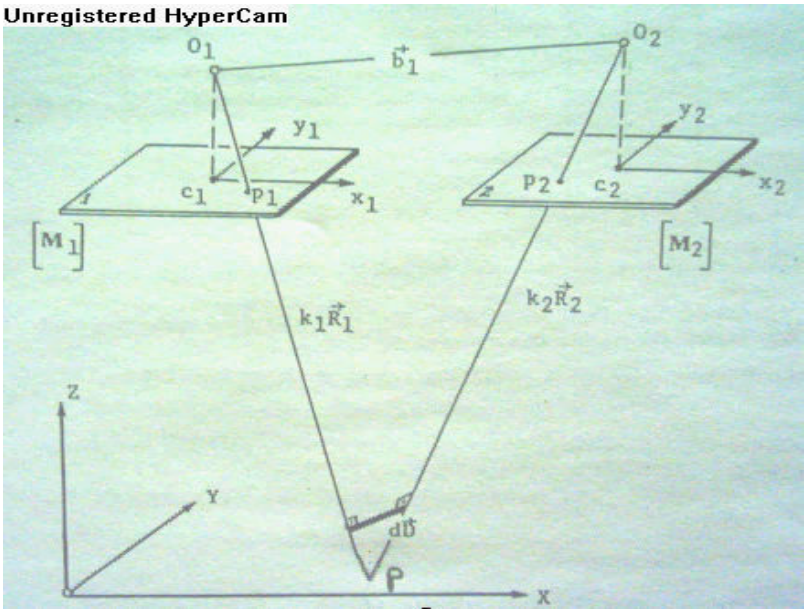

Fig. (2) The intersection concept in coplanarity condition

The direction (but not the length) of vector $\vec{D}$ which is perpendicular to both $\vec{R}_1$ and $\vec{R}_2$ is given by:

$$\vec{D} = \vec{R}_1 \times \vec{R}_2 \qquad \text{.....(31)}$$

From this it is apparent that

$$K_1 \cdot \vec{R}_1 + d \cdot \vec{D} + K_2 \cdot \vec{R}_2 = \vec{b} \quad (32)$$

Where K_1, K_2 and d are three unknown scalar multipliers (scale factors). Equation (32) has three components and, therefore, it may be solved for the three scalars.

The vectors $\vec{R}_1$ and $\vec{R}_2$ are determined using Eqs. (3) & (4) after evaluating the final matrices $[M_1]$ and $[M_2]$. The base components (b_x, b_y, b_z) are also determined after the relative orientation procedure.

Equation (31) can be written in the form:

$$\vec{D} = \begin{bmatrix} D_X \\ D_Y \\ D_Z \end{bmatrix} = \begin{bmatrix} Y_1 Z_2 - Z_1 Y_2 \\ Z_1 X_2 - X_1 Z_2 \\ X_1 Y_2 - Y_1 X_2 \end{bmatrix} \quad .(33)$$

Since the triangulation is performed in the X direction (of strip), it is possible, as a harmless approximation of this condition, to choose for $\vec{D}$ the unit vector along the Y direction (i.e.,Y Parallax in the model space). In this case the scalars K_1 and K_2 are given by:

$$K_1 = \frac{R_{2Z} \cdot b_x - R_{2X} \cdot b_z}{R_{2Z} \cdot R_{1X} - R_{2X} \cdot R_{1Z}} \quad (34)$$

And

$$K_2 = \frac{R_{1X} \cdot b_z - R_{1Z} \cdot b_x}{R_{2Z} \cdot R_{1X} - R_{2X} \cdot R_{1Z}} \quad .(35)$$

Here, the coordinates of the required point P are:

$$\left.\begin{aligned} X_P &= X_{O1} + K_1 \cdot R_{1X} \\ Y_P &= 1/2\left[\left(Y_{O2} + K_2 \cdot R_{2Y}\right) + \left(Y_{O1} + K_1 \cdot R_{1Y}\right)\right] \\ Z_P &= Z_{O1} + K_1 \cdot R_{1Z} \end{aligned}\right) \quad (36)$$

The residual Y parallax which is the scalar d_1 is given by:

$$d_1 = \left(Y_{O2} + K_2 \cdot R_{2Y}\right) - \left(Y_{O1} + K_1 \cdot R_{1Y}\right) \quad (37)$$

RESULTS

The results that have been gained in this research are:-

1- Relative Orientation:-

	Y_{L2} **(m.)**	Z_{L2} **(m.)**	ω **(rad.)**	ϕ **(rad.)**	κ **(rad.)**
value	2360.129	3699.116	-0.0093	-0.0099	2.1259
σ^2	1.8415	1.7578	5.143*10^-8	1.259*10^-7	1.625*10^-8

2- Space Intersection:-

point	X (m.)	Y (m.)	Z (m.)	Parallax (mm.)
1	5985.340	153.897	1079.300	0.532
2	7824.516	709.731	1089.001	0.400
3	8500.109	1568.394	1087.120	0.009
4	7911.999	2839.722	1104.580	0.987
5	7054.110	2061.984	1088.110	0.031
6	5610.441	930.651	1081.125	1.631

CONCLUSION

Methods for recovering the relative orientation of two cameras with respect to each other are of importance in aerotriangulation problem. An usual iterative method for finding the relative orientation parameters then easily computed the ground coordinate points that appear in the coplane between two pairs of stereo photographs, has been described here. This method does not use the traditional colliniarity condition equations, even in intersection problem; but it uses the coplanarity condition equation, which is rather hard equation (after linearization) as compared with the colliniarity. The results that have been gained were so good, and encourage to apply on more than two photos.

REFERENCES

Ayman Habib, Hsiang Tseng Lin & Michel Morgan, (2003), Autonomous space resection using point-and line-based representation of free-form control linear features, Internet document,.

Berthold K.P.Horn, (1990), Relative orientation , Internet document,.
Francis H.Moffitt & Edward M.Mikhail, (1980), Photogrammetry, 3rd edition,.

Paul R.Wolf, (1985), Elements of photogrammetry, 2nd edition,.

Salama C.C., (1980), Manual of photogrammetry, 4th edition,.

Sanjib K.Ghosh, (1985), Phototriangulation,.

EVALUATION OF THERMAL SRESSES IN CONTINOUOS CONCRETE BRIDGES

Dr.Ramzi B.Abdul-Ahad
Department of Building
Assistant Professor

Mrs. Shahala'a A.Al--Wakeel
Assistant Lecturer

Construction Engineering
University Of Technology
Iraq- Baghdad

ABSRACT
This search is mainly concerned with making a comparison between three methods for analyzing continuous concrete bridges, Priestly, Abdul-Ahad and finite elements. Three standard Design temperature distribution, New Zealand, AASHTO and British (5400) were used to analyze the concrete bridges in Baghdad. The analysis of two continues precast prestressed concrete bridges in Baghdad are presented. Another comparison as made between the thermal stresses and the stress associated with dead and live loads. Analytical results indicated that stresses and curvature values are very sensitive to the type of temperature distribution assumed. The suggested analytical models for the bridge can be used to be predict thermal movement and stresses due to any shape of temperature distribution.

الخلاصة

يتعلق هذا البحث بصورة رئيسية بعمل مقارنة بين ثلاث طرق للتحليل الحراري للجسور الخرسانية ذات العتبات المستمرة، طريقة برز تلي، عبد الأحد والعناصر المحددة. ثلاث من المواصفات القياسية للتوزيع الحراري، النيوزلندية، الأمريكية AASHTO والبريطانية رقم 5400 اعتمدت في تحليل الجسور الخرسانية. تم تحليل جسرين مشيدين من الخرسانة المسبقة الجهد والصب في منطقة بغداد، وعمل مقارنة أخرى بين الاجهادات الحرارية والاجهادات نتيجة الأحمال الميتة والحية. أظهرت النتائج التحليلية إن قيم الاجهادات والانحناءات تتأثر بصورة مباشرة بشكل التوزيع الحراري. الموديلات التي تم اقتراحها في هذا البحث يمكن استخدامها لحساب الاجهادات والازاحات الحرارية لأي شكل من التوزيع الحراري.

KEY WORDS
Bridge structures, finite elements, thermal stresses...

INTRODUCTION

General Effect of Temperature on Bridge

Bridge structures are usually subjected to a complex environmental exposure that changes with time. The ambient air temperature, solar radiation, air velocity, and humidity are the parameters most significant to produce changes in bridge temperatures. As indicated for a typical section in

Fig. (1), ambient air temperature and solar radiation can be expected to follow two cycles, diurnal and yearly. The daily cycle produces temperature fluctuations and variations in the bridge structure. The yearly cycle is responsible for overall expansion and contraction bridge deck movements (Emanuel, 1978) . Further

Understanding of bridge behavior due to thermal effects is needed for design purposes. Most of the existing codes have no direct provisions, which guide the designer on how to calculate thermally induced stresses. Temperature stresses in a bridge structure due to non-uniform temperature distribution have attracted the attention of several investigators. It has been established in general that temperature induced stresses must be considered in the design of bridge superstructures (Rodolli, M., 1975).

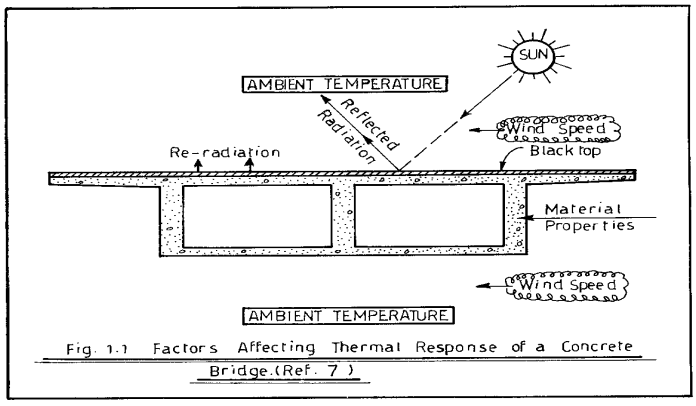

Fig. (1) Factors Affecting Thermal Response of a Concrete Bridge. (Priestly, M. J. ,1978)

Thermal Stresses (Johns, D. J. , 1965)

Most substances expand when their temperature is raised and contract when cooled, and for a wide range of temperatures this expansion or contraction is proportional to temperature changes. This proportionality is expressed by the coefficient of linear thermal expansion (α) which is defined as the change in length which a bar of unit length undergoes when its temperature is changed by 1˚c. If free expansion or contraction of all the fibers of a body is permitted, no stress is caused by the change in temperature. However, when the temperature rise in a homogeneous body is not uniform, different elements of the body tend to expand by different amounts and the requirement that the body remains continuous in the same initial shape conflicts with the requirement that each element expands by an amount proportional to the local temperature rise. Thus the various elements exert upon each other a restraining action resulting in continuous unique displacements at every point. The system of strains produced by this restraining action cancels out all, or part of, the free thermal expansions at every point. This system of strains must be accompanied by a corresponding system of self-equilibrating stresses. These stresses are known as thermal stresses. Also, if the temperature change in a homogeneous body is uniform and external restraint limits the amount of expansion or contraction, the stresses produced in the body are termed thermal stresses.

THERMAL MOVEMENT

Thermal movement of a concrete bridge involves a displacement and a rotation caused by a combination of many factors such as:

The time-dependent solar radiation, air temperature, material properties (coefficient of thermal expansion, modulus of elasticity, shrinkage, creep), surface characteristics, section geometry, span length, types of bearing[4].The movement discussed in this research is the longitudinal movement

(the longitudinal expansion and contraction movements). The magnitude of the range of movement experienced by a bridge during its life is one of the factors which influence the choice of both the type of expansion joints and the type of bearing to be used .(Emerson, M., 1981) Additional movements at joints can occur due to settlement, accidental structural damage, wind and vehicle impact. The magnitude of these movements is dependent on the severity condition. These movements are not considered in this paper.(Roland, L. P., 1983)

METHODS OF ANALYSIS

1- Priestly Method

A theory was presented by Priestly[7] enabling longitudinal temperature induced stresses to be predicted for an arbitrary section shape subjected to an arbitrary vertical temperature distribution. The following assumptions are made in developing the theory:

a- Material properties are independent of temperature.
b- Homogeneous isotropic behavior is assumed.
c- Plane sections remain plane after bending is valid.
d- Thermal stresses can be considered independently of stress or strain imposed by other loading conditions.
e- Temperature varies with depth, but it is constant at all points of equal elevation.

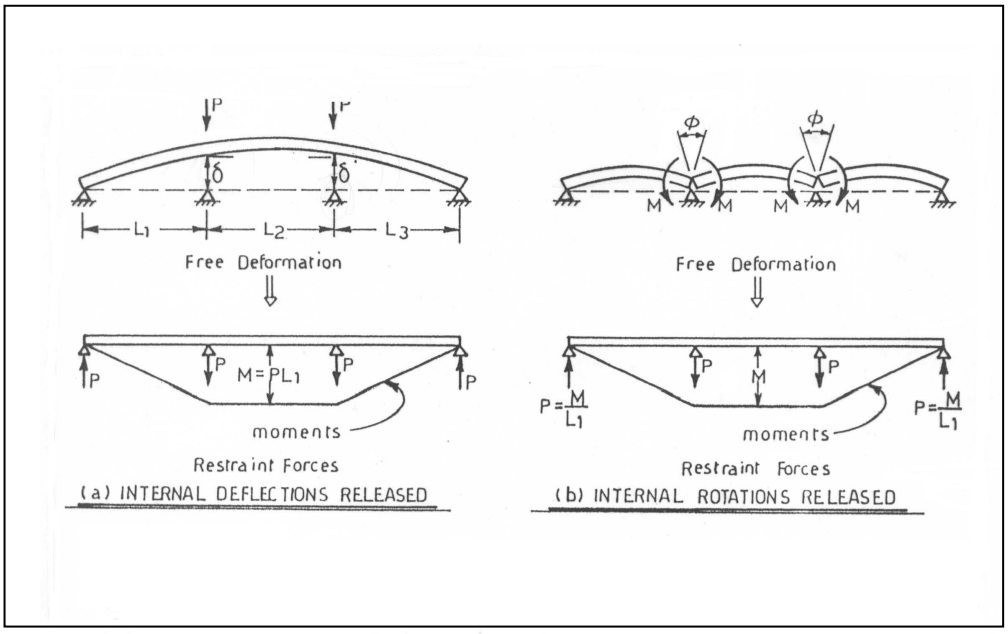

Fig.(2) Thermal Continuity Forces by Removal of Internal Redundancies. (Priestly, M. J. ,1978).

The Concept of Equivalent Temperature Difference

A procedure was developed by Abdul-Ahad[8] for calculating thermal stresses induced in continuous bridge structures by using the equivalent linear temperature distribution. The following steps are followed:

Step1-Compute the eigen stresses through the bridge cross section due to applied temperature distribution

Step2- Find the temperature required to produce eigen-stresses.

Step3- The temperature found in step 2 is subtracted from the applied Thermal load.

Step4-The temperature found in step3 is the linear temperature, which causes the deformation of the structure. The nonlinear part of the temperature which gives the eigen - stress does not cause any deformation because the resulting forces are self-equilibrating.

Step5- The linear temperature is applied as a load on the structure.

Through the use of this procedure, any shape of temperature distribution can be represented by an equivalent linear temperature distribution so that the linear temperature can be applied as a load on the structure using any readily available program by assuming a two – dimensional frame model to include the flexural stiffness of the piers.

The Finite Element Formulation

-A readily available computer program SAP86 was used. It is a finite element program for analyzing linear structural systems.

-The analysis was carried out by using 4-noded two-dimensional finite element.

-The Two-dimensional quadrilateral element which has been used in the mesh was plain stress elements. Each of the four nodes comprising the two-dimensional finite element has translational degrees of freedom in only Y and Z global coordinate directions.

- For the (2-dimensional) case plain stresses we have σ_y, σ_Z and τ_{yz} exist. The normal stress in x-direction is zero.

-For linear elastic isotropic material:

Ey=Ez=E

Vy=Vz=V

Gyz=G= $E \,/\, 2\,(1 + v)$

$\alpha y = \alpha z = \alpha$

-Thermal load: The program computes thermal load using the nodal temperature. The specified nodal temperatures describe the actual temperature distribution in the structure.

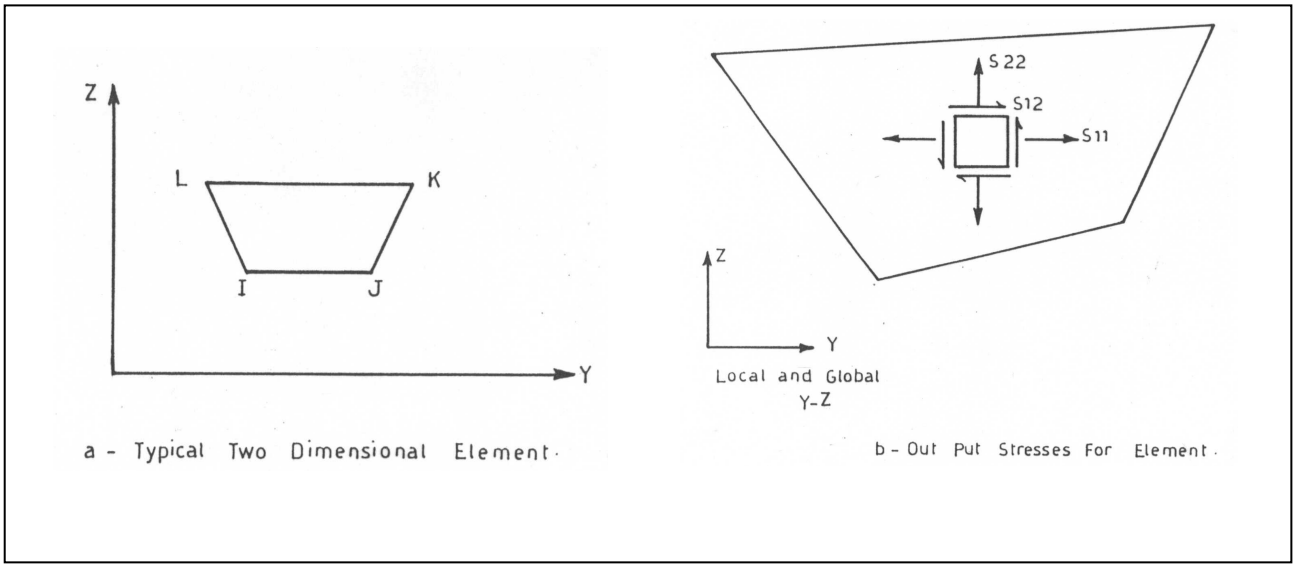

Fig.(3) Typical Element and Stress Output for Two Dimensional Finite Elements.

CASE STUDY

Tow types of prestressed concrete bridge have been investigated in this research. Thermal stresses and curvatures have been computed due to number of different temperature distributions.

1- Case A: Bab Al-Mouadam bridge (previously called 17 th July bridge).
2- Case B: Baghdad-Abughraib Bridge (A7).

In order to obtain an analytical solution, a model for the bridge is needed. Two analytical models are presented for each bridge:

Model No.1: A Simple Continuous Model.
Model No.2: Longitudinal Frame Model.

1-Case A: Bab Al-Mouadam bridge (previously called 17 th July bridge).:

After presenting the methods of the analysis, it is pertinent to apply the analysis to existing bridges.**Fig. (4)** shows the first model of the bridge the simple continuous one while **Fig. (5)** shows the second model of the bridge.

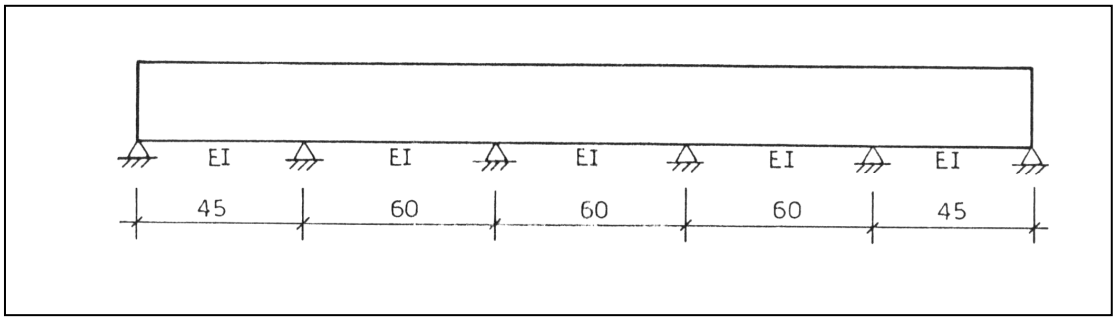

Fig. (4) Model No.1 of the Bridge Case A

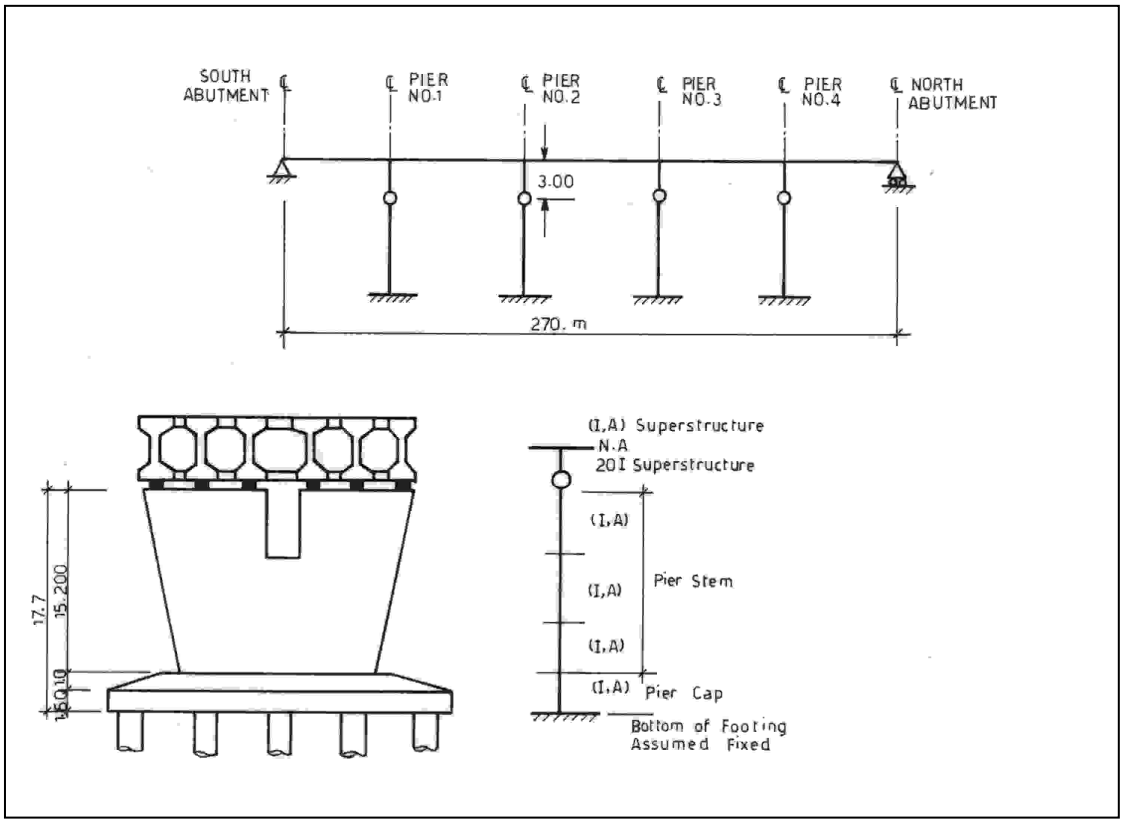

Fig. (5) Model No.2 of the Bridge Case A

Fig. (6) shows a typical comparison of curvature values due to different temperature gradients. The maximum value of curvature was obtained from ASSHTO Specification,($7.36*10^{-5}$ m^{-1}), while the value of curvature due to New Zealand and B.SSpecification are ($6.36*10^{-5}$ m^{-1}) and ($1.92*10^{-5}$ m^{-1}).

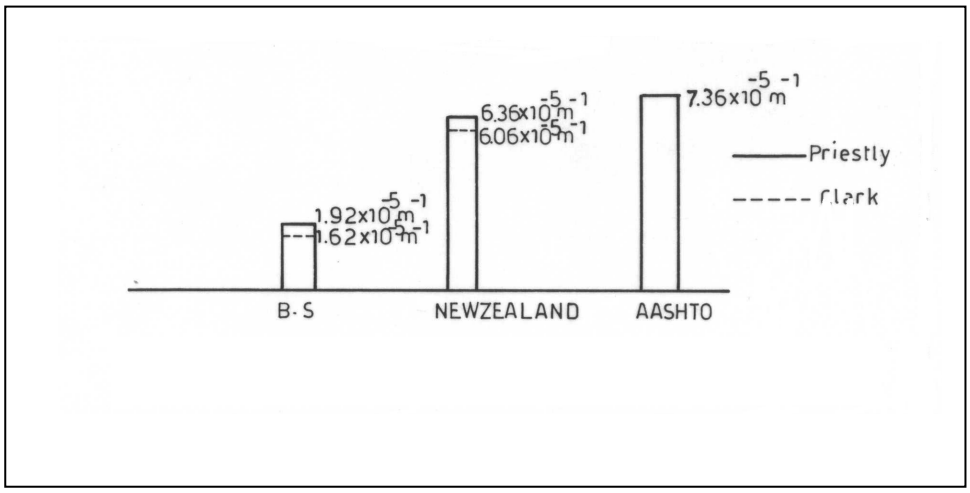

Fig. (6) Curvature Between Priestly and Clark Methods Due to Different Thermal Gradients for Bridge Case A.

Fig.(7) gives the maximum moment by AASHTO specification as (73.15 MN.m) by using Priestly method, while the values of moment by New Zealand and B.S. standards are (63.33MN.m) and (19.16 MN.m).

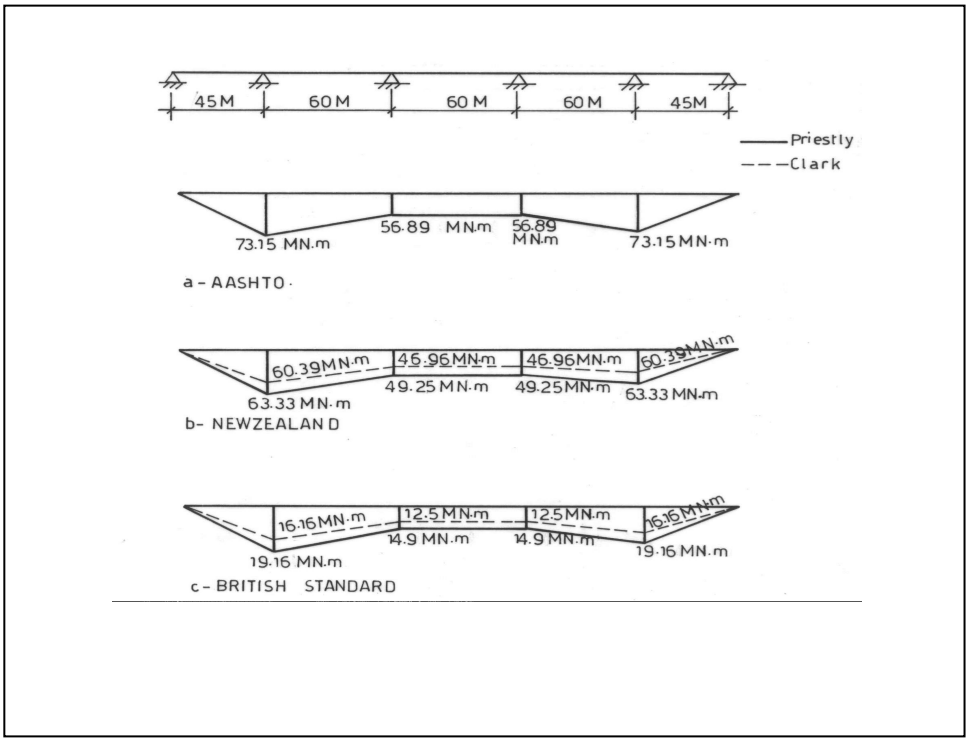

Fig. (7) Thermal Moment Comparison Between Priestly and Clark Methods Due to Different Thermal Gradients For Bridge Case A.

Fig. (8) indicates the sum of self -equilibrating and continuity stresses for different temperature distributions. Maximum value of compressive stress by New Zealand specification is about (2.2) times as large as those given by AASHTO and B.S. standards, while the maximum tensile stress by AASHTO is about (4) time as large as that obtained from B.S. standard and one time larger than that obtained from AASHTO specification.

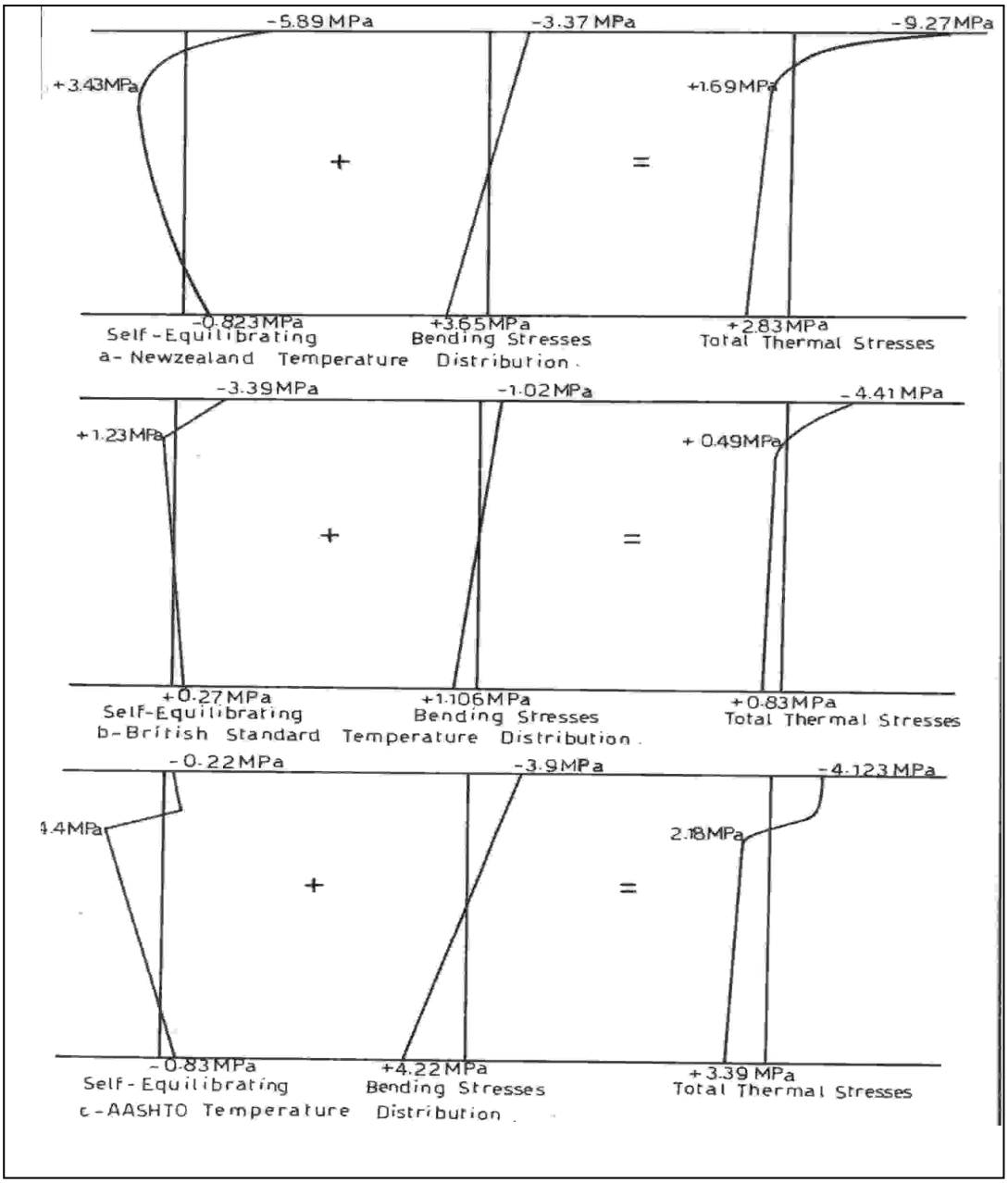

Fig. (8) Self-Equilibrating Continuity and Total Stresses Due to Different Temperature Distributions for Bridge Case A

Fig. (9) illustrates the equivalent linear temperature distribution for different temperature gradients. This temperature was applied as a load using model No.1. It is apparent that the bending moment and stresses computed by Priestly are about (81.3%) and (81.3%) of the moment and stresses computed by Abdu-Ahad using AASHTO specification.

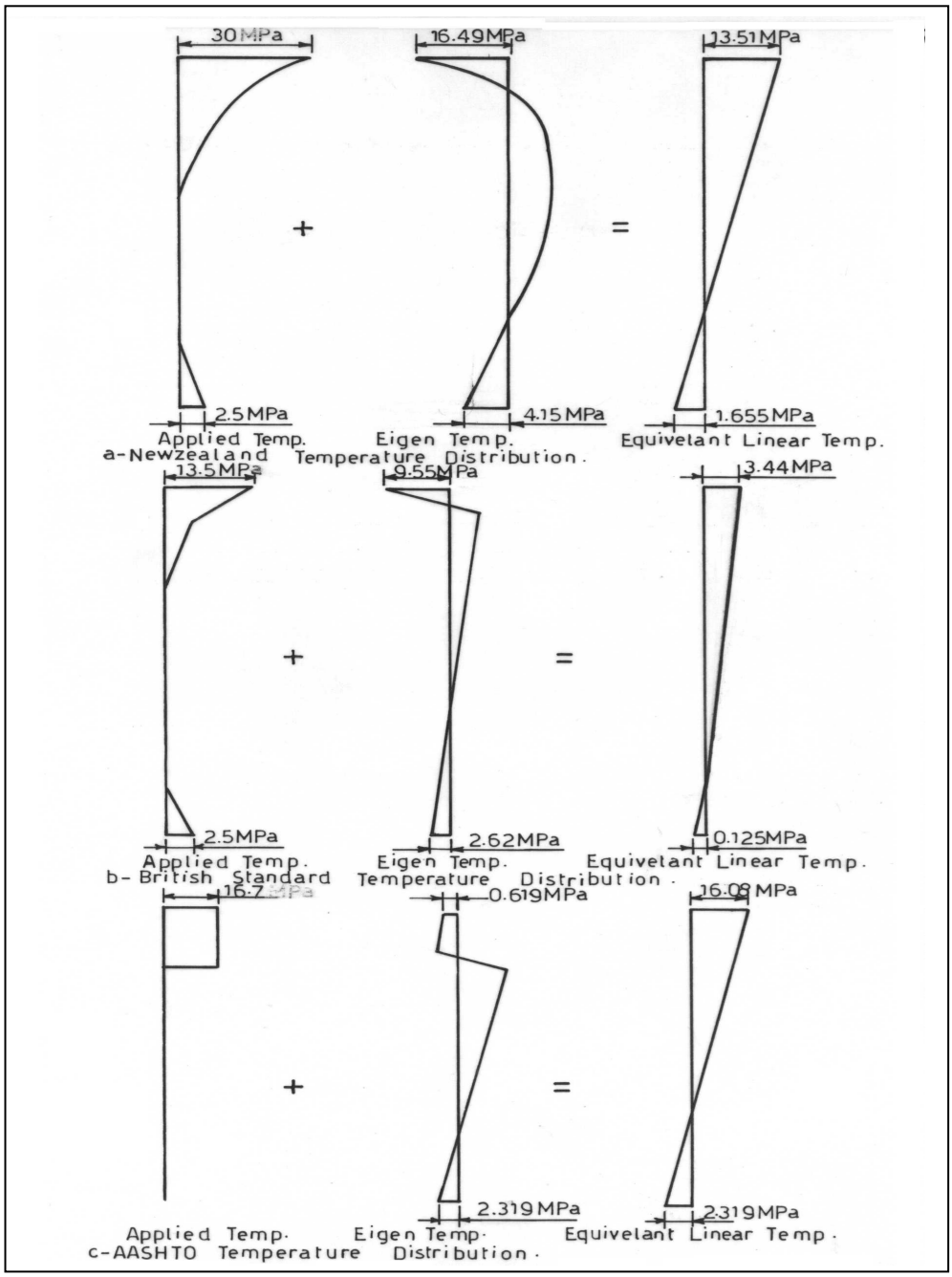

Fig. (9) the Equivalent Linear Temperature Distributions For Different Design Temperature Gradients For Bridge Case A.

Fig. (10) shows the longitudinal frame model for the bridge and using Abdul-Ahad method due to different temperature distributions. This model was used to predict the longitudinal movement at the abutment.

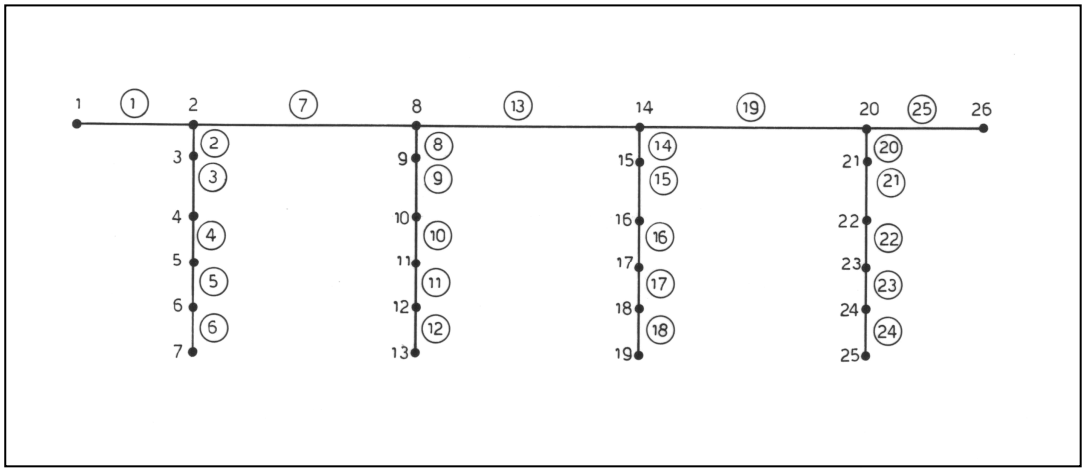

Fig.10) Beam Element of the Bridge Case A.

Fig (11) shows the mesh of the finite element for beam layout, the properties Listed in **Table (1.)** have been used as input data in the SAP Program.

Table1 Properties of Concrete

Property	Value
Modulus of Elasticity (Ec)	30×10^3 MPa
Poissen's Ratio (υ)	0.2
Shear Modulus (Gs)	12500 MPa
Coeffecient of Thermal Expansion (α)	$12 \times 10^{-6}/C^{\circ}$

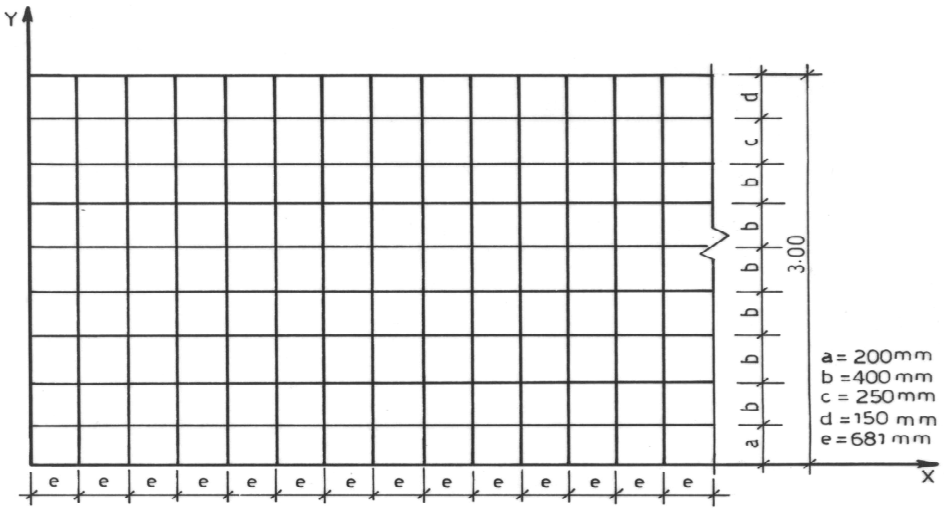

Fig. (11) The Mesh of The Finite Element Analysis For Beam of Bridge Case

Fig (12) shows a good agreement of stress values between Priestly and finite element methods using model **No.1** due to different temperature distributions.

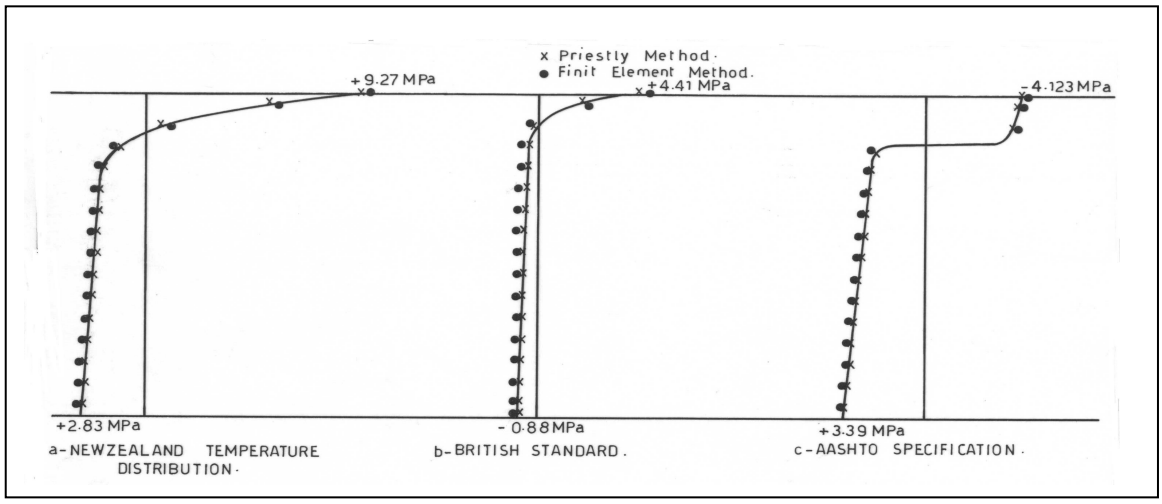

Fig.(12) Total Thermal Stresses Comparison Between Priestly And Finite Element Methods Due to Different Design Temperature Distributions For Bridge Case A.

Fig. (13) shows the stress distribution produced at the end of the first span by dead, live and thermal loads, due to New Zealand, British and AASHTO specifications. It appears that AASHTO specification overestimates the maximum tensile stress. While the maximum compressive stress induced by the New Zealand specification.

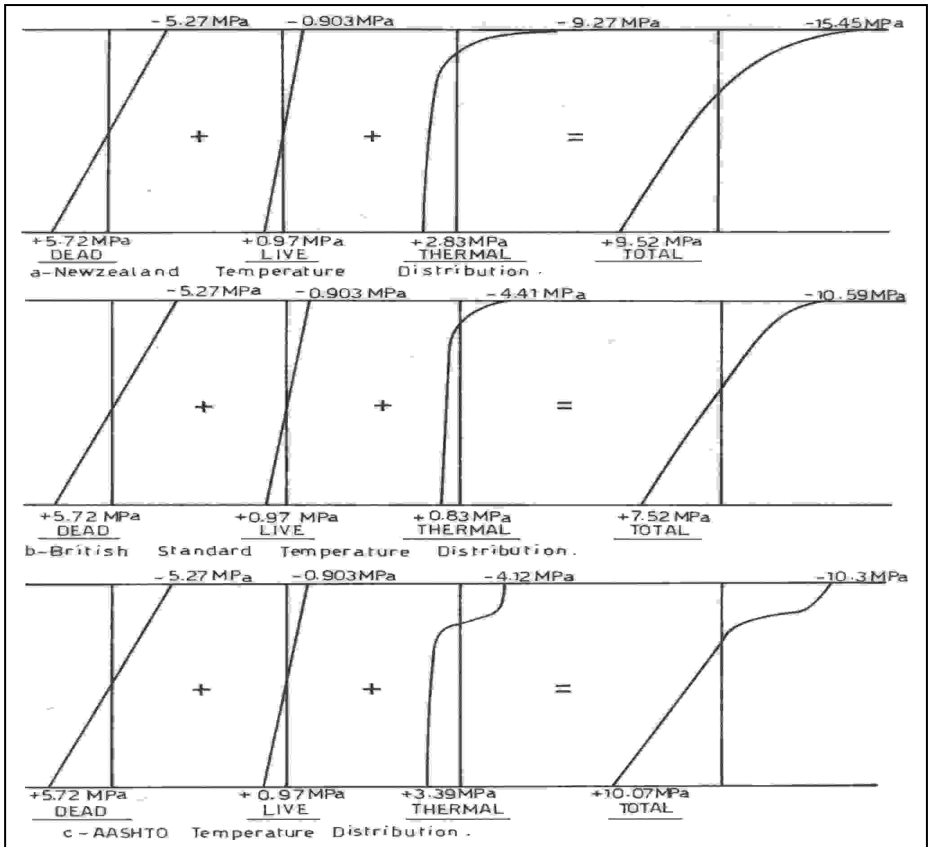

Fig.(13) Service Load Stresses Including Thermal Stresses Due to Different Temperature Distributions For Bridge Case A.

Case B: Baghdad-Abughraib Bridge (A7)

The same methods presented were used in the analysis of this bridge**.Fig. (14)** shows the first model of the bridge, the simple continuous one.

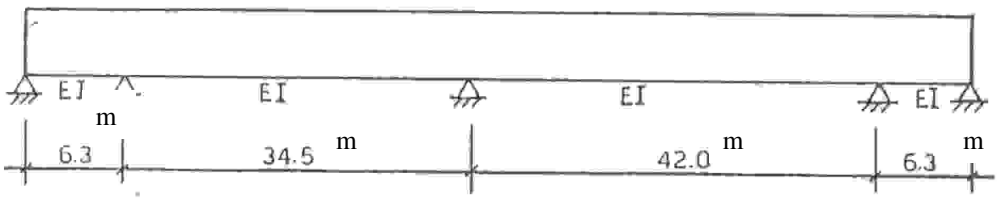

Fig.14 Model No.1 of the Bridge Case B.

Fig. (15) shows the second model of the bridge.

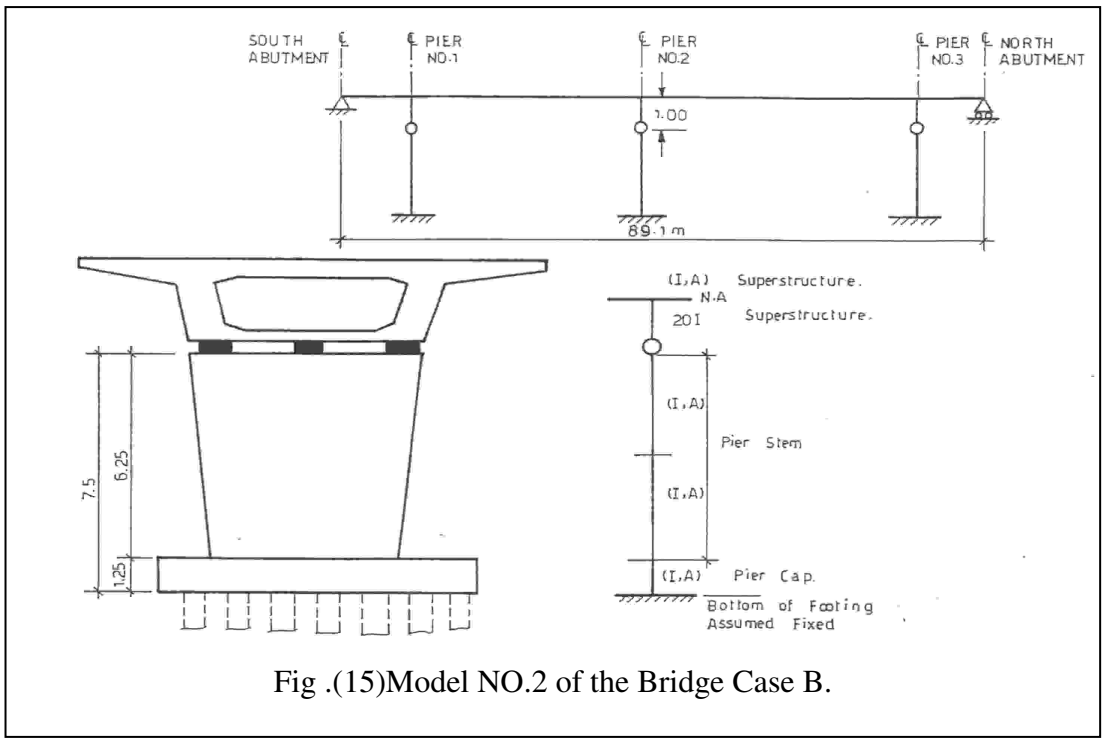

Fig .(15)Model NO.2 of the Bridge Case B.

Fig. (16) shows a typical comparison of curvature value due to different temperature gradients. A maximum value of curvature was obtained from AASHTO specification ($15.22*10^{-5}$ m^{-1}), while the value of curvature by New Zealand and B.S. specifications were ($12.96*10^{-5}$ m^{-1}) and ($3.96*10^{-5}$ m^{-1}).

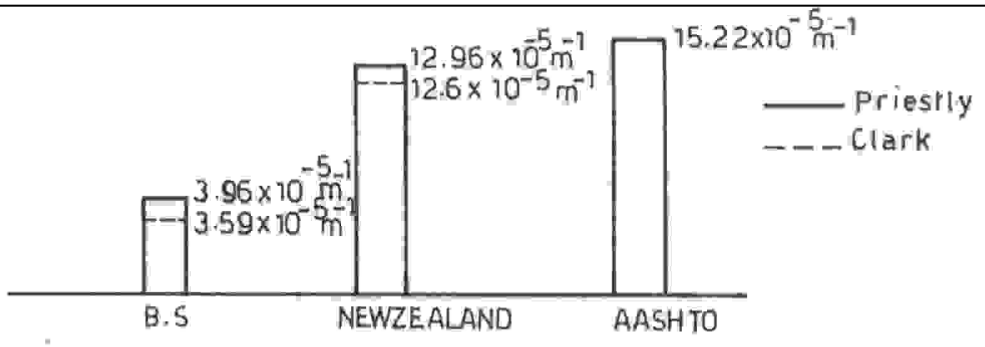

Fig.(16)Curvature Comparison Between Priestly and Clark Methods Due to Different Thermal Gradient for Bridge Case B

Fig. (17) indicates the maximum moment due to AASHTO (18.77MN.m) specification, using Priestly method, while the values of moment by New Zealand and B.S. were (15.99MN.m) and (4.88MN.m).

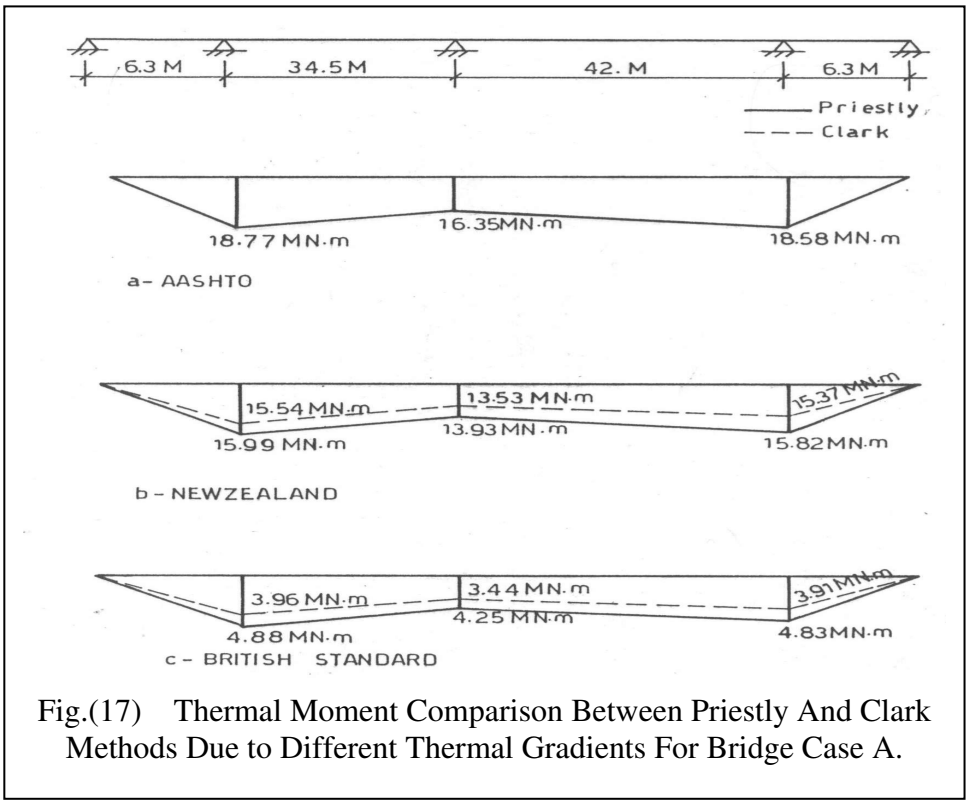

Fig.(17) Thermal Moment Comparison Between Priestly And Clark Methods Due to Different Thermal Gradients For Bridge Case A.

Fig. (18) indicates the sum of self-equilibrating and continuity stresses for different temperature distributions. The maximum value of compressive stress by New Zealand standard is about (2.0) times as large as those given by AASHTO and B.S.standards, and the maximum tensile stress by AASHTO is about (4.5) times as large as that obtained from B.S standard and (1.25) times larger than that obtained from AASHTO specification.

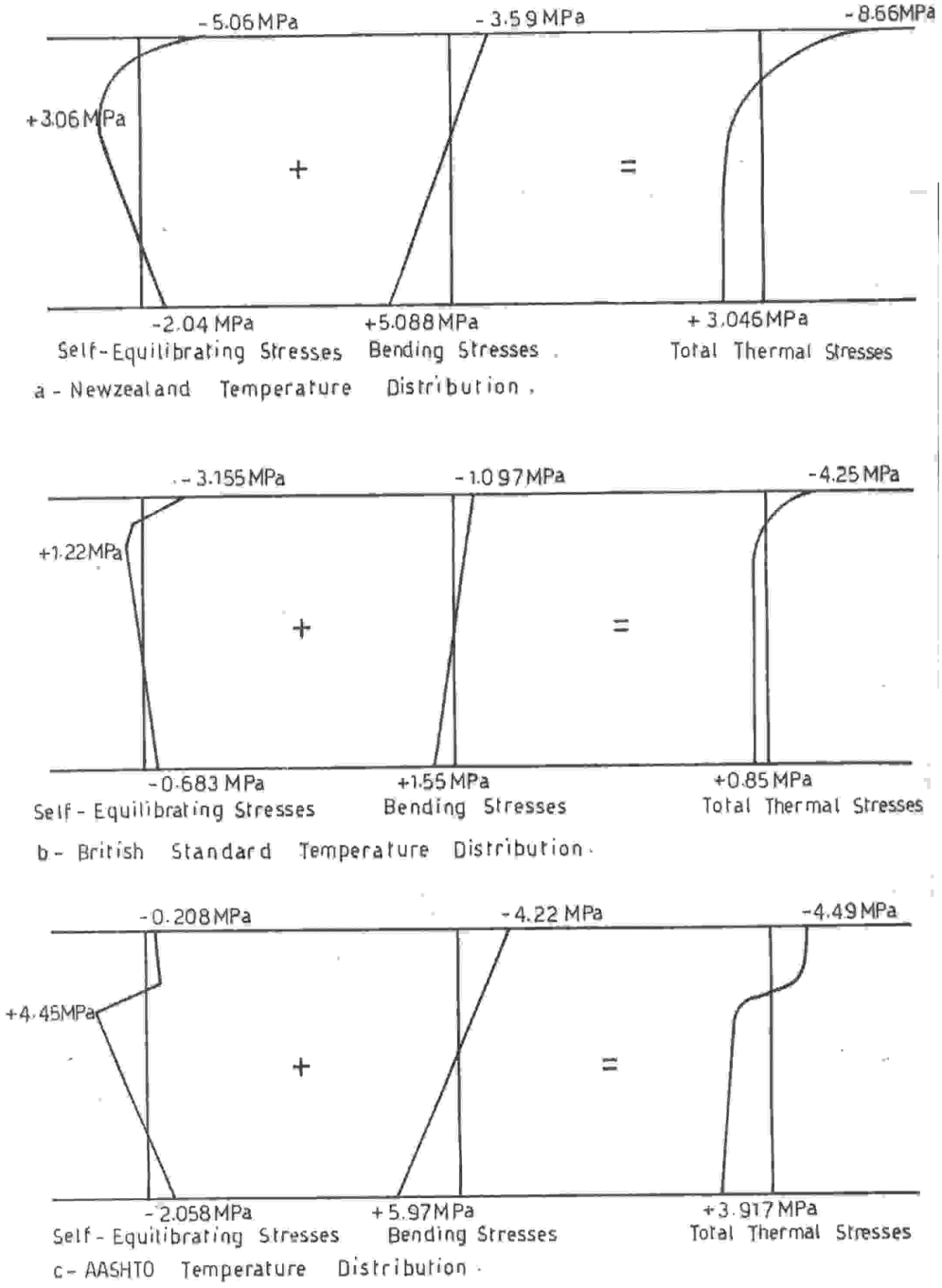

Fig.(18).Equilibrating, Continuity And Total Stresses Due to Different Temperature Distributions For Bridge Case B.

Fig. (19). illustrates the equivalent linear temperature distribution for different temperature gradients.

This temperature was applied as a load using model No.1, It is apparent that the bending moment and stresses computed by Priestly method are about (57.6%) and (57.6) of the moment and stresses computed by Abdul-Ahad using AASHTO specification.

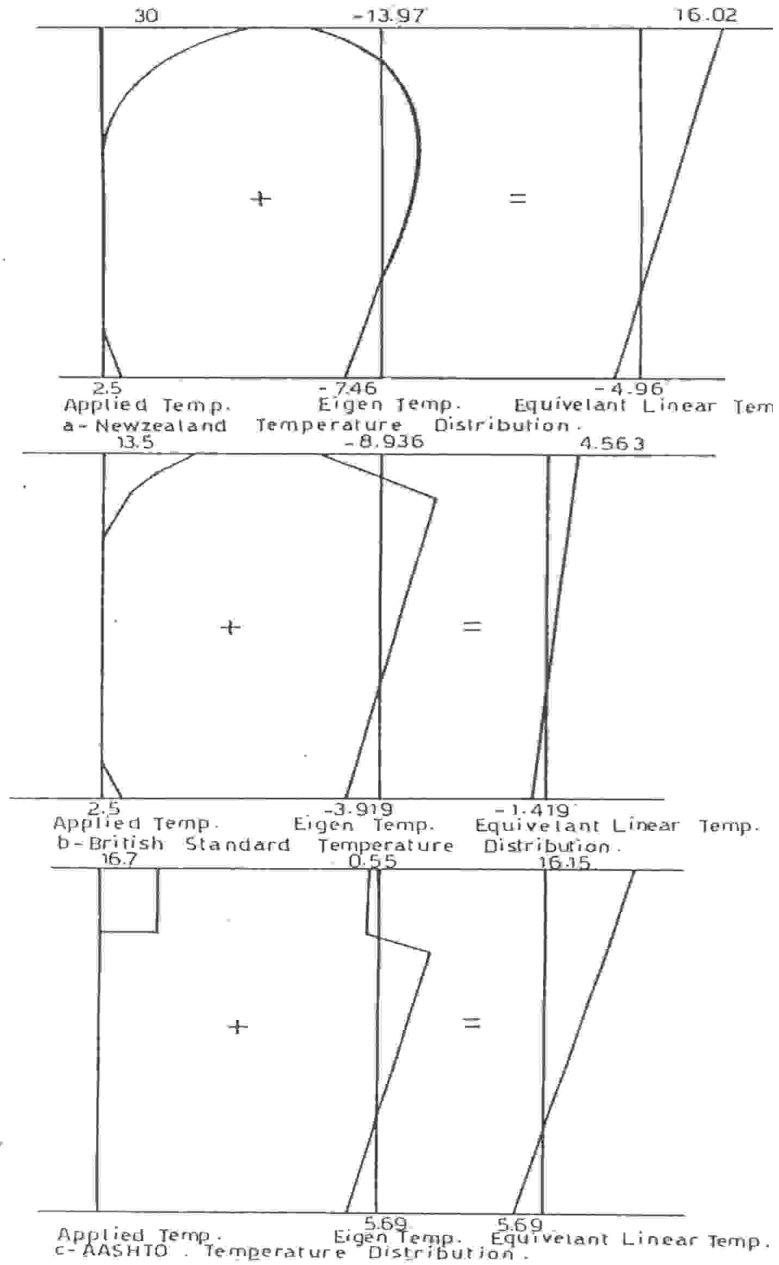

Fig. (19)The Equivalent Temperature Distribution For Different Design Temperature Gradients For Bridge Case B.

Fig. (20). shows the longitudinal frame model for the bridge using Abdul-Ahad method due to different temperature distributions, this model was used to predict the longitudinal movement at the abutment.

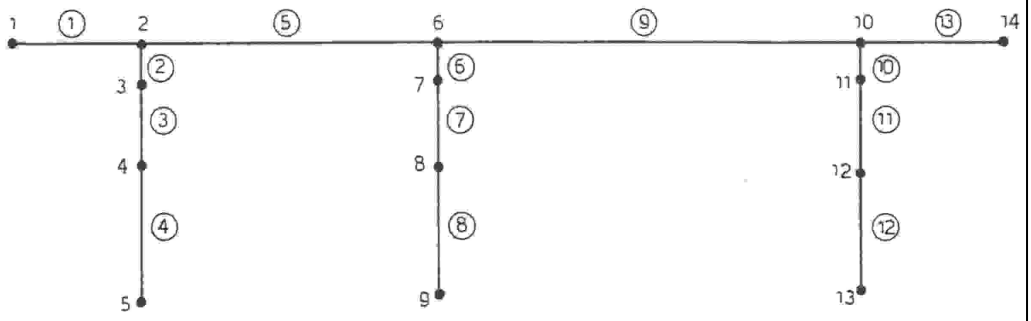

Fig.(20) Beam Element of The Bridge Case B.

Fig. (21) shows the mesh of the finite element for beam layout, the same properties listed in **Table 1** were used.

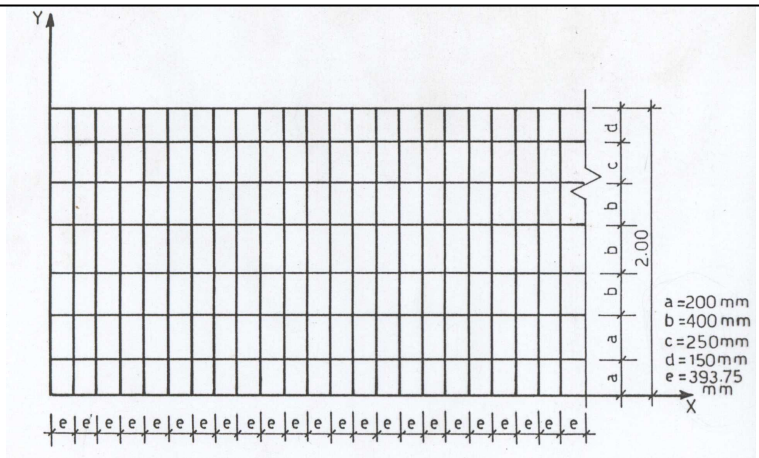

Fig. (21) the Mesh of the Finite Element Analysis for Beam of Bridge Case B.

Fig. (22) shows a good agreement of stress values between Priestly method and the finite element method using model No.1 due to different temperature distributions.

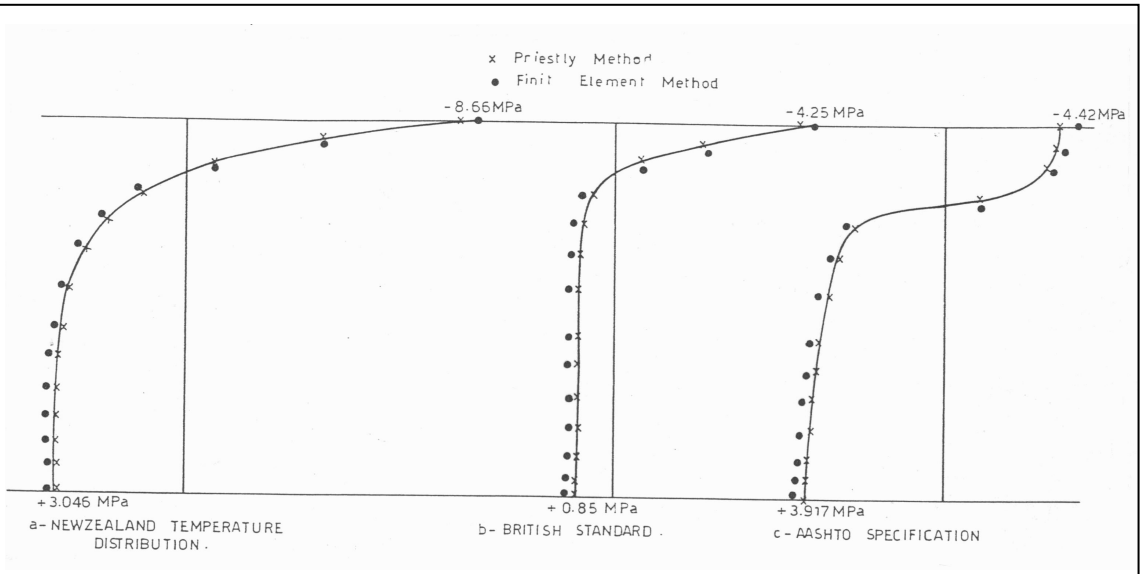

Fig. (22) Total Thermal Stresses Comparison Between Priestly And Finite Element Method Due to Different Temperature Distributions For Bridge Case B.

Fig. (23). shows the stress distribution produced at the end of the first span by dead, live and thermal loads, by New Zealand, British, AASHTO specifications. It appears that AASHTO specification overestimates the maximum tensile stress, while the maximum compressive stress induced by the New Zealand specification.

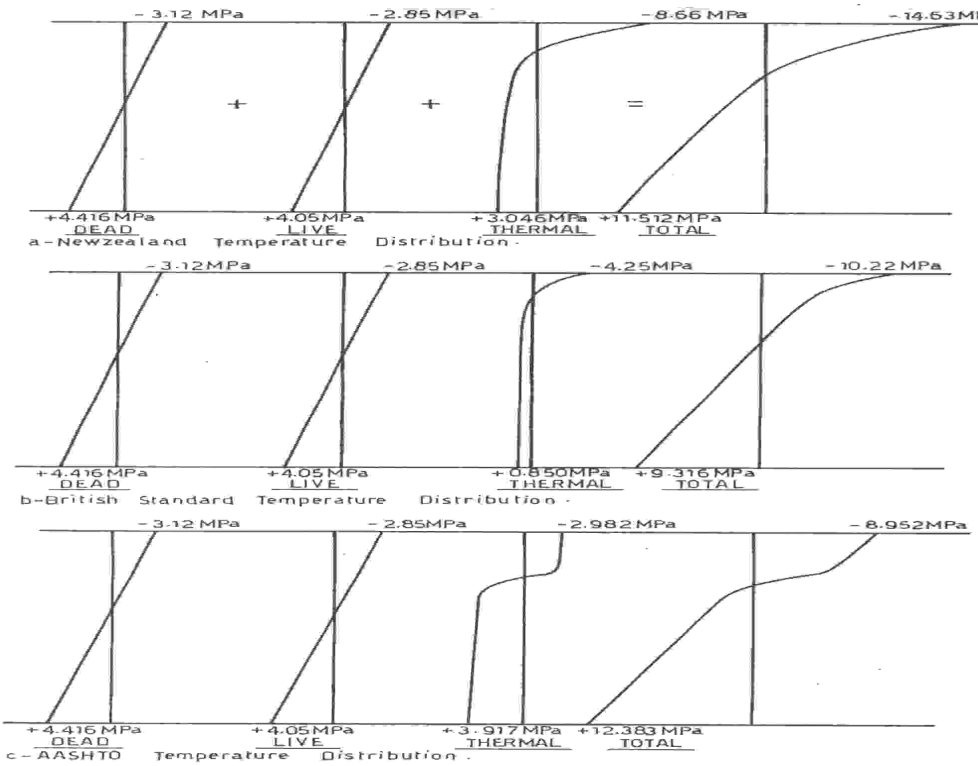

Fig.(23)Service Load Stresses Including Thermal Stresses Due to Different Temperature Distributions For Bridge Case B.

However, it can be concluded that thermal effects must be considered when assessing the serviceability of the bridge under design conditions.

CONCLUSIONS

- Results showed that the magnitudes of the longitudinal and continuity stresses depend on both the magnitude and the temperature distribution through the cross section of the bridge.
- The bridge geometry will influence the longitudinal movements that occur as a result of temperature change. Analysis of two selected bridges with various lengths indicates that the longer bridge exhibits larger movement.
- For the two cases studied, comparison between the three codes indicate that there is a convergence between the New Zealand and AASHTO specifications in calculating the curvature and the moment while the British standard underestimates these values.
- For higher temperature with B.S (5400), the agreement with the other two codes becomes better in calculating curvatures and moments.
- The analytical models developed for the bridge which greatly simplify the complexity and dimension of the problem, can be used to predict thermal stresses, due to any shape of temperature distribution.

REFRENCE

Emanuel, J.H. , (1978), Temperature Distributions in Composite Bridges., Journal of the Structural Division ASCE, Vol.140, No.ST1, Jan., pp.65-77.

Rodolli, M., and Green, R., (1975), Thermal Stresses in Concrete Bridge Superstructures Under Summer Conditions., Presented at the 54th Anual Meeting, Transportation Research Board, Washington, D.C., Jan., pp.23-36.

Johns, D.J., (1965), Thermal Stress Analysis., First Edition, Robert, Maxwell, M.C., M.P., New York, , pp.1-5.

Cope, R.J., (1987), Concrete Bridge Engineering Performance and Advances., ELSEVIER Applied Science Publishers Ltd., London, , pp.143-184.

Emerson, M., (1981), Thermal Movements of Concrete Bridges: Field Measurements and Methods of Prediction., Volume1, World congress on Joints and Bearings, Publication sp-70, American Concrete Institute, Detroit, , pp.77-94.

Roland, L.P. and Roland, H.B., (1983), Bridge Joint Maintenance., National Research Council, National Academy of Sciences, Washington, , pp.1-10.

Priestly, M.J.N., (1978), Design of Concrete Bridges for Temperature Gradients., American Concrete Institute, ACI, Journal, No.75, May, pp.209-217.

Abdul-ahad, R.B., (1981), Effects of Restrained Thermal Movement in A Continuous Prestressed Concrete Bridge Without Interior Expansion Joints., Thesis Presented to the University of Tennessee, at Knoxville, Tennessee, in, in Partial Fulfillment of the Requirements for the Degree of Doctor of Philosophy, with a major in Civil Engineering.

WATER PRESSURE EQUALIZATION IN PIPE NETWORK CASE STUDY: AL-KARADA AREAS IN BAGHDAD

Prof. Dr. Rafa Hashim Al-Suhaily Dr. Awatif Soaded Abdul-Hameed Hameed Mirza Mita´b
University of Baghdad/ College of Engineering/ Civil Dep

ABSTRACT
In order to make a balance between the increasing of potable water demand and the available quantity, a pipe network should be managed in an optimal hydraulic operation state. The optimal operation of a water supply network leads to minimize the effect of the variance in pressure between the available and minimum required pressure head. It simulates the hydraulic model and puts the optimized project with the constraints (minimum design head=20 m, and the available commercial pipe diameter, $1600 \geq D \geq 250$ mm). The objective function is to minimize the cost for the suggested hydraulic solution to a minimum value. Pressure uniformity coefficient (UC), Standard deviation (σ) and coefficient of variance (Cv) are used to show that the pressure head at the nodes of the network is uniformly distributed. The optimal design of the case study (R9 water supply network) has an actual cost of 561,169,310 ID and the uniformity indices of UC=99.565, σ=3.6508 and Cv=0.1543 while the existing design has cost of 856,617,170 ID with the uniformity indices of UC=97.909, σ=3.5977 and Cv=0.7906. Hence there is a benefit of 34.5% in the cost of the optimal design used in this study, with high uniformity coefficient. The effect of Hazen-William coefficient (C) on total cost showed an inversely linear effect. For the value of C=130, the actual cost was 600,898,300 ID, i.e., the penalty cost approached to zero and has no effect on the total cost.

الخلاصة

لغرض عمل موازنة بين ازدياد الاحتياج والكمية المتوفرة للمتطلب المائي وجب إدارة شبكة المياه بالشكل الأمثل للأداء الهيدروليكي.إن أفضل و أمثل ادارة هيدروليكية لشبكات المياه تقود إلى تقليل الفارق بين الضغط المتوفر من قبل الشبكة واقل ضغط مطلوب بالشبكة إلى اقل حد ممكن. عمل محاكاة إلى النموذج الهيدروليكي ووضع المشروع الأمثل مع المحددات وهي (اقل ضغط تصميمي هو 20 m و الأقطار التجارية المتوفرة $1600 \geq D \geq 250$). إن دالة الهدف تعمل على جعل كلفة الحل المقترح إلى اقل قيمة ممكنة. معامل انتظام الضغط UC, الانحراف المعياري σ والتباين Cv تستخدم كمؤشر إلى أن الضغط بالعقد للحل الأمثل للمشكلة يمتلك انتظاماً توزيعياً. أفضل تصميم لشبكة الدراسة الحقلية (شبكة ماء الكرادة R9) يمتلك كلفة هي 561,169,310 ID ومعامل الانتظام UC=99.565 , الانحراف المعياري σ=3.6508 والتباين Cv=0.1543 , بينما التصميم الحالي للشبكة بكلفة 856,617,170 ID ومعامل الانتظام UC=97.909 , الانحراف المعياري σ=3.5977 والتباين Cv=0.7906 و بذلك التصميم الأمثل في هذه الدراسة اقل كلفة بنسبة 34.5% من التصميم الحالي وكل معاملات الانتظام تدل على إن

الشبكة ذات توازن وانتظام عالي. إن تأثير معامل الاحتكاك Hazen-William على الكلفة الكلية يظهر تأثيراً عكسياً, ولقيمة C=130 تكون الكلفة الكلية وهي 600,898,300 ID . بذلك تكون ال(Penalty cost) صفراً ولايوجد لها تأثيراً على الكلفة الكلية.

KEY WORDS:
Water pressure, pressure equalization, Al-Karada water supply, pipe network, water supply, optimal design, pressure uniformity distribution

INTRODUCTION

Water is one of the essential elements of life, from early days men soon realized that rivers and streams in their natural states seldom provide, adequate water to satisfy their needs. Water is vital for human existence; without water there is no life on earth (Anis et.al., 1977) .

A water distribution network is a system containing pipes, reservoirs, pumps, valves of different types, which are connected to each other to provide water to consumers. It is a vital component of the urban infrastructure and requires significant investment(Abeb and Solomatine, 2000). The analysis of water distribution network means evaluation of quantity of water flowing through each pipe and pressure head at junction (node) of the system, while the design of water distribution network means evaluation of the diameter of each pipe and the optimum configuration according to specified requirements(Don, 1981).

The problem of optimal design of water distribution network has various aspects to be considered such as hydraulics, reliability, material availability, water quality, infrastructure and demand patterns. Even though each of these factors has its own part in the planning, design and management of the system and despite their inherent dependence, it is difficult to carry out the overall analysis. Previous research indicates that the formulation of the problem on a component basis is worthy doing. In the present study, the problem is posed as a global optimization. The optimization model determines whether the design is optimal or not, if not, the optimization model based on reducing the variance between the minimum required and modeled pressure head at the nodes. This paper deals with the determination of the optimal diameters of pipes in a network with a predetermined layout. This includes providing the pressure and quantity of water required at each demand node. An appropriate interface is created between a global optimization tool with the various random algorithms, and a network simulation model that can handle steady state condition.

EXTENT OF THE PROBLEM

The problem reduced to such an extent has two constraints from hydraulic requirements. The continuity constraints, states that the discharge into each node must be equal to that leaving the node, except for storage node (tanks and reservoirs). This secure, the overall mass balance in the network. For n nodes in the network, this constraints can be written as:

$$\sum_{i=1}^{n} Q_i = 0 \qquad (1)$$

where Q_i represents the discharges into or out of the node i (sign included).

The second hydraulic constraint is the energy constraint according to which the total head loss around any loop must add to zero or is equal to the energy delivered by a pump if there is any:

$$\sum hf = Ep \qquad (2)$$

where hf is the head loss due to friction in a pipe and Ep is the energy supplied by a pump. This embeds the fact that the head loss in any pipe which is a function of its diameter, length and hydraulic properties must be equal to the difference in the nodal heads. This constraint makes the problem highly non-linear owing to the nature of the equation that relates frictional head loss and flow. This equation can be written as:

$$hf = \frac{aQ^b}{D^c} \tag{3}$$

Where a is coefficient depending on length, roughness coefficient of the pipe, b is discharge exponent and c is exponent of pipe diameter (D) which is very close to 5 in most head loss equations(Abeb and Solomatine, 2000).

Considering the diameter of the pipes in the network as decision variables, the problem can be considered as a parameter optimization problem with dimension equal to the number of pipes in the network. Market constraints, however, dictate the use of commercially available (discrete) pipe diameters. With this constraint the problem can be formulated as a combinatorial optimization problem (Abeb and Solomatine 2000).

The minimum head requirement at the demand node is taken as a constraint for the choice of pipe diameter. Even though the use of an exhaustive search guarantees finding the global optimum, the fact that the computational time increases expontially with the dimension of the problem makes it impractical to apply them in a multimodal function like this, and especially for real life-size problems.

REVIEW OF PREVIOUS RESEARCH

Various researches have addressed this problem in a number of different ways during the past decodes. Thawat (1973), produced a non-linear programming model for computing the pipe sizes and pumping capacities that minimize the total cost, to satisfy the demand requirements. Pramod (1979), determined a method based on the critical path concept to select the optimal sets of pipe sizes for optimization of branch network by linear programming. Gerald et.al. (1981), described a gradient technique for optimization of pipe networks. It is possible to use the value of node head, the pipe flow, to calculate the gradient term ∂(cost)/∂(Hi) for each node in the network. Pramod (1983), developed a method for optimal design of multi source, looped, gravity- fed water distribution systems subjected to a single loading pattern. The method is based on linear programming technique and produces a locally optimal solution. Ronald and Karime (1983), proposed a method for least cost design of water distribution network which is based on a traditional technique of pipe network analysis. Cenedes et.al. in (1987), determined an optimal design and operation of closed hydraulic network with pumping stations and different flow rate conditions. Yu-chun et.al. (1987), utilized a model that can be used to determine the least cost design of water distribution system subjected to continuity, conservation of energy nodal heads, and reliability constraints. Kevin and Lary in (1989), determined the optimal settings for controls and pressure reducing valves. This methodology couples was based on non-linear programming technique. Ian and Fracols (1990), established a new methodology for reliability considerations directly into least cost optimization design and operation models for water supply networks. Nowar and Abbas, (1997), presented a linear programming gradient model with mathematical corrections to find the optimum (least cost) design to pipe networks for constant and variable pumping head. Objective function to be minimized represents the overall cost of the pipelines and cost of the pumping station in the case of variable pumping head. Bogumil et.al (1998), demonstrated optimization analysis by solving inverse problem such as optimal scheduling, model calibration and design. A new generic optimization approach based on a continuous assumption and the use of non-

linear mathematical programming is proposed. Abebe and Solomatine (2000), presented an approach to the optimal design of pipe networks for water distribution. The problem was solved using a global optimization tool with various random search algorithms and dynamic loading conditions. The proposed optimization setup can handle any type of loading condition and neither makes any restriction on the type of hydraulic components in the network nor does it need analytical cost functions for the pipe. Paul et.al (2002), established a new management model for optimal control and operation of water distribution systems. The proposed model makes use of the latest advances in genetic algorithm optimization to automatically determine the least cost pump scheduling operation policy for each pump station in the water distribution system while satisfying target hydraulic performance requirements.

PROBLEM FORMULATION

Constraint handling

The constraint in the problem can be grouped into the following: hydrodynamic, minimum head and commercial constraints. The hydrodynamic constraints are handled by the function network simulation model. The optimization function handled the upper and lower bound on parameter, while penalty function was used to handled minimum nodal constraints. Commercial constraints reduce the parameter space to a discrete one.
This can be adjusted to the number of available commercial pipe sizes, therefore, the search algorithms will be for the optimal pipe diameters.

Objective function

The objective function to be minimized by the optimization algorithms is the cost of the network. If the actual cost of the network is the sole objective function, then obviously the search will end up with the minimum possible diameters allocated to each of the pipes in the network. To tackle this, a penalty cost is added to the actual cost of the network based on the minimum head constraint.

Actual cost of the network

The actual cost of the network (Ca) is calculated based on the cost per unit length associated with the diameter and the length of the pipes

$$Ca = \sum_{i=1}^{n} C(D_i)\, L_i \qquad (4)$$

Where n is the number of pipes in the network and $C(D_i)$ is cost per unit length of the i^{th} pipe with diameter (D_i and length L_i.

Penalty cost

The penalty cost is superimposed on top of the actual cost of the network in such a way that it will discourage the search in the infeasible direction. It is defined on the basis of the difference between the minimum required pressure head (H_{req}) at the node and the lowest design pressure head obtained after simulation. It depends upon the degree of pressure violation and the cost of the network in some cases and is defined in the following way:

1- For networks in which all the nodal heads are greater than (H_{req}) the penalty cost is zero.
2- for the networks in which the minimum head is greater than zero but less than (H_{req}), it increases linearly with the nodal head deficit, i.e.:

$$C_{penalty} = P * \sum_{j=1}^{nn} (H_{\mathrm{mod.}} - H_{req.}) * CT \quad (5)$$

Where P is a penalty coefficient and CT is the possible cost for each variance between modeled pressure head (after simulation) and minimum required head (calculation on the cost of the commercial pipe available) in (ID/1m), CT is a function of the pipe diameter cost, i.e.:

$$CT = A D^{B} \quad (6)$$

Where A,B are a constant depending on the available commercial pipes, D is the pipe diameter in (mm) and H_{req} is the minimum required pressure head (m).
Hence the total cost (C_{total}) will be:

$$C_{total} = Ca + C_{penalty} \quad (7)$$

Optimal design of water supply network

The method used in this paper is suited for engineers of less experience in the design of water networks. The design procedure is performed by a computer program in the following manner:
After assuming the initial values of the diameter the network is analyzed by using the Hardy-Cross method (Quantity balance method). The pipes will be arranged according to the hydraulic gradient in a decreasing form, to find the lowest pressure in the network. If the modeled pressure (calculated after analysis) is less than the designed pressure then the pipe diameter of the high hydraulic gradient is increased, using larger commercial available diameter. After changing the pipe's diameter, the analysis will be repeated to finish the first attempt. The program will repeat this process until the lowest pressure reaches the designed pressure head.
For pipes of low hydraulic gradient the program will choose a smaller commercial diameter to ensure pressure equalization. The program will repeat maximization and minimization for the pipe diameter until the optimal design is reached, then the network cost is to be calculated to give the minimum cost.

INDICATORS OF THE UNIFORMITY OF THE NETWORK

To identify the uniformity of the pressure distribution in the network, the following indicators are used.

Standard Deviation (σ) and Coefficient of Variance (Cv)

Considering the Standard deviation (σ) an indicator to distribute the data from the arithmetic mean.The data used to calculate the Standard deviation (σ) are the modeled pressure heads.

$$\sigma = \sqrt{\frac{\sum_{i=1}^{nn} (P_i - P_m)^2}{n}} \quad (8)$$

Where P_i: Pressure head at node i in (m), P_m: Arithmetic mean (average pressure value in the nodes) in (m) and n total no. of nodes.
The coefficient of variance (Cv) is formed by:

$$Cv = \frac{\sigma}{P_m} \tag{9}$$

Whenever the value of the coefficient of variance (Cv) is near zero, this indicates that the pressure head in the nodes is uniform and the results are acceptable, (Subhi and Auath, 1990)

Pressure Uniformity Coefficient (UC)

UC is a measurable index of degree of uniformity obtainable for any pipe sizes operating under a specified consideration. The data used to calculate the Uniformity Coefficient (UC) are the modeled pressure heads in the nodes.

$$UC = 100\left[1 - \frac{\sum_{i=1}^{nn}\left(\left| Pi - \frac{\sum_{i=1}^{nn} Pi}{n}\right| - 0.15\right)}{\sum_{i=1}^{nn} Pi}\right] \tag{10}$$

Where P_i: Pressure head at node i in (m) and nn: total number of nodes.
A uniformity coefficient of 85% or more is considered to be satisfactory (indicative of absolutely uniform application) (Michael 1978).

WORKING ALGORITHM OF THE COST FUNCTION

The following steps are used to calculate the cost of a network **Fig. (1).**

1- Number generated by GLOBE are read from the parameter file and converted to indices of pipe sizes that represent one network.
2- The network simulation model is started.
3- The actual cost of the network (Cost1) is calculated based on pipe cost.
4- From the output file of the simulation, the nodal pressure heads are extracted and the minimum pressure is identified to calculate the penalty cost (Cost2).
5- The total cost of the network (Cost1+Cost2) is passed to the response file.
6- If the total cost is optimal then stop. If not, the input file of the simulation is updated (only the diameters are changed) and repeat steps (2-6).

CASE STUDY: AL-KARADA WATER SUPPLY NETWORK

Al-Karada (R9) water supply network located at near the end zone of Al-Rasafa section on the eastern bank of the Tigris river was the case study. Water supply network R9 is supplied from the 9-Nissan treatment plant by the main transmission pipeline and from Al-kadisia treatment plant from Al-Karak section. R9 network supplies potable water to the sections (919,921,915,913,923 ,911,907,909,925) in Al-Karada district. This distribution system was laid by the SOBEA Company and in order to define these pipes from the distribution pipeline, it is called SOBEA pipelines, see **Fig.(2), Table (1) and Table (2)** shows the properties of this network .

RESULTS OF THE COMPUTER PROGRAM FOR OPTIMAL DESIGN

To satisfy the required pressure head of ($H_{req.}$=20 m) in this network, the effect of the proposed storage tank (R9) was considered. Constructing this reservoir with a constant water level of 30 m may give the optimum design of the network as shown in **Table (3)** and **Fig. (3).** One may consider the difference in the diameter of the pipes that affect the network performance to achieve better pressure distribution as shown in **Fig. (4).** The uniformity of the optimum design for the hydraulic model is as shown in **Table (4).**

By using **Table (5),** the cost of the optimal design is 561,169,310 ID while the actual cost for the SOBEA design was 856,617,170 ID. The optimal design is 34.5% less than the actual cost of SOBEA.

EFFECT OF HAZEN-WILLIAM COEFFICIENT ON THE TOTAL COST

Water supply networks are considered important projects designed for longtime investments. The periodically design for such projects is within 50 years. Among the major factor considered in the design is the friction losses used to calculate the energy losses which affects the Hazen-William coefficient. The design diameters in the network are affected by Hazen-William coefficient. By using assuming a constant value for the Hazen-William coefficient for the whole network and Equation (7) the effect of the Hazen-William coefficient on the total cost is shown in **Table (6)** and **Fig. (5).** For example, if low value is assumed for this coefficient, the losses in the network will increase, which require using greater diameters to avoid losses in energy, as a result the network cost will increase and vice versa .The value of this coefficient is changed with time due to corrosion or incrustation in the internal pipe surface.

If the value of Hazen-William coefficient is greater than 130, the total cost is 600,893,300 ID, i.e., the penalty cost is zero and there is no effect for this coefficient on the total cost, only the cost of pipe is to be considered.

CONCLUSIONS

The following conclusions can be deduced:

1- It is possible to optimize networks with any kind of hydraulic facilities as long as network simulator is capable of handling it. Since global optimization method, work with any objective (cost) functions, they can also be efficiently be used to optimize not only design but also operation, maintenance and other aspects of water distribution networks.
2- Al-Karada water supply network is not within the optimal operating scheme.
3- The actual cost for SOBEA design pipes is greater than the optimal design by 34.5%.
4- The optimal design proposed by this study for Al-Karada water supply network has a minimum design pressure head of 20 m and uniformity indices as UC=99.565, σ =3.6508, and Cv =0.1543, i.e., uniform pressure distribution in pipe network.
5- The effect of Hazen-William coefficient (C) on the total cost of the network decreases linearly with increasing C up to 130, above this value the penalty cost will have no effect on the total cost.

REFERENCES

Abeb A. J., and Solomatine D. P. (2000), Application of global optimization to the design of pipe networks, Proceeding 3rd international conference on HYDROINFORMATICS A. S., Copenhagen, Balkema, Rotterdam, (E-mail: sol@ihe.nl).

Anis M. Al-layla, Shamim Ahmed, and E. Joe Middlebrook, (1977), Water supply engineering design, Mc-Graw Hill publication, United state of America.

Bogumil Ulanicki, Bryan Coulbeck, and Krystyana Ulanicka (1998), Generalized techniques for optimization of water networks, water software systems, De-Montfort university, The gate way, Leicester, LEI 9BK, UK, (E-mail: bul@admu.ac.uk), This work was supported by EPSRC, Grant ref: GR/K31923.

Cenedes A., Gallerano F., and Misiti A. (1987), Multi-objective analysis in optimal solution of hydraulic networks, Journal of hydraulic engineering, ASCE, 113(9), p.p. (1133-1143).

Don J. Wood, (1981), Algorithms for pipe network analysis and their reliability, University of Kentucky, water resources research institute, Lexington, Kentucky, research report no.: 127.

Gerald E. Quindry, Downey Brill E., and Jon C. Liebman (1981), Optimization of looped water distribution systems, Journal of environmental engineering, ASCE, 107(4), p.p. (665-679).

Ian C. Goulter, and Francols Bouchart (1990), Reliability- constrained pipe network model, Journal of hydraulic engineering, ASCE, 116(2), p.p. (211-229).

Kevin E. Lansey, Larry W. Mays (1989), Optimization model for water distribution systems design, Journal of hydraulic engineering, ASCE, 115(10), p.p. (1401-1418).

Michael A.M., (1978), Irrigation Theory and Practice, Printed at Rashrarani Printers, A-49/1, Mayapuri, New-Delhi.

Muhammed Subhi and Adnan Muhammed Auath, (1990), Introduction to the Statistics, Jordan Books Centre, (in Arabic).

Nowar B Abdul-Kareem and Abbas Z. Ijam, (1997), Optimazation model to pipe network with practical application, A thesis submitted to the college of engineering at Basrah university in partial fulfillment of the requirements for the degree of Master science in Civil engineering.

Paul F. Boulos, Chun Hou Orr, Michael Moore, Paul Hsiung, and Devan Thomas (2002), Optimal pump operation of water distribution systems using genetic algorithms, Journal of water resources planning and management, ASCE, (submitted for publication).

Pramod R. Bhave (1979), Selecting pipe size in network optimization by linear programming,, Journal of hydraulics division, ASCE, 105(7), p.p. (1019-1025).

Pramod R. Bhave (1983), Optimization of gravity- fed water distribution systems, Theory, Journal of environmental engineering, ASCE, 109(1), p.p. (189-205).

Ronald E. Featherstone, and Karim K. El-jumaily (1983), optimal diameter selection for pipe network, Journal of hydraulic engineering, ASCE, 109(2), p.p. (221-234).

Thawat Watanatada (1973), least-cost design of water distribution system, Journal of hydraulics division, ASCE, 99(9), p.p. (1497 -1513).

Yu-chun Su, Larry W. Mays, Ning Duan, Kevin E. Lansey (1987), Reliability- based optimization model for water distribution systems, Journal of hydraulic engineering, ASCE, 114(12), p.p. (1539-1556).

BWSA: Baghdad Water Supply Administration
R9: Al-Karada water Supply network
SOBEA: pipeline Engineering Company

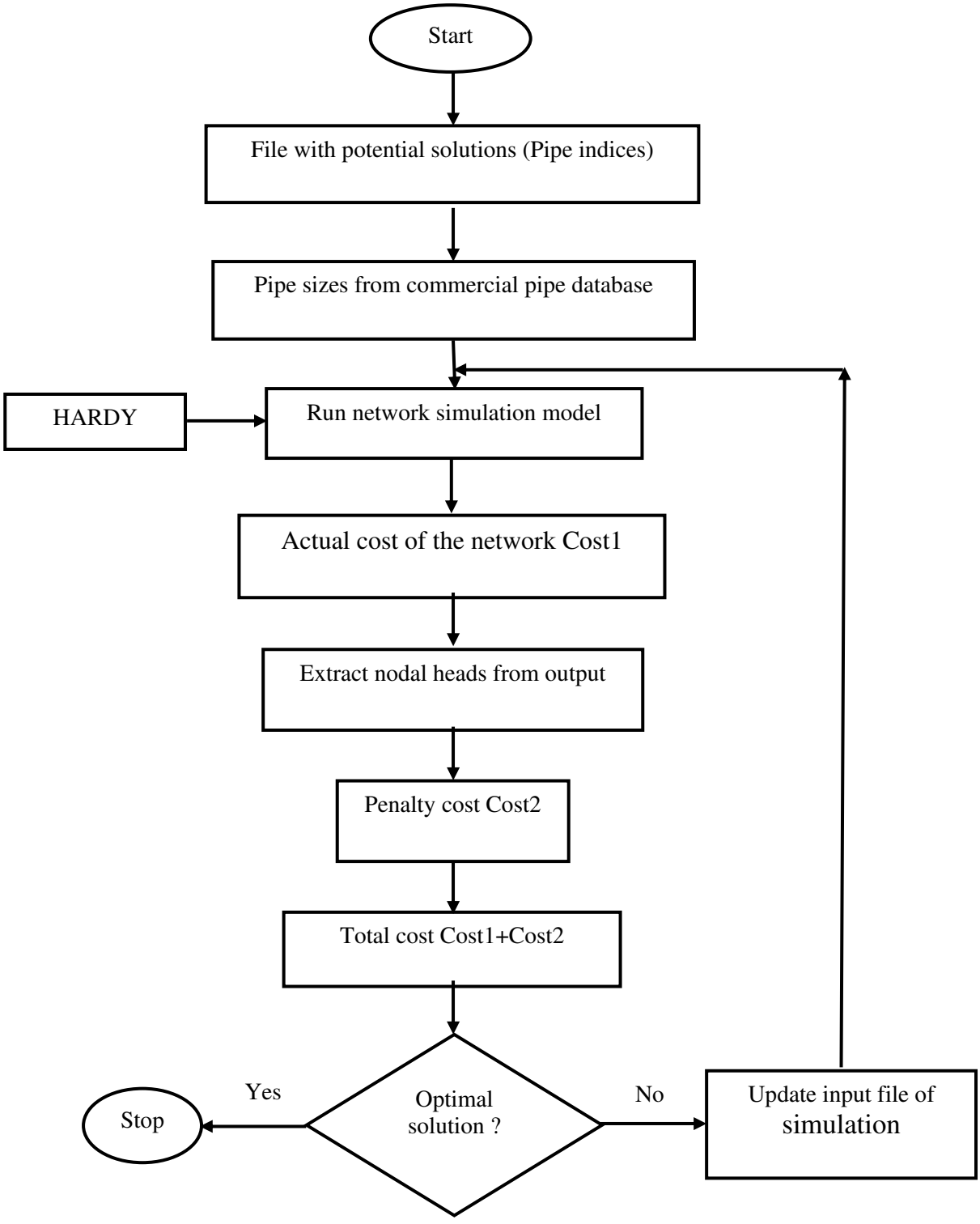

Fig. (1) Working Algorithm of the Cost Function

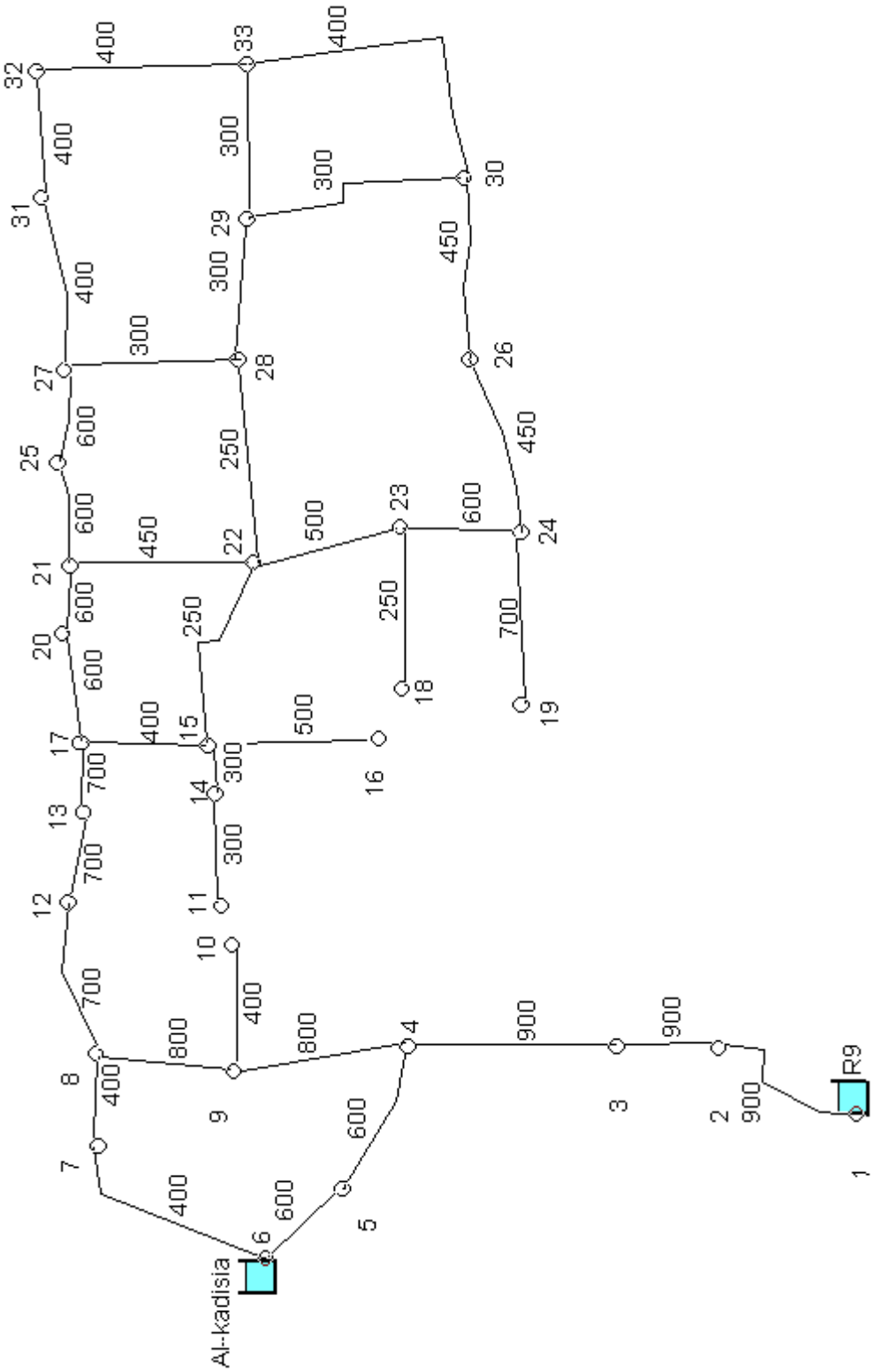

Fig.(2) Al-Karada Water Supply Network

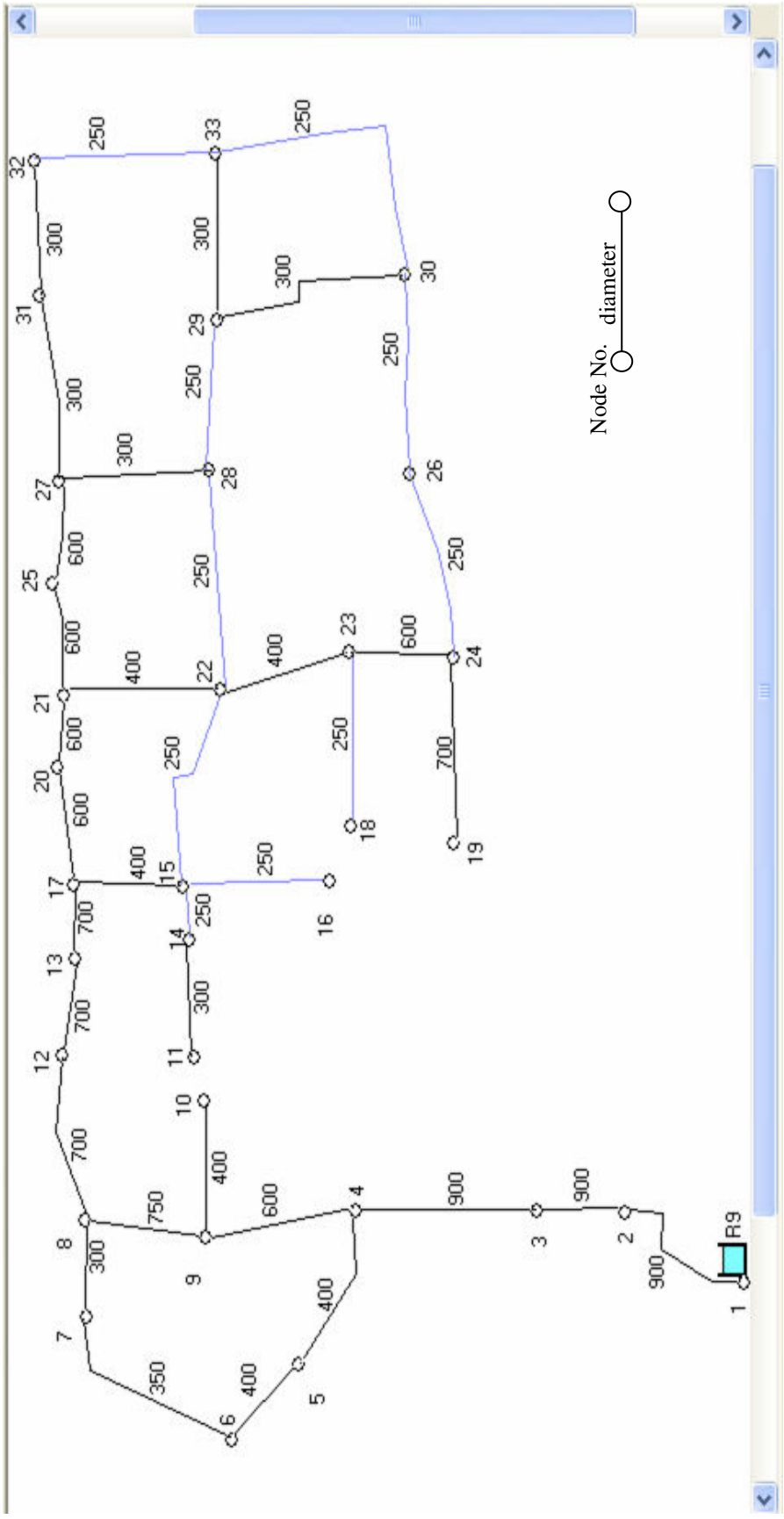

Fig. (3) Optimal design when R9 in operation

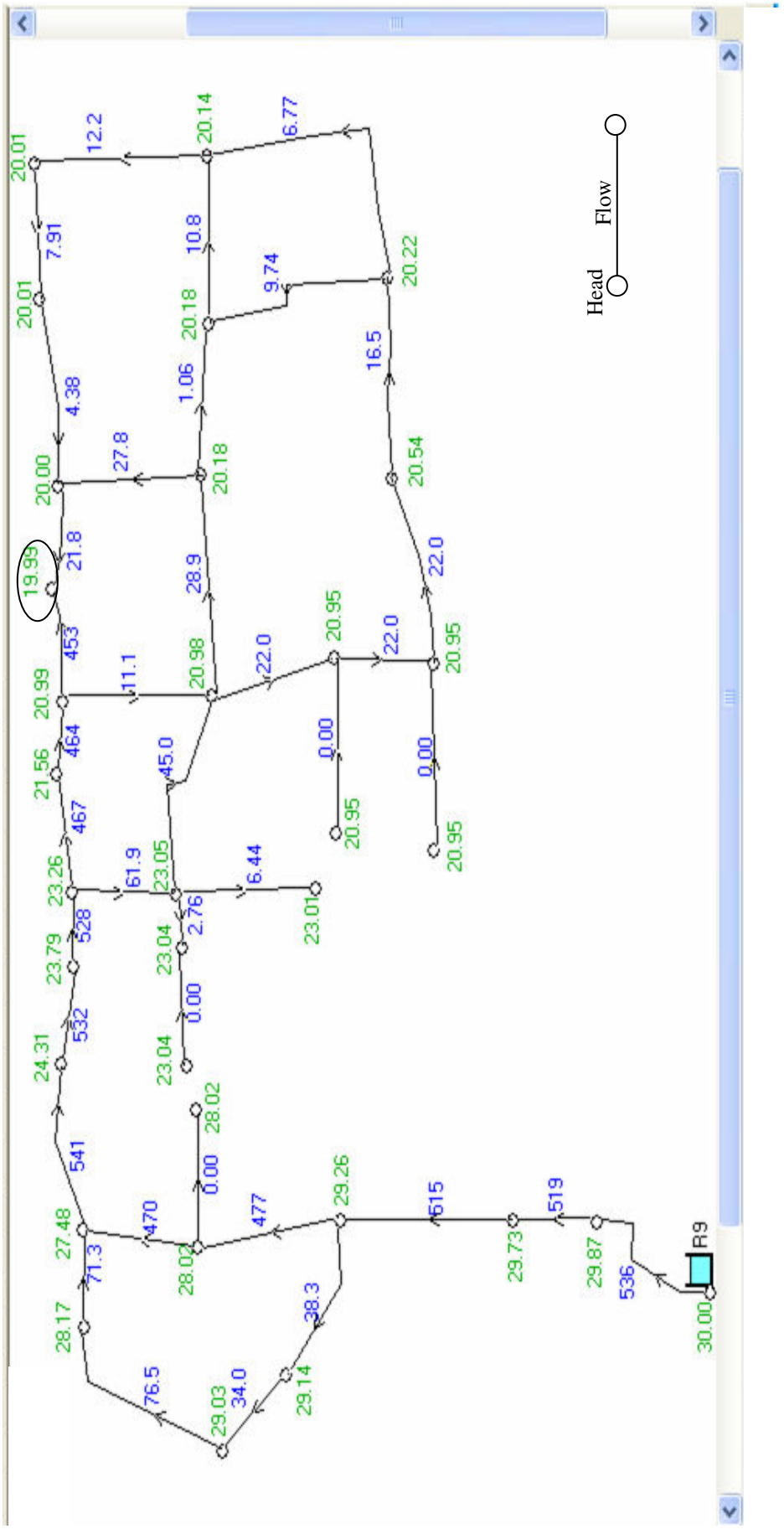

Fig. (4) Hydraulic analysis of the network (R9 in operation)

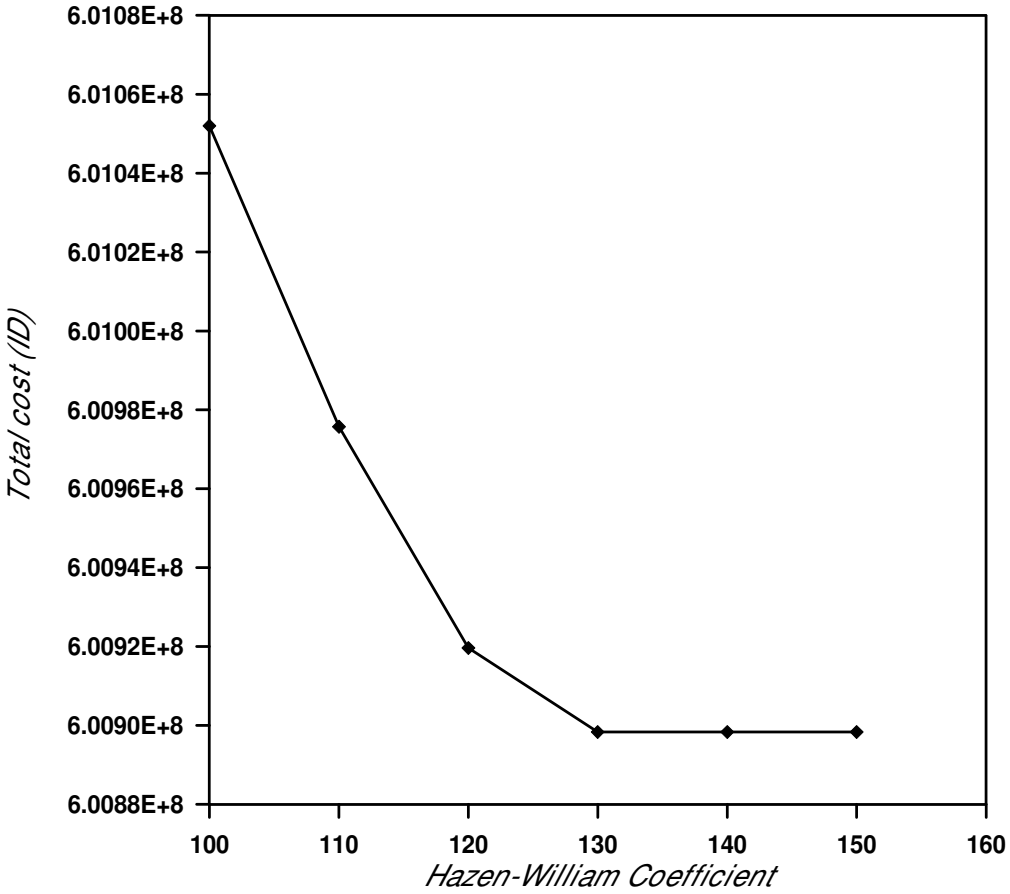

Fig. (5) Effect of the Hazen-William Coefficient on the Total Cost.

Table (1) Pipe Properties of Al-Karada Water Supply Network.

Pipe No.	From Node No.	To node No.	Pipe length (m)	Equivalent Length (m)	Pipe Diameter (mm)	Hazen-William coeff.
1.0	1.0	2.0	150.0	5.0	900	114.7
2.0	2.0	3.0	162.5	7.0	900	117
3.0	3.0	4.0	645.0	10.0	900	121.6
4.0	4.0	5.0	425.0	8.0	600	124.7
5.0	5.0	6.0	425.0	8.0	600	121.9
6.0	6.0	7.0	507.5	9.0	400	137.97
7.0	7.0	8.0	285.0	5.0	400	137.2
8.0	8.0	9.0	450.0	5.0	800	122.2
9.0	4.0	9.0	340.0	7.0	800	122.3
10.0	8.0	12.0	1212.5	13.0	700	124
11.0	9.0	10.	455.0	5.0	400	-
12.0	12.0	13.0	205.0	5.0	700	125.4
13.0	13.0	17.0	212.5	5.0	700	125.6
14.0	11.0	14.0	562.5	10.0	300	-
15.0	14.0	15.0	547.5	8.0	300	132.3
16.0	17.0	15.0	325.0	5.0	400	131.45
17.0	15.0	16.0	450.0	7.0	500	121.85
18.0	17.0	20.0	525.0	7.0	600	127.1
19.0	20.0	21.0	175.0	3.0	600	127.1
20.0	15.0	22.0	805.0	8.0	250	137.5
21.0	18.0	23.0	565.0	14.0	250	-
22.0	19.0	24.0	497.0	10.0	700	-
23.0	21.0	22.0	550.0	10.0	450	130.7
24.0	22.0	23.0	275.0	5.0	500	128.9
25.0	23.0	24.0	300.0	8.0	600	125.9
26.0	21.0	25.0	320.0	8.0	600	126.7
27.0	22.0	28.0	695.0	10.0	250	137.3
28.0	24.0	26.0	462.0	10.0	450	133.47
29.0	25.0	27.0	320.0	8.0	600	115.1
30.0	26.0	30.0	677.50	10.0	450	128.2
31.0	27.0	28.0	400.0	11.0	300	131.2
32.0	28.0	29.0	205.0	5.0	300	131.3
33.0	29.0	30.0	655.0	15.0	300	137.5

Table (1) Continue

Pipe No.	From Node No.	To node No.	Pipe length (m)	Equivalent Length (m)	Pipe Diameter (mm)	Hazen-William coeff.
34.0	27.0	31.0	630.0	10.0	400	126.9
35.0	29.0	33.0	585.0	15.0	300	128.8
36.0	30.0	33.0	980.0	40.0	400	128
37.0	31.0	32.0	75.0	5.0	400	121.7
38.0	32.0	33.0	547.5	12.0	400	140.3

Table (2) Nodes Properties of Al-Karada Water Supply

Node No.	Depth from Surface ground level (m)	No. of pipes connected to node	Draw-off from the node (m^3/s)	Supply to the node (m^3/s)
1.0	1.5	1.0	0	0.1608
2.0	1.4	2.0	0.03172	0
3.0	1.3	2.0	0.00985	0
4.0	1.4	3.0	0	0
5.0	1.5	2.0	0.008	0
6.0	1.3	2.0	0	0.08041
7.0	1.5	2.0	0.0112	0
8.0	1.4	3.0	0	0
9.0	1.4	3.0	0.01431	0
13.0	1.2	2.0	0.007587	0
14.0	1.0	2.0	0.006	0
15.0	1.5	4.0	0.0167	0
16.0	1.0	1.0	0.013976	0
17.0	1.0	3.0	0	0
18.0	1.1	1.0	0	0
19.0	1.0	1.0	0	0
20.0	1.2	2.0	0.007387	0
21.0	0.9	3.0	0	0
22.0	1.0	4.0	0.011314	0
23.00	1.0	3.0	0	0
24.0	1.2	3.0	0	0
25.0	1.0	2.0	0.011913	0
26.0	0.9	2.0	0.011913	0

Table (2) Continue

Node No.	Depth from Surface ground level (m)	No. of pipes connected to node	Draw-off from the node (m^3/s)	Supply to the node (m^3/s)
27.0	1.5	3.0	0.0225	0
28.0	1.3	3.0	0	0
29.0	1.5	3.0	0	0
30.0	1.7	3.0	0	0
31.0	1.5	2.0	0.0153	0
32.0	1.7	2.0	0.009317	0
33.0	1.5	3.0	0.011646	0

Table (3) Optimal design of the network

Pipe No.	From node	To node	Design diameter (mm)	Pipe length (m)
1.0	1.0	2.0	900	150.0
2.0	2.0	3.0	900	162.5
3.0	3.0	4.0	900	645.0
4.0	4.0	5.0	400	425.0
5.0	5.0	6.0	400	425.0
6.0	6.0	7.0	350	507.5
7.0	7.0	8.0	300	285.0
8.0	8.0	9.0	750	450.0
9.0	4.0	9.0	600	340.0
10.0	8.0	12.0	700	1212.5
11.0	9.0	10.0	*	*
12.0	12.0	13.0	700	205.0
13.0	13.0	17.0	700	212.5
14.0	11.0	14.0	*	*
15.0	14.0	15.0	250	547.5
16.0	17.0	15.0	400	325.0

Table (3) Continue

Pipe No.	From node	To node	Design diameter (mm)	Pipe length (m)
17.0	15.0	16.0	250	450.0
18.0	17.0	20.0	600	525.0
19.0	20.0	21.0	600	175.0
20.0	15.0	22.0	250	805.0
21.0	18.0	23.0	*	*
22.0	19.0	24.0	*	*
23.0	21.0	22.0	400	550.0
24.0	22.0	23.0	400	275.0
25.0	23.0	24.0	400	300.0
26.0	21.0	25.0	600	320.0
27.0	22.0	28.0	250	695.0
28.0	24.0	26.0	250	462.0
29.0	25.0	27.0	500	320.0
30.0	26.0	30.0	250	677.50
31.0	27.0	28.0	300	400.0
32.0	28.0	29.0	250	205.0
33.0	29.0	30.0	300	655.0
34.0	27.0	31.0	300	630.0
35.0	29.0	33.0	250	585.0
36.0	30.0	33.0	250	980.0
37.0	31.0	32.0	250	75.0
38.0	32.0	33.0	250	547.5

* Noted that these pipes can be neglected because there was no draw-off from the nodes which these pipes were connected to.

Table (4) uniformity Indicator results

Indicator	Result
Uniformity Coefficient (UC)	99.565
Standard deviation (σ)	3.6508
Coefficient of variance(Cv)	0.1543

Table (5) Prices of Commercial Diameters for Ductile Iron Pipes Including Rubber Joint for 1979 **

Diameter(mm)	Cost ID/m length	Diameter(mm)	Cost ID/m length
100	4,261	700	87,983
150	4,835	800	117,342
200	5,294	900	139,600
250	5,722	1000	166,750
300	18,220	1200	264,988
350	19,942	1300	268,550
400	25,197	1400	345,479
450	47,417	1500	356, 488
500	51,155	1600	390,000
600	66,007		

** This table was provided from the Baghdad Water Supply Administration (BWSA) which was very important for calculation of the actual cost of the optimal design.

Table (6) Effect of *Hazen-William* coefficient on the total cost

Hazen-William coefficient	Total cost (ID)
100	601,052,000
110	600,975,700
120	600,919,600
130	600,898,300
140	600,898,300
150	600,898,300

THE SELECTION OF OPTIMUM ROAD PATH USING GEOGRAPHIC INFORMATION SYSTEM (GIS)

Bashar S. Al-Joboory **Maitham M. Al-Bakry** **Oday Y. Al-Hamadany**
University of Baghdad – college of engineering – Department of Surveying

ABSTRACT
In this research a modern scientific procedure was used utilizing geographic information system GIS in selecting the optimum road path between two cities . All the programming facilities offered by ArcView GIS software with its extensions of spatial analysis and 3D analysis to solve the problem .The solution take a form of geographic map graduated in colors from best to bad portion of land that the suggested road could pass through.
The proposed procedure was checked by conventional mathematical solution used in such problems and the results were both agreed.

الخلاصة

في هذا البحث تم طرح أسلوب علمي حديث بالاستفادة من استخدام منظومة المعلومات الجغرافية GIS في اختيار أفضل مسار لطريق مقترح بين مدينتين وذلك باستخدام كل الإمكانيات البرمجية التي يوفرها برنامج Arc View GIS بملحقاته المتعلقة بإجراء التحليل المكاني والثلاثي لحل المسالة حيث يتم إنتاج خارطة جغرافية متدرجة لونيا من الأفضل إلى الأسوء التي يمكن أن يمر فيها الطريق المقترح, وقد تم التحقق من فعالية هذه الطريقة باستخدام الأساليب الرياضية التقليدية المتبعة في حل هكذا مسائل وكانت النتائج متوافقة.

KEYWORDS
TIN, GIS, 3D analyst, spatial analysis, model builder

INTRODUCTION

The problem of selecting and designing new roads between cities is considered a common problem in transportation engineering ,many papers presented in a try to solve the problem depending on many techniques like mathematics, optimization or/and logic.
In this paper a new technique is presented depending on the new computer technology which is known as model builder of geographic information system (GIS), the new method applied to real hilly Iraqi regions to construct new road between sulaymaniya province and qala desi district and the results were very promising, effective and successful.

SPATIAL MODEL IN GIS

In general terms, a spatial model is a representation of reality .The purpose of a model is to help you understand, describe, or predict how things work in the real world. By representing only those

factors that are important to some study, a model creates simplified, manageable view of the real world.

Geographic information systems (GIS) have not only made it easy to process, analyze and combine spatial data, but they have also made it easy to organize and integrate spatial processes into larger systems that model the real world. However, the more complex a spatial model becomes, the more difficult it is to keep track of the various datasets, processing procedures, parameters, and assumptions that you have used, and that was the reason to use ArcView ModelBuilder which is a technology from Environmental System Research Institute, Inc. (ESRI) that helps to create and manage spatial models that are automated and self – documenting. A spatial model in ModelBuilder is easy to build, run, save, modify, and share with others.

In ModelBuilder, a spatial model is represented as a diagram that looks like a flowchart **Fig (1)**. It has nodes that represent each component of a spatial process. Rectangles represent the input data, ovals represent functions that process the input data that is created when the model is run. The nodes are connected by arrows the shows the sequence of processing in the model.

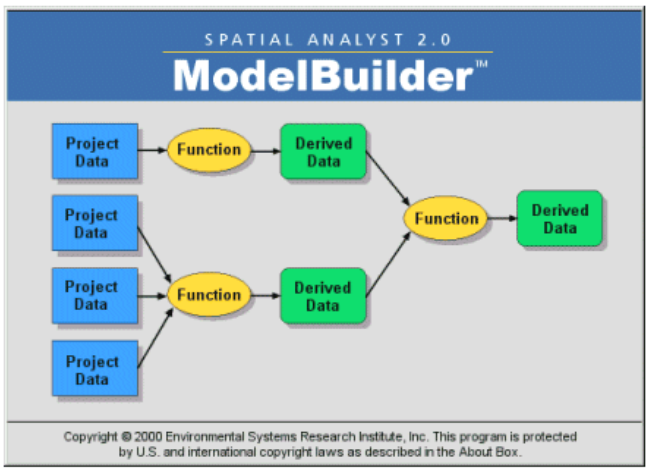

Fig. (1)

CASE STUDY

To explain the proposed method it was decided to select a case study to design a new road between sulaymaniya province and qala desi district northern Iraq due to the availability of topographic maps and the hilly nature of the region.

From the existed topographic maps and by scanning techniques the map of the whole region were recreated by AutoCAD and then converted to shape files by the ArcView GIS. The surface model was created by TIN (triangulated irregular network) command through the use of ArcView *3D surface analyst* with all feature themes as shown in **Fig.(2)** and **Fig. (3)** below.

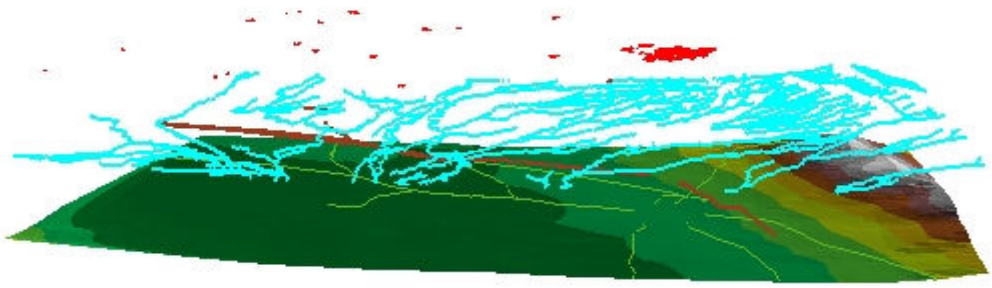

Fig. (2)

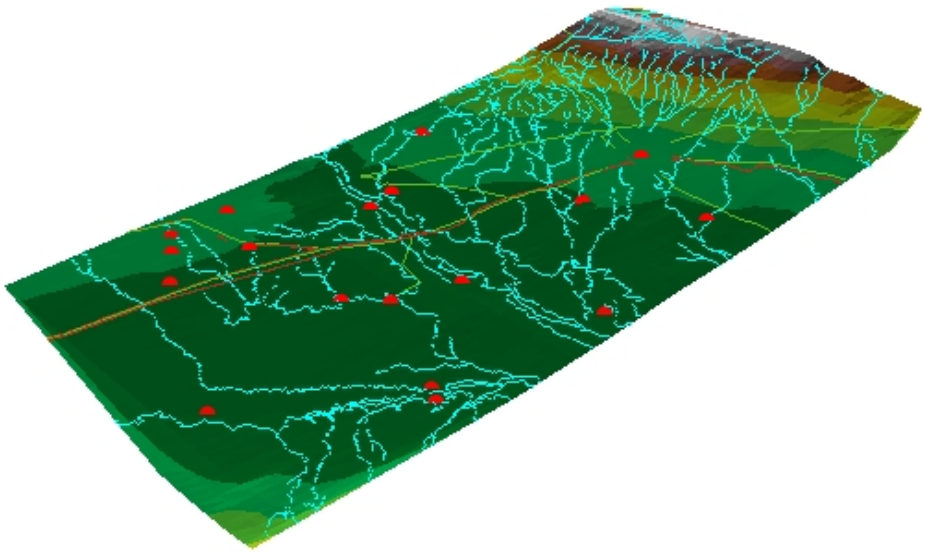

Fig. (3)

SPATIAL ANALYSIS

The GIS *spatial analysis* role is to select a suitable path for the new road by taking all possible constraints to establish the road in a way that gives the best results from economical and logical point of view, and also coincide with the national standards for designing highways.

The GIS *model builder* was used to arrange the spatial analysis for the problem and **Fig. (4)** illustrates the model that has been used in analyzing for the possible best road path.

The factors contribute in the model were slope of terrain, short path, existed forests or farms, cities, and existed roads or rivers .These factors were considered enough for theoretical study and many other factors like the soil types could be included in real practical problems.

The model below takes into account avoiding steep areas, farms, and rivers, also the model assign high weights for short paths, existed roads, and villages.

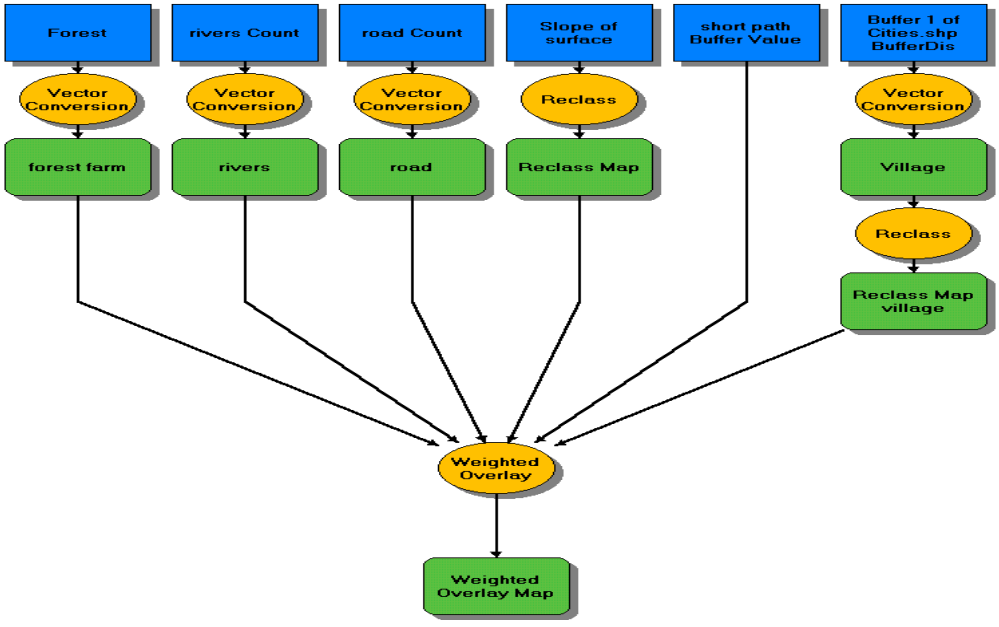

Fig.(4)

It is obvious from the model diagram above that a process of converting all the vector themes to grid themes is necessary to perform the analysis **Fig. (5)**

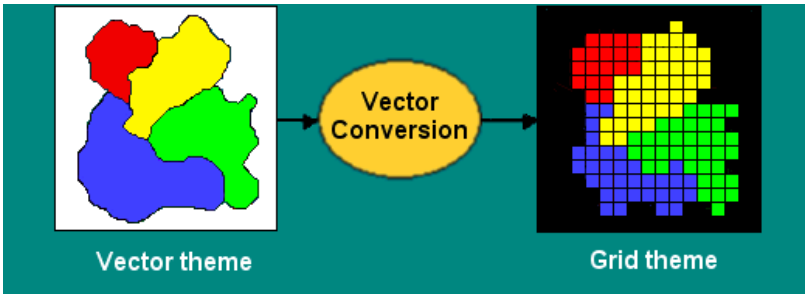

Fig. (5)

The buffering process in the model above is to create buffer zones around the short path between the two locations at some specific distance and around each city to assign that the proposed roads are preferred to be short, also pass through or near cities. **Fig. (6)** shows a part of the weighted overlay table that assigns different weights and scale values for each input theme to produce the final overlay map.

Weighted Overlay

Evaluation Scale | Overlay Table

Define the weighted overlay table

Specify the Percent (%) Influence for each theme and a Scale Value for each input Field value. Scale Values will be multiplied by the % Influence value before they are added to other themes. To edit a % Influence value, click on it and type a new one. To edit a Scale Value, click on it, then use the dropdown list or type a value. Cells with a Restricted value are not added to other themes and retain the Restricted value in the output theme. To add a new input theme, click the Add Theme button. To delete an input theme, click on its name, then click the Delete Theme button.

Input Theme	% Inf	Input Field	Input Label	Scale Value
forest farm	15	Value		
		1	1	1
		NODATA	No Data	9
rivers	15	Value		
		0	0	1
		NODATA	No Data	9
road	10	Value		
		0	0	8
		NODATA	No Data	1
Reclass Map	30	Value		
		1	0 - 0.6	9
		2	0.6 - 1.2	8
		3	1.2 - 1.8	7
		4	1.8 - 2.4	6
		5	2.4 - 3	5
		6	3 - 3.6	1
		7	3.6 - 4.2	1
		8	4.2 - 4.8	1
		9	4.8 - 5.4	1
		10	5.4 - 6	1
		NODATA	No Data	Restricted
short path Buffer	15	Value		
		1	1	9
		2	2	8
		3	3	7
		4	4	6
		5	5	5
		6	6	4
		7	7	3
		8	8	2

Fig. (6)

All the themes used in the analysis are shown in **Fig. (7)** below.

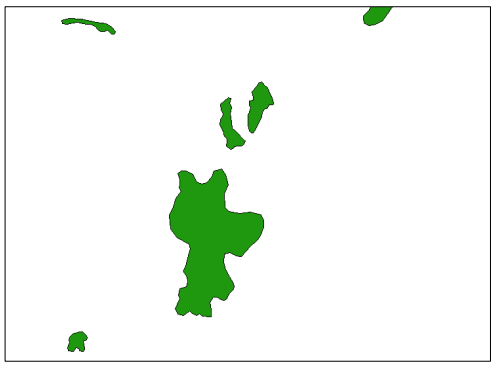

Farms or forests theme

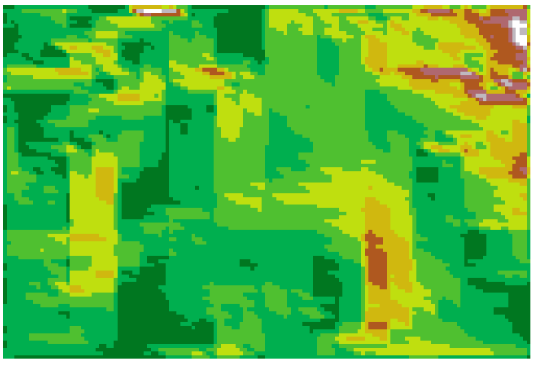

Slope of terrain theme

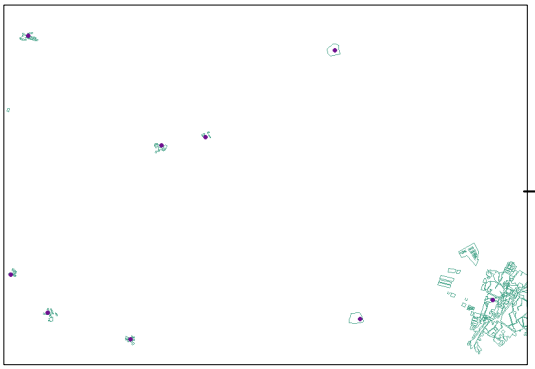

City, village theme

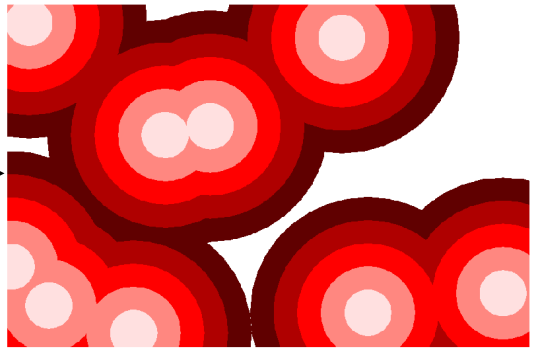

City buffer grid theme

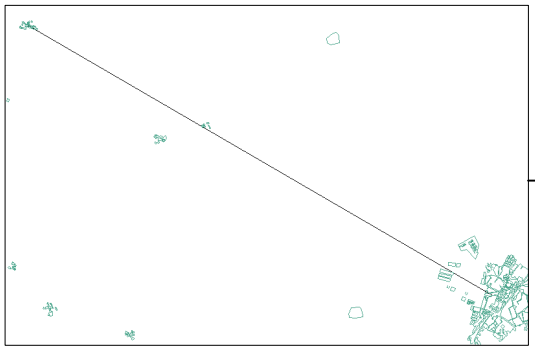

Short path theme

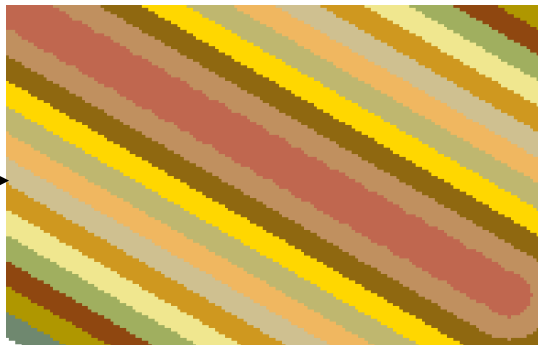

Short path buffer theme

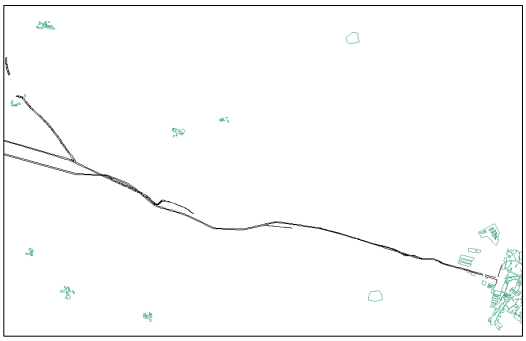

Existed roads theme

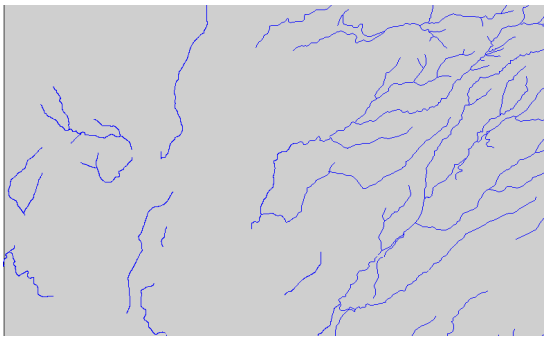

Rivers theme

Fig.(7)

The result after analysis is a map showing the different colored regions classified from very good to bad portion of land representing the suitability for selecting the road path as in **Fig. (8)** .The light green areas were assigned very good, yellow areas assigned good, green areas were assigned middle, orange areas were assigned bad, and red areas were assigned too bad.

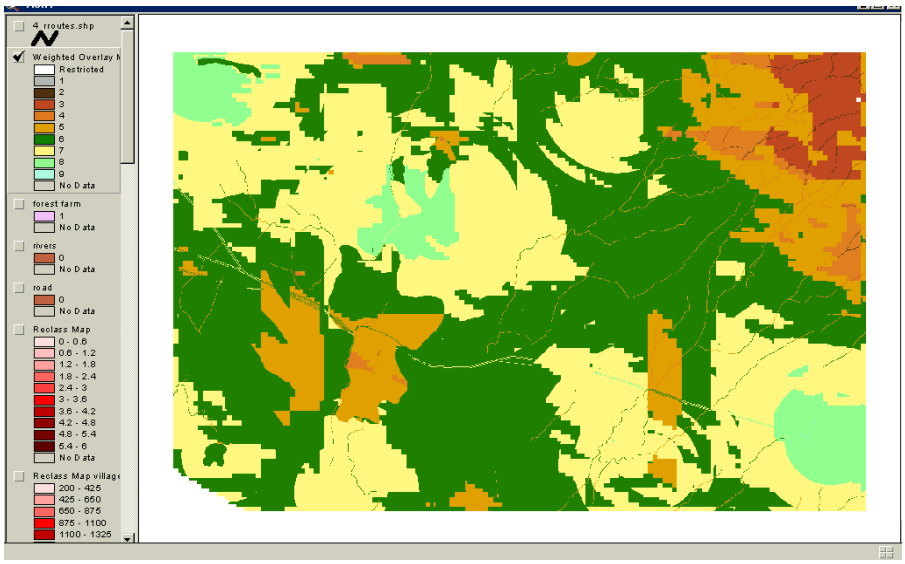

Fig. (8)

From the resulted weighted overlay map it could be decided to choose the optimum road path by carefully trying to design the path to pass through the colored areas that are indicated by good avoiding the bad one.

For verification goal it was decided to select four road paths labeled in red as illustrated in **Fig. (9);** the fourth road were selected carefully to pass through the best regions ,and according to the analysis map it must be the optimum road path, and that should be checked by conventional mathematical optimization techniques.

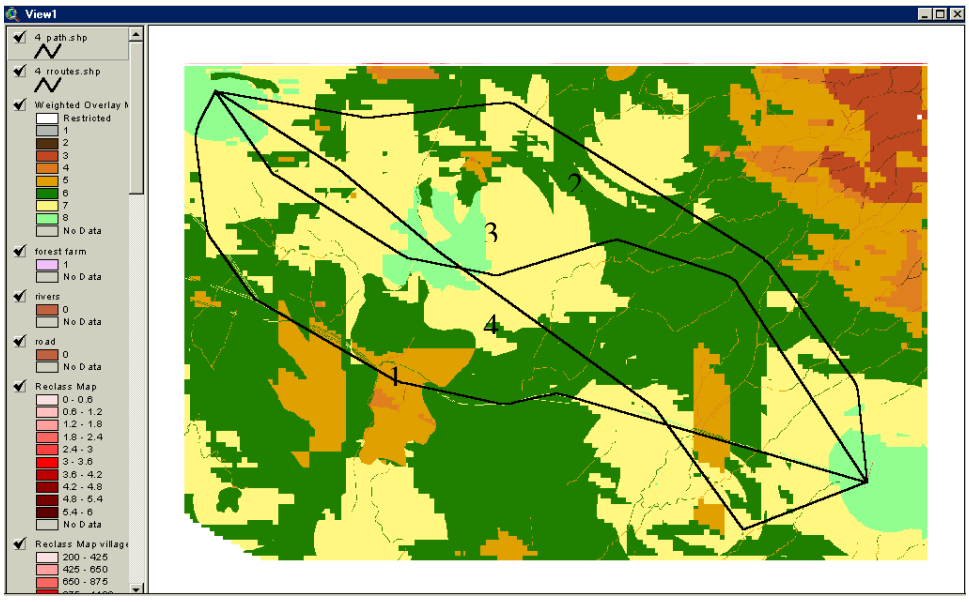

Fig. (9)

GEOMETRIC DESIGN OF PROPOSED ROADS

The next step is to geometrically design these suggested road paths including vertical and horizontal alignment, and then computing volumes which is an important factor in selection since it is proportional to cost, this is done by software like AutoDesk Survey, the resulted CAD drawings are then converted to shape files by ArcView GIS.

Profiles for these suggested paths could be also interpolated by ArcView GIS 3D analyst easily as shown in **Fig. (10)**

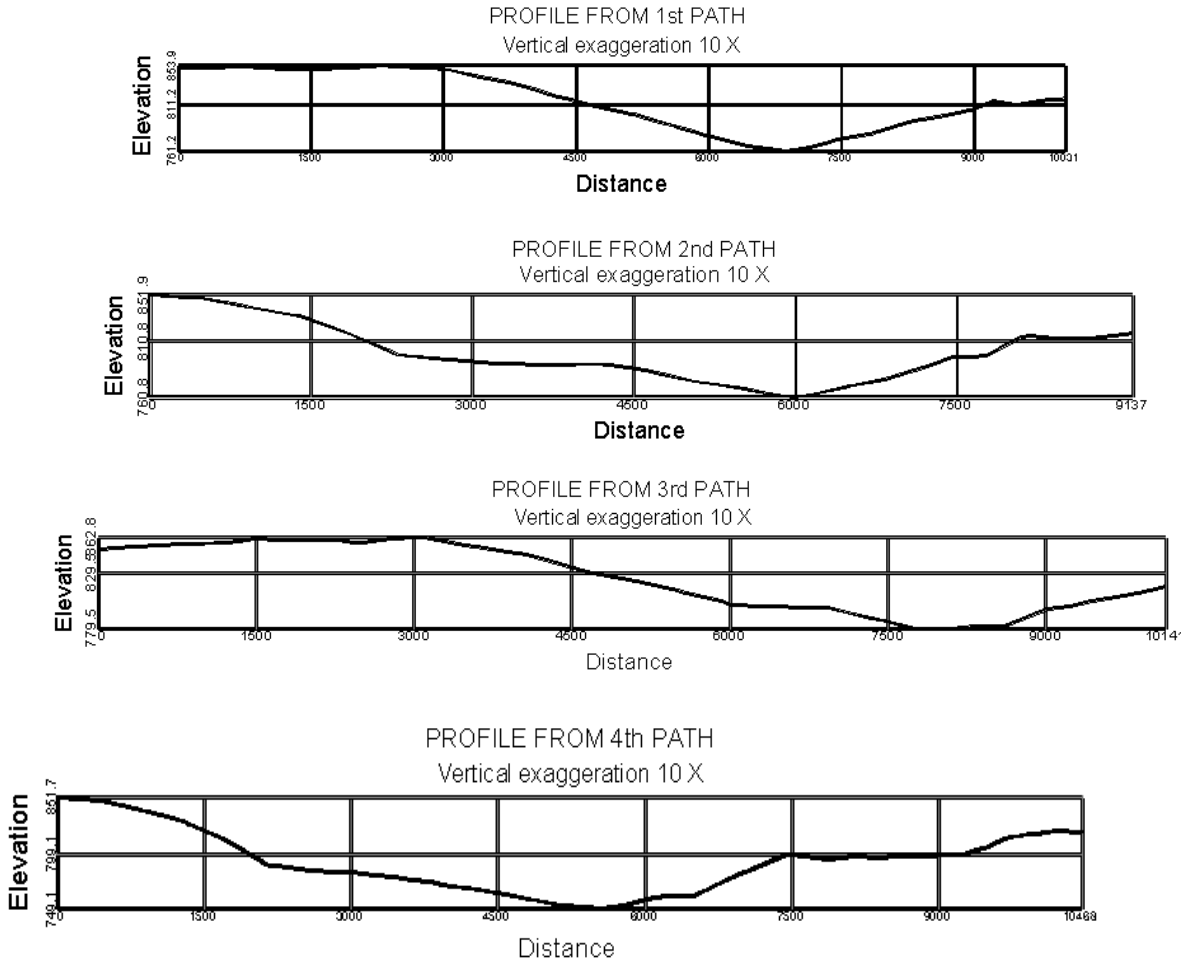

Fig. (10)

It was found that highway with two lanes **Fig. (11)** is the appropriate type for designing the four proposed roads in the presented problem, **Table (1)** illustrates the characteristics of two lane highways

Table (1) Highway Characteristics – Two Lane

CLASS			WIDTH (in meter)			
Letter symbol	**W (m)**	**Design speed(km/h)**	**a**	**v**	**c**	**e**
D2	9.5	70,60,50	3.00	0.25	1.25	0.25
***C2**	**11**	**80,70,60**	**3.50**	**0.25**	**1.25**	**0.50**
B2	12	80,70,60	3.50	0.25	1.75	0.50
A2	13.5	100,80,70	3.75	0.25	2.25	0.50

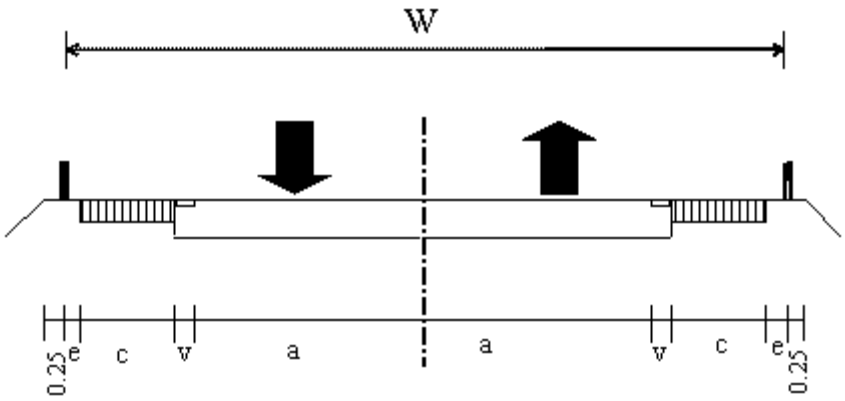

Fig. (11)

Where:-

W – Total width of highway.
a – Width of traffic lane.
c – Width of paved shoulder.
e – Width of unpaved shoulder.
c – Latter symbol of class
2 – Number of traffic lanes
v - Width of marginal strip

To prepare the road selection factors, it is necessary to study the designing elements for different classes of highways in different types of topography **Table (2)**.

Table (2) Design Elements for different classes

Class Of Highway		Type Of Topography								
		Flat			Rolling			Mountainous		
	Velocity	g	s(e)	r	g	s(e)	r	g	s(e)	r
D2	V	70			60			50		
		5	5.5	6.5	6.5	6.5	8.5	8	7	10
C2	V	80			70			60		
		4	5	6	5.5	6	7.5	7	6.5	8.5
B2	V	80			70			60		
		4	5	6	5.5	6	7.5	7	6.5	8.5
A2	V	100			80			70		
		3.5	4.5	5.5	4.5	5.5	6.5	5.5	6	7

MATHEMATICAL CHECK

The volumes, slopes, curves, lengths, population, bridges or culverts, and cities are all represents the important factors in selecting the final optimum road path and this is done by the usual mathematical techniques in transportation engineering**. Table 3** below explains these computed different factors for each suggested route and the final results.

Table (3) Road Selection Factors

Properties		The weights	First Suggested Path		Second Suggested Path		Third Suggested Path		Fourth Suggested Path	
			Properties	%	Properties	%	Properties	%	Properties	%
Length (km)		20%	10.5	18%	10.1	19%	10.0	19%	9.5	20%
NO. of horizontal curves		16%	6	10%	4	16%	5	13%	5	13%
No. of vertical curves		10%	13	5%	13	5%	10	7%	7	10%
Max. slop		8%	5%	5%	3%	8%	3%	8%	3%	8%
Cut Fill (m^3)	Cut(m^3)	13%	89345		132702		219273		206680	
	Fill(m^3)		87390		97907		148117		187223	
	Cut>fill 10%(fill)		93%	12%	123%	10%	135%	10%	100%	13%
No. of population		20%	21000	18%	20000	17%	19000	17%	23000	20%
No. of culverts		13%	9	9%	11	7%	10	8%	6	13%
Sum		100%		77 %		82 %		82 %		97 %

The final result shows that the fourth suggested road represents the optimum path with a success percent of 97%, and this result match the analysis map of **Fig. (8)**, the same results were obtained when using the method of *mini-max* in optimization

CONCLUSIONS

From the presented problem it was easy to conclude how a vital role the GIS analysis could play in selecting road paths, because of its effectiveness and its logical visual (geographic) solutions for such problems.

The weighted overlay analysis offered by the model builder technique is easy, logical, and flexible since it offers the facility to add new factors, change weights, scale values, and run the constructed model every time you need to get new solutions in a very short time.

It is also important to mention that GIS not only gives the solution for selecting optimum path, but also gives the geometric design that contains types of curves and the geographic coordinates necessary to set out the optimum road.

REFERENCES

ESRI educational services, (1998), Introduction to Arc View GIS ,.

Lan Heywood, Sarah Cornelius and Steve Carver, (1998), Introduction to Geographical Information Systems , Pearson Education Inc. ,.

Omar A. Jassim , (2005), The Use of Remote Sensing And GIS Techniques In Selecting The Best Highway Location For Mosul City, Ph.D. Thesis , Building and Construction Engineering Department, University of Technology,.

Thomas F. Hickerson, (1959), Route Surveys and Design", McGraw-Hill, 4th edition,.

PHYSICAL ADSORPTION OF REFORMING CATALYST BY NITROGEN

Abdul Halim A.K. Mohammed **Hussain K.Hussain** **Tariq M.Naife**
College of Engineering,Chemical Engineering Department ,
University of Baghdad,Iraq

ABSTRACT
Physical adsorption by nitrogen gas was studied on seven commercial platinum reforming catalysts (RG-402, RG-412, RG-432, RG-451, RG 422,RG-482, PS-10), four prepared platinum catalysts (0.1%Pt/alumina, 0.2 %Pt/alumina, 0.45 %Pt/alumina and 0.55% Pt/alumina), and γ-alumina support.
Physical adsorption was carried out by using Accelerated Surface Area and Porosimetry (ASAP 2400 device) at 77 K .
The results indicate that the surface area in genaral decreases with increasing platinum percentage,high platinum loaded (0.45% and 0.55%) it was found that the percent increasing in surface area was lower than those obtained for low platinum loaded catalysts , and at very higher platinum loading 0.6 %Pt , some reduction in surface area was observed . The precipitation of Re and Ir metals with 0.35 % and 0.6 % platinum increases the surface area , while precipitation of 0.57% Sn with 0.375% Pt/ γ-alumina deceases the surface area catalyst .

الخلاصة

تم دراسة الإمتزاز الفيزياوي باستخدام غازالنتروجين للعوامل المساعدة التالية:

سبعة عوامل مساعدة تجارية (RG-402, RG-412, RG-432, RG-451, RG 422,RG-482, PS-10) أربع عوامل مساعدة محضرة (0.1، 0.2، 0.45 و 0.55) % وزنا بلاتين (نسبة وزنية مئوية) محمل على الألومينا, اضافة الى كاما اوكسيد الالمنيوم.

تم إجراء الإمتزاز الفيزياوي في درجة حرارة النيتروجين السائل (77)كلفن باستعمال جهاز قياس المساحة السطحية والمسامية (ASAP 2400). أظهرت النتائج أن المساحة السطحية تنخفض مع زيادة نسبة البلاتين المحمل على الألومينا بشكل عام وفي نسب البلاتينيوم العالية (0.55,0.45)% وجد بأن نسبة الزيادة في المساحة السطحية هي أقل من التي تم الحصول عليها في نسب البلاتينيوم الواطئة للعوامل المساعدة ،وجد ايضا بانه عندما تكون نسبة البلاتين عالية جدا 0.6% لوحظ أنخفاض بسيط في المساحة السطحية.

أن ترسيب Reو Ir للعوامل المساعدة الثنائية المعدن بنسبة 0.35 % و 0.6 % من البلاتينيوم أدى الى زيادة في المساحة السطحية مقارنة بالعوامل المساعدة الاحادية المعدن , بينما ترسيب Sn بنسبة 0.57 % للعامل المساعد 0.357%البلاتين / كاما–الومينا أدى الى أنخفاض المساحة السطحية.

KEY WORDS
Physisorption;Nitrogen adsorption;BET method;Surface area.

INTRODUCTION

Physical adsorption defined as adsorption in which the forces involved are intermolecular forces (Vander Waals forces) of the same kind as those responsible for the imperfection of real gases and the condensation of vapours, and which do not involve a significant change in the electronic orbital patterns of the species involved[Lowell,1984].

Gas adsorption is of major importance for the characterisation of a wide range of porous materials.Many gases and vapours, which are readily available and could be used as adsorptives, nitrogen has remained universally pre-eminent. [Oscik,1982].

Physical adsorption or reversible adsorption is most sutaitable for surface area determinations. It is accompanied by low heats of adsorption with no violent or adsorption structural changes occurring to the surface during the adsorption measurement [Young,1962].The molecules physically adsorbed are not restricted to specific sites and are free to cover the entire surface.For this reason surface areas rather than number of sites can be calculated.[Van der Plas,1970].

During the adsorption,the increase of the pressure leads first to a monolayer coverage,then a multilayer coverage is generated .When the local condensation pressure is reached,a phase transition is produced and the pores are full with a liquid phase. This condensation pressure is an increasing function of the pore size. After the saturation, if the pressure is decreased gradually, the primary phenomena of the desorption is observed.On the contrary, if the desorption is started before the complete saturation, the secondary desorption was observed.[D.I Enach.2001].

Langmuir proposed equation 1 for monolayer adsorption on solid surface .

$$\frac{P}{V} = \frac{Po}{V_m C} + \frac{P}{V_m} \qquad (1)$$

Langmuir adsorption isotherm is based on the following assumptions, the surface contains a fixed number of adsorption sites(ϕ = fraction of sites covered; 1-ϕ = fraction of sites not covered), Each site can hold one adsorbed molecule,a monolayer is the maximum amount which can be adsorbed,the sites are independent and have no interaction and the binding energy is the same for each site and does not depend on ϕ.

The Langmuir isotherm makes no provision for more than one layer of gas adsorbing on the surface. Frequently however, the amount of gas adsorbed continuously increases as the pressure is increased indicating that gas sticks to the substrate and to gas already adsorbed.

Allowance for multilayer adsorption was introduced by Brunauer ,Emmett and Teller [Sing,1976 and Kenneth,2001]which develop the Langmuir equation, and they extended the monolayer coverage to multi-layer coverage as shown in equation 2.

$$\frac{P}{V(Po - p)} = \frac{1}{V_m C} + \frac{(C-1)P}{V_m C Po} \qquad (2)$$

The BET isotherm was a generalization of the Langmuir isotherm and assumes the following,the surface is uniform and all sites are equivalent. (i.e., no pores, steps, etc.), molecules adsorbed on the surface sites are localized,each molecule in the first layer provides a site for adsorption of a second layer, each molecule in the second layer provides a site for adsorption of a third layer, and so on, there is no interaction between molecules in a given layer and molecules in

the second and higher layers are held together by the forces in the bulk liquid whereas molecules in the first layer are different by virtue of being bound to the surface.
In spite of the perceived theoretical limitations of the BET model, the BET-nitrogen method soon became established as a standard procedure for surface area determination.
Empirical evidence indicated that the changeover from monolayer to multilayer adsorption occurred at the beginning of the middle, nearly linear section of the isotherm ,and was taken by them to indicate the completion of the monolayer .
The plot of $P/V(P^o-P)$ Versus P/P^o from equation 2 gives a straight line usually with range of P/P^o (0.05-0.35)[Loweel,1984] with slope S and intercept I which are calculated by equations 3 and 4 respectively.

$$I = 1/V_m C \quad (3)$$

$$S = C-1/V_m C \quad (4)$$

It is evident that the location and extent of the linear region of a BET plot is dependent on the adsorption system (both adsorbent and adsorptive) and the operational temperature. In view of this situation, it is strongly recommended [Gregg,1982] that the BET monolayer capacity(V_m) evaluted by equation 5.

$$V_m = 1/(S+I) \quad (5)$$

Then surface area calculated by equation 6.

$$S_{BET}\,(m^2/g) = N_s * N * V_m / 22414 * 10^{18}\ nm^2/m^2 \quad (6)$$

The evaluation of S_{BET} is,of course, dependent on the average area, N_s, occupied by each molecule in the completed monolayer. In the case of nitrogen at 77 K, N_s of nitrogen is usually taken as 0.162 nm^2, this value was originally proposed by [Emmett and Brunuaer ,1938] and was based on the assumption that the monolayer had the liquid form of close-packed structure.
High value of the parameter C, is an indication of strong adsorbent–adsorbate interactions. Typical C values in the range 80–150 for nitrogen at 77 K are consistent with the formation of well-defined monolayers on many non-porous and mesoporous adsorbents [Dubinin(1955)and Gregg1982].
Physical adsorption of gas or vapours is normally characterized by the liberation of between 10 to 40 kJ/mol of heat which is close to values associated with heats of liquification of gases . The heat evolved on adsorption of a gas or vapours onto solid from a liquid,however,is strongly dependent on the source and history of the solid adsorbent[Jhon and Barry,1998].

C value calculated by equation 7.

$$C = S + I/I \quad (7)$$

Heat of adsorption was calculated from constant C by equation 8 [Brunauer,1938].

$$C = \exp^{(E_1 - E_2)/RT} \quad (8)$$

This work deals with preparation of platinum γ- Al_2O_3 catalysts wih different Platinum content and calculation of the surface area and heat of adsorption for γ- Al_2O_3 ,prepared and commercial catalysts by physical adsorption of nitrogen at 77K.

EXPERMINTAL WORK

Material

Commercial Catalysts:

Table (1) shows the properties of commercial catalysts and γ- Alumina support .

Symbol	Form	Pt Content (wt. %)	Cl Content (wt. %)	Diameter mm	Length mm	Bulk density g/cm^3	Pore volume cm^3/g	Porosity
γ- Al_2O_3	Extrudate	-	-	2.5	4-8	0.68	0.62	0.56
RG-412 0.35 % Pt/ γ- Al_2O_3	Extrudate	0.35	1	1.8	5	0.75	-	-
RG-402 0.6 % Pt/ γ- Al_2O_3	Cylindrical	0.6	1.02	1.5	7-9	0.75	-	-
RG-422 0.6 %Pt- 0.03 % Ir/ γ- Al_2O_3	Cylindrical	0.6	1.2	1.6	1.8	-	-	-
RG-432 0.35%Pt- 0.03 %Ir/ γ- Al_2O_3	Cylindrical	0.35	1	1.8	9	-	-	-
RG-451 0.35%Pt- 0.03%Ir- Promoter/ γ- Al_2O_3	Sphere	0.35	1.1	-	-	0.75	-	-
RG-482 0.3%Pt- 0.3%Re/ γ- Al_2O_3	Cylindrical	0.3	1	1.4	8-9	0.75	-	-
PS-10 0.375%Pt- 0.57%Sn/ γ- Al_2O_3	Sphere	0.375	1.02	-		-	0.82	0.75

Gases

a- Nitrogen:

It was supplied from Baghdad Factory for Drug Industry with purity 99.9 % and it is used as adsorbent.

b- Hydrogen:

It was supplied from AL-Mansour plant with purity 99.9 and it is used as a reduction material in preparation step.

c-Helium:

It was supplied from AL-Mansour plant with purity 99.9 and it is used in dead volume measurments.

d-Liquid nitrogen:

It was supplied from Baghdad factory for drug industry with purity 99.9 %.

e-liquid chloroplatinic acid:

It was supplied from Fluka Chemi AG with purity 99.9% and 40wt % platinum.

Catalysts Preperation

Four platinum supported with γ- Alumina catalyst containing different percentage of Pt were prepared .The impregnation method was applied for catalyst preparation.This includes preparations of hydrochloroplatinic solution with different concentration with a quantity just sufficient to fill the pores of γ- Alumina support as seen from **Table (2)** .

Table (2) Preparation of different Pt/ γ -Al_2O_3 percent

Catalyst with different Pt % loaded	Hydrochloroplatinic acid, g	H_2O, ml	γ -Al_2O_3, g
0.1 Pt/Al_2O_3	0.065	80	25
0.2 Pt/Al_2O_3	0.1375	92	26
0.45 Pt/Al_2O_3	0.283	84	29
0.55 Pt/Al_2O_3	0.345	98	27

Each sample of γ- Alumina was charged in 250 ml flask and connected to a vacuum pump in one side and from top side to a separation funnel where the impregnation solution was contained .The impegnation carried out at room temperture and 5 mmHg vacuum pressure for 4 h.The catalyst dried at 110 ° C for 6 h, and then calcined at 500 ° C in flowing dry air for 4 h to convert the metal salt into a metal oxide. The oxide was reduced by hydrogen at 350 Cº and for 3 h to give zero-valent metal.

General description of the(ASAP) Instrument

Accelerated Surface Area and Porosimetry instrument (ASAP-2400) is programmed to perform physical adsorption and desorption analysis completely under computer control. The (ASAP-2400) is actually two independent instruments in a single cabinet, one to degas samples and the other has to analyze sample.The specification of ASAP 2400 Instrument is shown in **Table (3).**

The sample degassing part of the (ASAP-2400) consists of a vacuum pump, a manifold with six degas ports , a vacuum transducer to monitor manifold pressure, a pressure limit switch, heating mantles and controls for heating samples, and individual sets of controls to govern the out gassing of each sample. Samples may be added to or removed from degas ports without disturbing the treatment of other samples sharing the manifold as shown in **Fig. (1).**

The analysis part of the (ASAP-2400) consists of vacuum pump, manifold with six sample ports and six Po tubes, an individual pressure transducer for each sample port, a master pressure transducer for the manifold, a precision volume to check the manifold volume calibration, a liquid nitrogen thermos flask and a status display panel a shown in **Figs. (2) and (3).**

Table (3) Specification of ASAP 2400 Instrument

Specification	Value
Minimum surface area ,m^2/g	5
Minimum pore volume ,cm^3/g	0.02
Pore size range ,Å	10-600
Environment temperature , ^oC	10-35
Pressure measurement range,mm Hg	0-950
Analysis manifold capacity, sample	6
Liquid N_2 system capacity ,(liter per one Dewar flask).	1.9
Minimum pressure ,mm Hg	0.005
Degas system capacity,sample	6
Temperature range , ^oC	Ambient to 350

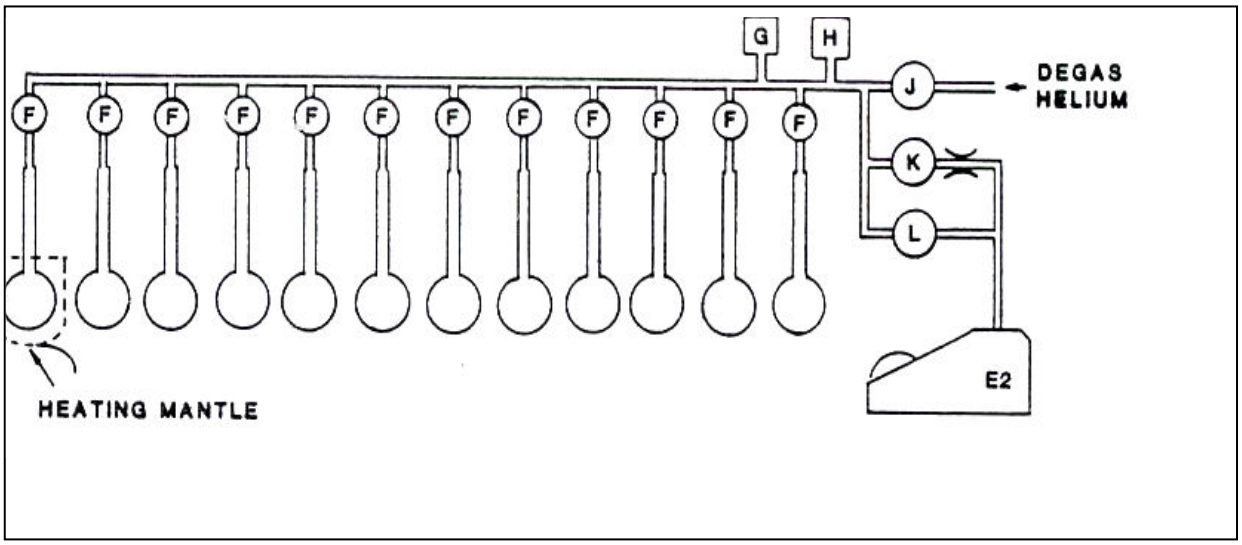

E_2 Degas vacuum pump
F Degas port valve
G 1 psig pressure switch
H Degas vacuum Gauge
K Vacuum valve
L Vacuum valve

Fig. (1) Degassing part

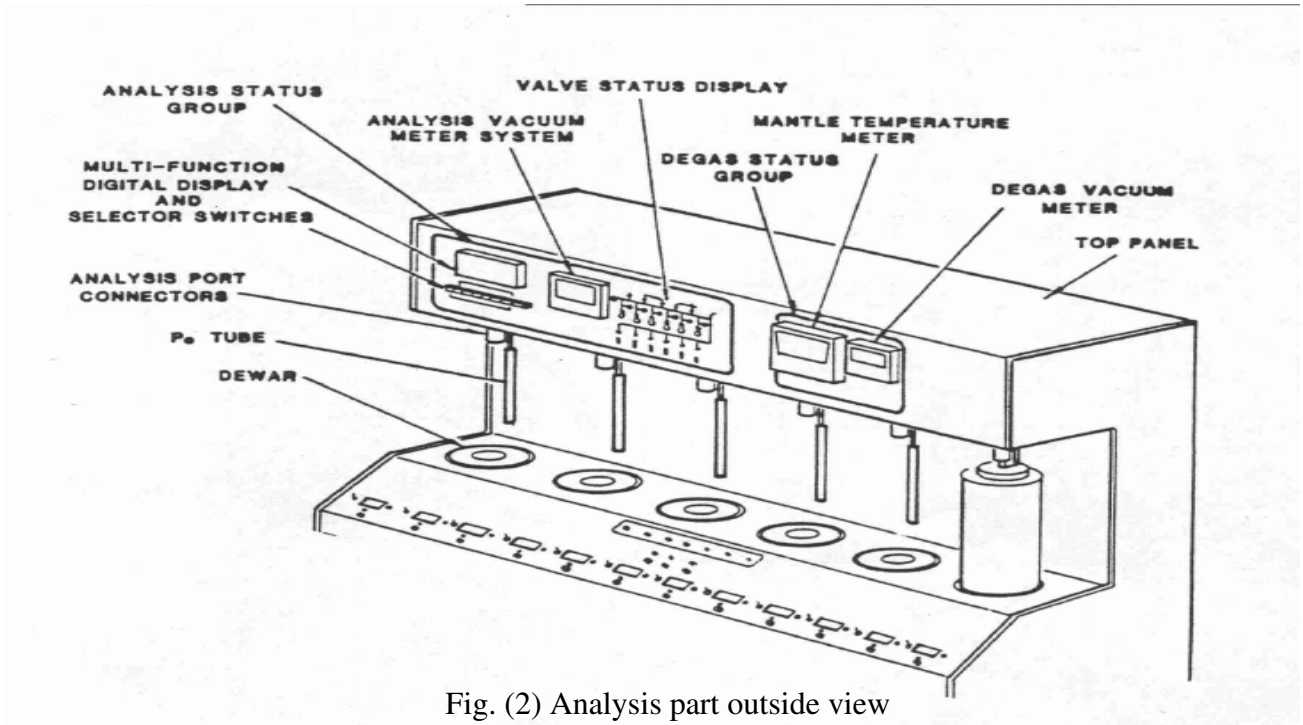

Fig. (2) Analysis part outside view

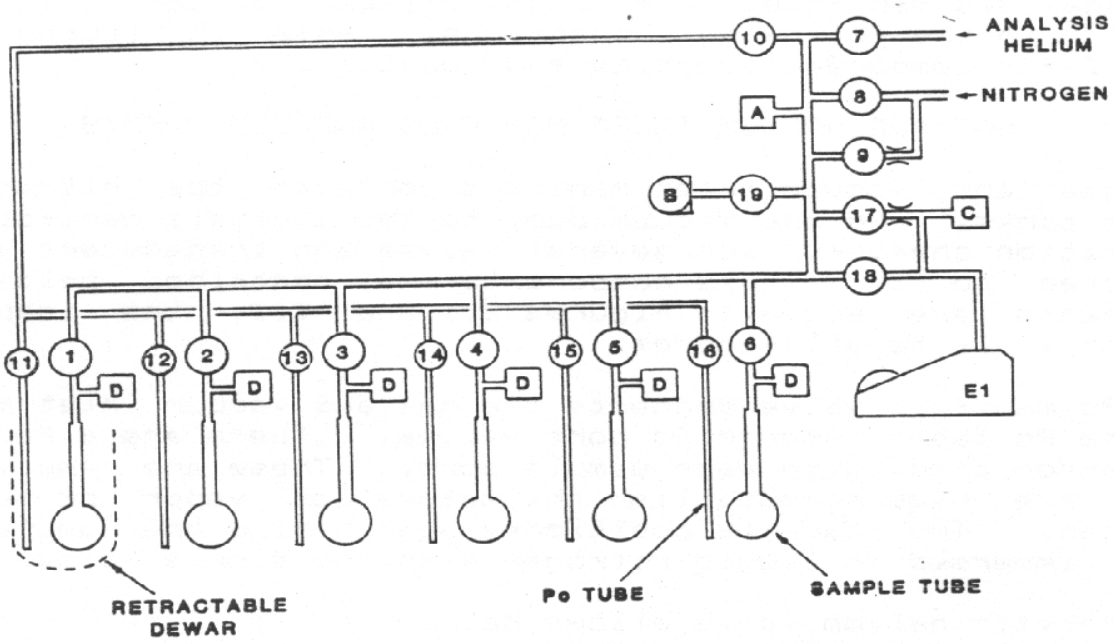

Fig. (3) Analysis part scheme .

Procedure

Appropirate quantities of samples loaded into sample flasks and then sample holders were mounted into degas ports.The sample flasks attached heating mantles to apply the degassing step. The degas vacuum meter set point 500 millitorr was mounted for each catalyst sample at 150 Cº for 3 h.When degassing completed , the heating mantles were removed and allow the sample to cool to the room temperature,then the samples were weighted . For dead volume measurment the sample flasks were covered with isothermal jacket and attached to a liquid nitrogen thermas.Pulses of helium gas were admitted up to equilibrium pressure. For adsorption measurements pulses of nitrogen gas were admitted until reaching the different equilibrium pressure.

Results and discussion

The physisorption of nitrogen gas were carried out for γ-Alumina,prepared catalysts and commercial catalysts at 77 K and relative pressure (P/P^o) from 0-1.

Figs. (1-12) show the BET plot for γ-Alumina ,prepared catalysts and commercial catalysts.The slopes and the intercepts of the plotes of $P/V(P^o-P)$ verses P/P^o (BET plots) were used to calculate the volumes adsorbed at monolayer coverage (V_m) for all samples by Eq. 5 .The surface area of the samples were calculated by Eq. 6 .**Table (4)** showes the obtained values of the surface areas for γ-Alumina ,Prepared Catalysts and commercial catalysts.

γ-Alumina has higher surface area compared with all catalysts,because it has more porous structure.This is also observed by Savitzky and Golay[Savitzky and Golay,1964].The surface area of monometallic platinum catalysts genarally decreases by platinum content increasing from 0.1 to 0.35 %. This is presumably due to bulky platinum catalyst crystallites,which block up some pores and hence reduces the surface area as mentioned also by [Vanden,1979].Higher content than 0.3 % up to 0.55 % slightly promotes the surface area increasing. This is may be due to creation a new pore which increase the surface area .At very high platinum content 0.6 % there is some reduction in surface area and this may be due to slight reduction in the number of pores.

0.3% Pt-0.3% Re/ γ-Al_2O_3 catalyst has a high surface area compared with a monometallic 0.35% Pt/ Al_2O_3 catalyst .Addition of 0.3 % Re to Pt catalyst may be made a good alloy (Pt-Re) which could be create a new pores resulting in an increasing in surface area as mentioned by [Michael.1982].

The addition of 0.03 % Ir to Pt / γ-Al_2O_3 gave lower surface area compared with 0.3% Pt-0.3% Re/ γ- Al_2O_3 catalyst and slightly higher surface area compared with 0.35% Pt/ γ- Al_2O_3 catalyst.

The values of constant C in BET equation were calculated by by Eq.7 and presented in column 6 of **Table (4) .**

The constant C is an indicator of adsorbate -surface interaction [Loweel,1984].The value of C for 0.35 % Pt-Ir / γ-Al_2O_3 and 0.3 % Pt-0.3%Re higher than 100 and this means that higher interaction between nitrogen and catalyst surface took place.When the value of C approximate (100),this means, that some fraction of surface is unoccupied as observed for γ- alumina where C= 86.58.

The C values were used for the heat of adsorption calculation of nitrogen gas on γ- alumina, prepared catalyst and commercial catalysts according to Eq. 7 .The values of heat adsorption were presented in column 7. **Table (4) .**

The heat of adsorption represents the affinity between nitrogen gas and catalyst surface. [Sing,1982].As the heat of adsorption increases, the volume adsorbed at high relative pressure decreases which can be consider due to the increase in the temperature of catalyst surface.

Table (4) Monolayer Capacity, Surface Area , constant C and heat of Adsorption

Catalyst	V_m cm^3/g	S g/cm^3	I g/cm^3	S_{BET} cm^2/g	C	E_1-E_2 J/gmol
γ-Al_2O_3	63.857	0.01469	0.000893	277.889	86.580	2855.309
0.1 Pt/ γ- Al_2O_3	59.1160	0.01273	0.004185	257.344	115.060	3037.935
0.2 Pt/ γ- Al_2O_3	49.995	0.01634	0.002375	232.604	142.87	3176.52
0.45 Pt/ γ- Al_2O_3	59.948	0.017453	0.002242	221.022	127.67	3104.51
0.55 Pt/ γ- Al_2O_3	51.839	0.019142	0.000148	225.665	130.1184	3116.67
RG-412 0.35% Pt/ γ- Al_2O_3	49.2996	0.020097	0.000187	214.611	108.342	2999.42
RG-402 0.6 %Pt/ γ- Al_2O_3	46.6555	0.021290	0.000143	203.100	149.23	3204.4
RG-482 0.3 %Pt-0.3 % Re/ γ- Al_2O_3	52.759	0.018135	0.000225	238.428	138.35	3155.94
RG-432 0.35% Pt- 0.03% Ir/ γ- Al_2O_3	53.2874	0.018636	0.002406	231.971	144.424	3183.497
RG-422 0.6% Pt-0.03%Ir/ γ- Al_2O_3	55.229	0.017972	0.000134	240.423	134.547	3138.097
RG-451 0.35% Pt-0.03 %Ir-Promotor/ γ- Al_2O_3	49.127	0.020226	0.000129	213.860	157.9369	3240.706
PS-10 0.375 %Pt-0.57 % Sn/ γ- Al_2O_3	44.0147	0.022530	0.000189	191.605	119.877	3064.19

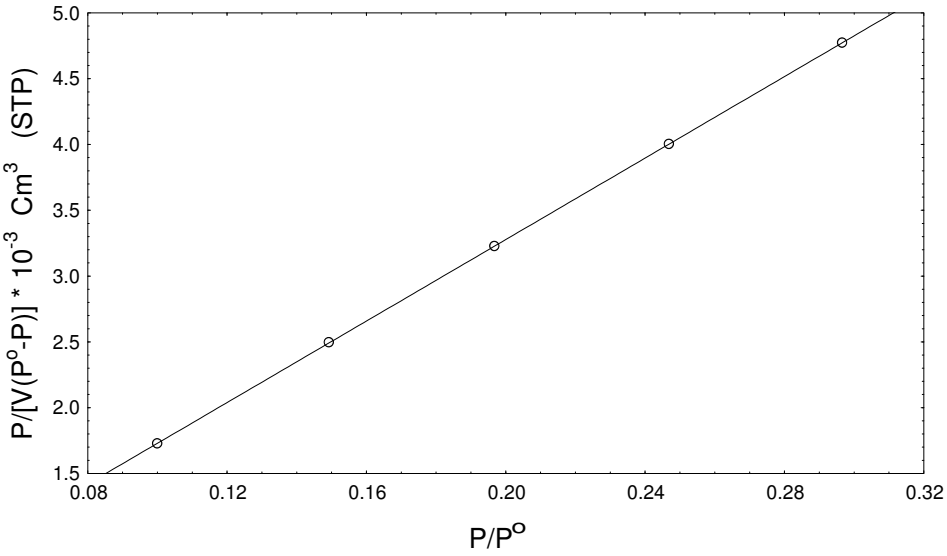

Fig.1 BET plot of adsorption data for Alumina

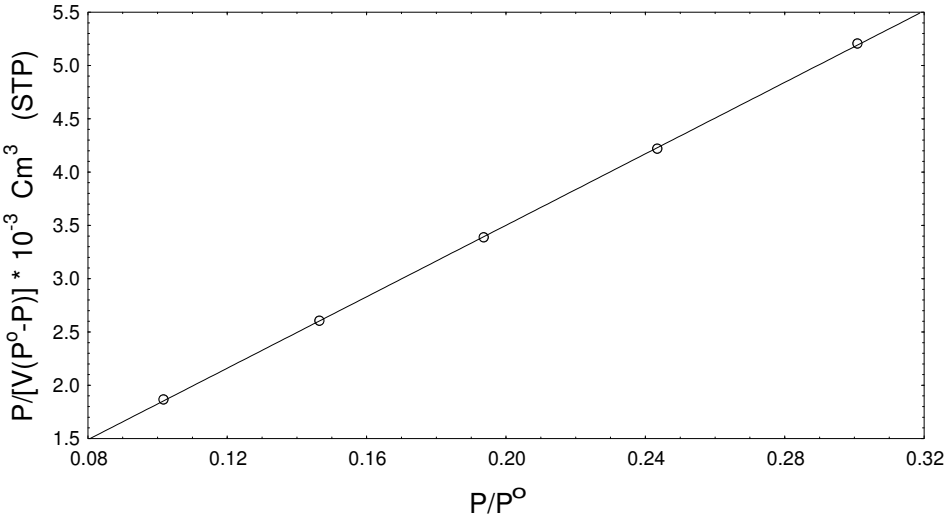

Fig.2 BET plot of adsorption data for 0.1 % Pt/Al_2O_3 catalyst

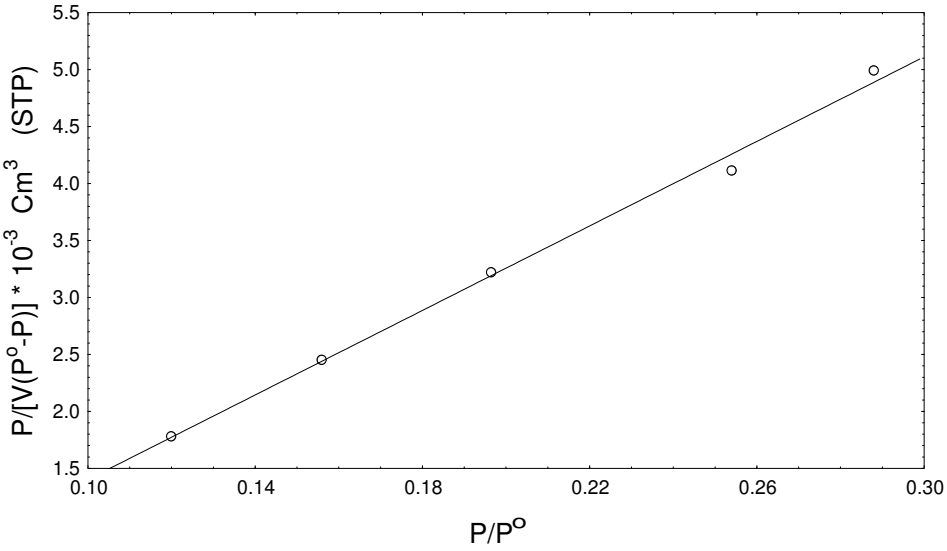

Fig.3 BET plot of adsorption data for 0.2 % Pt/Al_2O_3 catalyst

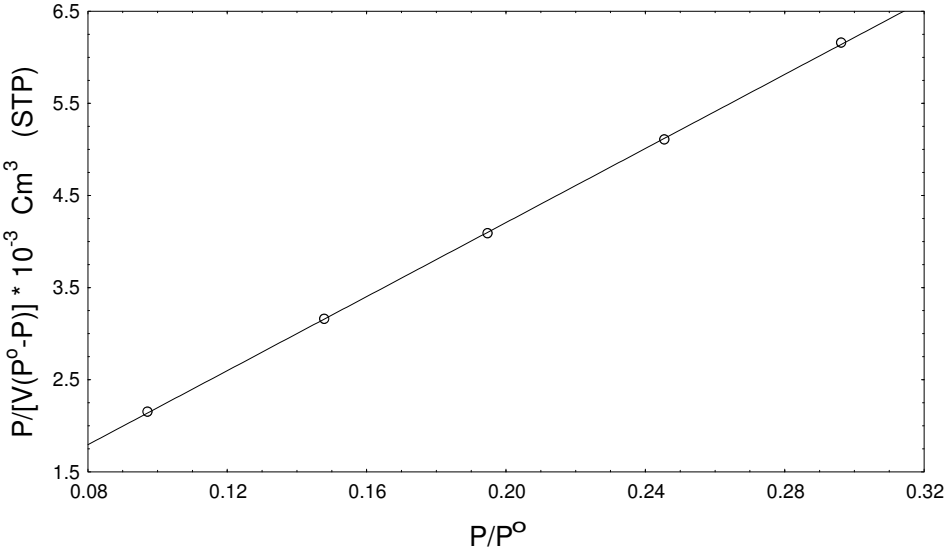

Fig.4 BET plot of adsorption data for RG-412 catalyst

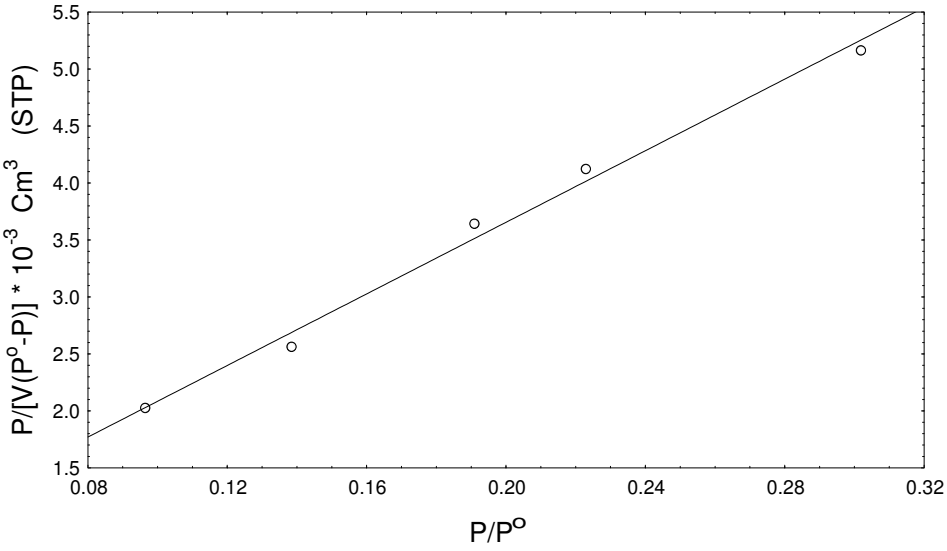

Fig. 5 BET plot of adsorption data for 0.45 % Pt/ Al_2O_3 catalyst

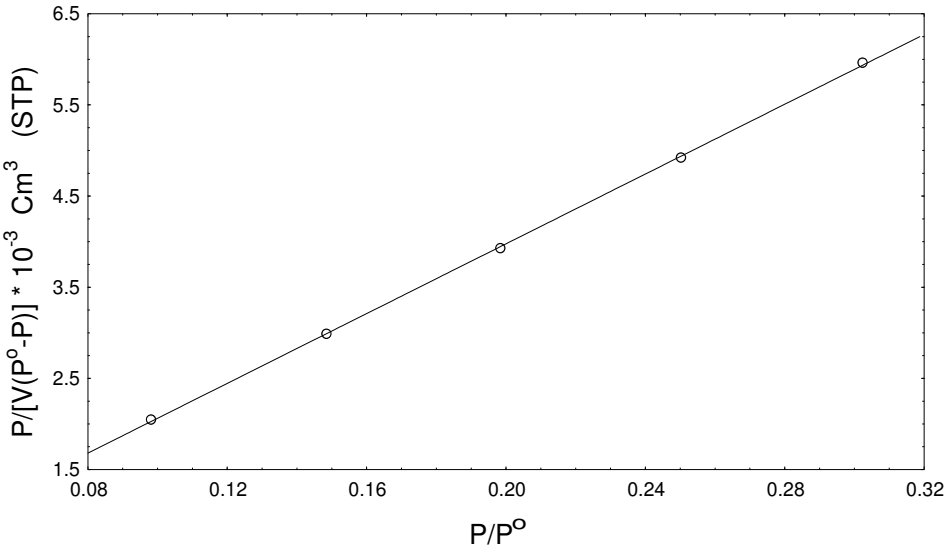

Fig. 6 BET plot of adsorption data for 0.55 %Pt/ Al_2O_3 catalyst

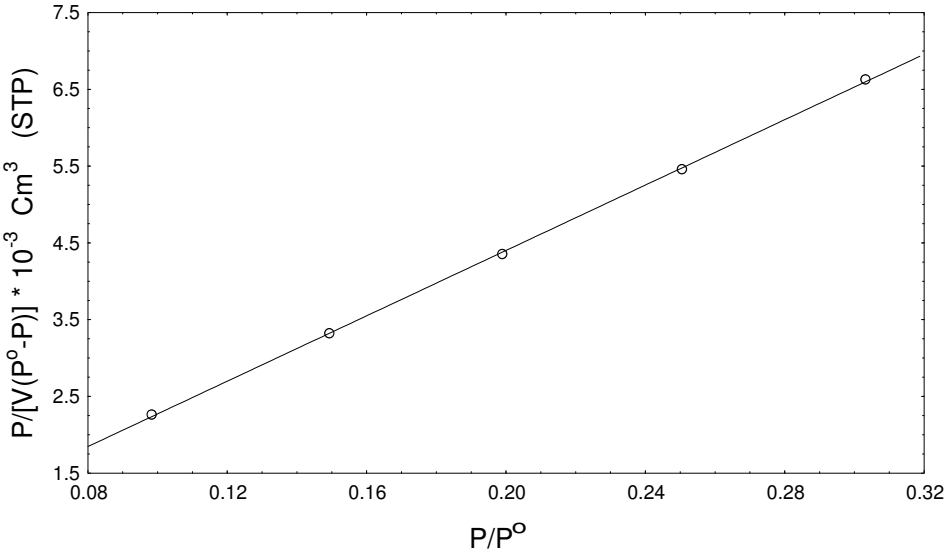

Fig. 7 BET plot of adsorption data for RG-402 catalyst

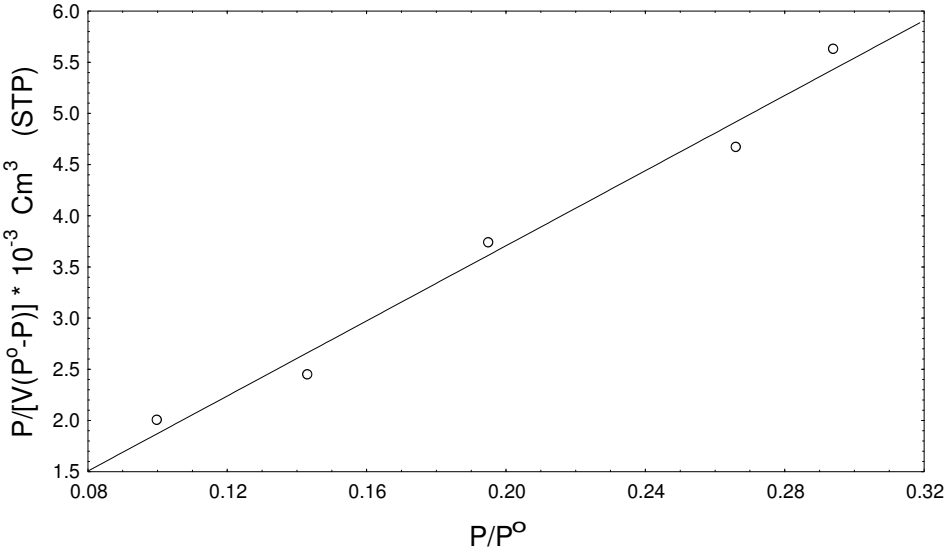

Fig.8 BET plot of adsorption data for RG-482 catalyst

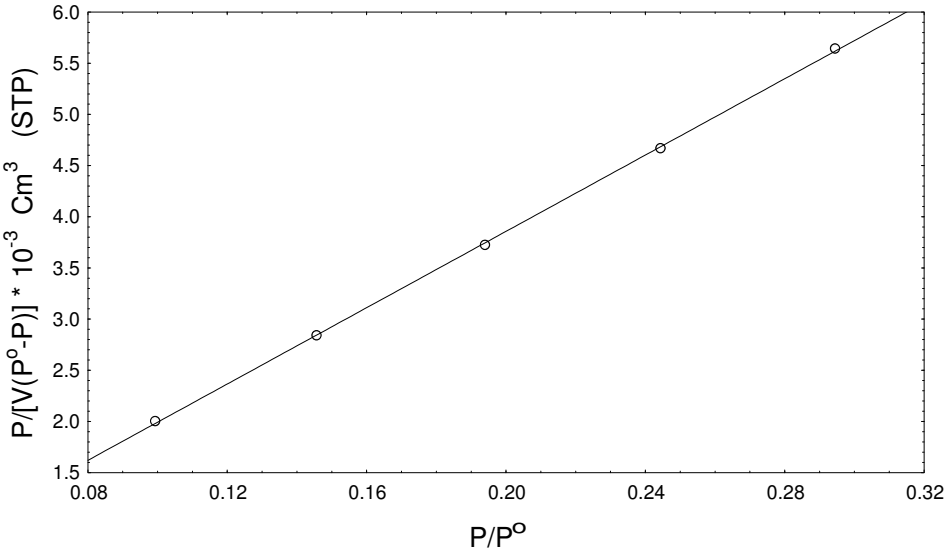

Fig.9 BET plot of adsorption data for RG-432 catalyst

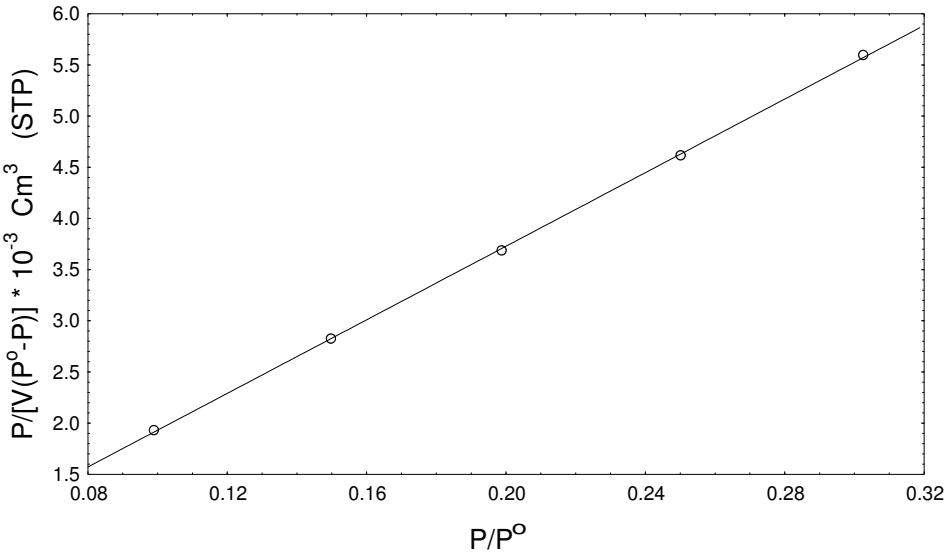

Fig.10 BET plot of adsorption data for RG-422 catalyst

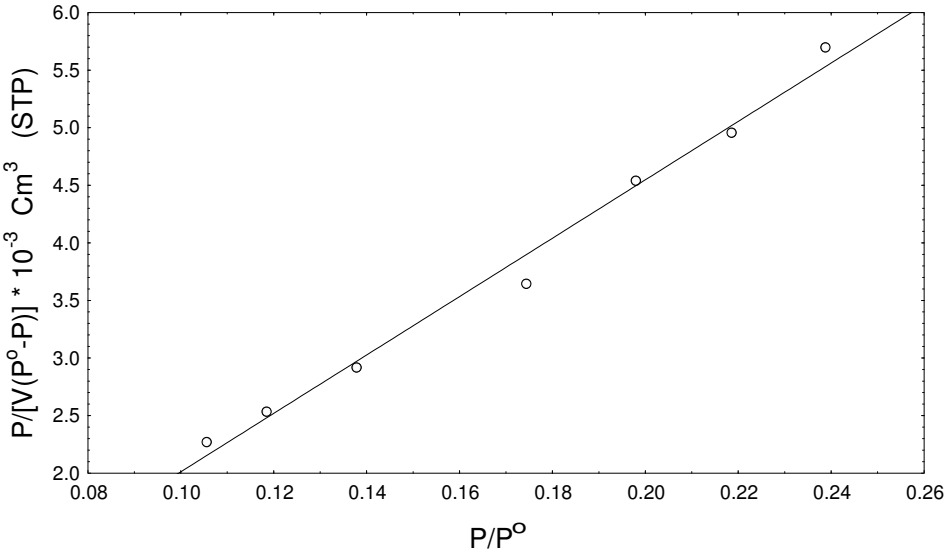

Fig.11 BET plot of adsorption data for RG-451 catalyst

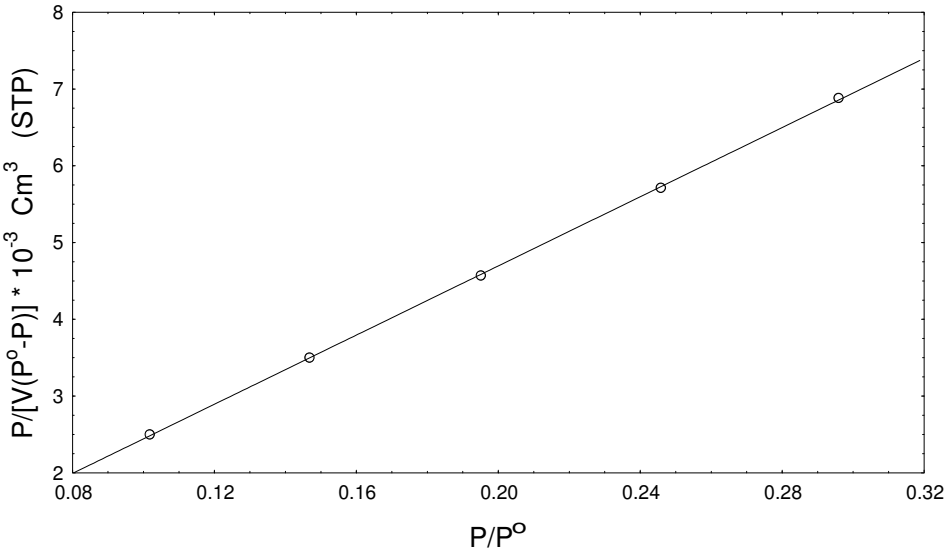

Fig.12 BET plot of adsorption data for PS-10 catalyst

REFERENCES

Brunauer, S. P.H. Emmett, E. Teller, J. Am. Chem. (1938), Soc.60 309.

Charlton,J.S.,Cordey-Hayes,M.,and Harris,I.R.,J.Less (1970),Common Met.20,105

Dubinin, M.M. (1955), Quart. Rev. Chem. Soc. 9 101.

D.I Enache,V. (2001), Dumitresce,Al.,Buletinul UPG,.

Jhon.Thomas.W and Barry (1998), adsorption technology and design,.

Gregg, S.J. K.S.W. Sing, (1982), Adsorption, Surface Area and Porosity, Academic Press, London,.

Kenneth Sing.J. (2001), Collids and Surface . 3.

Lowell, S., and John, E., Shields, (1984), Powder Surface Area and Porosity, Chapman and Hall, London and New York,.

Michael,J.K.,Robert,L.F and Denis, G.s., (1982), Distribution of Pt and Re in Pt-Re/Alumina Naphtha Reforming Catalysts, J.Catal.,178.445.

Oscik, J., (1982), Adsorption, Halsted Press, New York,.

Richardson, J.T., (1989), Principle of Catalyst Development, Houston, Texas, plenum press, New York,.

Savitzky,A., and Golay,M.J.E., (1964), Anal.Chem.,36,1627

Sing, K.S.W. (1976), Characterization of Powder Surfaces, Academic press, London,.

Van der Plas (1970), Physical and Chemical Aspects of Adsorbent and Catalysts,Academic Press,

Vanden,G.H.,and Rijnten,H., (1979), The Impergnation and Drying Step in Catalyst Manufacturing, studies in surface science and catalysis,Vol.3,265.

Young.D.M and A.D, (1962), Physical adsorption of gases, Butter Worths,London.

Nomenclature

C= Constant. Eq.7
E_1 = Average heat of adsorption in monolayer.(J/gmole) Eq.8
E_2 = Heat of condensation.(J/gmole) Eq.8
I=Intercept (g/cm^3) Eq.3
N= Avagadro number =$6.023 * 10^{23}$ (molecule/mole) Eq. 6
Ns= Nitrogen molecular cross sectional area= 0.162 nm^2 Eq.6
P= Equilibrium pressure (mmHg).
Po= Saturation pressure (mmHg).
R = gas constant = 8.314 (J/gmole.K) .
S= Slope(g/cm^3) Eq.4
T = Temperature (K)
V= Volume adsorbed (cm^3/g).
V_m= Monolayer coverage volume (cm^3/g)
ϕ = fraction of sites covered.
1-ϕ = fraction of sites not covered.

EFFECT OF STARVATION ON THERMO-ELASTOHYDRODYNAMIC LUBRICATION OF ROLLING / SLIDING CONTACT

Dr. Basim A. Abbas
Faculity member/College of Engineering/
Babylon University/Iraq

Dr. Somer M. Nacy
Assit. Prof. / Al-Khawarizmi
Engineering College/Iraq

ABSTRACT
A complete numerical solution of thermal compressible elastohydrodynamic lubrication of rolling / sliding contact was achieved to determine the effect of inlet boundary condition on the film shape, film pressure, and film temperature in an elastohydrodynamic line contact problem.
The direct iterative technique is used to solve the simultaneous system of Reynolds' ,elasticity , and energy equations for different locations of inlet oil fed . The effect of various load, speed , and slip conditions have been investigated . the results indicate that the effects of starvation are an increase of oil film temperature and decrease in oil film thickness so that the temperature effect are significant and can not be neglected.

الخلاصة

يتضمن البحث حلا" عدديا لمسألة التزييت الهيدروديناميكي المرن مع الأخذ بنظر الاعتبار التغير بـــدرجات الحرارة وذلك لدراسة تأثير منطقة الدخول على شكل طبقة الزيت, وتوزيع الضغط خـــلال طبقـــة الزيـــت وتوزيع درجة الحرارة خلال تلك الطبقة مع التركيز على المسائل ذات التلامس الخطي. تم اســـتخدام تقنيـــة الاختيار المباشر لحل المعادلات الحاكمة انيا والتي تتضمن معادلة رينولد ومعادلة المرونة ومعادلة الطاقـــة باستخدام طريقة الفروقات المحددة لمائع تزييت ذو علاقة لزوجة– ضغط تتبع قانون باروس. تمت مناقـــشة تأثير مختلف العوامل مثل الحمل والسرعة والانزلاق على شكل توزيع ضغط الزيت وتوزيع ســـمك طبقـــة الزيت ودرجة الحرارة خلال تلك الطبقة. أظهرت النتائج ان نقصان كمية الزيت تؤدي الـــى زيـــادة درجـــة الحرارة وتقليل سمك طبقة الزيت لذا يوصى بعدم اهمال تأثير درجة الحرارة عند العمـــل فـــي مثـــل هـــذه الظروف.

KEY WORDS
Hydrodynamic lubrication , Porous, Journal Bearing

INTRODUCTION

Rolling sliding machine elements such as bearings , gears, cams and their followers are frequently subjected to high load, speed , and slip conditions. The problem of thermo-elastohydrodynamic lubrication had been treated by many workers, Cheng et.al. (1965), Daow et.al (1987) and Sadeghi et.al. (1990,1987).

Most the published works have not consider the effect of the starvation on pressure distribution , film thickness and oil film temperature so the location of the inlet meniscus is considered as known. However the reduction in film thickness due to starvation has been studied by Chiu (1972) . He conconcluded that the starvation effect in most rolling element bearing are considerably greater than the inlet heating effect.

Full solutions for estimating film thickness of point contacts were made by Hamrock and Dowson (1976,1977) for flooded as well as starved contact. They found a dimensionless central and minimum film thickness for the flooded contacts indicating that the film thickness decreases for the starved condition as compared to the flooded condition.

Johns- Rahngat and Gohar (1994) proved that the results obtained from the work of Hamrock and Dowson are quite realistic when employing starvation conditions at the contact.

The present work is an attempt to study the thermal effect on the performance of contacting element in line contact with starved inlet boundary condition.

Direct iterative method was adopted to solve the governing equations of the problem.

GOVERNING EQUITIONS

The governing equations describing the steady state , thermo-elasto hydrodynamic lubrication of the line contact using Newtonian lubricant can be discribed as follows:

Reynolds' Equation:

Reynolds' equation which govern the pressure distribution inside the oil film presented between two non conformal surfaces in line contact can be written here as follows:

$$\frac{d}{dx}\left(\frac{\rho h^3}{\mu}\frac{dp}{dx}\right) = 12U\frac{d(\rho h)}{dx} \qquad (1)$$

The pressure distribution in the contact zone is subjected to positivity constraint.The boundary conditions for Reynolds equation are given by

$P(x_i)=0$, $P(x_o)=dP_{xo}/dx=0$

Elasticity Equation:

Oil film thickness distribution can be evaluated in this case by using the following equation used by Wolff et.al. (1992)

$$h = h_o + \frac{x^2}{2R} - \frac{2}{\pi E}\int_{x_i}^{x_o} p(s)\ln[(x-s)/s]^2 ds \qquad (2)$$

Equations of State

The lubricant viscosity is modeled by Baru's pressure viscosity formula. The equation was modified to include the thermal effect. It can be written as presented by previous reference

$$\mu = \mu_o e^{[\alpha p + \gamma(T-T_o]} \qquad (3)$$

The dependence of density on pressure and temperature can be expressed by the following equation:

$$\rho = \rho_o\left[1 + \frac{.58*10^{-9}P}{1+1.7*10^{-9}P}\right]*\left[1-\varepsilon_t(T-T_o)\right] \qquad (4)$$

Energy Equation

The temperature distribution a cross the oil film is expressed by solving the energy equation reported by Wolf (1992) and Gohr (1988)

$$\varepsilon_T u T \frac{\partial p}{\partial x} + \mu\left(\frac{\partial u}{\partial y}\right)^2 = \rho C u \frac{\partial T}{\partial x} - k\frac{\partial^2 T}{\partial y^2} \quad (5)$$

The boundary conditions used with the above equation are given by

At y=0 ; $T=T_o$

At y=h ; $T_2 = \frac{k}{\sqrt{\pi \rho_2 C_2 k_2 U}} \int_{-\infty}^{x} \frac{\partial T}{\partial y} \frac{d\zeta}{(x-\zeta)^{1/2}}$ (6)

Where,

ρ_2 = density of the solid disk (Kg/m^3)=7800 Kg/m^3 for steel disk

C_2= heat capacity of the solid disk (KJ/Kg.K)=52 KJ/Kg.K for steel disc.

U= speed of the solid disk (m/s).

The mean oil film temperature can be expressed as follows

$$Tm = \frac{1}{h}\int_0^h T dy \quad (7)$$

by making the suitable substitutions, the mean oil film temperature can be evaluated as:

$$T_m = \left\{ \begin{array}{l} (T_1+T_2)/2 + N_{UD}\eta^2\left[\frac{16}{15\eta^2 U^2}(\frac{WH}{\pi})^4(\frac{dp}{dx})^2 + \frac{Sp^2}{12} - \frac{h_f sp}{3}\right] + \\ N_{cu}\rho H^2 \frac{dT_m}{dx}\left[\frac{2}{15\bar{\eta}\bar{U}}(\frac{WH}{\pi})^2\frac{dp}{dx} - \frac{Sp}{24} - \frac{U_1}{12(U_1+U_2)}\right] \end{array} \right\} / \left\{ \begin{array}{l} 1 + N_{AC} H^2 \frac{dp}{dx} * \{ \frac{2}{15\eta\bar{U}} \\ (\frac{WH}{\pi})^2\frac{dp}{dx} - \frac{Sp}{24} - \frac{U_1}{12(U_1+U_2)} \} \end{array} \right\} \quad (8)$$

Where,

$$N_{UD} = \frac{(E' R\bar{U})^2}{T_o \eta_o K} \quad (9)$$

$$N_{AC} = \frac{\varepsilon (E' R)^2 \bar{U}}{4\eta_o K}(\frac{8W}{\pi})^2 \quad (10)$$

$$N_{CU} = \frac{C\rho_o E' R^2 \bar{U}}{\eta_o K}(\frac{8W}{\pi})^{\frac{3}{2}} \quad (11)$$

$$h_f = \frac{8}{\eta\bar{U}}(\frac{WH}{\pi})^2 \frac{dP}{dx} \quad (12)$$

NUMERICAL TECHNIQUE

To obtain a complete numerical solution to the problem of compressible thermo-elastohydrodynamic lubrication of rolling/ sliding contacts the direct iterative procedure was followed to solve the simultaneous system of compressible Reynolds' Eq.(1), elasticity Eq.(2), and the energy Eq.(5) together with the Equations of state, Eqs.(3,4) . The flow chart shown in **Fig.(1)** illustrates the computational procedure used for calculating the pressure, film thickness , and temperature distribution within the lubricant film.

The isothermal pressure and film shape are obtained and these values are then used to arrive at the initial temperature field within the lubricant film. The influence of temperature is introduced on viscosity , and density and the new pressure and film thickness are calculated. The iterative procedure is continued until the resulted temperature and pressure satisfied the following convergence criteria .

$$\frac{\sum |P^n - P^o|}{\sum |P^n|} \le 0.0001 \quad \text{and} \quad \frac{\sum |T^n - T^o|}{\sum |T^n|} \le 0.0001$$

RESULT AND DISCUSSION

The analysis was carried out for three different nondimensional load parameters, namely (1.36E-7), (2.28E-7), and (3.42E-7). Three different slide to roll ratios are also been considered, namely (0.5,1.07,1.32). Five inlet positions were invistigated, one considered for the flooded condition, Xi=-4a while the other four account for the starved conditions in which Xi=-3.5a ,3a ,2.5a and 2a.The results in **Figs. (2,5,8)** show that the pressure spike decreases and diminshes for all the above cases. The pressure spike try to move outward towared the outlet with the increase of the applied load. The maximum pressure increses as the degree of starvation increases to maintaine a constant applied load.

The oil film thickness decreases with increasing the degree of starvation and the applied load as shown in **Figs. (3,6,9).** Also the nip that occurs in the nondimensional film shape at the fully flooded case diminishes as the amount of starvation increased and the film shape changes to that of flatened type. This is can be explained with refering to **Figs. (4,7,10)** since the oil film temperature increases with increasing the degree of starvation and the applied load which lead to low oil viscosity.

The results presented in **Fig. (12)** also shows that the oil film thickness decreases as the the slide to roll ratio increases. This can be explained with the aid of **Fig. (13),** since it can be shown from this figure that the oil film temperature increases with increasing the slide to roll ratio. The maximum pressure increases as the slide to roll ratio increases in order to maintain constant applied load.

CONCLUSIONS

The concluding remarks which can be withdrawn from the present results are :

1- There is a significant increase in oil film temperature as the degree of starvation and the slide/ roll ratio increases.
2- The pressure spike is decreased (nearly vanshes) as the amount of starvation and slid / roll ratio increases. The pressures pike tends to move toward the outlet as the applied load increases.
3- The oil film thickness decreases as the amount of starvation increased which is dangerous phenomenon leading to occurrence of film rapture due to metal to metal contact at the tip of the mating surfaces.
4- The results indicate that the temperature effect and the position of oil feed have significant effects and must be taken into consideration for proper design.

NOMENCLEATURE

a Hertizian half width = $\sqrt{2RW/((l/2)E^2(\pi/2))}$

E1 modulus of elasticity of roller (1) (N / m^2)

E2 modulus of elasticity of roller (2) (N / m^2)

E equivalent modulus of elasticity = $2/((1-\nu_1^2)/E1+(1-\nu_2^2)/E2)$ (N/m^2)

H oil film thickness (m)

h_o central oil film thickness (m)

P′ oil pressure (N/m^2)

P non dimensional oil pressure = $p / P_{hertizian}$

$P_{hertizian}$ non dimensional oil pressure= $aE/4R$ (N/m^2)

R equivalent radius of the two rollers = $R_1R_2/(R_1+R_2)$ (m)

R_1 radius of roller (1) (m)

R_2 radius of roller (2) (m)

S_p slide to roll ratio=$2(U_2-U_1)/(U_1-U_2)$

$\overline{U} = \eta_o(U_1+U_2)/4E'R$

$\overline{W} = W/E'LR$ Dimensionless load parameter

α pressure viscosity coefficient

ϵ oil thermal expansivity (K^{-1})
γ temperature viscosity coefficient
$\nu_{1,2}$ poisons ratio for the upper and lower disks=0.3

REFERENCES

Chin Y. P. , (1972), exploratory analysis of EHD. properties of lubrication , SKF. Technical Report No. Al. 72P010 ,.

F. Sadeghi , Thomas A. Daow, (1987), Thermal effect in rolling /sliding contact part (2) . analysis of thermal effect in fluid film, transection of the ASME , vol. 109, July, pp. 512-520.

F. Sadeghi , (1987), Thomas A. Dow ,Richard R .Johnson, Thermal effect in rolling / sliding contacts part 3 – Approximate method for prediction of mid film temperature and sliding traction, J. of Tribology , July, Vol. 109, PP. 519-524.

F. Sadeghi , Ping C. Sui , (1990), Thermal Elastohydrodynamic lubrication of rough surfaces , ASME journal of lubrication technology, vol. 112, pp. 341- 346.

Hamrock, B. J. and Dowson D., (1976), Isothermal elastohydrodynamic lubrication of point contacts part I – Theoretical formulation , J. of lub. Tech. Trans. of the ASME , vol. 98 ,.

Hamrock , B. J. and Dowson D. (1977), Isothermal elastohydrodynamic lubrication of point contacts part III – Fully flooded results, J. of Lub. Tech. Trans ASME vol. 99,.

H.S. Cheng and B. Sterlicht , (1965), A numerical solution for the pressure, temperature , and film thickness between two infinitely long lubricated rolling and sliding, cylinders under heavy loads . J. of basic engineering, sept..

Johns – Rahenjat , P.M. and Gohar, R , (1994), measuring contact pressure distribution under elastohydrodynamic point contacts, Tribo test Journal,1-1,.

R. J. Gohar, (1988), Elastohydrodynamic lubrication, Ellis Horwood Limited.

R. Wolff, T. Nonaka , A kubo, K. Matso ., (1992), Thermal elastohydrodynamic lubrication of rolling / sliding line contacts, Trans. of the ASME, vol.114, October, pp. 706 –713.

T. A. Daow R.D. Stockwell, J. W. Kannel, (1987), Thermal effect in Rolling / Sliding EHD contacts: part (1) experimental measurement of surface pressure and temperature. J. of tribology, July vol. 109, pp. 503-511.

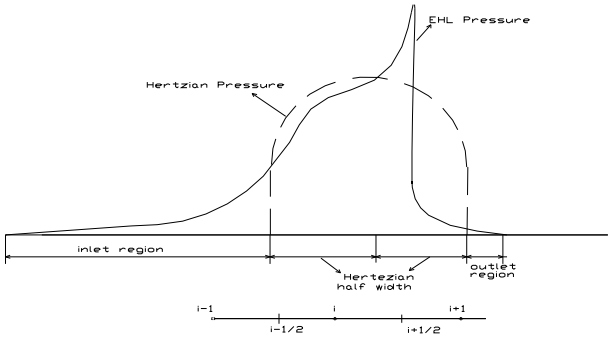

Fig.(1.a) Discretization Scheme

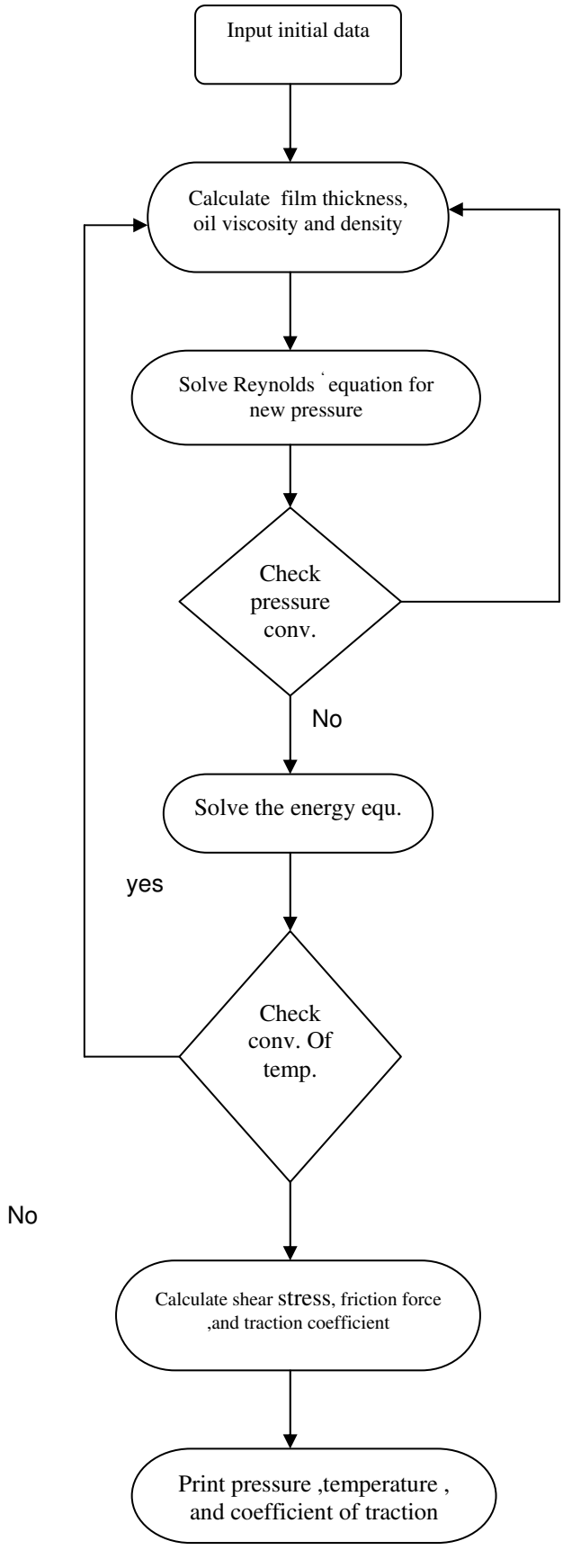

Fig.(1.b): Flow chart for computer program

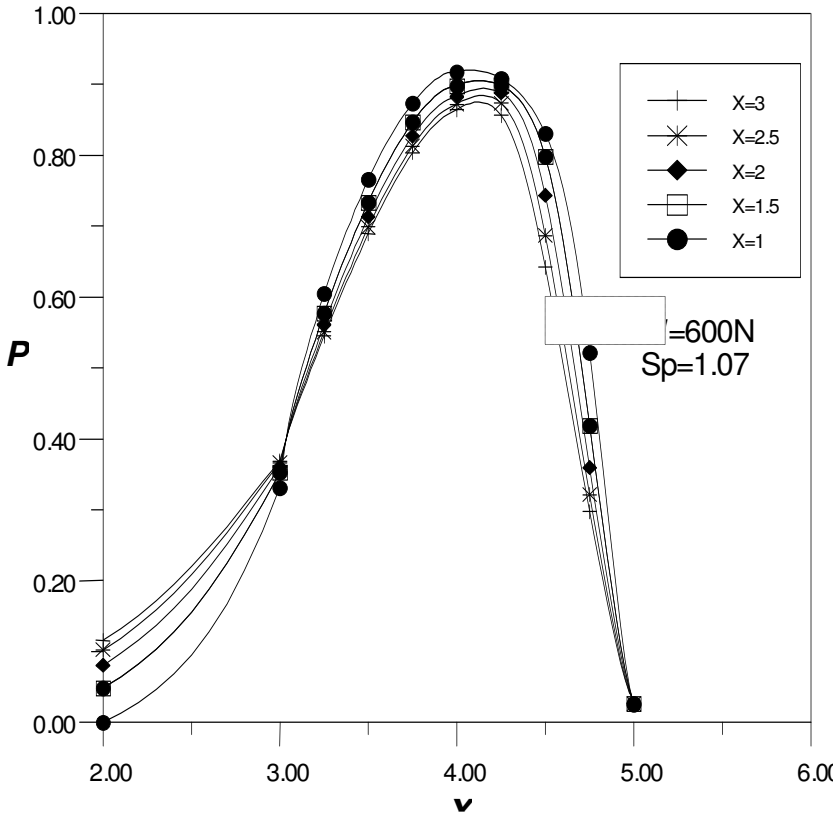

Fig.(2): Effect of starvation on oil pressure distribution
$\overline{W}=1.3*10^{-7}$

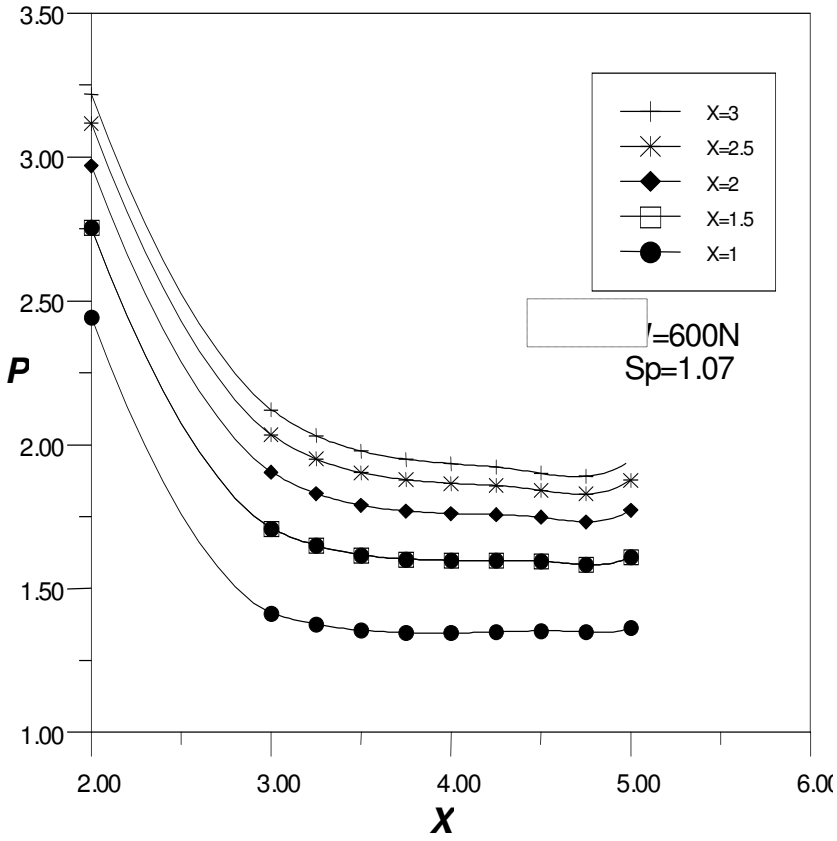

Fig.(3): Effect of load on oil film distribution for different oil inlet boundary condition. $\overline{W}=1.3*10^{-7}$

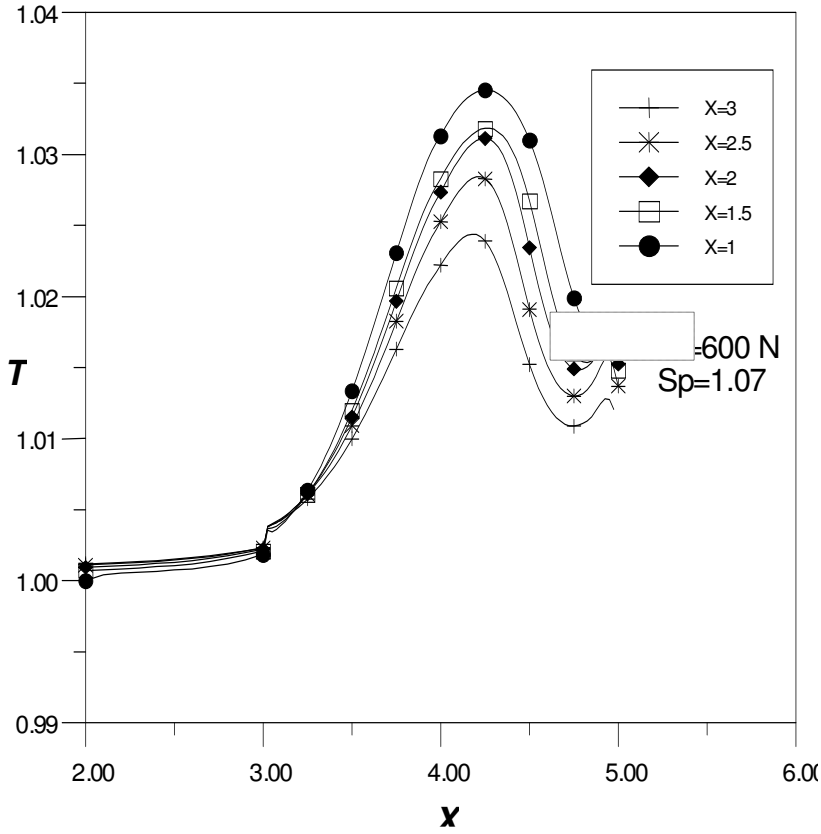

Fig.(4): Temperature distribution for different oil inlet $W=1.3*10^{-7}$

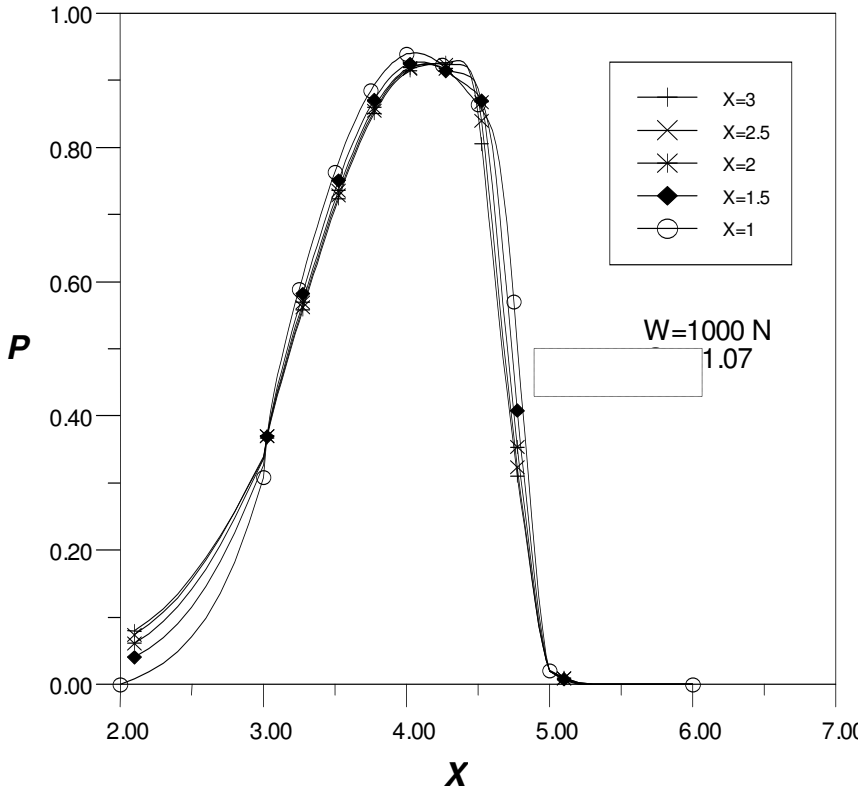

Fig.(5): Pressure distribution for different oil inlet $W=2.28*10^{-7}$

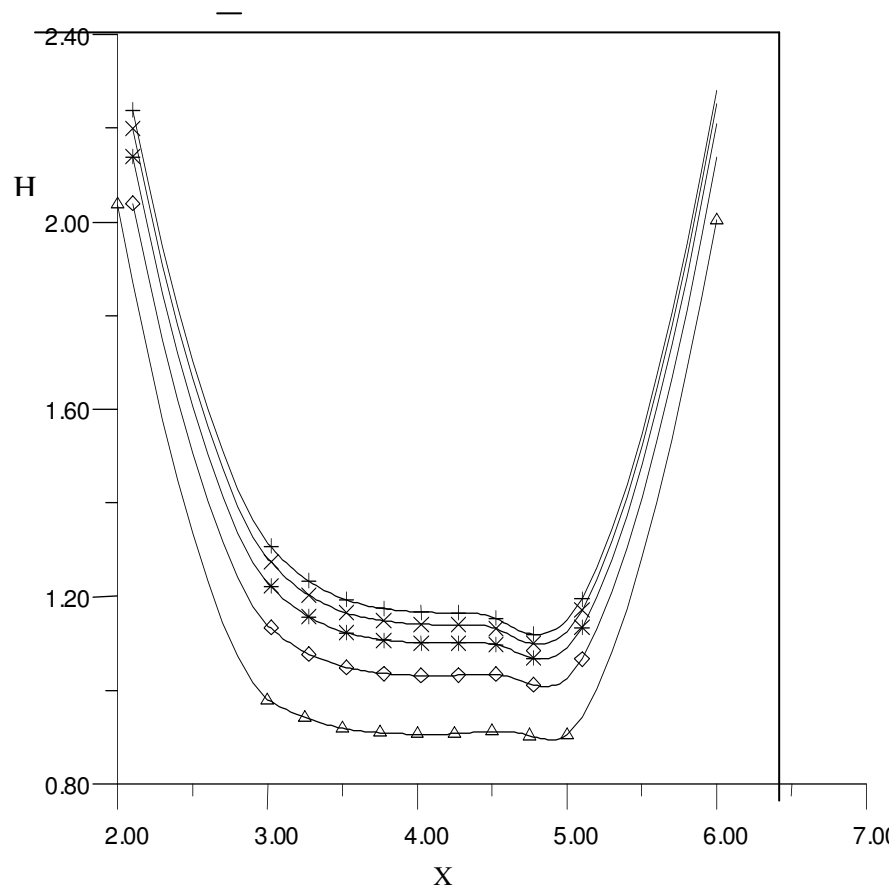

Fig. (6): Oil film thickness for different oil inlet
W=2.28*10^{-7}

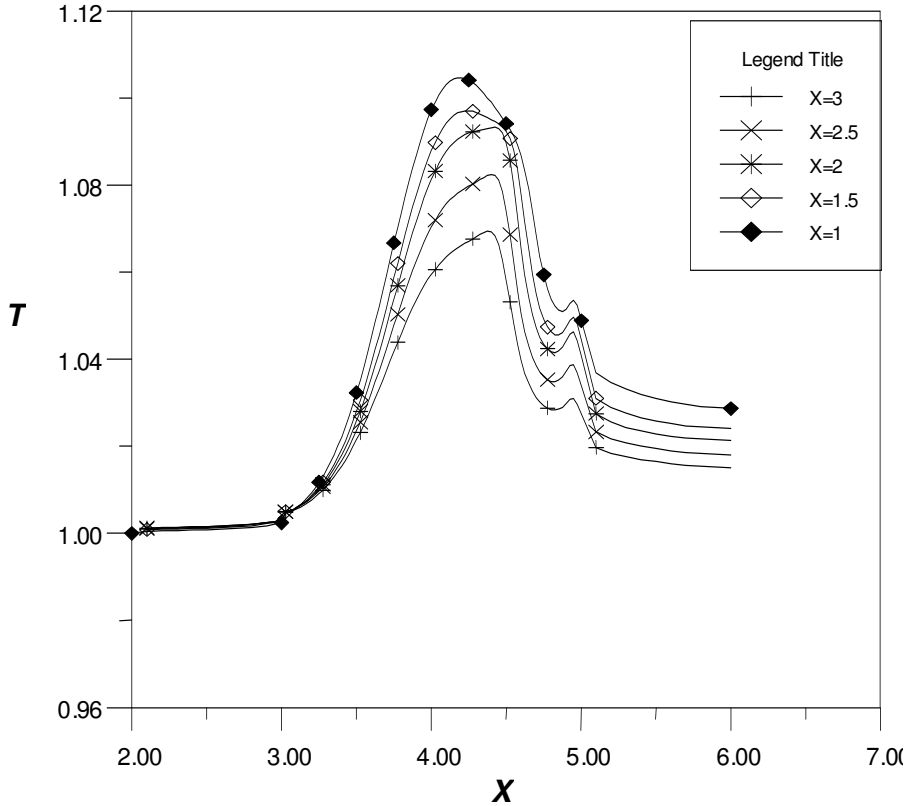

Fig.(7): Oil temperature distribution for different oil inlet
W=2.28*10^{-7}

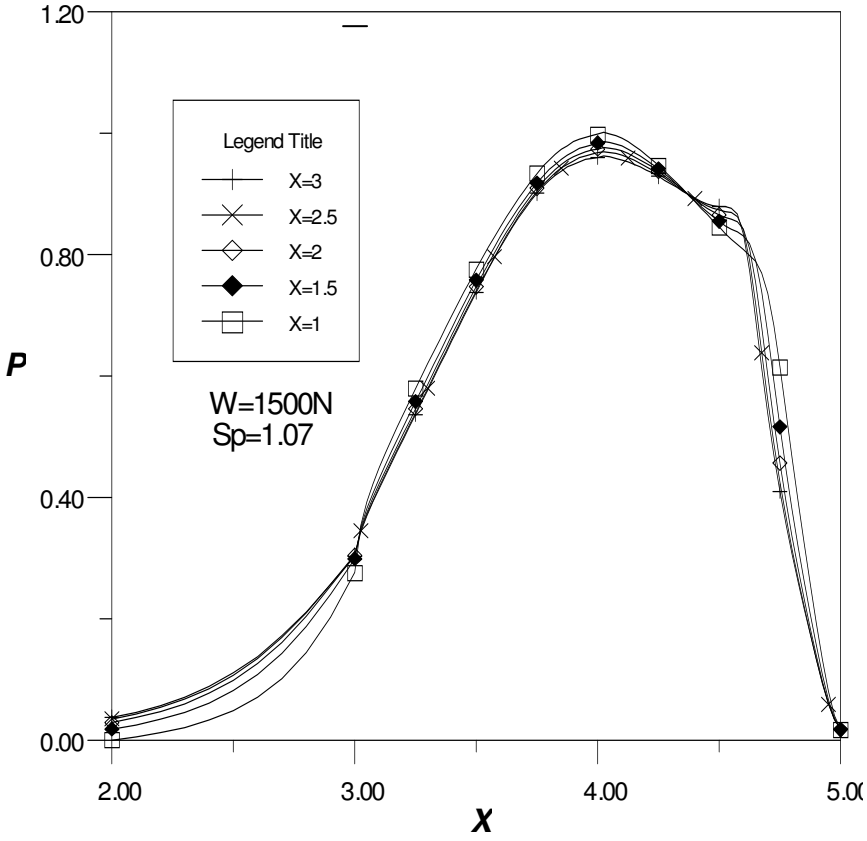

Fig. (8):Pressure distribution for different inlet boundary condition
$W=3.42*10^{-7}$

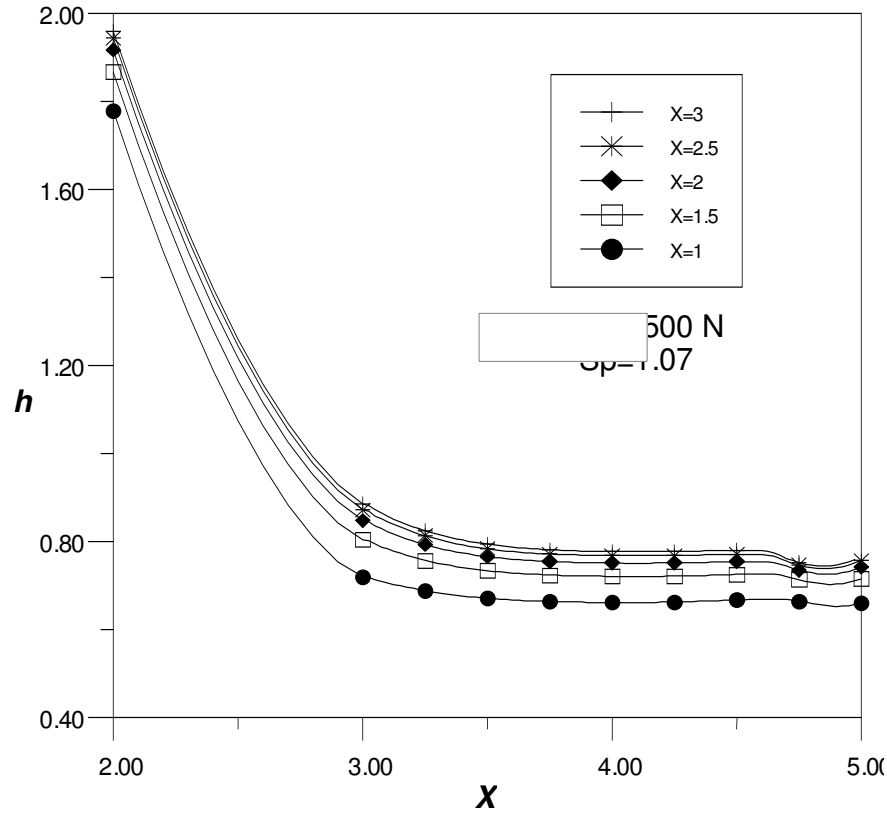

Fig. (9):Oil film thickness for different oil inlet
$W=3.42*10^{-7}$

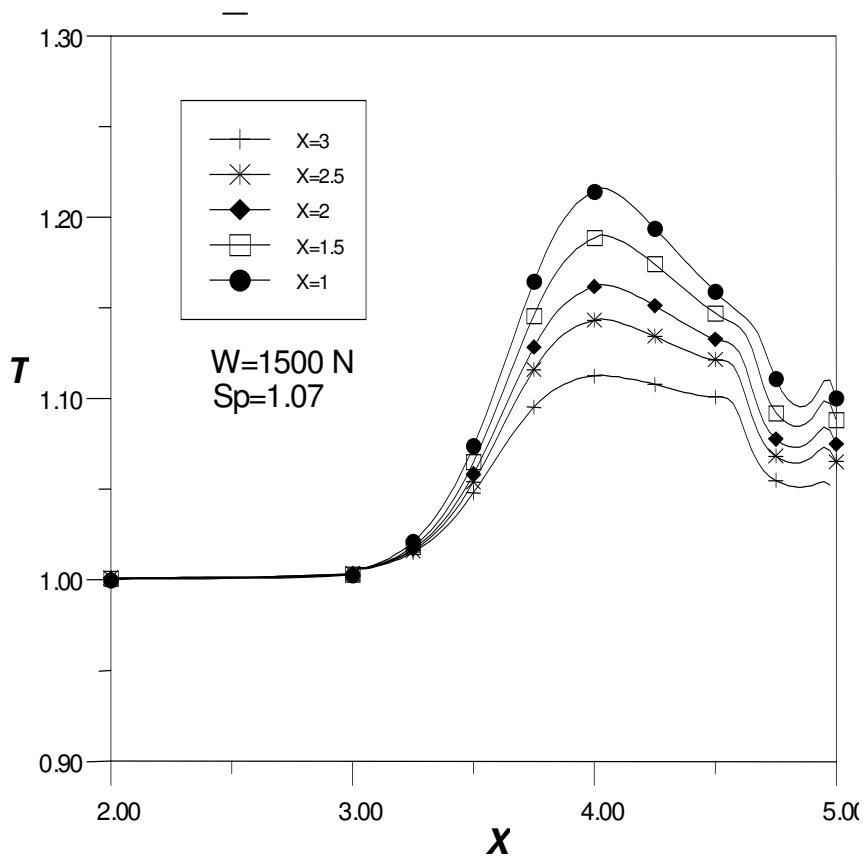

Fig. (10):Oil temperature distribution for different oil inlet $W=3.42*10^{-7}$

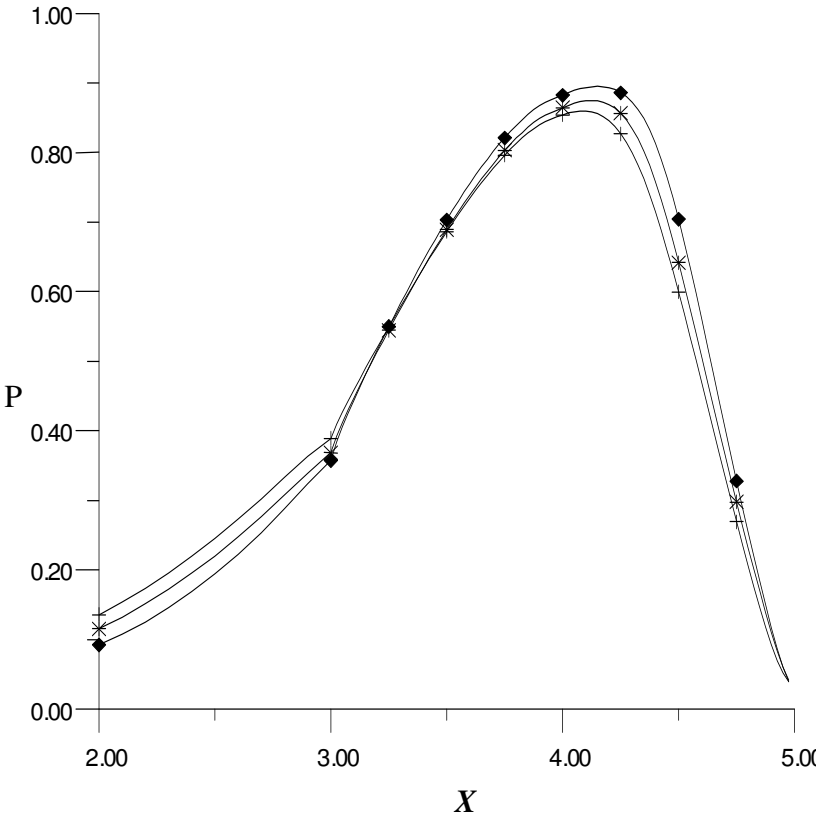

Fig.(11):Effect of slide to roll ratio on the pressure distribution for different oil inlet positions $W=3.42*10^{-7}$

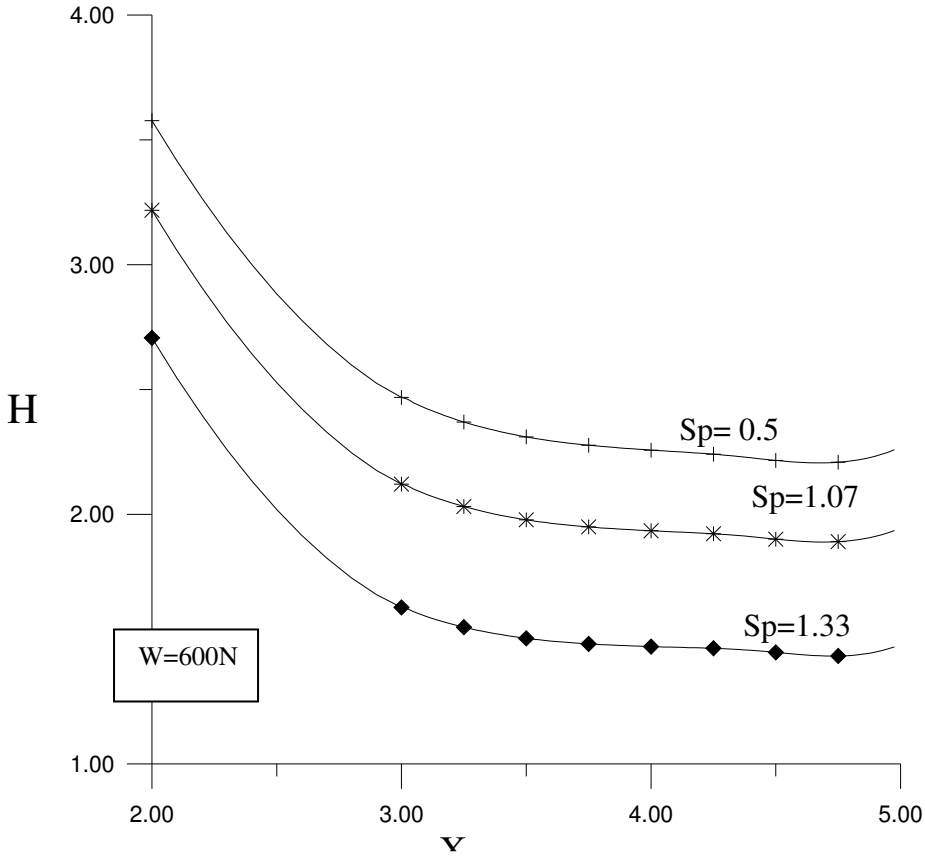

Fig. (12): Effect of slide to roll ratio on film thickness for different oil inlet

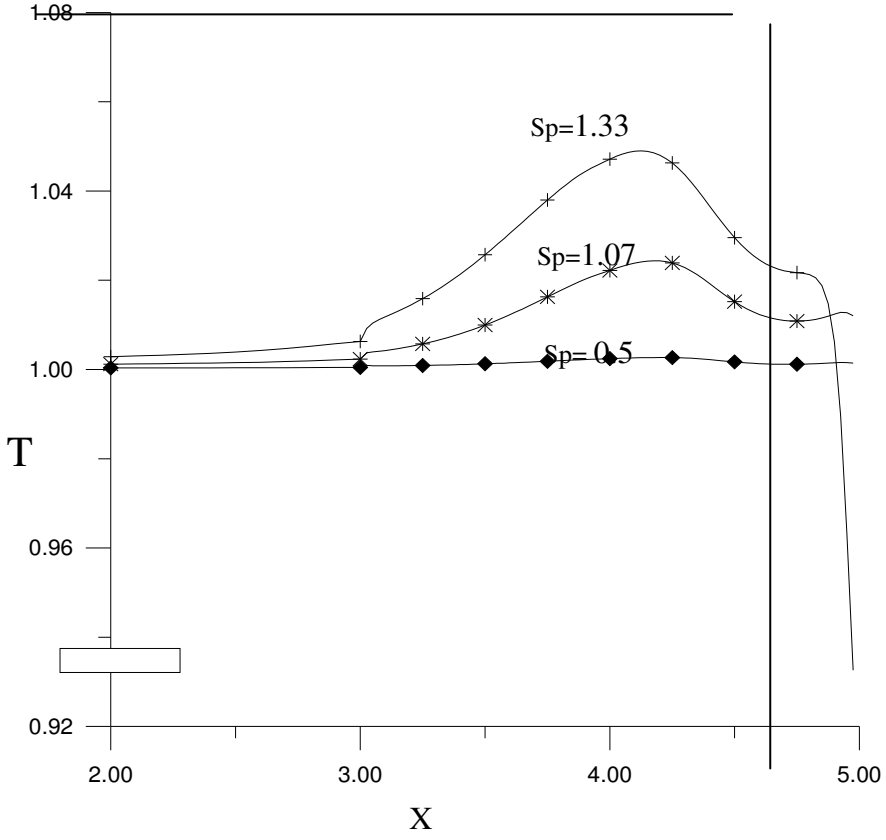

Fig. (13): Effect of slide to roll ratio on oil film temperature distribution for different oil inlet

CONSTRUCTION RISK MANAGEMENT

Assistance Professor Mr. Zuhair M. Saco, Abbas M. Burhan
Civil Engineering, College of Engineering,
University of Babylon.

ABSTRACT
In most of the construction projects, there are many events or risks may occur during the execution of project. These risks (e.g. the excess of project cost or the expected time, increasing the prices of material and labor, accidents, changes, engineering errors or omissions, bad quality, delay in reaching the facilities to the site, etc.) may effect negatively on the project and the parties. Therefore, these risks must be identified and assessed accurately to avoid or reduce the negative effects for these risks. The concept of risk is used to assess and evaluate uncertainties associated with an event or a process. A construction process includes many uncertainties, therefore, the construction project's parties are becoming aware of the construction process and thus the risks within this process are seeking more and more clarification that all is being done to remove foreseeable risk and minimize unforeseeable risk. It is also becoming clear that generic approaches to the management of risk are maturing and becoming easier to apply.

الخلاصة

في أغلب المشاريع الإنشائية يتوقع حدوث الكثير من الأحداث أو المخاطر أثناء التنفيذ. تلك المخاطر (مثل زيادة كلفة المشروع أو الزمن المتوقع لإنهائه، زيادة أسعار المواد أو العمال، الحوادث، التغيرات، الأخطاء والأهمالات، النوعية السيئة، ألخ) ممكن أن تؤثر بصورة سلبية على المشروع وأطراف المشروع. لذا فأن تلك المخاطر يجب أ، تكون محددة ومقيمة بصورة دقيقة من أجل تجنب أو تقليل التأثيرات السلبية لتلك المخاطر. أن صناعة الإنشاء هي محاولة خطرة مع العديد من الشكوك المرتبطة بأحداث أو ظروف. تلك الأحداث ممكن أن تكون مخاطر منظورة (مثل تأخيرات، أضرا بات، إصابات، أخطاء وأهمالات، الخ) أو قد تكون مخاطر غير منظورة (مثل فيضانات، زلازل، حروب، الخ). أن مفهوم المخاطر يكون مستخدم لتقييم تلك الشكوك المرتبطة بحدث أو عملية. ولما كانت تلك الصناعة تتضمن الكثير من الشكوك (أو عدم التأكيد) فأن أطراف المشروع أصبحوا قلقين من تلك العملية الإنشائية التي فيها كل الأطراف يحاولون أن يتجنبوا المخاطر المنظورة ويقللوا من المخاطر غير المنظورة. كذلك أصبح واضح بأن مداخل كثيرة لإدارة المخاطر أصبحت مدروسة وسهلة التطبيق.

KEY WORDS
Risk, Risk Management, Project Management, Risk analysis

DEFINITION OF RISK AND RISK MANAGEMENT

Risk can be defined as the possibility of losses, injuries, damages, and/or delays arising during the execution of a project which may adversely affect its success. While risk management can be defined as a technique that helps to identify the elements that could potentially have a major negative impact on a project. Risk management process is a system that enables the management to evaluate the level of impact of a risk and then develop a plan or contingency for his eventuality and reducing this impact (Simmons,1998).

POTENTIAL AREAS OF RISK

When focusing on risk, it has been traditional to focus on the following items:

Cost

The focusing on cost generally means failure to keep the project within the budget, cost forecast, initial estimate, or the original tender.

Time

The focusing on time means failure to keep the project within its schedule or the time in which the project must complete.

Quality

This generally means a lack of focus on meeting the standards for function, fitness for purpose and the environment (Latham,1999).

Generally, risks encountered throughout a construction project can include:

1- Failure to complete within the time.
2- Failure to get the right planning and building regulations approval within the time.
3- Unforeseen ground conditions.
4- Exceptionally bad weather delaying a project.
5- Strike by labor force.
6- Unexpected price rises for labor and material.
7- An accident to an operative causing physical injury.
8- Latent defects through poor workmanship.
9- The occurrence of fire, flood, earthquake, etc.
10- Loss and expense claim which caused by late delivery of design by design team.
11- Failure to complete project within client's budget allowance.

THE TYPES OF RISK

There are risks to all projects and risk management is the process of identifying and containing them to ensure a project success. The following are some types of risk that are inherent in most construction projects (Bent & Thuman,1990):

Engineering Risk

The engineer is responsible for any engineering errors and omissions resulted from his negligence that can result in costly change orders, damage to equipment, or injury to persons.

Construction Risk

Almost, the contractor is responsible for many of the risks occurred during the execution of project. These risks may effect on the amount of contractor's profit or may lead to the loss. The contractor's risk can be minimized and that depends directly on the contractor's perceived abilities to forecast, assess, and manage those elements of exposure that are directly under its control. Normally, construction cost overruns are attributable to inaccurate estimation of construction requirements.

Inaccurate estimates result from inadequate scope of the project. For example, design or specifications may be inadequate; or contingency, allowances, engineering changes, inflation, or site conditions may not have been adequate foreseen.

Schedule Risk

Delays in the completion of a project result in increased overhead expenses and a general escalation of construction costs. Delays can result from such conditions as poor design or construction management, inadequate scheduling estimates, labor strikes or slowdowns, unexpected site conditions, delays in delivery of equipment, or defective equipment.

THE FIVE STEPS IN RISK MANAGEMENT PROCESS

Risk management is the identification, measurement, and treatment of property, liability, and personnel risk exposures. The process includes five steps (Williams & Heins,1985):

1- The risk of project must be identified. Risk identification is the first and perhaps the most difficult function that the project management must perform. Risk identification can be defined as determining which risks are likely to affect the project and documenting the characteristics of each. Failure to identify all the risks of the firm means that the management will have no opportunity to deal with these unknown risks intelligently. Identifying project risks should start early in the conception phase. The emphasis at that time is on identifying the high risk factors that might make the project difficult to execute or destine it to failure.

2- After risk identification, the next important step is the proper measurement of the losses associated with the risk. This measurement includes a determination of the probability or chance that the risk will occur, the impact of risk, and the ability to predict the losses that will actually occur during the budget period. The measurement process is important because it indicates the exposures that are most serious and consequently most in need of urgent attention.

3- Once the risk had been identified and measured, the various tools of risk management should be considered and a decision made with respect to the best combination of tools to be used in attacking the problem. These tools include primarily avoiding the risk, reducing the chance that the loss will occur or reducing its magnitude if it does occur, transferring the risk to some other party, and retaining or bearing the risk.

4- After deciding among the alternative tools of risk treatment, the project management must implement the decisions made.

5- The results of the decisions made and implemented in the first four steps must be monitored to evaluate the wisdom of those decisions and to determine whether changing conditions suggest different solutions.

THE RELATIONSHIP BETWEEN RISK AND OTHER TERMS

The term “Risk” is related to other engineering terms such as reliability and PERT (Project Evaluation and Review Technique) as illustrated:

Reliability

Reliability concerns with what can go right and how to maximize the likelihood that things will go right. But the risk concerns with what can go wrong, what happens if some things go wrong, what are the risks inherent to a project, and how could the project parties protect themselves from the consequences of something going wrong.

The reliability of an item (or an activity in the project) is the probability that the item will be performed successively under specified operational and environmental conditions throughout a specified time. The reliability of an item for a project can be calculated from the equation (1) (Kales,1998):

$R(t) = e^{(-\lambda t)}$ Eq. (1)

Where: $R(t)$ = the reliability at the time t .
λ = constant failure rate.

Where:

$0 \leq R(t) \leq 1$

$R(t) = 1$ implies certainty of success.

$R(t) = 0$ implies certainty of failure.

$R(t) + Q(t) = 1$, where $Q(t)$ is the unreliability or the risk at the time t; so $Q(t) = 1 - R(t)$.

λ can be estimated from test of field data as shown in equation (2):

$\lambda = C / T$ Eq. (2)

Where C is the number of failures during total time T (e.g. number of injuries, number of delays of arriving materials, or number of change orders).

Consider a simple example, a project has a target completion time. The project manager expected that delays will occur during the execution. Over 12-weeks period (84 days), 5 delays were reported. What is the probability of occurrence the risk of delays for 3-weeks? Hence:

$C = 5$

$T = 84*24 = 2016$ hours $t = 3*7*24 = 504$ hours

$\lambda = C / T = 5/2016 = 0.00248$ per hours

The project reliability over 3-weeks (504 hours) period:

$R(t) = e^{(-\lambda t)} = e^{-(0.00248)(504)} = 0.287$

Which is the probability that the project will be performed for 3-weeks without delays. Hence, the risk of delays for 3-weeks is:

$Q(t) = 1 - R(t) = 1 - 0.287 = 0.713$

PERT Method

The PERT method (Project Evaluation and Review Technique) was devised to take account of the difficulty of estimating the duration of activities which can not be established conclusively from past experience. It was intended by its originators to account for risk and uncertainty in project scheduling. It is a way to warn managers of the need to compensate for the consequence of a risk on project duration.

The PERT method incorporates risk into project schedules by using three estimates for each project activity (a, m, and b) which enter in equation (3) to account the average time (t_e) as shown (Pilcher,1976):

$t_e = (a + 4m + b) / 6$ Eq. (3)

Where:

t_e = the average time or the mean of the *Beta* distribution. Wherever, the originator of PERT method assumed that the plots of duration of the activities almost fitted a *Beta* distribution curve.

m = the most likely duration of the activity.

a = the optimistic time that is the shortest time which could be anticipated for the activity.

b = the pessimistic estimate of the time, that is, the duration of the activity assuming that everything goes at its worst

.

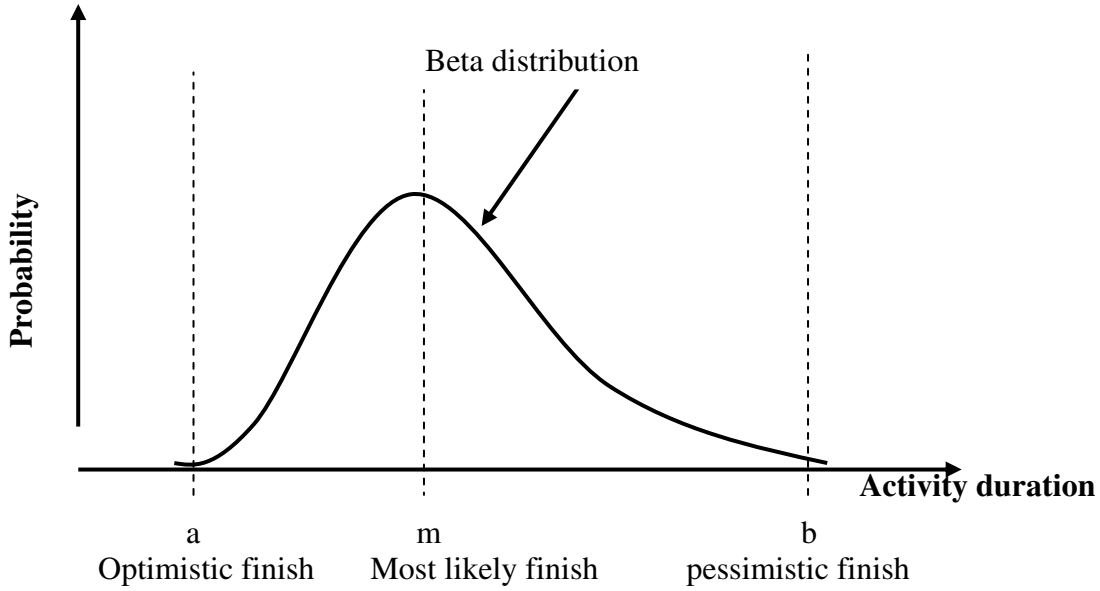

Fig. (1), An Activity Times in PERT Related to the Beta Distribution.

Greater risk in an activity is reflected by a greater spread between m and b, as shown in **Fig. (1)**. For an activity with no perceived risk, a, m, and b would be identical. If, however, hazards are identified, the way to account for them is to raise the values of b and m. In general, the greater the perceived consequence of risk hazards on time, the further b is from m. Thus, for a particular activity with given optimistic and most likely values (a and m), using a large value of b to account for greater risk will result in a large value of t_e , which logically would allow more time to complete the activity and compensate for things that might go wrong (risks). In addition, however, the larger value of b also results in a larger time variance for the activity because variance is:

$$V = (b - a) / 6 \qquad \text{Eq. (4)}$$

This larger V will result in a larger variance for the project completion time, which would spur the cautious project manager to add a time buffer to the project schedule (Nicholas,2001).

Consider a simple example, an activity within a project has a target completion time of (8 months). Suppose the activity has little risk and the values of (a, m, and b) are estimated as (5, 6, and 7 months), respectively. From equation (3) and (4), the values of t_e and V are thus (6 months) and (0.33 months). Using a normal approximation values for project duration, we can compute the probability of completing the project in (8 months), thus:

$$Z = (D - t_e) / \sqrt{V} \qquad \text{Eq. (5)}$$

$$Z = (8 - 6) / \sqrt{0.33} = 3.46$$

Where:

Z= a normal approximation value for calculating the probability.

D= the target completion time.

From the table of normal distribution, this Z-value yields a probability of over 99 percent. Assuming management trusts the time estimates, they would likely proceed with the project without worry.

Now, take the same one-activity project and suppose a major risk is identified that would increase the estimate of the pessimistic value from 7 to 12 months. In that case, t_e and V would be (6.83 months) and (1.167 months), and Z would be:

$$Z = (8 - 6.83) / \sqrt{1.167} = 1.08$$

and from the table, this Z-value yields a probability of about 86 percent. Given the lower probability of meeting the (8 months) target time, management might add a time buffer to the schedule (extend the target time), or take action to reduce the risk (which would allow a lower value for b). In short, assuming that the estimates for a, m, and b are credible, the PERT method provides a way for measuring the consequence of risk on project completion times.

RISK RESPONSE PLANNING

Risk response planning addresses the matter of how to deal with risk. In general, the ways of dealing with an identified risk include transferring the risk, altering plans or procedures to avoid or reduce the risk, preparing contingency plans, or accepting the risk.

Transferring the Risk

Risk can be transferred partly or fully from the owner to the contractor, or vice versa, using contractual incentives, warranties, or penalties attached to project performance, cost, or schedule measures. The contractor and the owner may decide to split the risk through a contractual agreement in which each manages the risks they can handle best. Different types of contracts split the risks in different ways. For example, in fixed price contract (e.g. lump sum contract), the contractor assumes almost all of the risk for cost overruns, while in cost plus fixed fee, the owner assumes almost all of the risk.

Of course it is impossible to entirely transfer the risk to one party or another. Even with a fixed price contract, where the contractor takes all the risk, the owner still incur damages or hardship should the project exceed the target schedule or the contractor declare bankruptcy. The project still must be completed and someone has to pay for it. Coming along with the transfer of risk usually is a transfer of authority, so that an owner agreeing to a cost plus fixed fee contract also will almost certainly argue for a large measure of management oversight on the project (Nicholas,2001).

Avoiding the Risk

Risk can be avoided by eliminating risky activities, minimizing the complexities, changing contractors, incorporating redundancy and safety procedures, and so on. Even though many risk factors can be avoided, not all can be eliminated, especially in large or complex projects. Attempting to eliminate risk usually entail adding innumerable management controls and monitoring systems that increase system complexity and introduce new sources of risk. Research projects and innovative, new product development projects are inherently risky, but they offer potential for huge benefits later on. Because the potential benefits of such a project is proportionate to the size of the risk, it is better to reduce risk to an acceptable level rather than completely avoid risk.

Reducing the Risk

Key elements, which can reduce the risks, include (Office of Financial Management,1998):

1- Early establishment of project definition.
2- Clear and coordinated project responsibilities.
3- Adequate construction administration services are included in the contract with consultants.
4- The necessity of experience of project staff.
5- Project scope, schedule, and budget are balanced and determined at outset and reviewed regularly during the project.
6- Differences and disputes are resolved immediately.
7- A systematic and thorough review of construction documents is performed before bidding the project.

Risks can be reduced through many ways associated with technical performance, meeting schedules, and meeting project cost target as illustrated (Nicholas,2001):

❖ The ways of reducing risk associated with technical performance are:

1- Employ the best technical team.
2- Base decisions on models and simulations of key technical parameters.
3- Use mature, computer-aided system engineering tools.
4- The technical team need incentives for encouraging the success of work .
5- Hire outside specialists for critical review and assessment of work.
6- Perform extensive tests and evaluations.
7- Minimize system complexity.

❖ The ways of reducing risk associated with meeting schedules are:

1- Create a master project schedule and strive to adhere to it.
2- Schedule the most risky tasks as early as possible to allow time for failure recovery.
3- Maintain close focus on critical and near-critical activities.
4- Put the best workers on time-critical tasks.
5- Provide incentives for overtime work.
6- Organize the project early and be careful to adequately staff it.

❖ The ways of reducing risk associated with meeting project cost targets are:

1- Identify and monitor the key cost drivers.
2- Use low-cost design alternative reviews and assessments.
3- Verify system design and performance through modeling and assessment.
4- Maximize usage of proven technology.

Contingency Planning

Contingency is the amount of money (or time) that should be added to the base estimate in order to predict the total installed cost and the accurate completion time for the project. Contingency may also be interpreted as the amount of money that must be added to the base estimate to account for work that is difficult or impossible to identify at the time a base estimate is being prepared. Sometimes, contingency is intended to cover known unknowns. That is, the estimator knows there are additional costs, but the precise amount is unknown (Oberlender,2000).

So, contingency is a necessary component of an estimate. Engineering and construction are risk endeavors with many uncertainties, particularly in the early stages of project development. Contingency is assigned based on uncertainty and may be assigned for many uncertainties, such as pricing ¸ escalation, schedule, omission, and errors.

Traditional Methods of Assigning Contingency

There are many methods of assigning contingency, and the estimator must select the method considered most appropriate for each project, based on information provided by the project management team.

1- Percentage of Base Estimate:

Contingency may be assigned based on personal experience. A percentage is applied to the base estimate to derive the total contingency. Although this is a simple method, the success depends on extensive experience of the estimator and historical cost information from similar projects.

Contingency may be determined as a percentage of major cost items rather than as a percentage of the total base estimate. This method typically relies on the personal experience and judgement of the estimator, but the percentage can also be from established standard percentage based on historical data. This method has the advantage of considering risk and uncertainty at a lower level than that used when contingency is based on a percentage of the total base estimate (Oberlender,2000).

Generally, many companies use this method to assign contingency needed to be added to the base estimate. Since, after the estimator estimates the costs of items of a project such as civil works, electrical works, mechanical works, etc., he adds contingency as a percentage of each major cost

item about depending on the type of item and the personal experience of estimator. Therefore, the personal experience and judgement of the estimators and engineers should not be overlooked in the process of assigning contingency. Even the most advanced computers are not substituting for the knowledge and experience of the human mind. Estimators with many years of experience with a particular type of facility can often be quite accurate in assigning contingency based on how they feel about the level of uncertainty and risk associated with a project, the cost data used in preparing the estimate, and the thoroughness of the effort in preparing the base estimate.

2- Expected Net Risk:

The estimator may determine contingency based on expected maximum risk and likelihood. The expected value for risk is a function of the risk impact (or outcome) and likelihood of occurrence as shown below:

Expected value = $\sum$ [(outcome) × (likelihood)]

This method is used if the project was repeated many times. The risk consequence on project duration is called the risk time, RT. It is the expected value of the estimated time required for risk correction, computed as (Nicholas,2001):

RT = (corrective time) × (likelihood) Eq. (6)

The risk consequence on project cost is called the risk cost, RC. It is the expected value of the estimated cost required for risk correction, computed as:

RC = (corrective cost) × (likelihood) Eq.(7)

For example, suppose the base time estimate (BTE) for project completion is (26 weeks) and the base cost estimate (BCE) is ($71,000). Assume that the risk likelihood for the project as a whole is (0.3), and should the risk materialize, it would delay the project by (5 weeks) and increase the cost by ($10,000). Hence,

RT = (5) × (0.3) = 1.5 weeks

RC = ($10,000) × (0.3) = $3000

These RT and RC would be included as contingency or buffer amounts in the project schedule and budget to account for risk and must be added to the base estimate to result the final estimate. The final estimate for time and cost is computed as:

ET = BTE + RT = 26 + 1.5 = 27.5 weeks

EC = BCE + RC = $71,000 + $3000 = $74,000

Where ET and EC are the expected project completion time and cost respectively.

The above way is used for risk factors that affect the project as a whole. Another way to determine the expected net risk value is to estimate the risk likelihood and corrective time (and cost) for each element of the project. For example, a project has eight work packages, and for each the base cost estimate (BCE), risk likelihood, and corrective cost have been estimated. The **Table (1)** lists the information for each work package and gives EC, where EC is computed as:

EC = BCE + [(corrective cost) × (likelihood)] Eq. (8)

For the same eight work package project, assume the base time estimated (BTE), risk likelihood, and corrective time have been estimated for each work package. The **Table (2)** lists the information for each work package and gives ET, where ET is computed as:

ET = BTE + [(corrective time) × (likelihood)] Eq. (9)

Table (1), Expected Net Risk Analysis for Cost.

Element	BCE	Corrective cost	Likelihood	Expected net risk	EC
A	$10,000	$2,000	0.2	$400	$10,400
B	$8000	$1,000	0.3	$300	$8,300
C	$16,000	$4,000	0.1	$400	$16,400
D	$10,000	$6,000	0.2	$1,200	$11,200
E	$8000	$2,000	0.3	$600	$8,600
F	$9000	$2,000	0.1	$200	$9,200
G	$5000	$1,000	0.3	$300	$5,300
H	$5000	$1,500	0.3	$450	$5,450
Total	$71,000			$3,850	$74,850

Table (2), Expected Net Risk Analysis for Time.

Element	BTE (week)	Corrective time (week)	Likelihood	Expected net risk	ET
A	6	1	0.2	0.2 week	6.2
B	4	1	0.3	0.3	4.3
C	6	2	0.1	0.2	6.2
D	10	3	0.2	0.6	10.6
E	2	1	0.3	0.3	2.3
F	8	1	0.1	0.1	8.1
G	1	1	0.3	0.3	1.3
H	1	1	0.3	0.3	1.3

Suppose the **Fig. (2)** represents the network for the project of the above example. In this example, without considering the risk time, the critical path would be [A-B-D-E-G-H], which gives a project BTE of (24 weeks). Accounting for risk consequences, the critical path does not change but the duration is increased to (26 weeks). This is the project ET. Although activities on critical and near critical paths should be monitored carefully, in general, any activity that poses a high risk consequence (high likelihood and/or high impact) should also be monitored carefully, even if not on critical path.

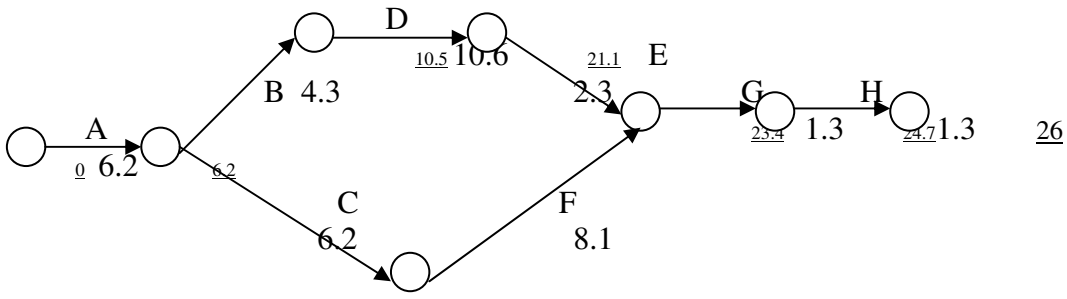

Fig. (2), Project Network, Accounting for Risk Time.

Accept Risk (Do Nothing)

Not all impacts are severe or fatal, and if the cost of avoiding, reducing, or transferring the risk exceeds the benefit, then "do nothing" might be advisable. Of course, this response would not be chosen for risks where the impacts or consequences are potentially severe.

RIGHTS AND RESPONSIBILITIES OF PROJECT PARTIES

The contract includes many rights and responsibilities for the project's parties, especially those for the owner and the contractor, and there are many conditions that effect on those parties and may lead to disputes or differences between them. Therefore, it must identify the rights and the responsibilities for each party and who must bear the risks that occur during the execution of contract.

Rights and Responsibilities of Owner

The owner, as a contracting party, has several rights especially reserved for him. Depending on the type of contract and its specific wording, he may be authorized to award other contracts in connection with the work, to require contract bonds from the contractor, to approve the surety proposed, to retain a specified portion of the contractor periodic payments, to make changes in the work, to carry out portions of the work himself in case of contractor default or neglect, to withhold payments to the contractor for adequate reason, and to terminate the contract for cause. The right of the owner to inspect the work as it proceeds, to direct the contractor to expedite the work, to use completed portions of the project before contract termination, and to make payment deductions for uncompleted or default work are common construction contract provisions (Clough,1975).

By the same token, the contract between owner and contractor imposes certain responsibilities on the owner. For example, construction contracts make the owner responsible for furnishing or arranging financing, providing site and access, acquiring permits and licenses, contracts for all necessary services, and making periodic payments to the contractor. The owner must assume all risks that have not been assigned to or assumed by others. He is required to make extra payment and grant extensions of time in the event of certain risks provided for in the contract. When there are two or more prime contractors on a project, the owner has a duty to coordinate them and synchronize their field operations.

Generally, the owner is responsible for the following exceptional risks (Ministry of Planning,1988):

1- War (whether war be declared or not), invasion, act of foreign enemies, or civil war.
2- Riot, commotion, or disorder by persons other than the contractor's personnel and other employees of the contractor and subcontractors.
3- Ionizing radiation or contamination by radio-activity, except as may be attributable to the contractor's use of such radiation or radio-activity.
4- Use or occupation by the owner of any part of the permanent works, except as may be specified in the contract.
5- Design of any part of the works by the owner's personnel or by others for whom the owner is responsible.
6- Any operation of the forces of nature which is unforeseeable and against which an experienced contractor could not reasonably have been expected to take precautions.

The owner must protect himself from exposure to risks. One key in the protection of owner from risk is the type of contract. The owner must select the appropriate type of contract depending on the circumstances that prevail. For example, the "lump-sum" contract affords the owner some protection against cost overruns by placing responsibility for construction on the contractor. While, the "cost-plus" contract may expose the owner to the risk of increasing prices of materials and labors.

Rights and Responsibilities of Contractor

The contractor has few rights and many obligations under the contract. His major responsibility, of course, is to construct the project in conformance with the contract documents. Although some casualties and risks are considered as justification for allowing him more construction time, only severe contingencies such as impossibility of performance can serve to relieve him from his obligations under the contract.

The contractor is expected to give his personal attention to the conduct of the work, and either he or his representative must be on the job site at all times during working hours. The contractor is required to conform with laws and ordinances concerning job safety, licensing, sanitation, and other aspects of the work. The contractor is also responsible for and warrants all materials and workmanship whether put into place by his own forces or those of his subcontractors. Contracts typically provide that the contractor shall be responsible for the work until its final acceptance (Clough,1975).

The expertise of contractor may play an important role in protecting him from the risks that may occur during the execution of the project. The contractor must be able to predict the risk, assess it, and add the contingency amount for his bid to cover this risk. For risks that are within the contractor's control, contingency amount will be at a minimum. For risks that are beyond the contractor's control, contingency amount will be at a maximum. The owner pays for the risk whether it occurs or not. If the risks do not occur, the contractor realizes more profit. In the reality of the marketplace, however, a contractor who prices each and every risk into a bid will not win the job. Since, other contractors may be willing to accept some risks in order to secure the work.

The most important contractor rights concern progress payments, termination of the contract for cause, right to extra payment and extensions of time for reason, and appeals from decisions of the owner or the architect engineer.

Duties of Architect-Engineer (The Designer)

The architect-engineer provides preliminary engineering and detailed design, specifies and may procure engineering items, and may provide construction management services. The architect-engineer is not a party to the construction contract, and no contractual relationship exists between him and the contractor. He is a third party who derives his authority and responsibility under the contract from the owner. However, the jurisdiction of the architect-engineer to make determinations and render decisions is limited to and circumscribed by the terms of the construction contract. The architect-engineer represents the owner in the administration of the contract and acts for him during day-to-day construction operations. The architect-engineer advises and consults with the owner, and communications between owner and contractor are made through the architect-engineer.

The architect-engineer's risks are usually mistakes "errors and omissions". These can lead to costly change order, damage to equipment, or injury to persons. For example, the engineer's fees will usually not exceed (5 – 8)% of the total project cost, while the damages resulting from an engineering errors may exceed the total project cost. Mistakes can occur even though the engineer is not negligent. This has been the owner's risk because the engineer is obligated only to perform with ordinary engineering skill and diligence. Therefore, the owner should determine whether the engineer would be willing to guarantee the work. If so, the remedy to the owner is clear. In most cases, however, engineers will limit responsibility reperforming the defective engineering only. They will not assume liability for any resulting loss or damage (Bent & Thuman,1990).

CONTRACTUAL RISK

The construction industry is notoriously risky. Much of the preparatory paperwork that precedes construction projects can be viewed as the formulation of risk allocation between the owner, the contractor, and the designer.

The owner is taking the risk that his project will not get built on schedule, that it will not get built for what he has budgeted, and that it will not be of the quality he expected. The owner naturally seeks to insure that these three factors will be satisfied, and he often thinks he can accomplish this through the contract language. In the investment projects, the owner is also taking the risk that his project will not give the appropriate returns according the preliminary studies. In some cases, the owner has other risks beyond these, for example, building a nuclear power plant or some other project subject to public protest or environmental and regulatory delays. Typically, however, an

owner will seek to control whatever risks he can through his contract documents. On other hand, the contractor faces a multitude of risks. Among them are inflation, bad weather, strikes and other labor problems, shortage of materials, accidents, and unforeseen conditions at the construction site. Ultimately, the contractor faces the possibility of losing a great deal of money or of being forced out of the business. Naturally, he too would like the contract wording to be protective of his interests. Many owners still view the obligatory contract as consummate protection. In reality, such contracts often turn out to be bad business, for the following reasons (Rubin, Guy, Maevis, and Fairweather,1983):

1- Obligatory contracts discourage responsible bidders. The only way a responsible contractor can protect himself from a high risk situation is to include a high contingency in his bid. If the risk and the contingency are sufficiently high, his bid will not be competitive, and probably not within the owner's budget.
2- Ambiguous language or exculpatory clauses through which the owner hopes to escape responsibility almost result in conflict. When the conflict escalates to the courtroom, judges almost rule against the party who drew up the ambiguous contract (the owner).
3- Such contracts attract those bidders willing to take any kind of chance or those who expect from the outset to make up their money via claims.

CONTRACTUAL ALLOCATION OF RISK FOR PROJECT'S PARTIES

Owners use contract language to assign some or all of the risks to the contractor. But, fundamentally, regardless of the contract language, contractors can not and do not assume the risk for some conditions, and continue to expect owners to share the risk. Contractors do not accept the idea that the responsibility for some risks belongs to them or can be assigned to them (Halligan, Hester, and Thomas,1987).

There is no fixed rule to help answer the question that who should bear what risks, but the chart in **Table (3)** suggests a starting position for determining who should bear what risks. In this chart, the types of risks and allocation of those risks for each party are showed (Fisk,1988).

Risk allocation form, as shown in table 3, is not a standard state for all types of contracts, however, some risks can be transferred from one party to another according the type of contract. For example, the design-built contract may transfer the engineering risks (errors and omissions, conflicts in documents, defective design and drawings) from the owner to the contractor. While, cost plus contract may expose the owner to the risk of increasing prices of material and labor.

Table (3), Construction Risk Allocation to Participants

Type of risk	contractor	owner	engineer
Site access		*	
Subsurface conditions		*	
Quantity variations	*	*	
Weather	*		
Acts of God		*	
Financial failure	*	*	*
Subcontractor failure	*		
Accidents at site	*		
Defective work	*		
Management incompetence	*	*	*
Inflation	*	*	
Materials and equipment	*		
Labor problems	*		
Owner-furnished equipment		*	
Delays in the work	*	*	*
Environmental controls		*	
Regulations		*	
Safety at site	*		
Public disorder		*	
Errors and omissions			*
Conflicts in documents			*
Drawings			*

Site access is obviously an early risk and one that the owner should retain.
Subsurface conditions of soils, geology, or ground water can be transferred to the contractor, who is in a better position to assess the impact of these conditions on the project cost and time. However, as an essential party of the transfer process, the owner has the responsibility to undertake pre-contract exploration measures and the designer has the responsibility to design for the conditions expected. The extent that this is not feasible should determine the degree to which the owner retains a portion of the risk under an "unforeseen conditions" clause.
Weather, except for extremely abnormal conditions, is a risk for the contractor to assume, as its impact on construction methods can be better assessed by the contractor.
Acts of God, such as flood or earthquake are owner's risks.
Quantity variations are another form of risk frequently encountered. Within reasonable tolerances, quantities of work can be reasonably estimated and any variances assumed by the contractor for all quantities in excess of, for example, 15 to 25 percent. Where quantities are dependent upon subsurface or other less known conditions, significant variations should be shared only to the extent that exploratory information is available. Quantity changes triggered by late changes in the owner's requirements, should be at the owner's risk.
Defective design is a risk usually associated with the engineer. The tremendous expansion of construction has placed great burdens upon the design professions. Maintaining performance standards in the face of this is quite difficult, and occasionally, design and specification defects occur that create construction problems. Unfortunately, it is usually the owner and the contractor who suffer the consequences of such failures instead of the engineer who creates the problem in the first face. Design failures are becoming more and more apparent, and the engineer should bear the true cost of such failures.
Subcontractor failure is a risk that is properly assumed by the contractor except where it arises from one of the other listed risks attributable to the owner or the engineer. The general contractors are in the best position to assess the capacity of their subcontractors.
Defective work of construction, to the extent that the problem is not caused by a design defect, should be the contractor's risk.
Accident exposures are inherent to the nature of the work and are best assessed by the contractors. Furthermore, the contractors have the most control over site conditions that can increase or decrease accident exposure.
Management incompetence is a risk that must be shared by each party. It is an ongoing challenge for each organization to assign personnel according to their respective competence levels.
Financial failure is a risk not frequently mentioned, and can happen to any of the parties to a contract. Although infrequent, the order of magnitude of such failure should be considered. It is a shared risk, as the parties need to look at the financial resources of themselves.
Inflation is one of the world's realities. Every owner is conscious of its impact on the viability of the project. It is important that the owner retain the true cost. The government experts in finance have so far been unable to predict where the country will be a few years from now, so it is unfair to expect the contractor to do better than the so-called government experts.
Labor, materials, and equipment involve considerable risks. The availability and productivity of these resources necessary to construct the project are risks that it is proper for the contractor to assume. The expertise of the contractor should follow the assessment of cost and time required to obtain and apply these resources. This is the basic service that the owner is paying for.
Delays in the work are common risk in most of the construction projects, and can happen by any of the parties to a contract.
Environmental risks rightfully belong to the owner alone and should be retained by the owner except to the extent that they are influenced by construction methods determined by the contractor, or created by suppliers controlled by the contractor.

Regulations by government in the social area, such as safety and economic opportunity are the rules under which the contractor rightfully must operate.
Public disorder and war are political catastrophes of such impact that their risk is best retained by the owner, lest it becomes necessary to pay an unusually high price for transferring the risk to another party.

CONCLUSIONS

There are group of conclusions can be summarized by the following points:

1- The experience of project team may play an important role in reducing the risks. Since from their experience, they could anticipate the risks of a project and know the procedures required to reduce the negative impacts of these risks.
2- The accuracy of bid price depends on the acquaintance level of owner (or contractor) for anticipation, assessment, and management of risks that may lead to excess in the project cost; and then included the costs of these risks in the bid.
3- Some of owners attempt to transfer the risks to the contractor by adopting a specific contractual form. This manner sometimes decreases from the owner cost because of decreasing his risks. On other hand, it is impossible to entirely transfer the risks to the contractor. Even when the contractor takes all the risks, the owner still incur damages or hardship should the project exceed the target schedule or the contractor declare bankruptcy. Also, the contractor may put a high price for his bid to cover the risks.
4- The owner, who selects the appropriate type of contract according to the prevail conditions, may gain some of protection against the risks that may occur. For example, the “lump-sum” contract affords the owner some protection against cost overruns by placing the responsibility of construction on the contractor. While, the “cost-plus” contract may expose the owner to the risk of increasing prices of material and labor.
5- Some of owners attempt to use an ambiguous contract language to protect themselves from the risks. This manner is not correct and may cause problems and differences between the parties.
6- The contractor, who prices each risk in his bid, will not win in the bidding because of existence other contractors welling to bear some of risks in order to win in the bidding.
7- The risk and the responsibility on it can be identified in the contract clauses, and this manner can avoid the parties any disputes or differences between them as that risk occurs in the future.
8- The owner must bear any engineering risk resulted from errors, omissions, or changes in design, plans, or specification; especially when is responsible on furnishing these documents. On other hand, the contractor is responsible on the engineering risks resulted from his errors and omission during the execution.

APPENDIX.-REFERENCES

Bent, J. A., and Thuman, A., (1990), Project management for engineering and construction, Fairmont Press, Inc., Indian, 2nd Ed.

Clough, R. H., (1975), Construction contracting, John Wiley & Sons, New York, 3rd Ed.

Fisk, E. R., (1988), Construction project administration, John Wiley & Sons, New York, 3rd Ed.

Halligan, D. W., Hester, W. T., and Thomas, H. R., June (1987), Managing unforeseen site conditions) Journal of Construction Engineering and Management, ASCE, Vol.113, No.2.

Kales, P., Reliability for technology, engineering and management, Printice-Hall, Inc., U.S., 1St. Ed.

Latham, J., (1999), Risk management, Internet, www.blissuk.com/buildersbible/risk.

Ministry of Planning, (1988), Contract conditions for civil engineering works, Iraq, Baghdad.
Nicholas, J. M., (2001), Project management for business and technology: principles and practice, Printice-Hall, Inc., U.S.A, 2nd Ed.

Oberlender, G. D., (2000), Project management for engineering and construction, McGraw-Hill companies, Inc., Singapore, 2nd Ed.

Office of Financial Management, December (1998), A strategy for risk management in capital construction, Internet, www.ofm.wa.gov/risk/risktoc.

Pilcher, R., (1976), Principles of construction management, McGraw-Hill companies, Inc., New York, 2nd Ed.

Simmons, C., (1998), Risk management, Internet, www.airtime.co.uk./users/wysywig/risk.

Williams, C. A., and Heins, D. B., (1985), Risk management and insurance, McGraw-Hill, Inc., U.S.A, 5th Ed.

HARDNESS REMOVAL FROM DRINKING WATER

Nawar O. A. Nasser
Civil engineering
Department
College of engineering
University of baghdad

Prof. Dr. Ahmed A. M. Ali
Water resources engineering
Department
College of engineering
University of baghdad

ABSTRACT

This study included three trials that were made during December 2003 by using lime, of 98% w/w calcium hydroxide to find the relation between lime doses to be added and the hardness removed .The trials were performed by adding various doses of lime and measuring the hardness, electrical conductivity and pH in water produce by three plants, Nissan in the north of Baghdad, Al-Karama and Al-Wathba water treatment plant in Baghdad center. The objective of this study is to find the optimum lime dose that gives the minimum hardness content.

The results indicate a non linear relation between lime dose added and the hardness removed .

The results represented a 36% removal in hardness when using an optimum dose of lime 200 ppm in Nissan water treatment plant, while a percentage removal of 34% was obtained in both Al-Karama and Wathba water treatment plants with 300 ppm dose of lime.

The low percentage removal indicates the presence of non-carbonate hardness which could not be removed by lime alone.

الخلاصه

تضمنت هذه الدر اسه ثلاث محاولات أجريت خلال كانون الأول 2003باستخدام هيدروكسيد الكالسيوم 98% نسبه وزنيه لإيجاد العلاقة بين جرعة هيدروكسيد الكالسيوم وإزالة العسرة ,المحاولات تمت بإضافة جرع مختلفة من هيدروكسيد الكالسيوم وقياس العسرة والتوصيل الكهربائي وقوة أيون الهيدروجين للماء المسحوب من ثلاث محطات لتصفية ماء الشرب وهي مشروع نيسان شمال مدينة بغداد ,مشروع الكرامة ومشروع الوثبة مركز مدينة بغداد ,الهدف من هذه الدر اسه هو إيجاد الجرعة القصوى من هيدروكسيد الكالسيوم التي تعطي اقل تركيز للعسره .

النتائج أظهرت أن هناك علاقة لا خطيه بين جرع هيدروكسيد الكالسيوم المضافة والعسره المزالة ,النتائج تمثلت بإزالة 36% من العسره عند إضافة أقصى جرعه من هيدروكسيد الكالسيوم 200 ملغم\التر في مشروع نيسان بينما نسبة أزاله 34% تم الحصول عليها في مشروعي الكرامة والوثبة لجرع 300 ملغم\التر النسبة القليلة للازاله أشارت إلى وجود عسره لا كاربونيه والتي لا يمكن أزالتها باستخدام هيدروكسيد الكالسيوم لوحده

KEY WARDS
Lime ,hardness, water treatment plant

INTRODUCTION

The publics now demand that the water works operator does more than furnish water which is clear and free of disease-causing organisms. They desire water that is soft, free of taste and odor, and doesn't discolor plumbing fixtures or corrodes metals. Industry also require water that will not interfere with its processes (Steel, 1984). Most natural waters have dissolved matters in them. that may cause such properties

With today's awareness of the many unwanted substances in various water supplies, specialized devices are being marketed to treat small quantities of water just before drinking or for cooking purposes. This awareness has been heightened by the wide media coverage given to chemical spills, toxic waste dumps, and the under-treatment of community waters and improper sewage disposal. All of which seem to cause short or long term effects on potable water sources. Together, these factors tend to create doubts to the quality of water we consume. Bottled water, sold in supermarket as well as home delivery, has met a good deal of need for safer drinking water when doubts persist in mind of the homemaker as to the local water quality. This product is also used for aesthetic quality reasons or to satisfy dietetic needs. (Water facts, 2000)

WATER HARDNESS

Hardness of water is the measure of water capacity to precipitate soaps. Hardness minerals are calcium and magnesium in parts per million. Water hardness may be either carbonate or non carbonate .The carbonate hardness caused by the bicarbonate of calcium and magnesium while non carbonate hardness caused by the sulfate and chlorides of calcium and magnesium. W.H.O, 1984 classified drinking water according to its hardness as in **Table(1)**

Table (1)
Classification of drinking water according to its hardness

Hardness in ppm	***Description of water***
0-60	Soft water
60-120	Medium hard water
120-160	Hard water
>160	Very hard water

SOFTENING METHODS:

One of the main problems in water is the increase in amount of hardness that should be decreased to the desirable concentration There are many methods used in softening of drinking water such as Reveres Osmoses, Ion Exchange, Chemical Precipitation and others.

The Chemical Precipitation which is most suitable in Iraq because of the availability of lime locally produced and its low cost.

That precipitate most commonly used in water treatment are those calcium carbonate and metallic hydroxides. Such as lime.

Chemical precipitation-lime softening

The aim of this process is to remove the carbonate hardness (temporary hardness) attributed to calcium and magnesium. The non-carbonate hardness (permanent hardness) is not affected.

The assessment of lime softening equipment should be primarily based on its ability to produce a homogenous mixture of raw water reagent and $CaCO_3$ nuclei, in a reaction zone of a suitable size. In order to increase the settling velocity, an organic flocculants may be injected following the

growing phase of the crystals. When the aim is to obtain particularly clear carbonate-free water, lime softening should always be followed by filtration. (Degremont, 1991).

Basic Reactions

The chemical reactions for lime softening are as follows: -

$$Ca(OH)_2+Ca(HCO_3)_2 \longrightarrow 2CaCO_3\downarrow +2H_2O \quad (1)$$

$$Ca(OH)_2+Mg(HCO_3)_2 \longrightarrow CaCO_3\downarrow +MgCO_3+2H_2O \quad (2)$$

As magnesium carbonate is relatively soluble (solubility about 70mg/l), an excess of lime will bring about the following reaction: -

$$Ca(OH)_2+MgCO_3 \longrightarrow CaCO_3\downarrow +Mg(OH)_2 \quad (3)$$

PROPERTIES OF LIME

A very fine powder, which is usually white. The form used is hydrated lime, which varies from source to source. For example (limbux) lime from UK has 98%w/w calcium hydroxide, and Iraqi lime from Kerbala has been analyzed as having about 95%w/w

Initially the lime will be delivered in bags stacked on pallets, provision has been made for possible future bulk delivery by special rod vehicles which can be pneumatically discharged direct into lime silos also in (big bags) of one ton capacity.

Being a caustic alkali, lime requires careful handling but is not corrosive to iron, steel, most metals or general construction materials. The dust will however roughen glass over a period of time.

Storage areas must be kept dry and free from draught and if the lime is not contaminated or caked, any recently damaged or split bags must be used immediately.

Long exposure to the atmosphere may cause carbonated lime that should be rejected

Stocks should be used in rotation and care must be taken to keep them separated from other chemicals.

Careful handling is required to minimize dust formation at all dry lime handling stages and the dust extractors provided at key points must be used and be properly maintained.

Hydrated lime doesn't produce heat on mixing with water or when subsequently diluted. However, as its solubility is very low, the slurry, must be continually agitated otherwise it will settle. The mixing tanks must have stirrers, which run continuously while containing lime slurry.

When lime is first mixed with hard water, local softening occurs with a precipitation of calcium carbonate and magnesium hydroxide. This reaction initially takes place in the slurry mixing tanks and later in mixers where further water is added.

Beyond the need to clean out the mixing tanks and mixers, from time to time, no operational problems are expected from such reactions. (Operation Instruction, 1986)

EXPERIMENTAL WORK AND DISCUSSION

Three trials were made during Dec. 2003 by using lime, of 98%w/w calcium hydroxide to find the relation between the doses added and hardness removal in three plants, Nissan WTP, Al-Karama WTP and Wathba WTP as discussed below: -

Calculation of Lime Required for Optimum Precipitation

Notation:-

CaH:- Calcium hardness in French degrees representing the total calcium salts content.

MgH:- Magnesium hardness in French degrees representing the total magnesium salts content.

Malk:- Alkalinity Measurement due to adding Methyl Orange

C:- Free CO_2 content in French degrees is calculated as: -

$$C = \frac{\text{Free } CO_2 \text{ (mg/l)}}{4.4} \quad (4)$$

Amount of lime: -
The theoretical amount of lime required for optimum precipitation of calcium carbonate alone is: -

$$Ca(OH)_2 = 7.4(Malk + C)\ g/m^3 \quad (5)$$

To precipitate calcium carbonate and magnesium oxide simultaneously: -

$$Ca(OH)_2 = 7.4(2Malk - CaH + C)\ g/m^3 \quad (6)$$

$$CO_2 \text{ (mg/l)} = \frac{\text{ml of titration} * N * 44000}{\text{ml of sample}} \quad (7)$$

First Trial

In Nissan WTP which is in the north of Baghdad its intake is an upstream disposal area of many industries on the Tigris River, this region is considered a good quality source.
CO_2 =34.32 mg/l from the experimental work.
C= 7.8 mg/l from equation 4.
Malk = 13.6 F.D. from the experimental work.
CaH =8.3 F.D from the experimental work.
The amount of lime required to precipitate calcium carbonate and magnesium oxide simultaneously is 197.58mg/l ≅ 200 mg/l from equation 6.
The results of this trial was as follows:-

Table (2)
The Result of the First Trial of Lime Softening.

Lime dose(ppm)	*Ha(ppm)*	*Ha removal(ppm)*	*% removal*	*PH*	*Ec*
0	352	0	0	7.75	960
50	341	11	3	8.5	920
100	328	24	7	9	800
150	270	82	23	9.1	756
200	226	126	36	10.25	659
250	245	107	30	10.5	700
300	276	76	22	10.6	727
350	279	73	21	10.7	776
400	280	72	20	10.75	796
450	285	67	19	11	799
500	296	56	16	11.2	801

Second Trial

In Al-Karama WTP at Baghdad center on Al-Karkh side which is the region of poor water quality because of the disposal of industrial effluents.
CO_2 =98 mg/l from the experimental work.
C= 22.27 mg/l from equation 4.
Malk=15.7 F.D. from the experimental work.
CaH =13.3 F.D. from the experimental work.
The lime dose =298.7mg/l ≅ 300 mg/l for optimum precipitation from equation 6.
The results of the second trial were as follows:-

Table (3)
The Result of the Second Trial of Lime Softening

Lime(ppm)	*Ha(ppm)*	*Ha removal (ppm)*	*% removal*	*PH*	*Ec*
0	**507**	**0**	**0**	**7.8**	**1089**
50	**497**	**10**	**2**	**7.83**	**1084**
100	**453**	**54**	**11**	**7.85**	**1080**
150	**437**	**70**	**14**	**7.88**	**1077**
200	**404**	**103**	**20**	**7.9**	**1036**
250	**365**	**142**	**28**	**8.2**	**1010**
300	**334**	**173**	**34**	**9.3**	**1022**
350	**357**	**150**	**30**	**9.5**	**1050**
400	**384**	**123**	**24**	**9.8**	**1075**
450	**390**	**117**	**23**	**9.85**	**1090**
500	**396**	**111**	**22**	**9.9**	**1122**

Third Trial

In Al-Wathba WTP at Baghdad center on Al-Rasafa side about 3.0 km south Al-Karama WTP with water of poor quality also.
CO_2 =64 mg/l
C= 14.5 mg/l
Malk=16.1 F.D.
CaH=12.4 F.D.
The lime dose=254.1mg/l $\cong$ 300 mg/l for optimum precipitation.
The results of the third trial was as follows:-

Table (4)
The Result of the Third Trial of Lime Softening

Lime(ppm)	*Ha(ppm)*	*Ha removal (ppm)*	*% removal*	*PH*	*Ec*
0	**488**	**0**	**0**	**7.2**	**1250**
50	**465**	**23**	**5**	**7.5**	**1240**
100	**440**	**48**	**10**	**7.8**	**1200**
150	**425**	**63**	**13**	**8**	**1170**
200	**400**	**88**	**18**	**8.58**	**1100**
250	**350**	**138**	**28**	**9.7**	**1095**
300	**322**	**166**	**34**	**9.8**	**1190**
350	**358**	**130**	**27**	**10**	**1160**
400	400	88	18	10.35	1200
450	407	81	17	10.5	1280
500	412	76	16	10.65	1310

From **Tables (2),(3) and (4)** the hardness values began with high value and decreased on adding lime ,reaching the minimum value at the optimum dose, the pH value increased as the lime dose increased.
The removal of hardness began with low values then increased to a maximum value at the optimum dose of lime then decreased when lime dose increased as shown in Fig. **(1-a), (1-b) and (1-c).**
The regression equations of the relation between lime dose and hardness removal was to be of a non-linear form as follows:-
The best regression was:

$Y=ax^b \exp(cx)$ (8)

1- In Nissan WTP:-

$Y=2.31 * 10^{-4} x^{2.892} e^{-0.0117x}$ (9)
R=0.888

2- In Al-Karama WTP:-

$Y=1.61 * 10^{-4} x^{2.897} e^{-0.00922x}$ (10)
R=0.961

3- In Al-Wathba WTP:-

$Y=2.19 * 10^{-4} x^{2.862} e^{-0.010x}$ (11)
R=0.905

Fig.(2) shows the best fit curve for the mean data of the three plants with regression equation as follow:-

$Y=1.81 * 10^{-4} x^{2.896} e^{-0.0102x}$ (12)
R=0.988

The best regression equation in Al-Karama WTP with a correlation coefficient of 0.961.**Fig. (3)** shows the percentage removal of hardness versus lime dose in the three plants Nissan WTP north of Baghdad and Al-Karama WTP, Al-Wathba WTP in Baghdad center. The figure represent high percentage removal in Nissan WTP for low doses but high percentage removal in Al-Karama then Al-Wathba for high lime doses, also the percentage removal 36% when optimum dose of lime in Nissan WTP, while the percentage removal of 34% when optimum lime dose in both Al-Karama and Al-Wathba WTP

The low percentage removal indicates the presence of non - carbonate hardness which can not be removed by lime only.

CONCLUSION

1- The relation between lime dose and % removal of hardness is of a non-linear form with the best regression equation in Al-Karama WTP with a correlation coefficient of 0.961 . this correlation is of 0.988 for the mean data for the three plants.
2- The maximum decrease of carbonate hardness was at the optimal lime dose with percentage removal of 36% in Nissan WTP and 34% in both Al-Karama and Al-Wathba WTP.
3- Softening with Lime need to adjust the pH of the treated water, also ferric chloride is the clarifying reagent to be used because Aluminum Sulfate would solubilize the Alumina, which might subsequently reflocculate.
4- The principle difficulty with using lime for carbonate hardness removal is the large amounts of sludge generated which has to be disposed, although this sludge is easily dried.

RECOMMENDATION AND SUGGESTION

1- To make use of lime plant which is present at Al-Karkh project, which is out of work for the time being, to use it in another project when needed.
2- Studies should be conducted to improve hardness removal by using the combination of Lime and Sodium Carbonate for removing carbonate and non-carbonate hardness.

REFERENCES

Degremont,G., (1991), Water treatment handbook,vol.1,English Edition,.

Operation Instruction of Al-Karkh project, (1986), ime plant,vol.4, ,Baghdad water administration.

Steel,E.W,and McGhee,T.J, (1984), Water supply and sewarge,5th Edition,McGraw-Hill Book comp..

Water facs,General information on drinking water, (2000), water information, free water information.http://www.pangea.org/orgs/UNSCO.

WHO, (1984), Guidelinesfor drinkin water quality,2nd Edition,vol.1and2,Geneva,.

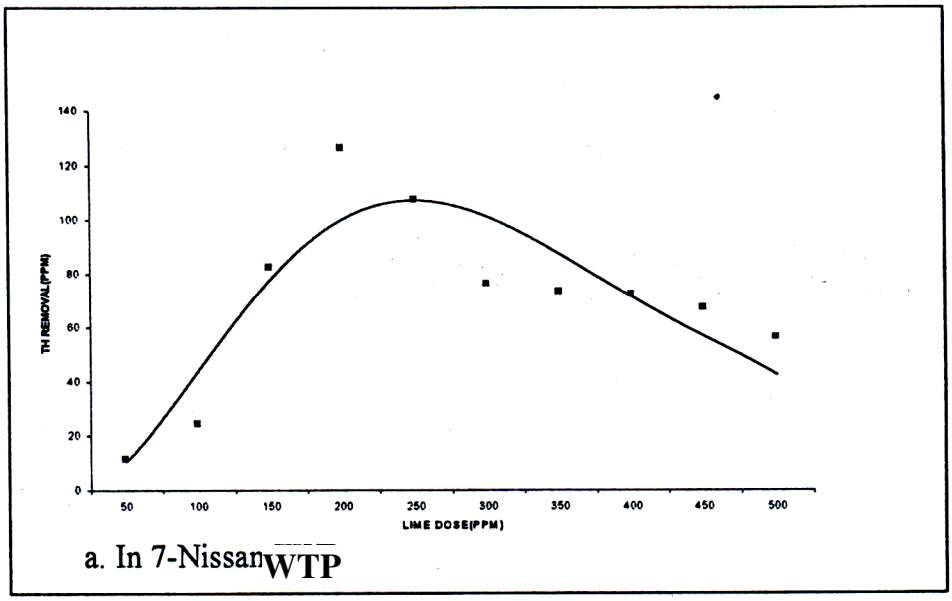

a. In 7-Nissan WTP

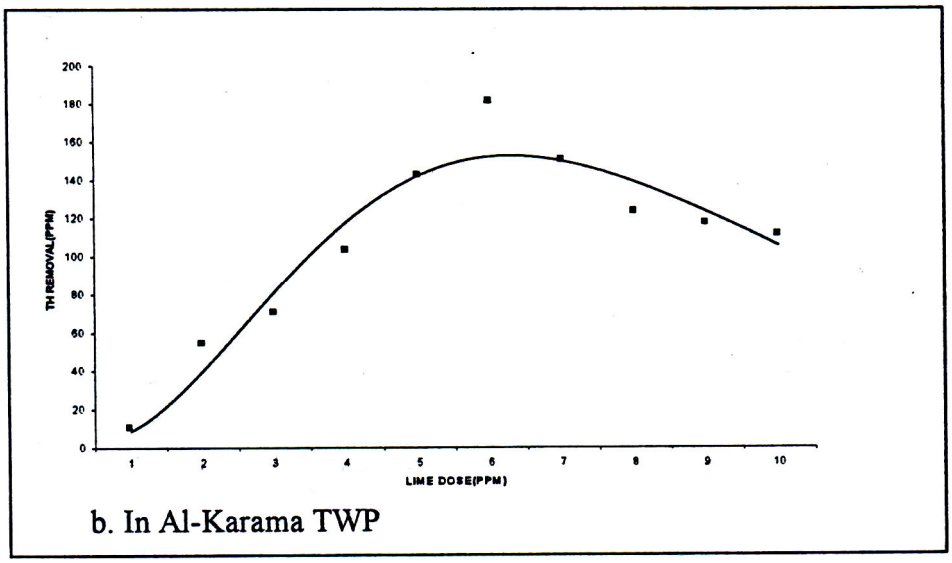

b. In Al-Karama TWP

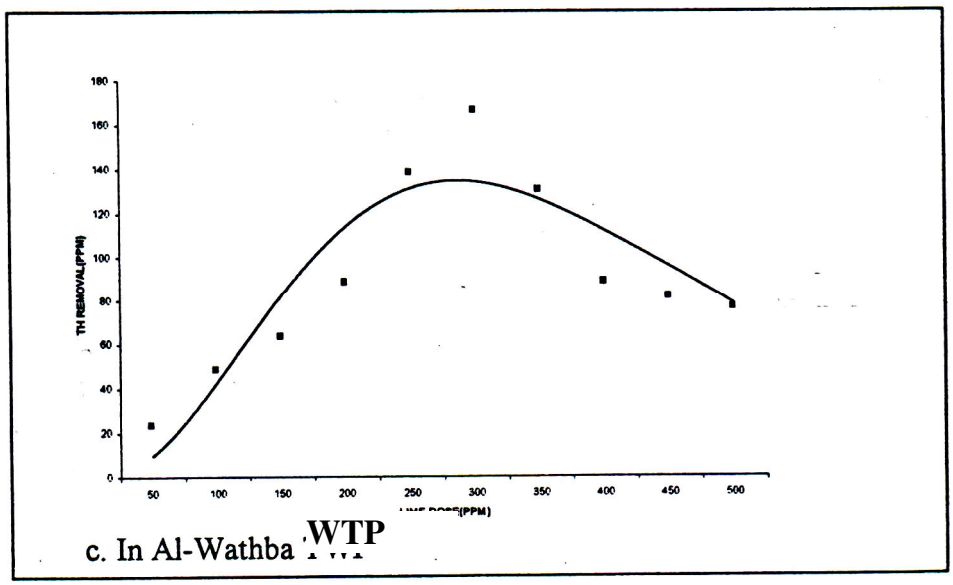

Fig. (1)
The Relationship Between the Hardness Removal and Lime Doses

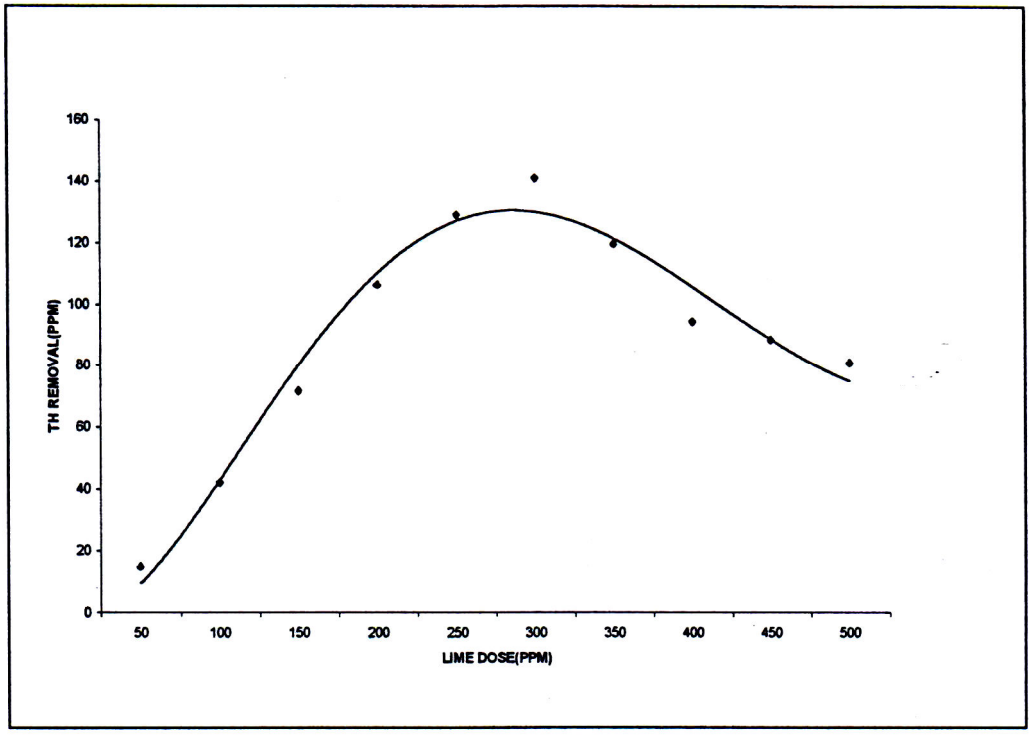

Fig. (2)
The Relationship Between the Hardness Removal and Lime Doses for the Mean Data of the Three Plants

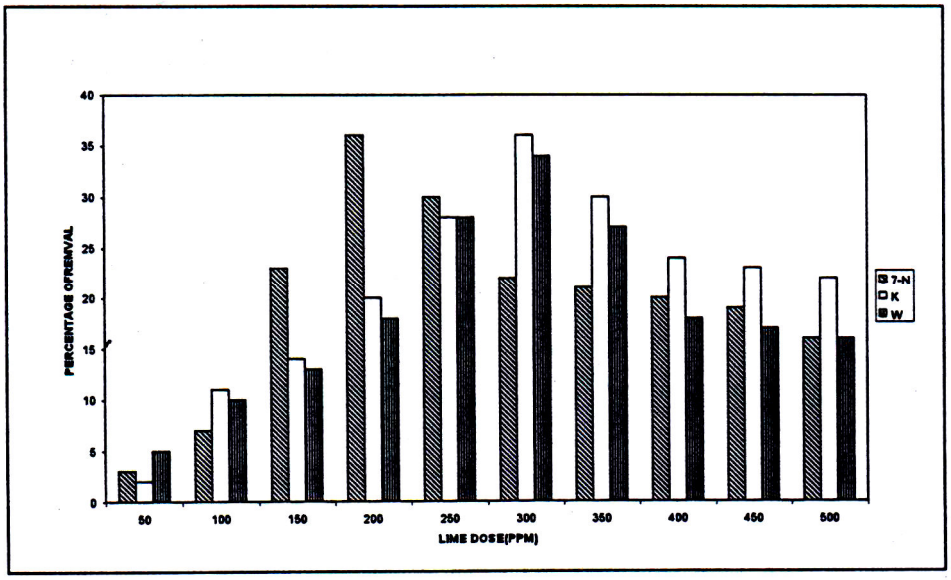

Fig. (3)
The Percentage Removal of Hardness Versus Lime Doses in the Three Plants

DESIGN & IMPLEMENTATION OF FRACTIONAL – N FREQUENCY SYNTHESIZER

Ali M. N. Hassan
Assistant Lecturer
University of Baghdad – Al khawarizmi Engineering College

ABSTRACT

This research involves design & implementation of fractional – N frequency synthesizer with the following specifications: Frequency range (2350– 2750) MHz,Step size (1 kHz), Switching time 8.9 µs, & phase noise @10 kHz = -115dBc & spurious -69 dBc

The third order Fractional –N technique was chosen to satisfy the design requirements. In this system the ΣΔmodulator placed on digital phase-locked loop to control the fractional value of the frequency division ratio thereby eliminating spurious and allowing good phase noise performance. The development in I.C. technology provides the simplicity in the design of fractional –N frequency synthesizer because it implements the phase frequency detector(PFD) , prescalar, ΣΔmodulator & reference divider in single chip. Therefore our system consists of a single chip contains (low phase noise PFD, charge pump, prescalar, ΣΔmodulator & reference divider), voltage controlled oscillator , loop filter & reference oscillator.

The application of this synthesizer in frequency hopping systems, wireless transceivers ,GSM & radar because it has high switching speed ,low phase noise & low spurious level.

يصف هذا البحث تصميم وبناء مركب ترددات من نوع (Fractional - N) وبالمواصفات التالية : مدى الترددات الخارجة (2350–2750) ميكا هرتز، واقل سعة قفزة 1كيلو هرتز ،زمن تحويل 8.9مايكرو ثانية ومستوى ضوضاء طوري – 115. ديسبيل عند 10000 هرتز من التردد الخارج.ومستوى الطفيليات – 69 ديسبيل.ان تقنية الجيل الثالث (Fractional - N) تم اختيارها لتحقيق متطلبات التصميم. في هذه المنظومة , مرحلة تضمين من نوع (ΣΔ) تم وضعها في دائرة إقفال الطور الرقمية للسيطرة على على القيم الكسرية لمقسم التردد.وبهذا تم ابعاد الترددات الطفيلية وتحسين ضوضاء الطور.

التطور الحاصل في الدوائر المتكاملة جهز البساطة في تصميم مركب الترددات من نوع (Fractional - N) وذلك لأنه دمج كاشف التردد والطور ,ومقسم التردد الثنائي , ومقسم التردد ومرحلة تضمين من نوع (ΣΔ) في شريحة رقيقة واحدة. لذلك منظومتنا تتكون من شريحة تحتوي على كل من (كاشف ترددات وطور ذو ضوضاء طوري قليل،مضخة شحنة دقيقة،مقسم ترددات مبرمج ، ومقسم تردد ثنائي(p/(p+1)) مبرمج ومرحلة تضمين من نوع (ΣΔ)) مرشح ترددات واطئة ،مذبذب ترددات ذو سيطرة جهدية، ومذبذب مرجعي. هذه الشرحة الرقيقة التي تحتوي كل من كاشف ترددات وطور مقسم ترددات مبرمج ومقسم تردد ثنائي .

التطبيقات لهذا المركب في منظومات القفز بالتردد , و الرادار, و المرسلات والمستلمات اللاسلكية،GSM وذلك لأنها تمتلك خاصية ضوضاء طوري قليل وسرعة تحويل عالية ومستوى طفيليات اقل.

KEY WORDS
Fractional- N, ΣΔ modulator, PLL(phase lock loop)

INTRODUCTION

Fractional –N was originally developed 31 to 36 years ago then called Digi-phase and later Fractional –N by Racal and H.P.[Li, Lin, 2000].there are three types of fractional-N technique. In the first order technique , the fractional division can be used to increase the reference by an order of magnitude or to reduce the division ratio. The first order appears to be solution to the drawbacks of PLL ,but this type has not been the case. Naturally , fractional division generates a new periodicity within the Division by N and therefore, introduces spurious signals. An improvement can be achieved by analogue compensation of the phase error. The phase error exactly represents by the content of the accumulator. This allows to cancel the spurious. The analogue compensation represents the second order. But it has disadvantage in accuracy. An alternative to the second order is the third order fractional-N, it uses all digital spurious cancellation by implementing sigma-delta modulation.

A general rule and requirement in PLL designs to try to use the highest-frequency reference and the lowest division ratios. Also, the higher-frequency reference is easier to
filter out and yields a lower division ratio, which produces better phase noise, lower spurious signal response, and better switching time. However, in many cases these requirements conflict with the rest of the design parameters, since high resolution (fine step size) requires low reference frequency and therefore high division ratios. If the reference frequency is high, then the frequency resolution or the step size is high. To achieve small step size, it is necessary to either use low reference frequencies or resort to multiloop designs. This increases the complexity, size, and cost. All the designs that we demonstrated assumed the divider ratio *N* to be a whole number. But if *N* could include a
whole number plus a fraction, it would be possible to generate step sizes that are smaller than the reference frequency. The fractional N frequency synthesizer is a modified version of the PLL based synthesizer where the integer frequency divider is replaced by a fractional frequency divider. **Fig. (1)** shows the simplified block diagram of a fractional N synthesizer. The only difference from the PLL based synthesizer is that the frequency divider has a choice between two integers, *N* and *N+1*.

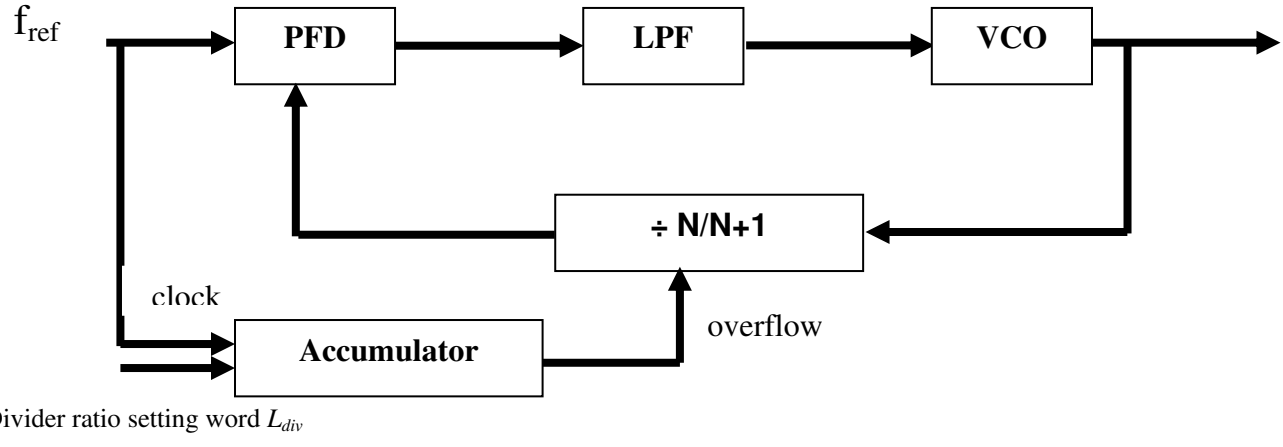

Fig. (1): Fractional N frequency synthesizer block diagram

The reference clock also provides the clock signal for the phase accumulator. The phase accumulator accumulates its output with a divider ratio setting the word of length L_{div} at each clock cycle. The dual-mode divider divides its input by N when the phase accumulator is not overflowed. When an overflow signal from the phase accumulator appears, the dual-mode divider divides its input by $N+1$. On average, the divider divides its input by a fractional value between N and $N+1$. To calculate the exact divider ratio, we assume the accumulator length to be L_{acc}. For every L_{acc} clock cycles, the accumulator overflows L_{div} times. That means for every L_{acc} clock cycles, the divider divides its input by $N+1$ L_{div} times, and divides by N for the rest of the times. If N_{avg} is the average dividing ratio, then

$$N_{avg} L_{acc} = N (L_{acc} - L_{div}) + (N + 1) L_{div} \quad eq(1.1)$$

And

$$N_{avg} = N + L_{div}/L_{acc} \quad eq(1.2)$$

The fractional divider ratio makes it possible to have a much smaller frequency step with the same reference frequency comparing to the PLL based synthesizer. In other words, the fractional N synthesizer can have a higher reference frequency and hence higher loop bandwidth without compromising the stability of the loop. But the fractional divider ratio is achieved through an averaging process. The alternating N, $N+1$ divide numbers cause the output frequency to vary between $N*f_{ref}$ and $(N+1)*f_{ref}$.

ADVANTAGES & DISADVANTAGES OF FRACTIONAL N SYNTHESIZER

In a fractional-N phase-locked loop, the division ratio N is switched between two or more integer values in such a way that the *average* value of N can be a fractional number. Consequently, the phase comparison frequency can be much higher than in integer-N synthesizers, and thus the division ratio can be much lower. For example in the DCS-1800 system, a phase comparison frequency of 13 MHz would result in N ranging from 131 to 145. A channel spacing of 200 kHz then requires the ability to change the division ratio in steps of $200/13000 \approx 0.0154$[Conkling, Craig , Feb,1998].

A reference frequency of 13 MHz, or 65 times higher than in the integer-N synthesizer, also (theoretically) enables up to 65 times higher loop bandwidth. This in turn results in up to 65 times faster switching. In practice, however, the maximum loop bandwidth is limited by factors other than the reference feedthrough, and cannot be increased as much. Still, the designer now has more freedom in choosing the loop bandwidth. If, for example, a very good reference suppression is required, the loop bandwidth can be made significantly smaller while still meeting the switching time requirements. In short, using a fractional-N PLL instead of an integer-N one loosens the coupling between the choice of loop bandwidth and the choice of the reference frequency.

Also, since the division ratio is smaller than in integer-N synthesizers, the phase noise of the reference oscillator is not amplified as much. In the above example, the reference frequency was increased from 200 kHz to 13 MHz. This reduces the amplification of the crystal oscillator phase noise in the DCS-1800 system from 40dB to 22dB.

The main source of problems in fractional-N synthesizers is the fact that although the *average* division ratio is a fractional number, the *instantaneous* division ratio must still always be an integer. In practice, the fractional division is typically performed by using an accumulator, i.e. a digital adder that adds a fraction F of its full scale value to its contents once every reference clock cycle. During the accumulation, the prescaler divides its input frequency by N. Every time the accumulator overflows, the prescaler divides by $N+1$ for one cycle. The average output frequency will now be

$$f_{out} = (N + F) f_{ref} \quad eq(2.1)$$

During the accumulation, the divided VCO frequency seen at the phase detector input is

$$f_{vco} = f_{ref} + (F/N) f_{ref} \quad eq(2.2)$$

On the other hand, the reference frequency seen at the other phase detector input is always *fref* . Thus, the phase error at the input of the phase detector increases at a rate of

$$\Delta\theta_e(t) = 2\pi\ (F/N)\ (t/T_{ref}) \qquad \text{eq(2.3)}$$

When an overflow occurs in the accumulator, the prescaler divides by N+1 for one period, corresponding to a 2π decrease in the phase error at the phase detector input. The resulting phase error has a sawtooth shape. The sawtooth shaped phase error, also known as a "beat note", causes spurious tones in the output spectrum at offsets of $\pm K \cdot F \cdot fref$, where $K = \{0, 1, 2\ldots\}$, i.e. at integer multiples of $F \cdot fref$. These spurious tones, having a large energy in a very small bandwidth, are well as the phase noise of the PLL, causing significant problems in almost all applications. What magnifies the problem is the fact that spurs occur at fractional multiples of *fref*, i.e. they can occur well within the channel bandwidth, and inside the PLL bandwidth as well.

SPUR CANCELLATION TECHNIQUES

Only the very first implementations of the fractional-N divider operated as above. The spurious tones limit the performance of the synthesizer so much that it is practically unusable in most applications. Different methods to eliminate the sawtooth phase error, and thus the spurs. These methods will be discussed in the following subsections.

Analog compensation

The first proposed means of correcting the sawtooth phase error was injecting an opposite ramp signal somewhere in the loop so that the sawteeth cancel each other. In the first order fractional-N synthesizer, the synthesizer has two identical digital accumulators, one controlling the prescaler modulus, and the other one controlling a "sideband reduction circuit". The sideband reduction circuit generates a sawtooth signal with an opposite polarity than the sawtooth at the input of the phase detector. This correction signal is then added to the VCO control voltage node. Ideally, the VCO control voltage is now constant when the loop is in lock. In this method , precision analog components are needed[j. Craeninkx & M. Steyaert, 1998].

Sigma delta modulation

This method will be used to implement fractional N synthesizer in my system to eliminate the fractional spurs. The basic principles of the digital ΣΔ modulation will be presented in the following.

Fundamentals

The accumulator used to control the modulus of the prescaler can be viewed as the digital counter part of a first-order analog ΣΔ-modulator. The carry of Accumulator changes the prescalar from N to N+1 for one cycle **Fig. (3.1)** shows the accumulator, i.e. an adder with a one clock cycle delay in the feedback path, with the corresponding signals. The frequency control word is fed into the *A* input, and added to the *B* input to produce a sum output Σ. When the adder overflows, the carry out bit *c* is set[Goldberg, Bar-Giora , 1999].

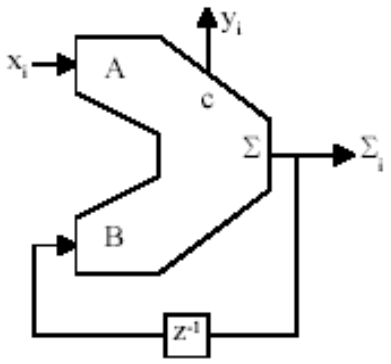

Fig. (3.1) The digital accumulator with the corresponding input and output signals.

Let us denote the frequency control signal fed to input *A* by *xi*, and carry output *c* of the accumulator by *yi*. When an overflow occurs, the contents of the accumulator are "flipped over", which can be viewed as subtracting the full scale of the accumulator from its contents.
The output of the accumulator at an arbitrary time is the sum of its input at that time and its contents one clock period earlier. If an overflow occurs, the full scale of the accumulator is subtracted. The output can thus be expressed as

$\Sigma_i = x_i + \Sigma_{i-1} - y_i$ eq(3.1)

$y_i = x_i + \Sigma_{i-1} - \Sigma_i$ eq(3.2)

$y_i = x_i - (\Sigma_i - \Sigma_{i-1})$ eq(3.3)

The z-transform of equation (3.3) is

$Y(z) = X(z) - \Sigma(z)(1 - z^{-1})$ eq(3.4)

Let us now look at the signal flow diagram of a first-order analog ΣΔ-modulator shown in **Fig. (3.2)**. The input is again denoted by *x*, and the output by *y*. The operation performed in the dashed box is the quantization, and *e* denotes the quantization error.

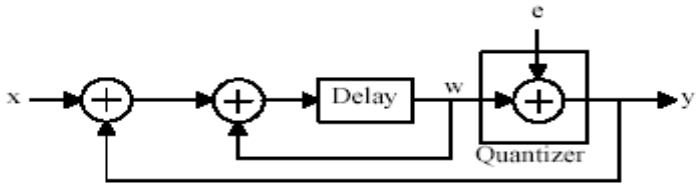

Fig. (3.2) The signal flow diagram of a first-order analog ΣΔ-modulator.

The above modulator is described by the following equations:

$w_i = w_{i-1} + x_{i-1} - y_{i-1}$ eq(3.5)

$y_i = w_i + e_i$ eq(3.6)

Combining these two, we get

$y_i - e_i = y_{i-1} - e_{i-1} + x_{i-1} - y_{i-1}$ eq(3.7)

$y_i = x_{i-1} + e_i - e_{i-1}$ eq(3.8)

The z-transformation of Equation (3.8) is

$Y(z) = z^{-1} X(z) + E(z)(1 - z^{-1})$ eq(3.9)

Comparing Equation (3.9) with Equation (3.4) shows great similarity. Ignoring the latency of one clock period in the signal path of the analog ΣΔ-modulator, and treating the contents of the digital accumulator as the negative of the quantization error, the equations are identical.
A ΣΔ-modulator shapes the quantization noise in a high pass fashion. In other words, the quantization noise is pushed to higher frequencies, and the signal-to-noise ratio at low frequencies can be very high. **Fig. (3.3)** shows the output spectrum of an analog first order ΣΔ-modulator with a low frequency input[Dean banerjee , 2005].

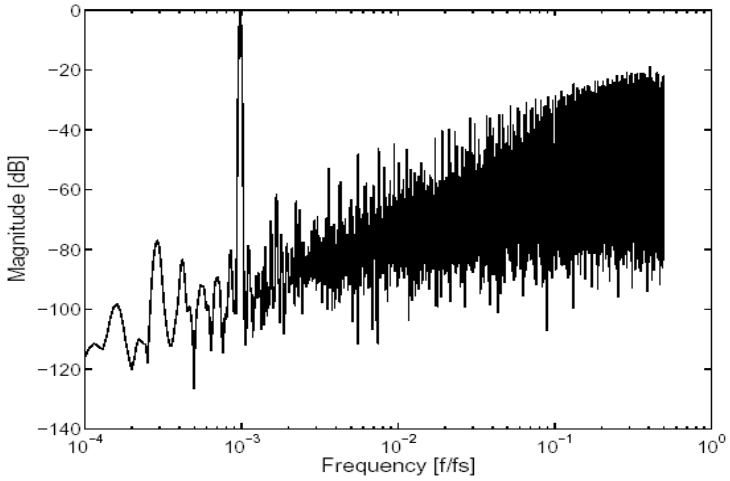

Fig. (3.3): The output spectrum of an analog ΣΔ-modulator with a low-frequency input signal.

Looking at **Fig. (3.3),** it would seem that the quantization noise is originally white, and then shaped into higher frequencies. The white noise assumption, however, holds only for "sufficiently busy" input signals. In fractional-N synthesizers, the input signal is normally constant, and the quantization noise is no longer white. The quantization noise power is concentrated into a finite number of spurious tones. The spurious performance combined with the relatively poor noise shaping (20dB/decade) make the first order ΣΔ-modulator quite useless in practical applications.

Cascaded (MASH) modulators

As explained above, the spurious tones at the output of the modulator result from the input being DC. The signal in the ΣΔ-output of the accumulator, however, is no longer at DC, although it is periodical. Now, this signal can be fed into the input of another accumulator, whose output will be much less periodic than the output of the first accumulator. The first accumulator carry changes the division ratio of the Divider from N to N+1 for one cycle. The output is digitally integrated by the second accumulator and its carry output changes the division ratio to N+1 and then N-1 on the next clock cycle. Combining the *c* outputs of the two accumulators in a suitable way(see **Fig (3.4),** the quantization noise of the first accumulator can be canceled[J.A Crawford , 1994].

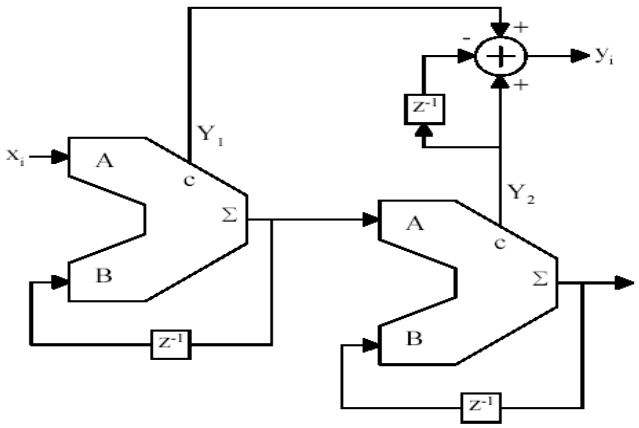

Fig. (3.4): The block diagram of a second-order MASH modulator.

As shown in Equations (3.1) to (3.4), the output of the first accumulator is

$Y(z) = X(z) - \Sigma_1(z)\,(1 - z^{-1})$ eq(3.10)

Feeding the Σ -output of the first accumulator into the input of the second one, the output of the second accumulator is

$Y_2(z) = \Sigma_1(z) - \Sigma_2(z)\,(1 - z^{-1})$ eq(3.11)

Combining the outputs of the accumulators as shown in Figure 3.4, we get the following as the output of the entire modulator:

$Y(z) = Y_1(z) + Y_2(z) - Y_2(z)\,z^{-1}$ eq(3.12)

$Y(z) = Y_1(z) + Y_2(z)\,(1 - z^{-1})$ eq(3.13)

$Y(z) = X(z) - \Sigma_1(z)\,(1 - z^{-1}) + \Sigma_1(z)\,(1 - z^{-1}) - \Sigma_2(z)\,(1 - z^{-1})^2$ eq(3.14)

$Y(z) = X(z) - \Sigma_2(z)\,(1 - z^{-1})^2$ eq(3.15)

As Equation (3.15) shows, the quantization noise of the first accumulator cancels out. This greatly improves the spurious performance of the modulator, since the first accumulator is the one with the more periodical output. Also, as Equation (3.15) shows,
the noise transfer function is now a second-order high pass function. Thus, the signal to noise ratio at low frequencies is higher than in a first-order modulator.

This concept, called the cascaded modulator or the MASH modulator, MASH modulators of any order are unconditionally stable if individual modulators comprising the MASH are stable. In this case, the individual modulators are first-order ones, and thus always stable. Hence, the order of the MASH modulator can be increased at will without causing any stability problems. In the case of three accumulator or more, the third accumulator changes the prescalar to N+1,N-2,N+1,the fourth uses the sequence N+1,N-3,N+3,N-1, and the more sequence will be shown in **Fig. (3.5)**. As shown in figure (3.5), the sequence forms a Pascal triangle but with the overall sum of each row being zero with exception of the output from the first accumulator. Hence the second and subsequent accumulators have no long term effect on the division ratio[Mike Curtin and Paul O'Brien, 1999].

In digital ΣΔ-modulators, increasing the order of the modulator improves the spurious performance and the low-frequency SNR basically unrestrictedly. However, a higher order noise transfer function of the modulator causes problems in the design of the loop filter. The quantization noise of the modulator is pushed to higher frequencies, and rises with frequency at a rate of 20 decibels per decade per modulator order. For example, the quantization noise of a third-order modulator rises at a rate of 60 dB/decade[Li Lin , 2000].

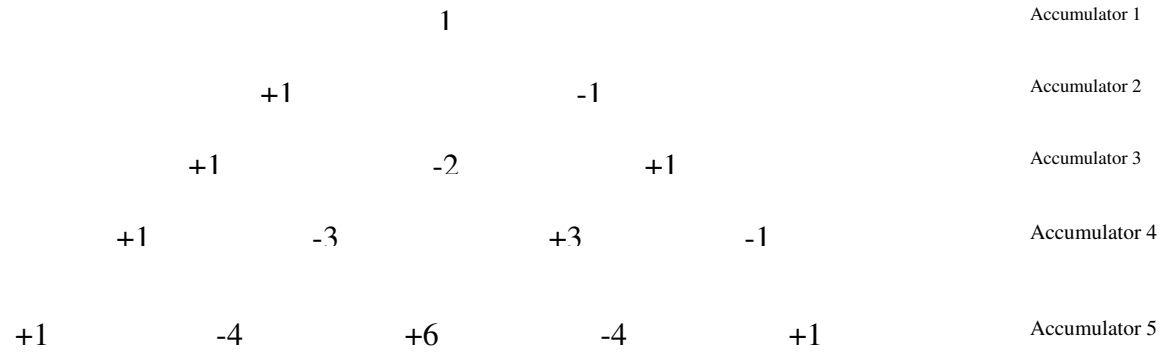

Fig. (3.5): Pascal's triangle

SYSTEM DESIGN

Based on theoretical analysis shown in section three a fractional –N synthesizer will be designed for the following requirements :

- Frequency range : 2450 MHz – 2750 MHz

- Step size : 1kHz
- Switching speed : less than 10 µsec
- Phase noise : less than -80dbc/Hz @ 10 kHz
- Spurious : -60 dB

The sigma delta modulator will be used to implement the system since it has the following properties:

- eliminating spurious digitally.
- Allowing good phase noise performance.

The sigma delta modulator in this system contains four stage of accumulator. The system contains on the following parts as shown in the schematic diagram**Fig. (4.1).**

- Single chip : contains phase frequency detector , charge pump , N-divider & ΣΔ-modulator.
- Voltage controlled oscillator.
- Loop filter.
- Frequency oscillator.

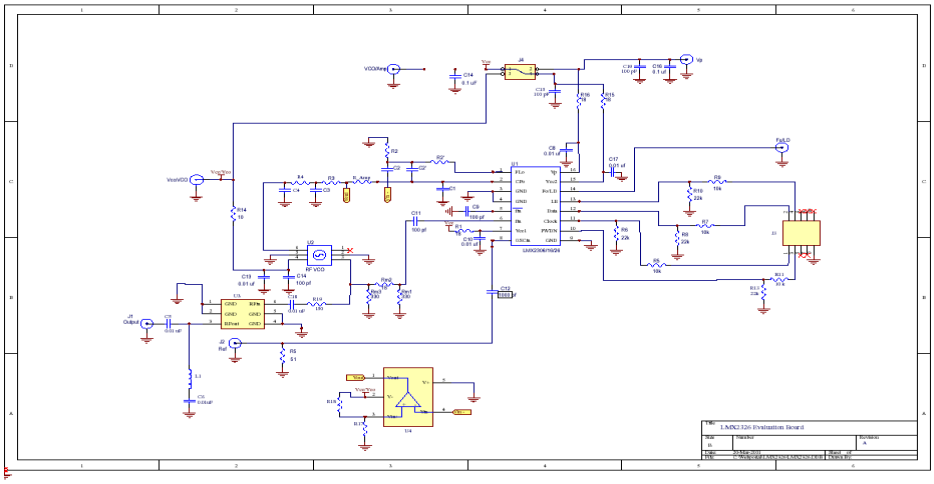

Fig. (4.1): Schematic Diagram

Single chip (LMX2486)

The LMX2486 consists of low phase noise phase frequency detector(PFD) ,N counters, R counters, ΣΔ-compensation and charge pump. The LMX2486 is fabricated using National Semiconductor's advanced process. The parts of single chip as shown in **Fig. (4.2)** is described as follow[The National Semiconductor data sheet, 2005]:

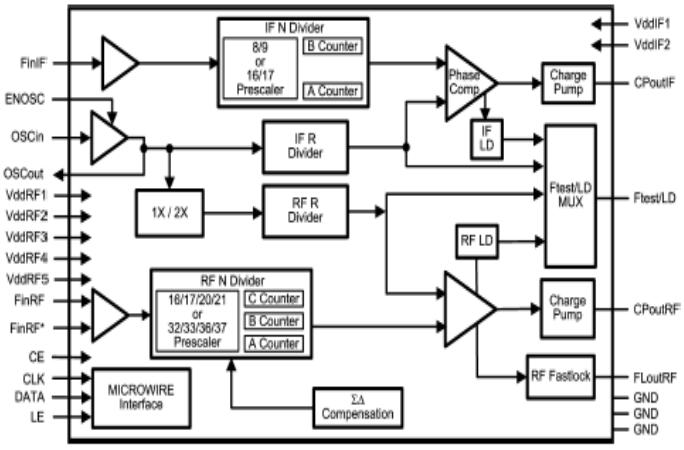

Fig. (4.2): Functional Block Diagram

- OSCILLATOR BUFFER, AND R COUNTER: The oscillator buffer must be driven single-ended by a signal source, such as a TCXO. The OSCout pin is included to provide a buffered output of this input signal and is active when the OSC_OUT bit is set to one. The ENOSC pin can be also pulled high to ensure that the OSCout pin is active, regardless of the status of the registers in the LMX2486. The R counter divides this TCXO frequency down to the comparison frequency.
- PHASE frequency DETECTOR: The maximum phase detector frequency for the LMX2486 RF PLL is 50 MHz. However, this is not possible in all circumstances due to illegal divide ratios of the N counter. The crystal reference frequency also limits the phase detector frequency, although the doubler helps with this limitation. There are trade-offs in choosing the phase detector frequency. If this frequency is run higher, then phase noise will be lower, but lock time may be increased due to cycle slipping and the capacitors in the loop filter may become rather large.
- CHARGE PUMP: For the majority of the time, the charge pump output is high impedance, and the only current through this pin is the TRI-STATE leakage. However, it does put out fast correction pulses that have a width that is proportional to the phase error presented at the phase detector. The charge pump converts the phase error presented at the phase detector into a correction current. The magnitude of this current is theoretically constant, but the duty cycle is proportional to the phase error. For the RF PLL this current is programmable in 16 steps. Also, the RF PLL allows for a higher charge pump current to be used when the PLL is locking in order to reduce the lock time.
- N COUNTERS & ΣΔ modulator: The N counter divides the VCO frequency down to the comparison frequency. The RF N counter contains an 16/17/20/21 and a 32/33/36/37 prescaler. The LMX2486 delta-sigma modulator is programmable up to fourth order, which allows to select the optimum modulator order to fit the phase noise, spur, and lock time requirements of the system. In our system fractional modulus is 15000.

Voltage controlled oscillator

The voltage controlled oscillator (VCO) is selected to achieve the frequency range(2350-2750)MHz with minimum phase noise. LMX2531LQ2570E I.C. is used to cover the required frequency range[8]. LMX2531LQ2570E has the following specifications:

- Frequency range: (2336 – 2790) MHz.
- Output power : (-1dBm - 4dBm).
- Fine tuning sensitivity (Kvtune): (10 - 23)MHz/V.
- Output impedance: 50Ω.

Loop filter

In cases where the VCO requires a higher tuning voltage than the charge pump can operate, active filters are necessary. VCOs with high voltage tuning requirements are most common in broadband tuning applications.

The loop filter impedance is defined as the voltage output at VCO to the current injected at the charge pump in the single chip synthesizer. The expression of loop filter impedance Z(s) & the corresponding poles & zeros are shown below at various filter orders is shown below[Dean banerjee, 2005]

$$Z(s) = \{1 + sT_2\}/\{s(A_3 s^3 + A_2 s^2 + A_1 s + A_0)\} \text{ , where } T_2 = R_2C_2 \qquad \text{eq(4.1)}$$

A_3, A_2, A_1 & A_0 are the coefficients of filter. For our system, the order of filter is three. Therefore $A_4 = 0$ & the values of the rest of coefficients as follows:

$A_0 = C1 + C2$, $A_1 = C1C2R2 + (C1+C2)C3\ R3$ & $A_2 = C1\ C2\ C3\ R2\ R3$

For our design, the values of components of Filter as follow:

C1 = 1pF, C2= 4.7pF, C3 = 1nF, R2 = 220kΩ & R3 = 10Ω.

Loop B.W. = 400 KHz, damping factor = 0.8.
The opamp in this filter must be a low phase noise, therefore we select LM6211. this op amp is fabricated by national semiconductor with following specifications:

- ❖ Input bias voltage : 2.75 volt.
- ❖ Opamp negative supply: 0 volt.
- ❖ Phase noise c/c of opamp in our system is shown in **Fig. (4.3)**.

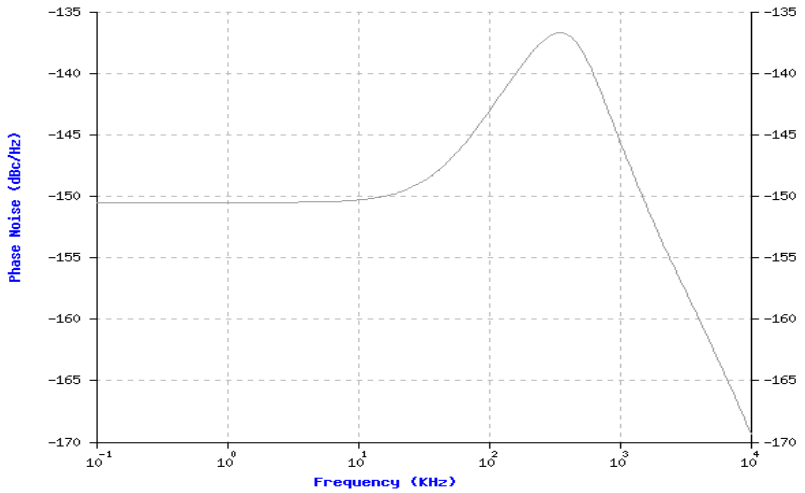

Fig. (4.3): phase noise c/c of op amp

frequency oscillator

The frequency of crystal oscillator (TCXO)in this system is 15 MHz , therefore the R counter is set to 3 to obtain 5 MHz. The phase noise c/c of TCXO in our system is shown in **Fig. (4.4).** From **Fig. (4.4) ,** it is clear that the TCXO is a low phase noise.

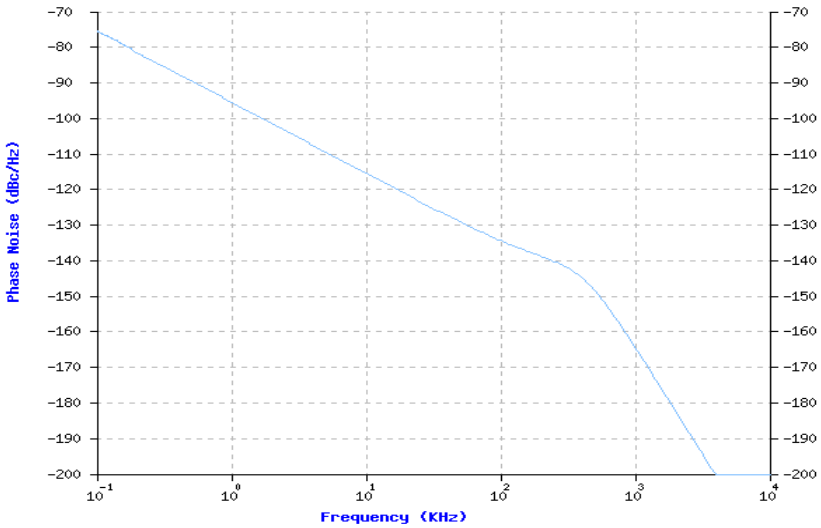

Fig. (4.4): phase noise c/c of TCXO

RESULTS

The system is simulated by software (WEBENCH) from National semiconductor company. The performance of frequency synthesizer consists of :

- Lock time: it is defined as the time needed for switching the synthesizer from one frequency to another . The lock time of our synthesizer is 8.9µsec for frequency switching (2350 - 2750)MHz as shown in **Fig. (5.1).**

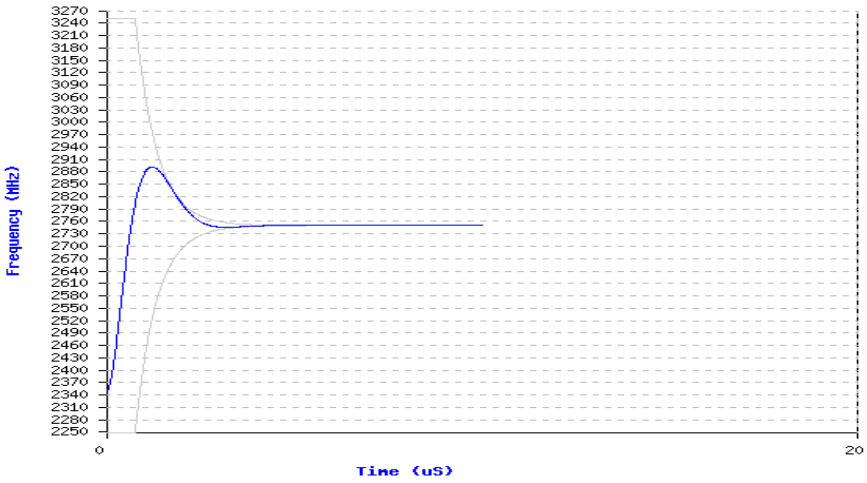

Fig. (5.1): lock time c/c of system

- Phase noise: it is the most critical parameters which describes short term frequency instability include fluctuations in signal's phase or frequency that less than 1sec. **Fig. (5.2)** shows the phase noise c/c of the system & VCO.

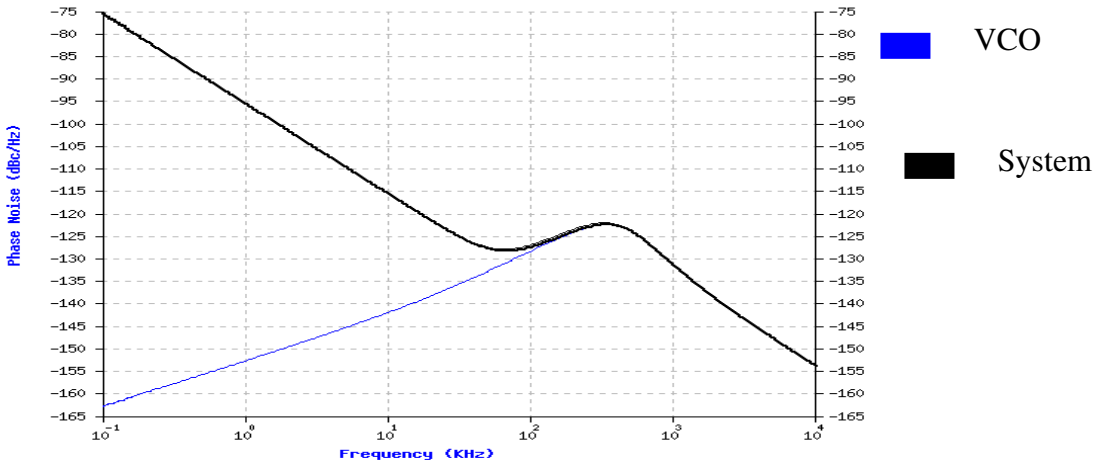

Fig. (5.2): phase noise c/c of TCXO

- Spurious output: denotes any unwanted products present at output of frequency synthesizer. The spurious level in this system is -69dB.

DISCUSSION & CONCLUSIONS

The implemented fractional N synthesizer has been presented with the basics of fractional PLL , including advantages & disadvantages. The implemented synthesizer achieve the requirements in section (4)with the following specifications:

- Frequency range : 2350 MHz – 2750 MHz
- Step size : 1kHz

- Switching speed : 8.9 μsec
- Phase noise : -115dbc/Hz @ 10 kHz
- Spurious : -69 dB

Among various techniques, the F-N technology has been selected since it has several advantages:

- Low feedback –divider ratio results in lower phase noise with fine step size.
- Low phase noise contributions are lowered by 20log(L),where L is the fractional modulus.
- Channel spacing is 1/L times smaller than an integer PLL.
- Larger loop B.W. results in lower lock time.

The development in I.C. technology provide the simplicity in the design of frequency synthesizer because it implements the PFD , prescalar, delta-sigma modulator & reference divider in single chip. this single chip has the following properties :

- Low power consumption.
- flexibility in selecting crystal oscillator frequencies.
- High reliability.

There is Direct digital synthesis (DDS) can be used to implement this system but it has drawbacks , its main disadvantage include the fundamentals limit of B.W. (maximum frequency o/p is less than one half the clock rate). Expanded B.W. requires higher clock rates , & therefore faster logic and more critical manufacturing & testing processes. There is Hybrid technique (DDS as reference oscillator) can be used to implement this system successfully but it has high cost relative to implemented system. Multi Loop PLL can satisfy this frequency range but these loops with their mixers increase spurious o/p signals , power dissipation , cost , size & complexity.

Table (6.1) shows a fair comparison with another work in 2003 includes design of an integrated CMOS PLL frequency synthesizer consists of two loops.

Table(6.1) comparison between implemented system with multi loop system

System parameters	Frequency range(GHz)	Step size	Switching time	Phase noise	Spurious level	Number of loops
Multi loop implemented In 2003	2.4 – 2.5	1MHz	30 μs	-83 dB/Hz @10 KHz	-60 dBc	2
System implemented.	2.35 – 2.75	1kHz	8.9 μs	-115dB/Hz @10 KHz	-69dBc	1

Table (6.2) shows a fair comparison with another work in 2004 includes design of a fully integrated Fractional-N frequency synthesizer for wireless communications.

Table(6.2) comparison between implemented system with a fully integrated Fractional-N frequency synthesizer

System parameters	Frequency range(GHz)	Step size	Switching time	Phase noise	Spurious level	Number of loops
Fractional-N implemented In 2004	2.4 – 2.4853	10kHz	10 μs	-90dB/Hz @10 KHz	-48 dBc	1
System implemented.	2.35 – 2.75	1kHz	8.9 μs	-115dB/Hz @10 KHz	-69dBc	1

REFERENCES

Conkling, Craig, (1998), Fractional-N synthesizers Trim current, phase noise", Microwave and RF, Feb,.

Dean banerjee (2005), PLL performance , simulation & design" 4th edition,

Goldberg, Bar-Giora., (1999), Digital frequency synthesis demystified, LLH,

J.A Crawford, (1994), Frequency synthesizer Design Handbook", Artech house, Norwood ,.

J. Craeninkx & M. Steyaert, (1998), Wireless CMOS Frequency Synthesizer Design, Kluwer Boston ,.

Li Lin, (2000), Design Techniques for High Performance Integrated Frequency Synthesizers for Multi-standard Wireless Communication Applications, UNIVERSITY OF CALIFORNIA , phD, Thesis,

Mike Curtin and Paul O'Brien. (1999), Phase locked loops for high frequency receivers and transmitters, Analog Dialogue Volume 33,.

The National Semiconductor series Data sheet, (2005).

STIFFNESS AND DAMPING PROPERTIES OF EMBEDDED MACHINE FOUNDATIONS

Dr. Thamir K. Al-Azawi
Prof. / Civil Eng. Dept.
College of Eng./ Univ. of Baghdad

Dr. Raad K. Al-Azawi
Lecturer/ Civil Eng. Dept.
College of Eng./ Univ. of Baghdad

Zuhair K. Al-Jaberi
Structural Engineer
College of Eng. / Univ. of Baghdad

ABSTRACT
In this study, a dynamic analysis of machine foundations under vertical excitations is carried out. The effect of embedment and foundation geometry has been taken into account. The stiffness and damping of soil are considered as frequency dependents. A computer program (**CPESP**) in FORTRAN POWER STATION has been coded to evaluate the stiffness and damping coefficients depending on excitation frequency and embedment depth. Results have shown that increasing the embedment depth leads to increasing the resonant frequency and decreasing the amplitude of vibration.

الخلاصة

في هذه الدراسة تم تنفيذ التحليل الديناميكي لأسس المكائن تحت تأثير الاهتزازات العمودية. تأثيرعمق الطمر (embedment) وشكل الأساس قد أُخِذا في الحسبان. إنّ الجسائة والتخميد للتربة قد اعتبرت معتمد التردد(frequency dependent).تم اعداد برنامجا(**CPESP**) بلغة (FORTRAN POWER STATION) لحساب معامل الجسائة والتخميد للتربة بالإضافة إلى حساب ثابت الجسائة الديناميكي(K) وثابت التخميد الديناميكي(C) المعتمدين على تردد الاهتزاز(ω) وعلى عمق الطمر(embedment). تمت المقارنة بين الدراسة الحالية وطريقة التقريب الدائري المكافئ(equivalent circular approximation).أظهرت النتائج إن زيادة عمق الطمر يؤدي إلى زيادة التردد ألرنيني ويقلل من سعة الاهتزاز.

KEY WORDS
Dynamic, Machine Foundation, Stiffness, Embedment.

INTRODUCTION

Most of the solution methods treat the machine foundation as a block resting on the surface of an elastic soil. The real footings are usually embedded and this considerably affects the dynamic response of footing, Barken.D.D (1962). The rigorous analytical solution of embedded footings has many mathematical difficulties. The most promising way of studying this problem is the finite element analysis as had been used by many researchers such as Lysmer.J(1979) and by kaldjian .M.J (1969) for static analysis.

Nevertheless, there is a need for alternative approximate solutions that would be able to predict the motion and to evaluate the stiffness and damping characteristics of embedded footings.

EQUATION OF MOTION

By applying de Alembert's principle, the equation of motion can be written as; **Fig. (1)**

$$m\ddot{U}_z(t) + C_z(\omega)\dot{U}_z(t) + K_z(\omega)U_z(t) = P_o \exp(i\omega t) \quad (1)$$

Where:-

m = Total mass.

$m\ddot{U}_z(t)$ = Inertia force.

$C_z(\omega)\dot{U}_z(t)$ =Damping force.

$K_z(\omega)U_z(t)$ = Elastic force.

$K_z(\omega)$ =Frequency dependent stiffness.

$C_z(\omega)$ =Frequency dependent damping.

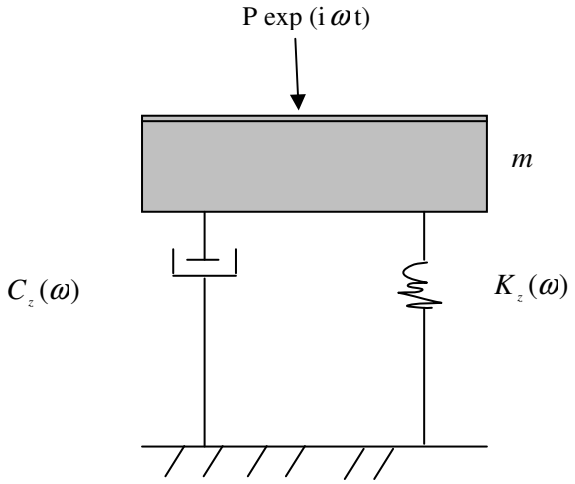

Fig. (1) Foundation resting on spring and dashpot

For harmonic loading with an excitation frequency of ω, the steady state solution can be assumed as:

$$U_z(t) = A_z \exp(i\omega t) \quad (2)$$

Substituting eq. (2) into eq. (1):-

$$-m\omega^2 A_z \exp(i\omega t) + \left[K_z(\omega) + i\omega C_z(\omega)\right]A_z \exp(i\omega t) = P_o \exp(i\omega t)$$

Dividing both sides of the equation by $\exp(i\omega t)$ and separating real and imaginary parts, the amplitude of motion A_z will be:-

$$A_z = \frac{P_o}{\left[(K_z(\omega) - m\omega^2) + i\omega C_z(\omega)\right]} \quad (3)$$

Let $a_1 = K_z(\omega) - m\omega^2$

$a_2 = -\omega C_z(\omega)$

Multiplying the numerator and denominator of eq. (3) by $(a_1 + ia_2)$, the amplitude can be written as:-

$$A_z = \frac{(a_1 + ia_2)P_o}{a_1^{\,2} + a_2^{\,2}} = \frac{\exp(i\phi)}{R} P_o \qquad (4)$$

Where:-

$R = \sqrt{a_1^{\,2} + a_2^{\,2}}$

And

$$\phi = \tan^{-1}(a_2/a_1) = \tan^{-1} \frac{-\omega_z C_z(\omega)}{K_z(\omega) - m\omega^2}$$

Substituting A_z into eq. (2) the steady state solution becomes:-

$$U_z(t) = \frac{\exp(i\phi)}{R} P_o \exp(i\omega t) = \frac{P_o \exp[i(\omega t + \phi)]}{\sqrt{(K_z(\omega) - m\omega^2)^2 + \omega^2 C_z^{\,2}(\omega)}} \qquad (5)$$

The real part of the amplitude of vibration is:-

$$A_Z = \frac{P_o}{\sqrt{(K_Z(\omega) - m\omega^2)^2 + \omega^2 C_Z^{\,2}(\omega)}}$$

where:-

Eq. (5) gives the dynamic response of the foundation in vertical vibration and for an exciting force of constant amplitude P_o.

The natural frequency of the undamped free vibration is:-

$$\omega_n = \sqrt{K_z(\omega)/m} \qquad (6)$$

In this study a rigid foundation will be studied which is located at depth D below the ground surface. This foundation is subjected to a steady-state vibration by a harmonic vertical force, $P(t) = P_o \exp(i\omega t)$, having an amplitude of P_o and a circular frequency ω, and acting through the centeroid of the base. This dynamic force is resisted by normal soil stresses against the base and by shear stresses along the vertical foundation sides. The rotational oscillations that may occur due to the lack of complete symmetry in the soil reactions at the base and especially at the foundation sides are ignored in this study. The steady-state response of the foundation is thus described by the vertical dynamic settlement $U = U_o \exp(i\omega t)$.

Due to damping the force, $P(t)$ is generally out of phase with the response $U(t)$. The latter can be divided into two components, one in phase $[U_1 \exp(i\omega t)]$ and the other 90^o out of phase $[U_2 \exp(i\omega t)]$ with P. [11]

The corrected dynamic stiffness, $\overline{K}(\beta)$ and the dynamic damping coefficient, $\overline{C}(\beta)$ are given by:-

$$\overline{K}(\beta) = \overline{K}(\omega) - \omega C \cdot \beta \qquad (7.a)$$

$$\overline{C}(\beta) = C + \frac{2\overline{K}(\omega)}{\omega} \cdot \beta \qquad (7.b)$$

Where:

β = frequency independent damping ratio. For most soils β ranges typically from 0.02 to 0.05, Richart.F.E. (1970).

Both the effective dynamic stiffness and the radiation damping coefficient of the soil–foundation system are functions of the frequency ω.It is convenient to express $K_{sur})_{dy}$ as a product of the static stiffness, K_{sur} of the system times a dynamic stiffness coefficient $k(\omega)$

$$K_{sur})_{dy} = K_{sur} \cdot k(\omega) \tag{8}$$

STATIC STIFFNESS OF SURFACE FOUNDATIONS

For a surface foundation of an arbitrary shape, the vertical static stiffness K_{sur}, is given by Dominguez,J(1978):

$$K_{sur} = \frac{2LG}{1-\upsilon} S_z \tag{9}$$

Where:-

L=Semi-length of a rectangle circumscribed to base surface.

G=Shear modulus of soil.

υ=Poisson's ratio.

S_z=Vertical static stiffness parameter.

For non-rectangular base, K_{sur} may be obtained as follows, Prakash,S(1988):-

$$K_{sur} = 4GR/(1-\upsilon) \tag{10}$$

Where:-

R= Radius of the equivalent circle = $\sqrt{A_b/\pi}$

The equivalent circle approximation predicts S_z as follows [10]:-

$$S_z = \frac{4}{\sqrt{\pi}} \sqrt{A_b/4L^2} \tag{11}$$

The equivalent circle approximation gives good results for L/B≤2 to 3 as calculated by Dobry and Gazetas (1986). **Fig (2)** shows that:-

$$\begin{aligned} S_z &= 0.8 && for\ A_b/4L^2 \langle 0.02 \\ S_z &= 0.73 + 1.54(A_b/4L^2)^{0.75} && for\ A_b/4L^2 \rangle 0.02 \end{aligned} \tag{12}$$

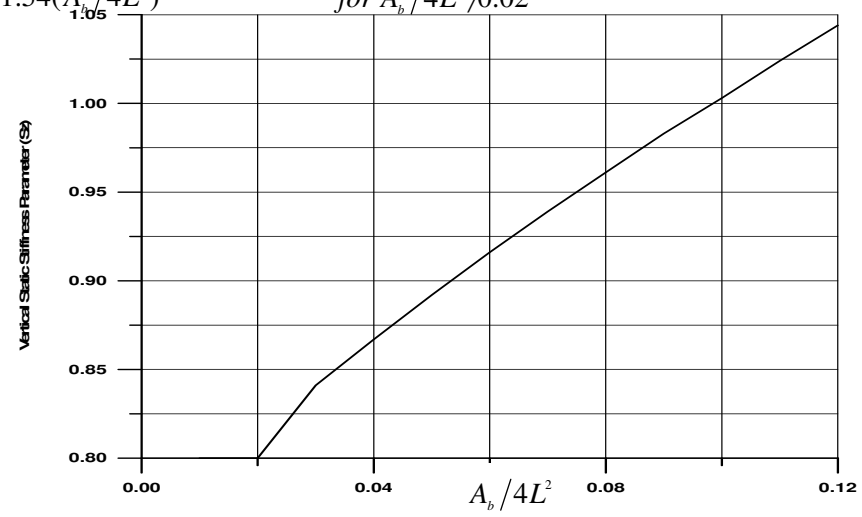

Fig. (2) vertical static stiffness parameter (Sz) versus base shape [10]

EFFECT OF EMBEDMENT ON STATTIC STIFFNESS

In practice, foundations are placed at a specified depth, say D below the ground surface and transmit the load to soil. Usually, increasing the depth D means increasing the foundation stiffness K.

The factors that modify the foundation stiffness are the "trench" and "sidewall contact" effects, that tend to increase the stiffness of the embedded foundation. These two effects are to be explained with the aid of **Fig. (3).**

Trench Effect

Even in perfectly homogenous soil a rigid footing will settle less if it is placed at the bottom of an open trench. The normal and shear stresses resulting from the overlying soil restricts the vertical movement and thus reducing the settlement of the foundation base by increasing its vertical stiffness.

The trench effect suggested by Gazetas and Dobry (1986) is:-

$$K_{tre} / K_{sur} = I_{tre} \rangle 1 \qquad (13)$$

Where:-

K_{tre} is the vertical static stiffness of an embedded foundation mat with no sidewall contact.

Sidewall Effect

Part of the applied load is transmitted to the ground through shear stresses along the vertical sides of the footing when the sides are in contact with the surrounding soil.

As a result, the overall stiffness of an embedded foundation K_{emb} is larger than K_{tre} stiffness corresponding to a foundation with the same depth of embedment but without side effect , Ricardo.D (1985).

$$\frac{K_{emb}}{K_{tre}} = I_{side} \rangle 1 \qquad (14)$$

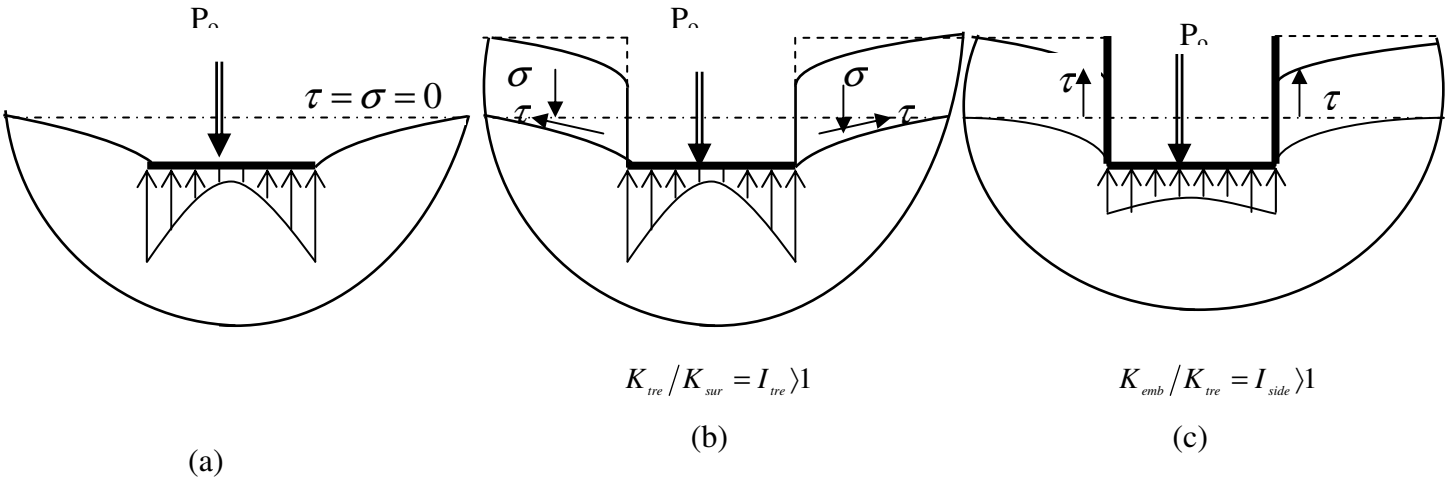

Fig. (3) effects of embedment on vertical static stiffness of foundation
(a) settlement due to surface foundation (b) trench effect
(c) combined trench and sidewall effects.

Experimental studies, such as those of Lysmer.j (1969), offer valuable guidance in this direction. Combining eqs. 13 and 14 lead to:

$K_{emb} = K_{sur} \cdot I_{tre} \cdot I_{side}$

Based on test results the following empirical equations had been derived:-

$$I_{tre} = 1 + \frac{D}{21B}\left(1 + \frac{4}{3}\frac{A_b}{4L^2}\right) \quad (15)$$

$$I_{side} = 1 + 0.19(A_s / A_b)^{0.666} \quad (16)$$

Where:-

I_{tre} =Trench factor.

I_{side} =Sidewall factor.

A_b =Base area of foundation.

A_s =Sides area of foundation.

Fig (4) shows that as (D/B) increases the ratio of (K_{tre} / K_{sur}) also increases. This trend is more pronounced for the case of a square foundation (L/B=1).

The foundation static stiffness (K_{emb}) for a full embedment case is:-

$$K_{emb} = \frac{2LG}{1-\upsilon} S_z \left[1 + \frac{1}{21}\frac{D}{B}(1 + \frac{4}{3}\frac{A_b}{4L^2})\right]\left[1 + 0.19(\frac{A_s}{A_b})^{0.666}\right] \quad (17)$$

Fig.(5) shows that as (D/B) increases the ratio (K_{emb} / K_{sur}) also increases. Again this trend is more pronounced for the case of a square foundation (L/B=1)

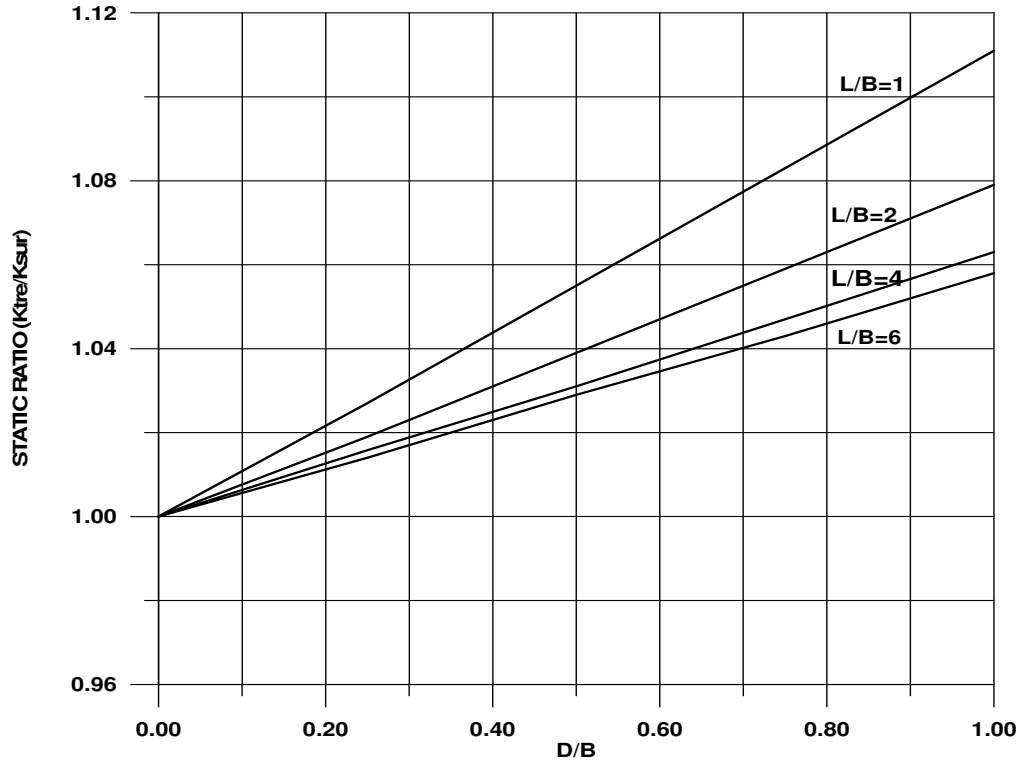

Fig. (4) effect of trench on static stiffness

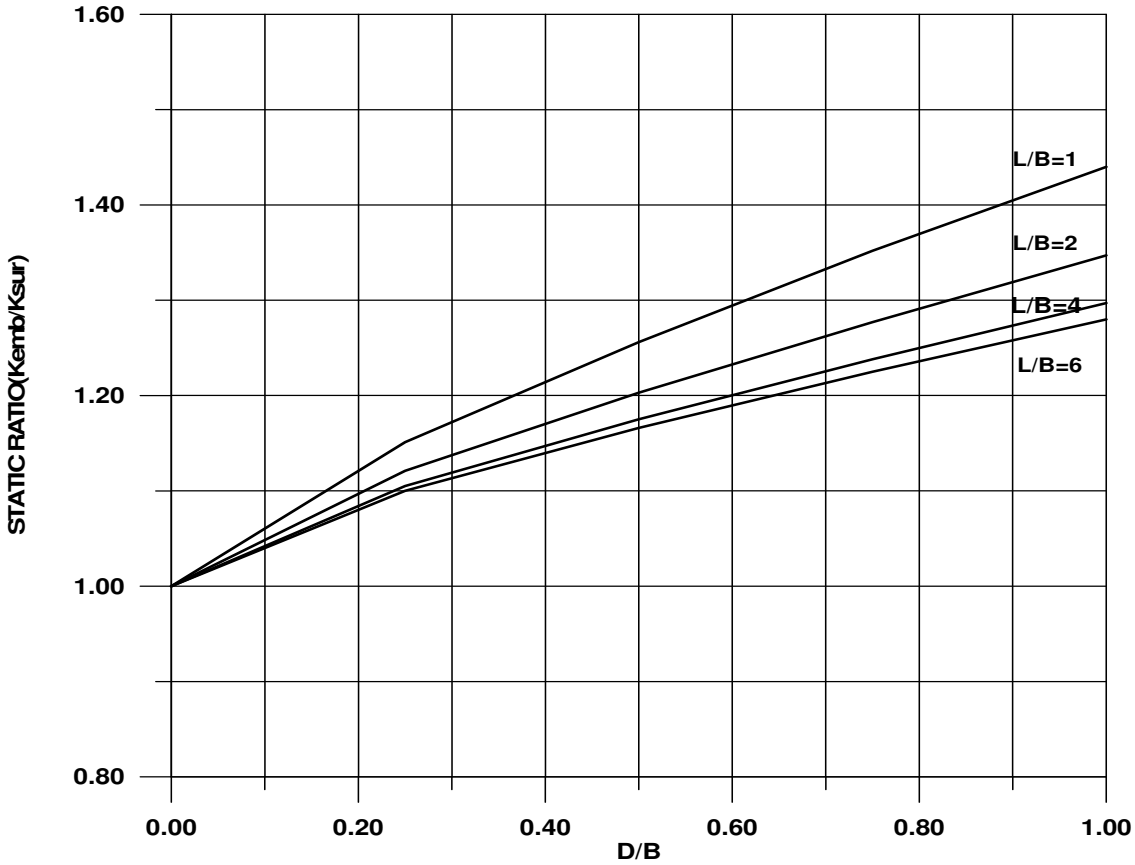

Fig. (5) effect of embedment on static stiffness

DYNAMIC STIFFNESS COEFFICIENT

It had been concluded empirically by George.G(1986) that the vertical stiffness of elastic foundation is frequency dependent. The main parameters affecting the dynamic stiffness are a_o, L/B and υ, where:-

a_o =Normalized frequency = $\omega B/V_s$

Where:-

V_s =Shear wave velocity.

L/B =Foundation aspect ratio.

υ =Poisson's ratio.

The frequency dependent stiffnesses are:-

For Poisson ratio $\upsilon = 0.33$ (unsaturated soil)

$$K_{emb})_{dy} = K_{emb} \cdot k(\omega) \cdot \left[1 - 0.09(a_o)^2 (D/B)^{0.75}\right] \quad (18.a)$$

$$K_{tre})_{dy} = K_{emb} \cdot k(\omega) \cdot \left[1 + 0.09(a_o)^2 (D/B)^{0.75}\right] \quad (18.b)$$

For Poisson ratio $\upsilon = 0.5$ (saturated soil)

$$K_{emb})_{dy} = K_{emb} \cdot k(\omega) \cdot \left[1 - 0.35(a_o)^2 (D/B)^{0.5}\right] \quad (18.c)$$

$$K_{tre})_{dy} = K_{emb} \cdot k(\omega) \cdot \left[1 + 0.35(a_o)^2 (D/B)^{0.5}\right] \quad (18.d)$$

These equations were obtained by Gazetas and Dobry (1986), Where:-
$K(\omega)$:is a dimensionless frequency dependent factor given in **Table (1)**. Hence the dynamic stiffness of an embedded foundation can be written as:-

$$K_{emb})_{dy} = K_{emb} \cdot k(\omega) \cdot F_e = K_{emb} \cdot \overline{F}_e \quad (19)$$

Where:-
$F_e = \left[1 - 0.09(a_o)^2 (D/B)^{0.75}\right]$
or
$F_e = \left[1 - 0.35(a_o)^2 (D/B)^{0.5}\right]$
as given in eq. (18).

The factor $\overline{F}_e$ of eq. (19) is the effective embedment factor. **Fig. (6)** Shows the variation of this factor with the normalized frequency parameter(a_o). The relationships have been obtained in the present study by coding the above equations through a short computer program.

Table (1) dynamic stiffness factor for surface foundation [$K(\omega)$]

Passion ratio	Frequency dependent stiffness factor [$K(\omega)$]	L/B
0.33	1.0035+0.051953 (a_o)-0.123599(a_o)^2	1 and 2
	0.966691+0.55445(a_o)-0.771009(a_o)^2	6
	1.02098+1.10380(a_o)-1.3743(a_o)^2	10
0.50	1.00055-0.0807878(a_o)-0.0362395(a_o)^2	1
	0.95004+0.46544(a_o)-0.35049(a_o)^2	4
	0.841195+1.34818(a_o)-0.823897(a_o)^2	≥6

DAMPING COEFFICIENT

The coefficient of damping $c = c(\omega)$ is a measure of vibration energy transmitted into the soil and carried away by spreading waves. These waves are generated at every point on the soil-foundation interface so that in general $c(\omega)$ increases with increasing area of contact.

The contact surface for a vertically oscillating embedded foundation consists of a horizontal base and vertical sides. The base transmits to the underlying ground compression-extension waves in propagation velocity close to the Lymers (1969) analogy.

$$V_{La} = 3.4 \cdot V_s / \left[\pi(1 - \upsilon)\right] \quad (20)$$

Where:
V_s = shear wave velocity
V_{La} = "Lysmer's analog" velocity
On the other hand the sides transmit mainly shear waves through the surrounding soil.
The two types of waves generated at the base and at the sides of an embedded foundation are independent. Summing up the respective radiated energies.

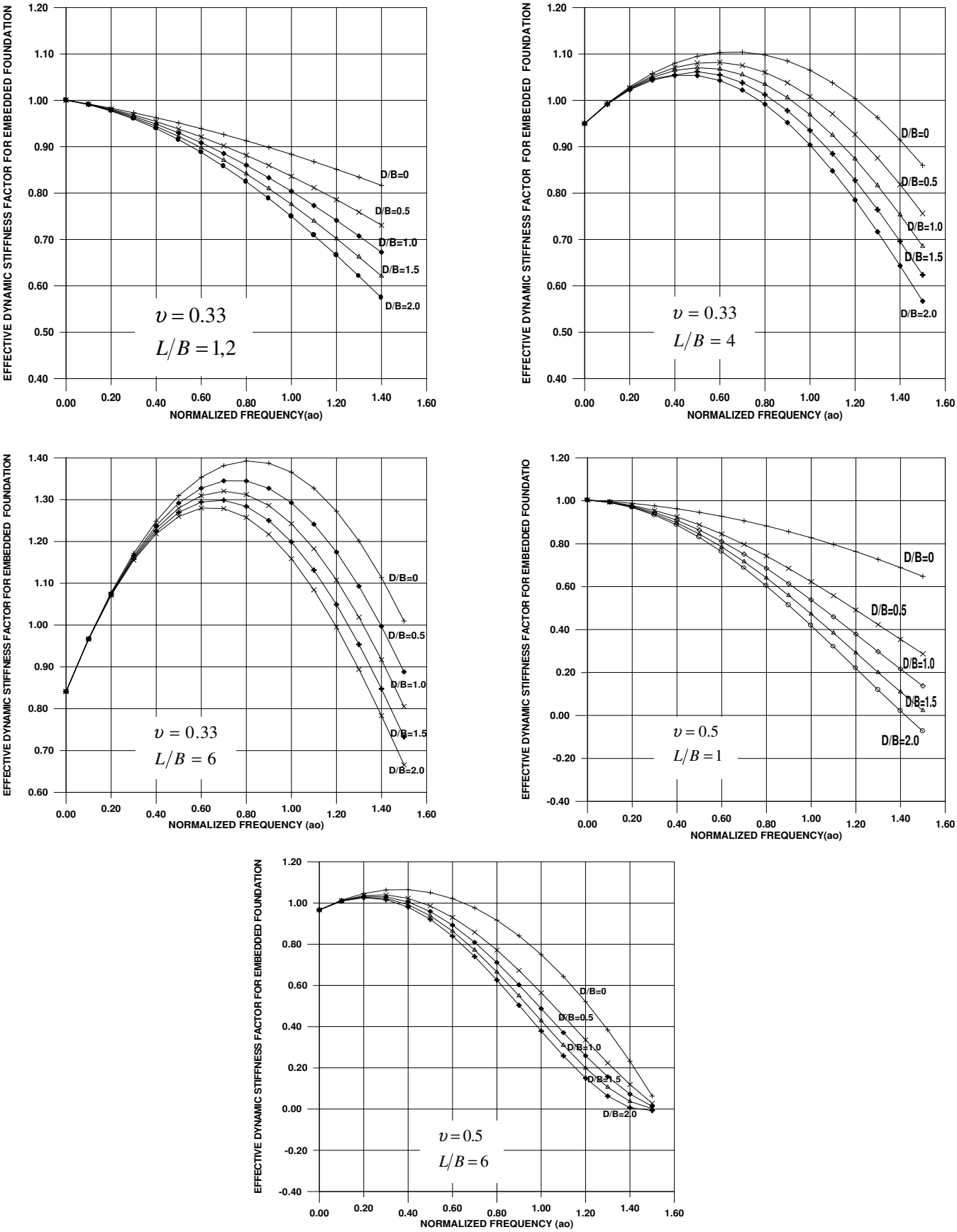

Fig. (6) effective dynamic stiffness factor $\overline{F}_e$ for embedded foundations

$$C = (\rho \cdot V_{La} \cdot A_b) \cdot c(\omega) + \rho \cdot V_s \cdot A_s \quad (21)$$

Where:-
$c(\omega)$: Coefficient of dynamic damping as given in **Table (2).**

Table (2) dynamic damping coefficient $[c(\omega)]$ (2)

Dynamic Damping coefficient $c(\omega)$	R= L/B
0.9716 -0.0500$(R a_o)^2$-0.0660exp $(R a_o)$	1
1.2080-0.164$(R a_o)$+0.0385$(R a_o)^2$+0.2515exp $(-R a_o)$	2
1.900-0.0025$(R a_o)$+0.0012 $(R a_o)^2$	4
1.2285-0.0359$(R a_o)$+0.0024$(R a_o)^2$+0.1515exp $(-R a_o)$	6
1.3112-0.0285$(R a_o)$+0.0011$(R a_o)^2$+0.4388exp$(-R a_o)$	10

COMPUTER PROGRAM

In this study a computer program **(CPESP)** (**C**omputer **P**rogram for **E**valuation of **S**oil **P**roperties) in Fortran Power Station language has been coded for calculating the dynamic stiffness and damping for surface and embedded foundations. In this program the input data are :-

- Dimensions B and L of the base.
- Side surface area of foundation $A_{s.}$
- Soil shear modulus G
- Soil poisson ratio υ
- Soil density ρ
- Soil damping factor β

The first step is to compute the Static Stiffness and damping coefficients .
The second step is to compute the dynamic factor for the stiffness and damping .
The effect of embedment was also considered in this program.

APPLICATIONS

Application (1)

The developed coefficient of dynamic stiffness and damping are applied to obtain the dynamic stiffness and damping using the (**CPESP**) program for the embedded foundation shown in **Fig. (7)**. The results are shown in **Table (3)**

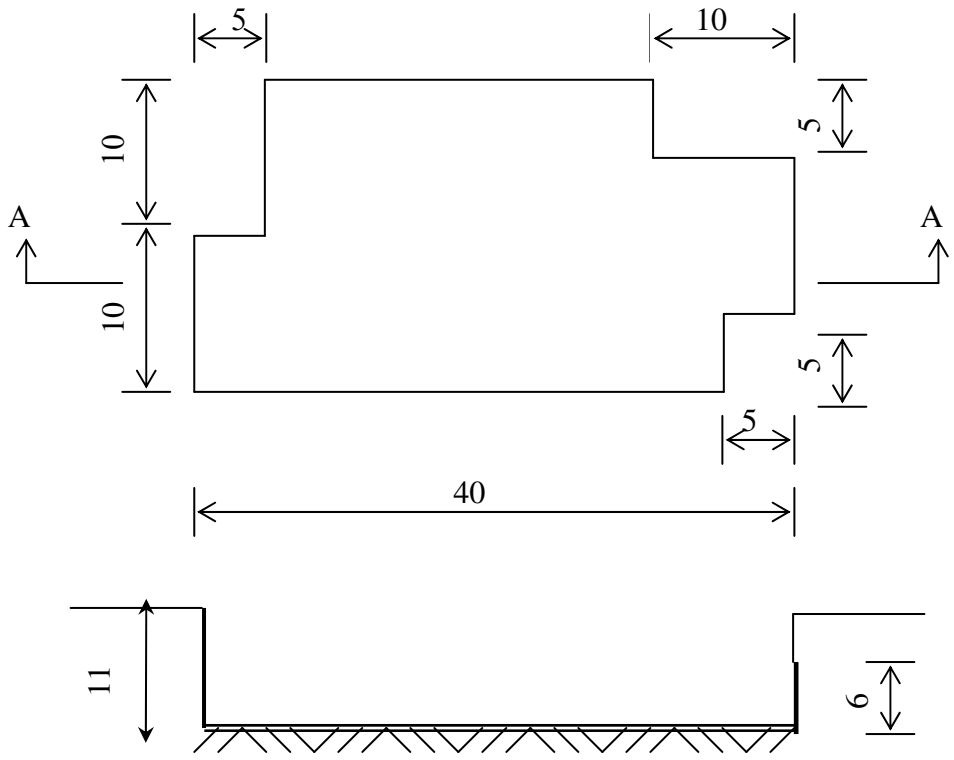

G =74 MPa
ρ =1.85 Mg/m^3
υ = 0.33
V_s =200 m/sec
ω = 30 rad/sec

All dimensions in (m)

Sec. A-A

Fig (7) geometry and material parameters, Gazetas.G(1979),application (1)

Application (2)

The foundation of application (1) has been solved using the equivalent circle approximation.

The effective radius of foundation(R) = $\sqrt{A_b/\pi}$ =14.65

The equivalent static surface stiffness $K_{sur} = \frac{4GR}{1-\upsilon}$

K_{sur} =6.472*10^6 kN/m

Using eqs. (15),(16) the results are :-

I_{tre} =1.055

I_{side} =1.211

The static embedment stiffness will be:-

K_{emb} =8.268*10^6 kN/m

From Table (1) and using eq. (18a) then the effective embedment factor is equal to 0.713.

$K_{emb})_{dy} = K_{emb} * \overline{F}_e$

$K_{emb})_{dy}$ =5.895*10^6 kN/m

Table (3) shows the final results for applications (1) and (2) .

Table (3) dynamic stiffness of embedded foundation using the present study and approximate methods.

Method of analysis	Surface static stiffness (kN/m)	Trench factor	Sidewall factor	Dynamic stiffness coefficient	Dynamic embedded stiffness (kN/m)
Present method (Application 1)	$7.333*10^6$	1.0818	1.211	0.684	$6.08*10^6$
Equivalent Circle Approximation (Application 2)	$8.633*10^6$	1.055	1.211	0.713	$5.895*10^6$

Table (3) compares the results of the present study and the equivalent circle approximation and the maximum discrepancy is about 3%.

The Lysmers analog velocity using eq. (20) is:-
V_{La} =323.06 m/sec

From **Table (2)** and using (a_o =1.5) then the dynamic damping coefficient is :-
$c(\omega)$ =1.075
The dynamic damping of soil using eq. (21) is:-
$C = 0.726*10^6$ kN.m^{-1}.sec

The corrected dynamic stiffness and damping using eq. (7) are:-
$\overline{K}(\beta)$ =$4.98*10^6$ kN/m
$\overline{C}(\beta)$ =$0.749*10^6$ kN.m^{-1}.sec

Application (3)
The obtained coefficients in this study **Table (1 and 2)** are used to study the dynamic response of machine foundation under vertical dynamic load by using SAP 2000. The analysis parameters are:-

Foundation Parameters
L=9.6 m
B=4.8 m
D= 1.55 m
Foundation weight=1714 kN

Soil Parameters
υ = 0.33
γ =18.725 kN/m^3
G = 98 Mpa

Machine Parameters
F_v=6.27 sin (ωt)
ω=61.36 rad/sec
Machine weight=260.65 kN

The result obtained are summarized in **Table (4)** and **Fig. (8)**.

Table (4) results obtained from the analysis of SAP2000(application 3)

D/B	Resonant Frequency (rad/sec)	Max. displacement (mm)
0.000	84.21	0.896
0.127	92.431	0.649
0.254	97.223	0.426
0.380	101.377	0.214
0.500	105.000	0.184
0.635	108.550	0.137

The same foundation has been analyzed for different embedment ratios (D/B) and the results for the displacement-time output are shown in **Fig.(8)**. It is evident that when the depth ratio increases the vertical displacement decreases.
A convergence in results is obvious when the depth ratio will be about 0.50. This means that the reduction in dynamic displacement will be less pronounced when the depth ratio is to be increased higher than 0.50.

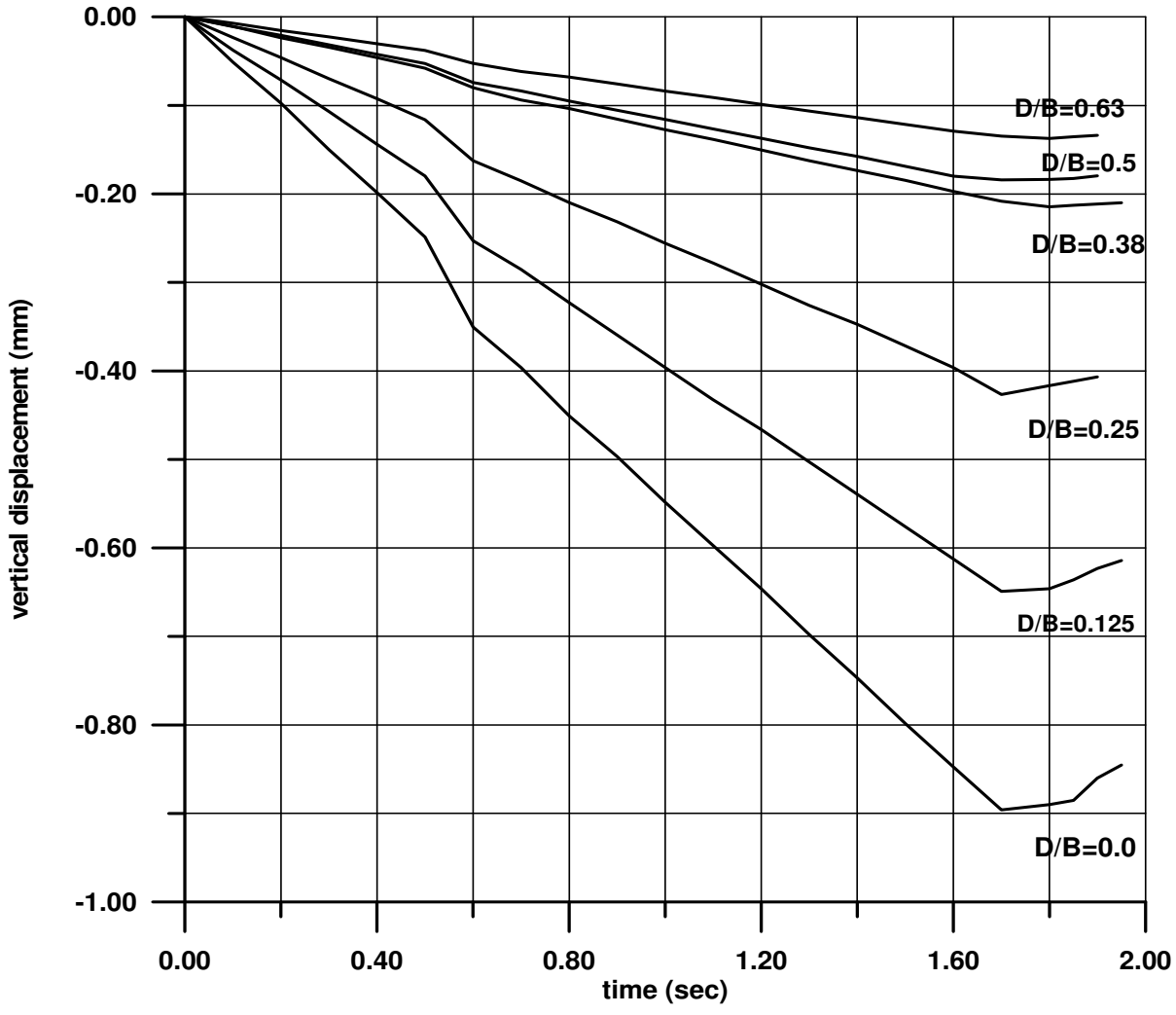

Fig.(8) effect of embedment on vertical response (application 3)

Also the increase in embedment depth leads to an increase in the resonant frequency of machine foundations, **Table (4)** shows this effect. The results show that increasing the embedment depth ratio (D/B) to 0.635 increases the resonant frequency by 22% .

EFFECTS OF USING A SQUARE FOUNDATION ON THE DYNAMIC RESPONSE

It is a matter of interest to study the effect of using a square foundation (L=6.8 m) and (B=6.8 m), i.e. B/L=1.0 instead of the rectangular foundation which has been studied in the previous sections (B/L=0.50). The dimensions of this foundation are based on equal foundation weight and soil pressure as compared to the case of the rectangular foundation.

Fig. (9) shows the vertical displacement-time relationships for different depth ratios (D/B) for the square foundation case. **Table (5)** gives the ratios of displacement amplitudes for the square and rectangular foundations for different depth ratios. The results indicate a reduction in the dynamic displacement in a range of (15%-17%) as compared to those of rectangular foundation.

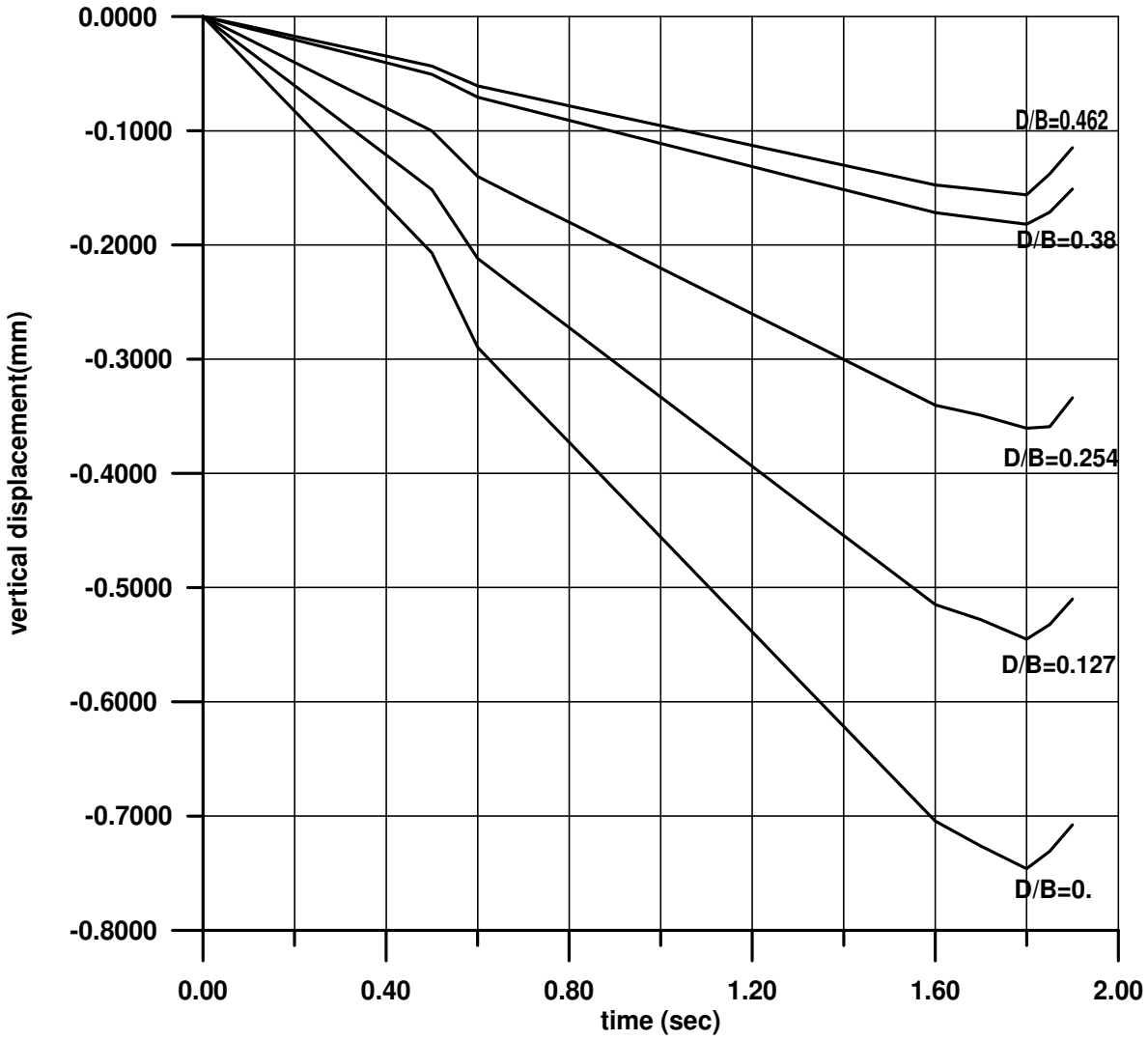

Fig. (9) effect of embedment on vertical displacement for different depth Ratios for a square foundation

Table (5) vertical displacement amplitudes (Δ)

	Depth Ratios (D/B)				
	0.00	0.127	0.254	0.380	Full embedded
Rectangular (B/L)=0.5	0.896	0.649	0.426	0.214	0.184
Square (B/L)=1.0	0.746	0.545	0.360	0.181	0.156
$\Delta S/\Delta R^*$	0.833	0.840	0.845	0.848	0.85

*ΔS=Vertical displacement amplitude for a square foundation.
ΔR=Vertical displacement amplitude for a rectangular foundation

CONCUSIONS

The effect of embedment upon vertical forced vibration of a rigid footing was investigated theoretically.

The conclusions can be summarized as follows:

1- The use of equivalent circle approach to estimate the dynamic stiffness and damping factors can cause errors as the aspect ratio of the foundation (L/B)and the soil Poisson's ratio (υ) being increased. The error will generally be increased at higher frequencies.

2- Embedment of foundations has a significant effect on the dynamic response. It causes an increase in the dynamic stiffness and damping coefficients and leads to increase the resonant frequency and to decrease the dynamic response of foundation. A convergence in results is obvious when the depth ratio will be about 0.50.This means that the reduction in dynamic displacement will be less pronounced when the depth ratio is to be increased higher than 0.50.

3- The dynamic displacement in the vertical direction is smaller for the case of square foundations as compared to those of rectangular foundations for the same weight and contact soil pressure. The results indicate a reduction in the dynamic displacement in a range of (15% - 17%)as compared to those of the rectangular foundation.

REFERENCES

Barken D.D (1962), Dynamic of base and foundations, Mc Graw-Hill Book Co. New Yourk, N.K. (translated from Russion) .

Bowels. J. (1988), Foundation Analysis and Design, McGraw-Hall book company

Dominguez, J. and Rosset, J.M (1978)"Dynamic stiffness of rectangular foundations" Research Report R 78-20 Dep. of Civil Eng. M.I.T.

Dosgupta, S.P. and Roa, K.N.S.N. (1978), Dynamics of Rectangular footings by finite elements, Journal of the Geotechnical Engineering Division ASCE , Vol.104, No.GT5.

George Gazetas, Ricardo Dobry and Kenneth H. Stokoe (1986), Dynamic Response of arbitrary shaped foundations: experimental verification, Journal of Geotechnical Engineering Division ASCE vol.111, Vol.2.

Gazetas. G. and Roesset. J.M (1979), Vertical vibration of machine foundations,Journal of Geotechnical Engineering Division ASCE, Vol 105, No Gt 12,. PP.1435-1454.

Kaldjian M.J. (1969), Discussion of Design procedures for Dynamically Loaded Foundations,by R.V. Whitman and F.E. Richard. Jr. Journal of soil Mechanics and Foundations Divisions ASCE. Vol.95, No.SM1, proc. Paper 6324, Jan.

Lysmer J., and Kuhlemeyer R.L (1969),Finite Dynamic Model for infinite Media,Journal of the Engineering Mechanics Division ASCE, Vol.95, No.EM4, proc. Paper 6719, Aug. PP. 859-877.

Prakash, S. and Puri, V.((1988), undations for Machines: Analysis and Design,Wiley& Sons

Ricardo Dobry and George Gazetas (1986), Dynamic Response of Arbitrary shaped foundations" Journal of Geotechnical Engineering Division ASCE Vol. 112 No.2.

Ricardo Dobry and George Gazetas (1985), Vertical Response of arbitrary shaped foundations, Journal of Geotechnical Engineering Division ASCE Vol.111, No.6.

Richart, F, E, Hall. J.R and woods R.D.(1970), Vibration of soil and foundations, Prentice-Hall. Inc. Englewood cliffs N.J

Stock, K.H. and Richart, F.E. (1974), Dynamic Response of embedded machine foundations, Journal of Geotechnical Engneering Division ASCE Vol.100, No.GTA,

NOTATIONS

The following symbols are used in this paper:

A_b= base area of foundation.

A_s= sides area of foundation.

a_o= normalized frequency.

B= semi-width of rectangle circumscribed to base surface.

C= dynamic damping of soil.

$\overline{C}_z$ =coefficient of dynamic damping.

D= trench depth.

G=shear modulus of soil.

I_{tre}=trench factor.

I_{wall} =sidewall factor.

K_{emb}= static embedment stiffness of soil.

$K_{emb})_{dy}$= coefficient of dynamic embedment stiffness of soil for trench effect only.

$K_{tre})_{dy}$=coefficient of dynamic stiffness for soil for trench effect only.

$K_{sur})_{dy}$=coefficient of dynamic stiffness for surface foundation.

L= Semi- length of rectangle circumscribed to base surface.

S_z= vertical static stiffness parameters.

V_{La}= "Lysmer's analog" velocity.

V_s=velocity of shear waves.

υ = Poisson's ratio.

ρ = mass soil density.

ω =circular frequency.

INFLUENCE OF VARIABILITY IN FLEXIBLE PAVEMENT PARAMETERS ON BACKCALCULATED MODULI

Dr.Namir G.Ahmed
Lecturer / Dept.of HWY's and Transportation Engineering
College of Engineering/University of Al-Mustansiriyah

ABSTRACT

Many researchers recommended Falling Weight Deflectometer (FWD) to be use for the purpose of stiffness profile determination of existing pavement. Several sources of uncertainties contribute to the inaccuracies in moduli obtained in this manner. these include: 1) the measured parameters (deflection basin and FWD load), 2) the back calculation model, and 3) the pavement parameters, such as Poisson's ratio and thickness of each pavement layer .

In the present study the influence of the variation in the thickness and other pavement parameters on the backcalcuted moduli are investigated .Theoretical deflection basins were generated for different pavement structure using program Mich-pave. Mich-back program was then utilized to backcalculate the moduli from these theoretical basins. To assess the influence of the variability in thickness, Poisson's ratio, FWD load and deflection, a Monte Carlo simulation process was employed.

Results show that the backcalculation of the layer moduli is greatly influence by the variability of the combined pavement. A sensitivity analysis showed that the uncertainties in thicknesses are the major contributor to variations of the backcalculated Moduli.

الخلاصة:

يوصي الكثير من الباحثين باستخدام جهاز (FWD) لغرض ايجاد قيم معاملات الصلادة (Stiffness) للتبليط الحالي بالرغم من ان بعض المصادر تشكك في حساب دقة المعاملات فيما لو استخدمت هذة الطريقة و التي تشمل:

1-المعاملات التي تم حسابها (الهبوط وكذلك احمال جهاز FWD) 2-النموذج (الموديل) الخاص بطريقة الحساب العكسي 3-معاملات التبليط (نسبة بواسان وكذلك سمك طبقات التبليط)

في الدراسة المقدمة فان تاثير التغييرات في السمك وكذلك بقية معاملات التبليط في الحساب العكسي للمعاملات قد تم التحري عنها. ان القيم النظرية للهبوط قد تم توليدها لانواع مختلفة من التبليط باستخدام برنامج Mich-Pave .بينما تم استخدام برنامج Mick-Back للحساب العكسي لقيمة المعاملات (Stiffness) حسب مقدار الهبوط النظري التي تم ذكرة.

لتقدير مقدار تاثير التغييرات في قيم معاملات التبليط المرن على السمك للطبقات ونسبة بواسان ومقدار الحمل الخاص بجهاز (FWD)وكذلك الهبوط فقد تم استخدام طريقة (Monte Carlo) لتمثيل هذة التاثيرات.

لقد اوضحت النتائج بانة الحساب العكسي للمعاملات الخاصة بطبقات التبليط تتاثر بشكل كبير بالمتغيرات الخاصة بالتبليط.وقد اظهرت نتائج التحليل الحساس (Sensitivity Analysis) بانة سمك طبقات التبليط هو العامل الرئيسي الموثر في التغييرات الحاصلة بالحسابات العكسية للمعاملات.

KEY WORDS:
Flexible pavement Parameters, Backcalculation Moduli, Mich-pave, Mich-back, Sensitivity Analysis, and Monte Carlo Simulation.

INTRODUCTION

Back-calculation is a process for estimating the elastic layer modulus in pavement structures that represent in situ conditions under a test load. Back-calculation gets its name from the fact that a load of known size and shape is applied to the pavement and deflections are measured by sensors at known distances from the load. Theoretical predictions are made of the deflections, assuming certain layer properties, and those properties (usually elastic layer modulus) are adjusted until the calculated deflections match the measured deflections within a reasonable error (goodness-of-fit between the measured and calculated deflection basins).

The falling weight Deflectometer (FWD) devise is strongly recommended to use throughout the world to determine the stiffness profiles of existing pavements. Surface deflections created by dropping a weight on the pavement are measured by seven sensor of the device. These deflections are then used to backcalculate the modulus of layer within a multi-layer pavement system. Form a pavement management point of view, understanding and quantifying how the uncertainties in the pavement parameters affect the backcalculated Moduli are very important. The design of a new pavement system or an overlay, and the calculated Moduli.

If the results of the Moduli are overestimated, thinner pavement layers will be design. Resulting in a lower life expectancy. The initial construction cost would decrease but the maintenance cost would increase or a complete rehabilitation would be necessary sooner than desired. Conversely, if the moduli are underestimated, thicker pavement layer would be designed.
This would increase the life expectancy of the pavement and at the same time; increase the cost of construction.
At least three major sources of uncertainty contribute to inaccuracies in the back calculated moduli. These uncertribute are associated with: 1) error in measured parameters (deflection and impact load).2) simplification and assumption used in backcalculation process and (3) random deviations of pavement Parameters form those assumed or specified.
Several investigators (Hudson et al., 1986 and Bentsen et al., 1989) have attempted to quantify the uncertainties in measured parameters. Their result shows that deflection and load are know within an accuracy of 2 to 5 percent.
The uncertainties associated with the model depend on the algorithm used and the nature of the pavement structure (Lytton.1989).These uncertainties can be determine by calibrating results cases or form past experience.
In this study the influence of random deviation in layer thickness, Poisson's ratio, FWD load and deflection on the backcalculates moduli are determined. Layer thickness usually deviate form those specified in the construction plans. Poisson's ratios vary due to variation in material consistency and compaction method. The impact load and deflection are known to be affected by measurement error. To assess the influence of the uncertainty of these parameters on back calculated moduli, Monte Carlo simulation technique was formulated and applied to three selected (three-layered) pavement. These are designated as P1, P2, and P3 their sections are shown in Fig's (1a, 1b and 1c respectively).The deflection basins associated with each determine using program Mich-Pave.
The procedure followed to quantify uncertainties the moduli for the pavement sections consisted of: (1) layer thickness of the AC and base layer Poisson's ratio of the AC, base and sub grade layers, the FWD load and the measured deflection were assumed to be random variable, (2) a Monte Carlo simulation technique was utilized to generate several sets if values of these variables for each pavement section, (3) each set was input into program Mich-back to backcalculate the modulus of each layer, and (4) the resulting samples of moduli were then statistically analyzed to determine the influence of the random variable on the predicated moduli. Details of the methodology utilized are discussed next.

METHODOLOGY

Pavement models

Three selected flexible (three-layer) pavement systems were studied. These pavement systems are shown in Fig.1. The thickness of the top layer was 3.0 in. or 5.0 in. Thinner layer were not considered because of the limitations with the backcalculation process used. The thickness of the second layer, which is either 6.0 in. or 12.0 in., is representative of the thickness of base layer usually used. The last was considered 240 in. as recommended by Bush (1980). The thinnest pavement structure Fig. (1a) corresponds to a low-volume road and the thickest one Fig. (1c) represent a major highway.

The actual Moduli and Poisson's ratios for each layer were kept constant in all pavement systems .The modulus of the AC, base and sub grade were assumed to be 450, 35, and 10 Ksi, respectively. These values are poisons ratios were assumed to be equal to 0.35, 0.40, and 0.45 for the AC, base and sub grade, respectively.

Determination of Deflection Basins

To eliminate the effects of the site relates and device related parameters on the back calculated moduli, it was necessary to determine the deflection basins theoretically .To obtain these deflection program Mich-Pave (Harichandran, and Baladi, 1993) was used. Deflection from program Mich-Pave was considered to be the representative field measurements.

ASPHALT T1=3in E1=450000psi V1=0.35	ASPHALT T1=3in E1=450000psi V1=0.35	ASPHALT T1=5in. E1=450000psi V1=0.35
BASE T2=6in E2=35000psi V2=0.40	BASE T2=12in E2=35000psi V2=0.40	BASE T2=12in. E2=35000psi V2=0.40
SUBAGRADE T3=240in E3=10000psi V3=0.45	SUBGRADE T3=240in. E3=10000psi V3=0.45	SUBGRADE T3=240in E3=10000psi V3=0.45
1a	1b	1c

Fig. (1) Pavement sections.

The deflection basin for each pavement section studied comprises of seven deflections at 12 in. intervals. A9000-1b load was used as the FWD load input. As Mich-pave is based upon linear-

elastic theory, selection of such a value would not affect the generality of the results presented in this research.

Backcalculation process

Program Mich-back (Harichandran, R. S. et, 1995) was used to backcalcuted the modulus of each layer. The required input pavement parameters to the program are: the thickness, Poisson's ratio, and resilient modulus for each layer. In addition, minimum and maximum acceptable moduli have to be defined. These values were assumed as 0.1 and 10 time that of the actual modulus, respectively. This insures that the only criterion for back calculating moduli was the closeness of the theoretical and the actual deflection.

Statistical simulation .

To compute the variability of the estimated back calculated Moduli, a Monte Carol simulation approach was used (Ang. and Tang, 1984) .In general, the method consists of: (1) numerically drawing a number of sets of observation of the input variable used by Mich-back using the statistical distribution of each variable ;(2) evaluating the random samples of backcalculated Moduli; (3) using these sample, statistical parameters and distributions of the Backcalculated Moduli were determined. A flow diagram of this process is shown in Fig.2.

For the simulation of the input parameters, the mean value of the layer thickness and Poisson's ratio were taken as those specified and given in Fig. (1). The mean value of the FWD load was assumed to be 9000-1b and mean values of the deflection were assumed to be these obtained for program Mich-Pave.

Coefficients of variation of 0.2 and 0.1 were assumed for the thickness of the layer and Poisson's ratio, respectively. These values were considered to reflect the uncertainty associated with the determination of these pavement parameters in practice. However, further work is required to validate this assumption. A Coefficient of variation of 0.05 was set of the FWD load and 0.02 for the deflection value, as previously discussed in the introduction.

All variables were tested to be independent and to follow a normal distribution. However, the distributions for the Poisson's ratios were truncated at a lower bound of 0.15 and an upper bound of 0.45. This account for the practical impossibility of having pavement materials with Poisson's ratio outside of these bounds.

Sample size.

The results of the Monte Carlo simulation are influenced by the size of the sample. In general, the larger the sample the highly accuracy is obtained.

In order to determine the sample size for this study, several calibration runs were performed using sample of 10, 50, 100, 500, and 1000. For these calibration runs only the thickness of layer 1 and 2 were considered to be random variables with mean values of 5 in. and 12 in. respectively.

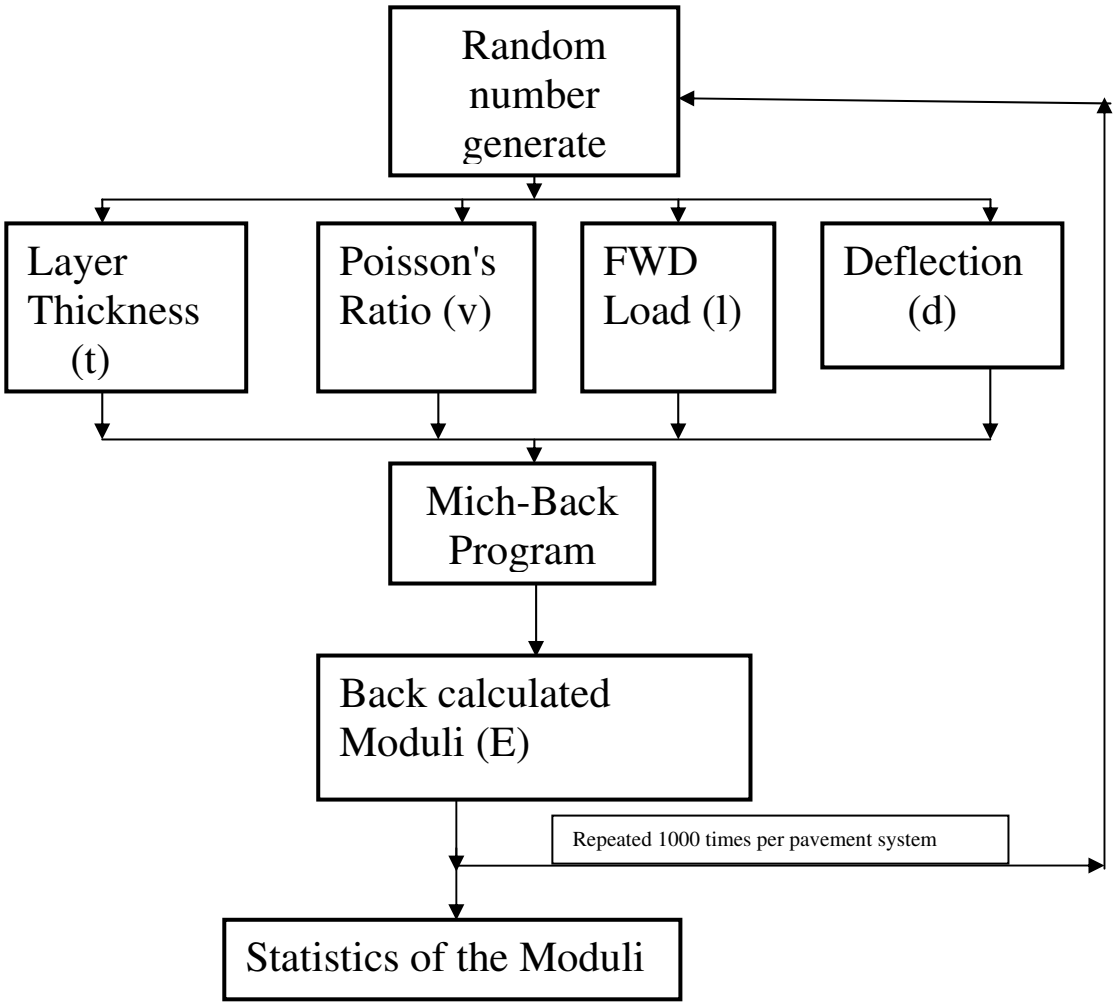

Fig. (2)- Statistical simulation of Backcalculated Moduli.

Table 1- Influence of sample size.

Number of simulations	Mean E1 (ksi)	Std. Dev.E1 (ksi)	Mean E2 (ksi)	Std. Dev.E2 (ksi)	Mean E3 (ksi)	Std. Dev.E3 (ksi)
10	766	1154	24.4	5.3	10.6	0.1
50	680	654	25.5	7.8	10.6	0.1
100	595	394	24.9	7.1	10.6	0.1
500	612	384	25.4	7.8	10.6	0.1
1000	605	406	26.1	8.9	10.6	0.1

A coefficient of variation of 0.1 was assumed for both variables. All other variables were assumed known as given in Fig.1. Results of the calibration runs are shown in Table 1. This table shows the computed means and standard deviation of the backcalculated moduli for each sample size.
The relative error between the results of the 100 and the 1000 simulations are small enough to suggest that the approximation optioned with a minimum sample size of 100 values provides degree of accuracy on the statistical parameters estimated.

RESULTS AND DISCUSSION

Combined Random Variables.

The Monte Carlo simulation was performed for all pavement sections shown in Fig. 1 considering all parameters, (thickness of AC and base, Poisson's ratio of AC, Base and sub grade, load and deflection) to be random variables. These results are shown in Tables 2 though 4 in the row entitled "All Variables" In all three pavement sections, the variability induced by the combined random variables on the back calculated moduli of layer 1 and 2 (i.e. the AC layer and base layer) is much greater than that for the backcalculated moduli of the sub grade. The computed coefficients of variation of the moduli for layer 1 and 2 ranged from 0.8 to 1.4. While the computed coefficients of variation for the moduli of layer 3 were either 0.06 or 0.07. These results indicate that the variability of the pavement parameters do not significantly influence the backcalculated Moduli of the sub grade.

The coefficient variation for the AC layer moduli in pavement sections P1 (3"AC layer thickness) and P2 (3"AC layer and 12" base layer) are similar, 1.08 and 1.15, respectively However, a greater difference exists between the coefficient of variation of the base layer moduli for the pavement section P1 and that of P2 (0.81). Similar results are obtained when comparing pavement section P3 (5"AC layer and 12" base layer).These results indicate that the variability of backcalculated Moduli in thinner pavement structure is more sensitive to the variability of the pavement parameters than those of thicker pavement structures. It is also evident form the results in Table 2 through 4 that the variability in the moduli are much larger for section P1 , a secondary road design, than for section P3, an interstate highway design. The larger variabilities associated with thinner pavement section might be due to existing limitation of Mich-Back in estimating the backcalculated Moduli.

The variation of variables of the backcalculated Moduli of each pavement section and each pavement layer are show in Fig. 3 through 5. The variation distribution of variables of backcalculated moduli are plotted against the normalized moduli. A normalized modulus of 1.0 represents the design or mean value of each layer.

It should be noted that the y-axis scale of the graphs are different for the normalized modulus of layer 3 than for the other two layers.

Sensitivity Analysis. In order to identify the influence that each variable has on the backcalculated Moduli, a stochastic sensitivity analysis was performed. This was accomplished by keeping all input variable, except one. Constant at their mean values as in Fig.1 the remaining parameter was considered to be random variable on which the Monte Carlo simulation was performed 100 times. The only exception to one variable being considered random at a time was the effect variations in the measured parameters were determined.

The FWD load, with a mean of 9000-lb, and the 7 deflection values, with means generated by Mich-Pave were randomly simulated at the same time. The variation of each variables plots of the back calculated Moduli generated for each case are shown in Fig.'s 3 through 5. Also, to facilitate the comparison of results. The coefficients of variation are summarized in Tables 2 through 4. A large coefficient of variation indicates that variability in the parameter has a major influence on the variability of the calculated moduli. Conversely, small coefficients of variation suggest that the variability of the moduli is insensitive to the given parameter.

Individual Random Variables; In all three pavement sections, the variability of the Poisson's ratio of the AC and base layers (v1 and v2) had very little effect on the backcalculated Moduli of all three layers. The small variability in the moduli is shown in the figures by variation of each variables plot. Then results also show that the Modulus of layer 3, in all three pavement, is not significantly influenced by any the variability of any of the input variables.

Table 2-Coefficient of variation.
Pavement section P1

Variable(s)	E1	E2	E3
V1	0.0273	0.0073	0.0000
V2	0.0082	0.0196	0.0022
V3	0.5094	0.3221	0.0483
T1	0.9193	0.1380	0.0022
T2	0.4656	0.8663	0.0066
L &d	0.3511	0.3402	0.0493
All variables	1.0840	1.3163	0.0727

Table 3-Coefficient of Variation.
Pavement section P2

Variable(s)	E1	E2	E3
V1	0.0333	0.0024	0.0003
V2	0.0084	0.0165	0.0036
V3	0.1856	0.1041	0.0361
T1	0.9672	0.0483	0.0023
T2	0.8521	0.7853	0.0023
L &d	0.2387	0.0862	0.0491
All variables	1.1464	1.8082	0.0661

Table 4-Coefficient of Variation
Pavement section P3

Variable(s)	E1	E2	E3
V1	0.0240	0.0186	0.0002
V2	0.0091	0.0343	0.0021
V3	0.2151	0.4185	0.0410
T1	0.8647	0.3273	0.0035
T2	0.1262	0.8813	0.0023
L &d	0.2503	0.3038	0.0551
All variables	0.9382	1.3706	0.0716

The remaining individual parameter influence the modulus of the AC layer and the base layer differently depending on the pavement section considered .In general the variability of the moduli for the first two layer of each pavement is greatly influenced by the uncertainty in the thickness of the layers. This result agrees with engineering intuition. For all pavement section, the variability in the measured deflection and load also has an important influence on the variability of the moduli. For thinner pavement this importance is large than for thicker ones. This highlights the necessity of improving the accuracy in measuring the thickness of the layer and in determining the deflection.
An interesting result is the large influence that Poisson's ratio of the sub grade layer has on the variability of the moduli when compared with the influence of the variability of the moduli when compared with the influence of the Poisson's ratio of the layers. A possible explanation is that the mass of the sub grade is much grate than that of the other two layers and therefore its properties dominate the measured deflection basin. This is confirmed by the fact that the influence of this variable is larger for thinner pavement than thicker.

Conclusions

A Monte Carlo simulation approach has been proposed to study the influence of random deviations in the parameter that define a pavement structure on the backcalculated Moduli. Results are shown in terms of coefficients of variation and distribution of moduli. The results show that the sub-grade modulus is not significantly influenced by the variability of any of the parameters. The moduli of the first two layers of thinner structures are more influenced by the variability of the pavement parameters. The parameters with major influence on the variability of the AC layer and the base are: the thickness of the AC and base layer, the Poisson's ratio of the sub grade and the combined effects of the measured FWD load and deflection basin.

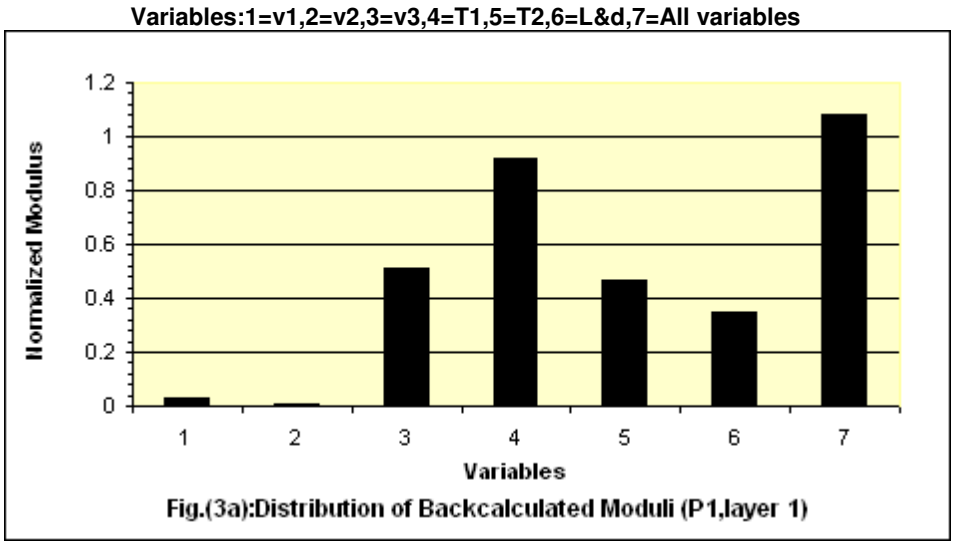

Fig.(3a):Distribution of Backcalculated Moduli (P1,layer 1)

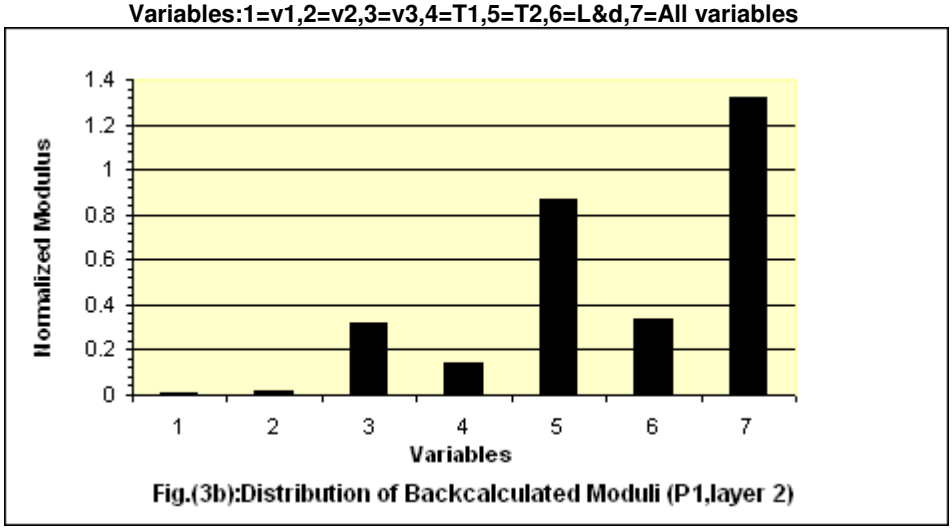

Fig.(3b):Distribution of Backcalculated Moduli (P1,layer 2)

Variables:1=v1,2=v2,3=v3,4=T1,5=T2,6=L&d,7=All variables

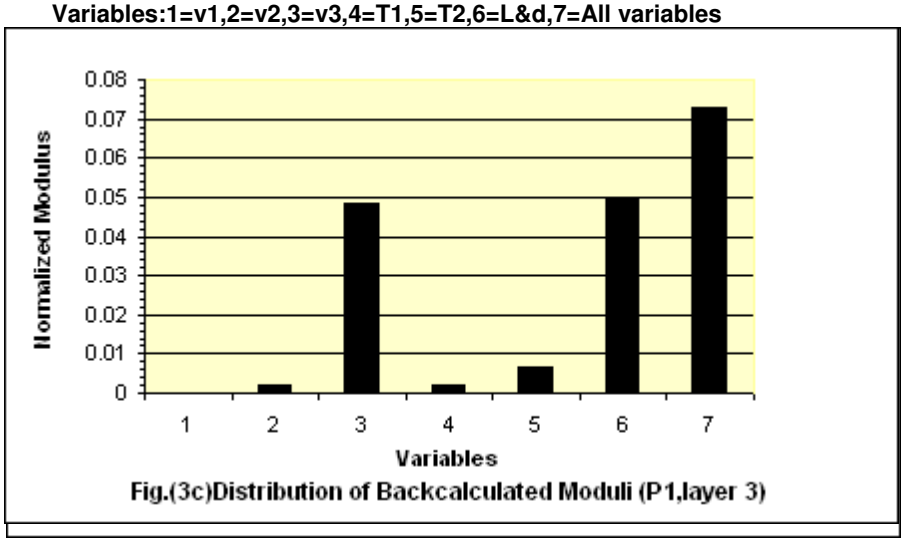

Fig.(3c)Distribution of Backcalculated Moduli (P1,layer 3)

Variables:1=v1,2=v2,3=v3,4=T1,5=T2,6=L&d,7=All variables

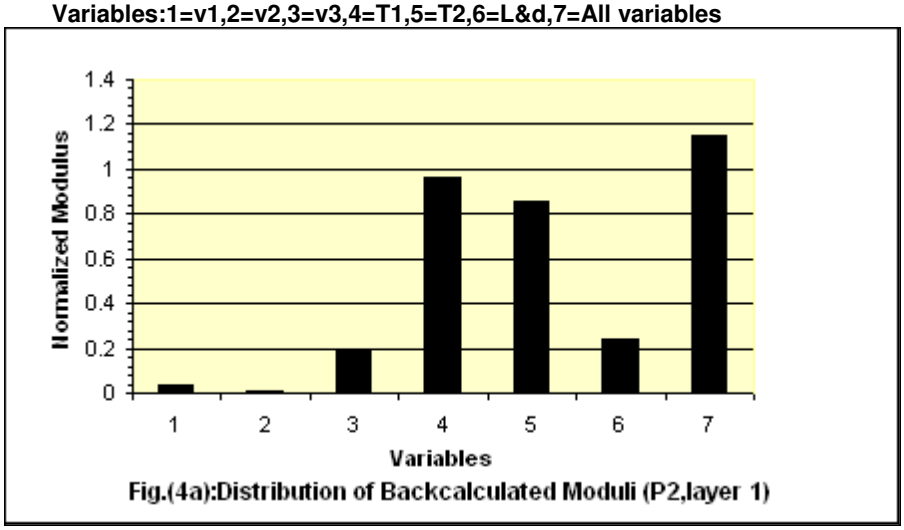

Fig.(4a):Distribution of Backcalculated Moduli (P2,layer 1)

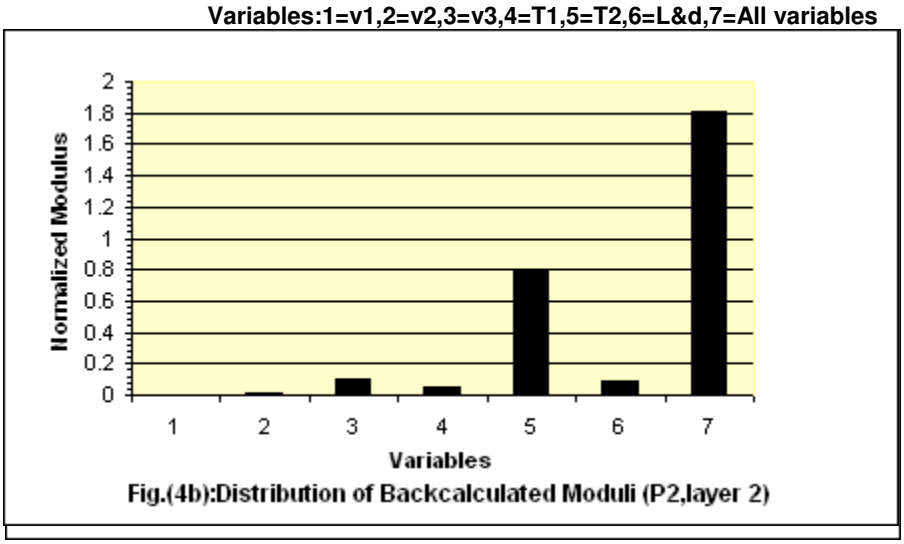

Fig.(4b):Distribution of Backcalculated Moduli (P2,layer 2)

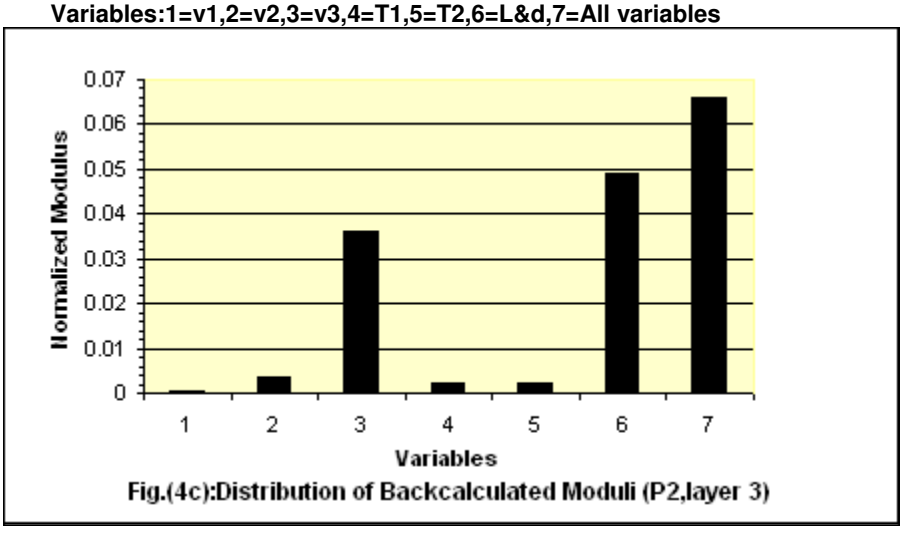

Fig.(4c):Distribution of Backcalculated Moduli (P2,layer 3)

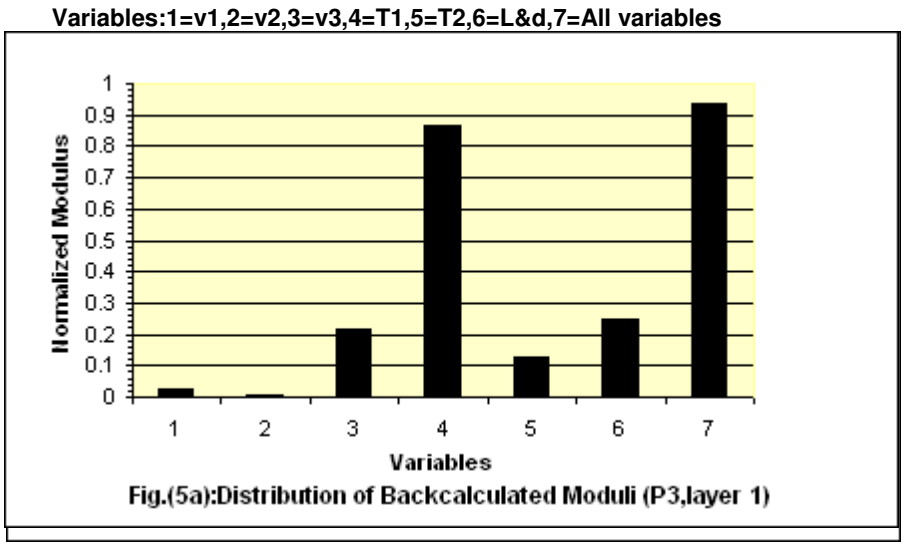

Fig.(5a):Distribution of Backcalculated Moduli (P3,layer 1)

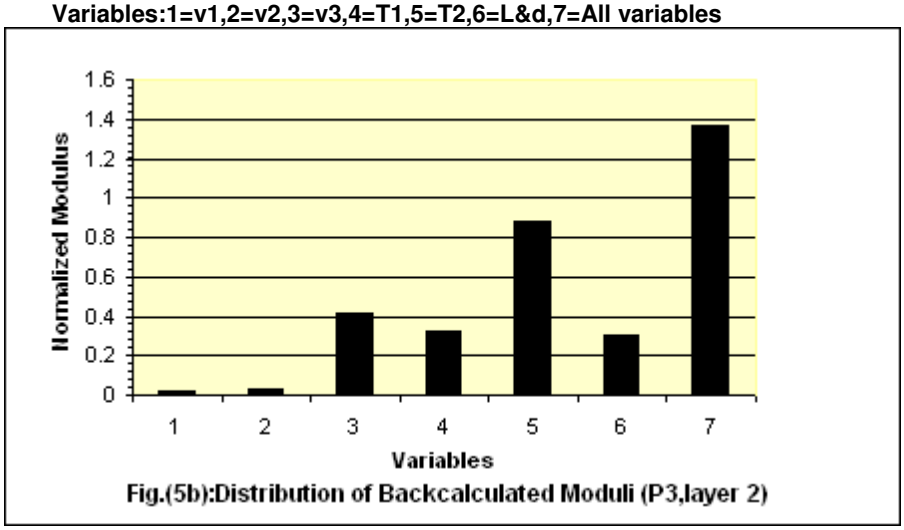

Fig.(5b):Distribution of Backcalculated Moduli (P3,layer 2)

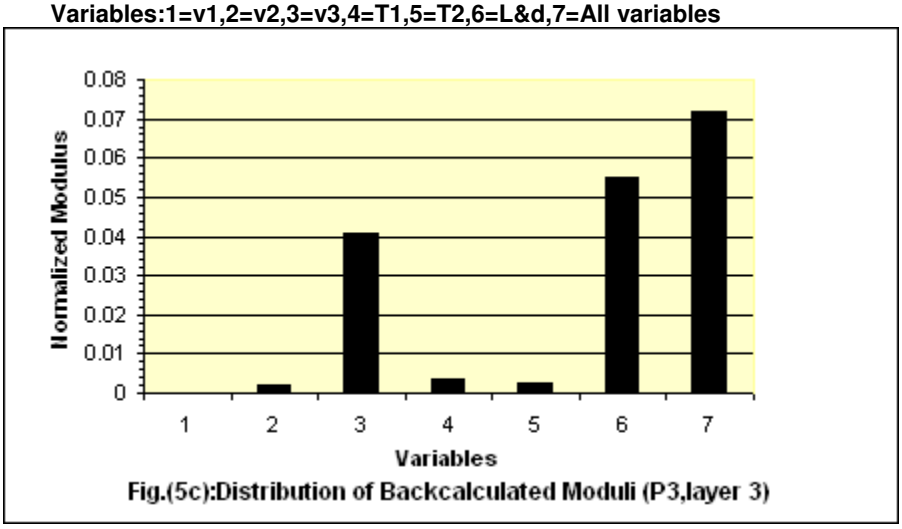

Fig.(5c):Distribution of Backcalculated Moduli (P3,layer 3)

References:

Ang, A.H, and Tang, W.H.,(1984)"Probability Concepts in Engineering Planning and Design,"Vol.2-Decision,Risk,and Reliability. John Wiley and Sons.

Bentsen, R.A., Nazarian, S., and Harrison, J.A., (1989)"Reliability Testing of Seven Nondestructive Pavement Testing Devices,"STP 1026, American Society for Testing and Material, Philadelphia, pp, 278-290.

Bush III, A.J., (1980)"Nondestructive Testing for Light Aircraft Pavements, Phase II: Development of the Nondestructive Evaluation Methodology" Report No.FAA-RD-80-9-II, FAA, Washington, D.C., November.

Harichandran, R. S. Baladi, G.Y., MICHPAVE *User's Manual*, Version 1.2 for DOS, Michigan State University, Lansing, MI, 1993.

Harichandran, R. S. et al, MICHBACK *User's Manual*, Version 1.0 for DOS, Michigan State University, Lansing, MI, 1995.

Hudson, W.R., Elkins,G.E., Uddin, W.,and Reilley.K.T.,(1986)"Pavement Condition Monitoring Methods and Equipment," Report No.FH67/1 ARE Inc.,Austin,TX,P.113.

Lytton, R.L.,(1989)"Backcalculation of Pavement Layer Properties," STP 1026,American Society for Testing and Materials,Philadelphia,pp.7-38.

بعض العوامل المؤثرة على نتائج فحص سرعة الذبذبات فوق الصوتية للخرسانة عالية المقاومة

م.ندى مهدي فوزي
كلية الهندسة–جامعة بغداد

م.أميد ادول علي
الشركة العامة للمشاريع الكهربائية

الخلاصة

تتميز الخرسانة عالية المقاومة بمقاومتها العالية ومساميتها القليلة وأدائها الجيد في الظروف التعرضية القاسية ويتضمن البحث دراسة أهم العوامل المؤثرة على قياس سرعة الذبذبات فوق الصوتية بالاعتماد على تجارب أجريت لنماذج على شكل مكعبات خرسانية عالية المقاومة. وهناك عدة عوامل تؤثر على نتائج الفحص أهمها نسبة الماء الى السمنت ونوع الركام ومستوى تردد المجسات وأبعاد النموذج وطول المسار.

وقد تم إيجاد معادلة تجريبية بين مقاومة الانضغاط وسرعة الذبذبات فوق الصوتية وبالطريقة المباشرة. ويمكن الاستفادة من هذه العلاقة في تخمين مقاومة الخرسانة عالية المقاومة والتي لا تنطبق عليها المعادلات التجريبية السابقة. ويمكن استخدام هذه الطريقة في معامل الصب الجاهز وغيرها والتي تنتج الخرسانة عالية المقاومة لغرض استعمالها في الجسور والعوارض ذات الأحمال العالية..

SOME FACTORS AFFECTING THE ULTRASONIC PULSE VELOSITY TEST RESULTS OF HIGH STRENGTH CONCRETE

Nada Mahdi Fawzi
College of Eng. – Univ. of Baghdad

A. A. Ali
General Company of Electrical Projects.

ABSTRACT

The high strength concrete is characterized by its high strength, low porosity and good performance under aggressive environmental conditions.

The paper presents some factors affecting the Ultrasonic Pulse Velocity test results for high strength concrete such as water/ cement ratio, type of aggregate, frequency level of transducers, dimension of the specimens and path length.

An experimental equation has been derived for the prediction of compressive strength of high strength concrete from pulse velocity, which can be used for the estimation of strength.

It provides more reliable prediction and can be used in precast concrete factories manufacturing precast concrete girders for bridges.

المقدمة:

تمهيد

تتميز الخرسانة عالية المقاومة بمقاومتها العالية التي تكون عادة أكثر من 41 ميكاباسكال كحد أدنى. وقد أدى تحسين نوعية السمنت من حيث النعومة، درجة الحرق والمواد المضافة الى إنتاج أنواع جديدة من الخرسانة تصل مقاومتها إلى أكثر من 140 نت/ملم2 (ACI 363R-97) وفي الآونة الأخيرة ازدادت استخدامات هذا النوع من الخرسانة عالميا ومحليا, وفي بغداد تم إنشاء جسر ذو الطابقين باستخدام خرسانة تتراوح مقاومتها ما بين(48–63)نت/ملم2 (د.زين العابدين رؤوف 1993).

تستخدم الخرسانة عالية المقاومة عادة في العوارض الخرسانية المسبقة الإجهاد في الجسور وكذلك في الركائز مسبقة الصب والتي تتطلب مقاومة عالية أثناء الدق لكي لا تتعرض إلى الكسر أو التثلم. وتحتاج ضبط الجودة في هذه المعامل إلى طرق سريعة وكفوءة لتقدير مقاومة الأنضغاط وفي عمر مبكر.

أن طريقة سرعة الذبذبات فوق الصوتية التي أشيع استعمالها في العالم وفي العراق تعتبر إحدى هذه الطرق. وهناك عوامل عديدة تؤثر على قياس سرعة الذبذبات منها أبعاد النموذج وطول مسار الموجة ونسبة الرطوبة وغيرها. أن المعادلات المستخدمة حاليا مبنية على تجارب أجريت على الخرسانة الاعتيادية التي تتراوح مقاومتها ما بين 20–35 ميكاباسكال لنوعية ركام متواجد في وسط العراق أي بغداد وضواحيها فلذا لا يمكن استخدامها في تخمين المقاومة للخرسانة عالية المقاومة أو عند استخدام ركام آخر ذات نوعية تختلف عن ركام منطقة النباعي أو مقالع الصدور على سبيل المثال، الركام الكلسي الموجود في الصحراء الغربية.

ويتضمن هذا البحث تجارب مختبرية اجريت من أجل تخمين مدى تأثير نسبة الماء الى السمنت وشكل النماذج وطول المسار على نتائج فحص مكعبات خرسانية ذات مقاومة عالية. ويمكن الاستفادة من هذه النتائج في تخمين مقاومة الانضغاط في معامل الصب الجاهز للخرسانة عالية المقاومة.

طريقة توليد الذبذبات فوق الصوتية

تتولد الذبذبات فوق الصوتية من عملية إثارة الاهتزازات الطبيعية لبلورات بعض المواد كالكوارتز وملح روشل Rochelle وتيتانات الباريوم BaTIO2 وتسمى الأجهزة التي يتم بواسطتها توليد واستلام وتحويل الطاقة الكهربائية إلى طاقة اهتزازية فوق صوتية بمجسات التذبذب ويتراوح تردد المذبذبات المستخدمة لفحص الخرسانة بين (20 - 250) كيلوهرتز.

التطبيقات العملية للذبذبات فوق الصوتية

إن فكرة استخدام الذبذبات فوق السمعية في فحص الخرسانة هي إمكانية إيجاد علاقة بين سرعة الذبذبات وخواص الخرسانة كمقاومة الانضغاط أو معامل المرونة وغيرها.

ويمكن الاستدلال من سرعة الذبذبات على مدى تجانس الكتلة الخرسانية ويمكن تلخيص أهم التطبيقات العملية للذبذبات فوق الصوتية كما يلي:

1- فحص مدى تجانس الكتلة الخرسانية في المنشأ.

2- الكشف عن أماكن التشققات والفجوات الكبيرة وتحديدها.

3- متابعة التغيرات التي تحدث في الخرسانة وبمرور الزمن أو بفعل العوامل المؤثرة الأخرى.

4- إيجاد معامل المرونة الديناميكي (Ed).

5- إيجاد نسبة بواسن الديناميكية (α).

6- إيجاد مقاومة انضغاط الخرسانة بصورة غير مباشرة وعلى أساس العلاقات التجريبية.

7- إيجاد الخواص الديناميكية للصفائح القشرية الخرسانية.

8- إيجاد سمك التبليط الخرساني دون الحاجة إلى أخذ لباب الخرسانة.

العلاقة بين سرعة الذبذبات ومقاومة الانضغاط

وضعJones(Jones,R.1962) حدوداً عامة لسرعة الذبذبات لأنواع مختلفة من الخرسانة يمكن الاستفادة منها عند المقارنة وكما في **الجدول (1)** أدناه:

جدول (1) يبين الحدود العامة لسرعة الذبذبات لأنواع مختلفة من الخرسانة

نوعية الخرسانة	السرعة كم/ثانية
ممتازة	أكثر من 4.58
جيدة	4,57 - 3.66
مقبولة	3,66 - 3.05
ضعيفة	3,05 - 2.14
ضعيفة جداً	أقل من 2.14

كما ويمكن ايجاد علاقات بين سرعة الذبذبات ومقاومة الخرسانة موقعيا بالاعتماد على فحص لباب الخرسانة (Core Test).

وفي سنة 1986 قدم رؤوف وآخرون(فريدة يونس، زين العابدين رؤوف1986)علاقة بين سرعة الذبذبات ومقاومة الانضغاط بموجب معادلة تجريبية اعتمدت على أكثر من (800) نتيجة فحص إلا أن النتائج المعتمدة كانت محصورة ما بين مقاومة إنضغاط

(20ميكاباسكال الى35ميكاباسكال). وعند تطبيق هذه المعادلة للخرسانة عالية المقاومة يلاحظ بأن المقاومة المخمنة تكون قليلة مقارنة بالمقاومة الواقعية لمكعبات السيطرة النوعية.

وليس من السهل تحديد معادلة يمكن تطبيقها لمختلف أنواع الخرسانة المصنوعة من مختلف المواد الأولية من سمنت وركام (خشن وناعم) بل لكل معادلة تجريبية محدداتها الخاصة ومن الضروري تطبيقها ضمن هذه المحددات.

بعض العوامل المؤثرة على فحص سرعة الذبذبات فوق الصوتية

لغرض تحديد سرعة الذبذبات فوق الصوتية بشكل دقيق من الضروري الألمام بالعوامل التي تؤثر على قياس السرعة خلال الخرسانة وأن العلاقة بين مقاومة انضغاط الخرسانة وسرعة الذبذبات تعتمد الى درجة كبيرة على دقة قياس سرعة الذبذبات وفيما يلي بعض العوامل التي تؤثر على دقة قياس السرعة.

رطوبة سطح النموذج

تزداد سرعة الذبذبات عندما يكون سطح النموذج رطبا وتكون قراءات السرعة متجانسة بسبب سهولة انتقال الصوت خلال مسار الموجة وعدم ضياع الطاقة الصوتية خلال التشققات الشعرية في الخرسانة فلذا يفضل ترطيب أسطح النماذج أو الأجزاء الإنشائية قبل فحصها بفترة وجيزة.

المسامية

تقل سرعة الذبذبات كلما زادت نسبة الماء الى السمنت وفي حالة الخرسانة عالية المقاومة تكون نسبة الماء الى السمنت أقل من 0.4 عادة فلذا تكون تأثير المسامية قليلة مقارنة بالخرسانة التقليدية وخاصة عند استخدام مضافات معدنية دقيقة التجزئة مثل غبار السليكا(فراس فاضل 2001) أو ركام الخبث المنعم وغيرها من المواد. ويبين الشكل (1)العلاقة التجريبية بين المسامية الظاهرية وسرعة الذبذبات فوق الصوتية.

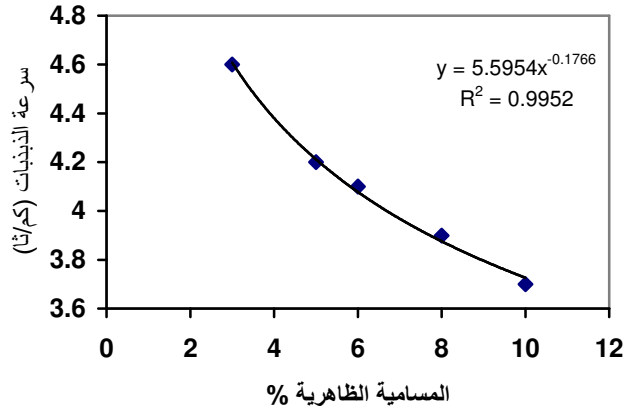

لشكل (1) العلاقة بين المسامية وسرعة الذبذبات

طول المسار

أقترح جونس وفيكارو (Jones,R, Facaoaru 1969) بأن لا تقل طول مسار الموجة عن 100 ملم للركام عندما يكون مقاسه الأقصى أقل من 30 ملم وفي حالة الخرسانة عالية المقاومة حيث المقاس الأقصى يكون أقل من 20 ملم عادة فتكون مكعبات 100 ملم مناسبة لغرض الفحص.

طرق وضع المذبذبات

طريقة الانتقال المباشر

كما في **الشكل (2)** إن تركيب المذبذبين بهذا الشكل يؤمن انتقال أكبر كمية من الطاقة الصوتية إلى النموذج بشكل مباشر حيث يتقابل المذبذب المرسل مع المذبذب المستقبل في الطرف الآخر من النموذج أو المنشأ

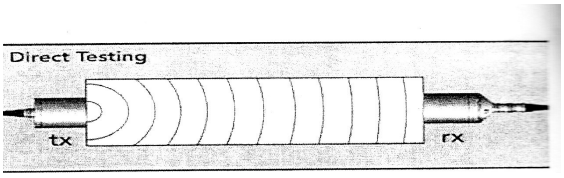

الشكل (2) طريقة الأنتقال المباشر

طريقة الانتقال غير المباشر

كما في **الشكل (3)** وهذه الطريقة تكون أقل دقة من طريقة الأنتقال المباشر ويكون موضع المذبذبين على نفس الجهة وبذلك يكون أنتقال الامواج على الطبقة السطحية وبطاقة اقل وغالبا ما تستخدم هذه الطريقة في فحص البلاطات.

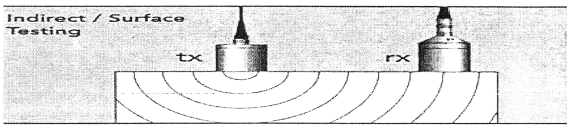

شكل (3) طريقة الانتقال غير المباشر

طريقة الانتقال شبه المباشر

كما في **الشكل (4)** حيث يكون موضع أحد المذبذبين على حافة الجزء المراد فحصه والآخر على السطح الأسفل المجاور وتستخدم هذه الطريقة غالباً لفحص الجسور التي يمكن فحصها بالطريقة المباشرة.

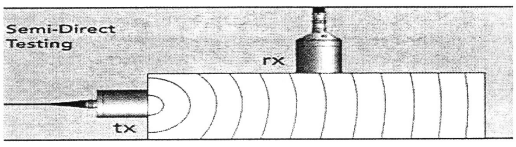

الشكل (4) الانتقال شبة المباشر

تطوير إنتاج البلاطات الخرسانية (الشتايكر)

أ. د. شاكر أحمد المشهداني
قسم هندسة البناء والانشاءات
الجامعة التكنولوجية

د. طارق صالح آل عطار
قسم هندسة البناء والانشاءات
الجامعة التكنولوجية

المهندس الاستشاري علاء مهدي الخطيب
قسم هندسة البناء والانشاءات
الجامعة التكنولوجية

الخلاصة:

تضمن البحث إجراء دراسه شامله لواقع حال وآفاق تطوير منتوج بلاطات التسطيح الخرسانيه (الشتايكر) الشائع ألإستخدام وألإنتاج في العراق. تَـبَـيَـنَ إن أغلب , إن لم يكن كل , المنتوج يفشل في تحقيق متطلبات المواصفه القياسية العراقيه 1107 لسنة 1988. تم إعداد نماذج تتضمن مكعبات وإسطوانات ومواشير ومن ثم قطع شتايكر لمحاكاة ألأساليب المتبعه محلياً وجرى فحصها لمعرفة مقاومتها للإنضغاط وألإنشطار وألإنثناء ومن ثم تحملها للحمل المستعرض وقياس قابليتها للإمتصاص , وقد إتضح من خلال الفحص بأنها دون المستوى القياسي المطلوب. من خلال معرفة قوة التحمل المستعرض المطلوبه تم حساب مقاومة ألإنثناء الدنيا المستهدفه ومن ثم جرى تصميم حلطه خرسانيه تُـلَـبي ذلك وقد أُطلق عليها إسم الخلطه الجديده. تم تكرار إعداد النماذج (التي بلغ مجموع عيناتها الكلي 60 عينه) ولكن بإستخدام الخلطه الجديده مع ألإهتمام بتدرج الركام وإسلوب المعالجه.أثبتت الفحوصات بإن نماذج الشتايكر تفوق متطلبات المواصفه.

رغم نجاح النماذج الجديده مختبرياً , لازال ألإعتقاد قائماً بوجود إمكانيه لفشل بعض النماذج عندما يستمر ألإنتاج النمطي وتضعف المراقبه والسيطره النوعيه, وعليه تم تجريب طريقه جديده لتعزيز بلاطات الخلطة الجديدة بمشبكات سلكيه. أدت هذه الطريقة الى زيادة قوة التحمل المستعرض بمقدار 21%.

كلمات رئيسية: بلاطات التسطيح, مقاومة الانضغاط, مقاومة الشد بالانشطار, مقاومة الانثناء, مشبك سلكي.

DEVELOPING OF CONCRETE TILES

Prof. Dr. Shakier A. Al-Mashhadani[1] Dr. Tariq S. Al-Attar[1] Cons. Eng. Alaa M. Al-Khateeb[1]

Abstract

A case study had been made to investigate the reasons of the repetitive failure during concrete tiles testing. Cubes, cylinders, and prisms in addition to full-scale concrete tiles had been prepared. Half of

these samples were made using the same popular concrete mix. Test results indicated that, these samples were below standard requirements. The second half of the test samples was prepared using a newly designed concrete mix. Based upon the recommended breaking load, the required flexural strength of the tiles was calculated. This mix was designed to comply a flexural strength that was recommended by specifications. Care had been also concentrated on aggregate grading and concrete curing. Tests showed positive results.
In spite of this success it is still believed that there is a possibility of some failures may be due to mass production or due to bad quality control. A new proposed model had been prepared and tested. Finally these newly proposed tiles had shown that it was more resistant to breaking loads by +21% in comparison with the previous samples. This result might insure the production of safe concrete tiles.

1: Building & Construction Engineering Department, University of Technology.

تطوير إنتاج البلاطات الخرسانية (الشتايكر)

المقدمة:

تنسجم فكرة هذا البحث التطبيقي مع التطلعات الخاصه بتطوير المواد ألإنشائيه عن طريق ألإستخدام ألأمثل للموارد وألإمكانيات المتاحه في القطر. لُوحِظَ بأن البلاطات الخرسانية (المستخدمة للتسطيح والمعروفة تجارياً بالشتايكر) المُنتَجَه في شركات القطاع العام ومعامل القطاع الخاص تُعاني بإستمرار من فشلها في الفحوصات المختبريه ولا تُلَبي متطلبات المواصفه القياسيه العراقيه المُعتَمَدَه (م ق ع 1107 – 1988). إن تَرَدي نوعية الشتايكر المُنتَج وإنخفاض جودته عن الحدود القياسيه المطلوبه يُعَرِضَه للتلف إثناء الخزن والمناقله ويكون سَهل الكَسر إثناء تنفيذه في موقعه النهائي. كل ذلك يُشَكل هدراً إقتصادياً كبيراً , خصوصاً إن هذا المنتوج شائع ألإستخدام في العراق.

من خلال التشخيص الدقيق للمشكله وبعد إجراء العديد من أللِقاءات مع المُنتِجين تأكَدَ لنا بأن هناك عدم عنايه في كافة خطوات سير العمليه ألإنتاجيه إبتداءاً من إنتقاء المواد ألأوليه وفحوصاتها وإنتهاءاً بإسلوب الخزن والمداوله. كل ذلك يؤدي إلى تَرَدي نوعية المنتوج وفشله في فحوصات السيطره النوعيه خصوصاً في فحص قوة التحمل المستَعرَض.

إن تحسين خواص منتوج الشتايكر من خلال تحسين خواص الخلطه الخرسانيه امر بديهي ، حيث ان زيادة محتوى الإسمنت او استخدام ركام خشن مكسر او مقاس اقصى للركام غير كبير وتخفيض نسبة الماء/الأسمنت وإستخدام المضافات والرص الجيد إثناء العمل والمعالجه المستمره ، سينعكس إيجابياً على كافة خواص الخرسانه المنتجه وبالتالي تأمين متطلبات المواصفات (Neville and Brooks – 1987 ,

Neville – 1995). إن سبب الإخفاق في هذا المجال بالنسبه للخرسانه المسبقة الصب قد اشار إليه أحد الباحثين حيث أكد على ضرورة توحيد الغايات والأهداف بين المصممين والعاملين في معامل الصب المسبق وخصوصاً أن فحوصات السيطره النوعيه في هذه المعامل تجرى على نماذج بمقاساتها الفعليه ويتم إختيارها بشكل عشوائي من أكداس متراكمه من المنتوج (Newman and Choa – 2003).

إن قلة مهارة العاملين وعدم إكتراثهم بالعديد من المتطلبات إثناء عملية الإنتاج يؤدي دائماً إلى إخفاقهم في الوصول إلى الهدف المنشود ألا وهو إنتاج شتايكر ذو مواصفاتٍ عاليه ، ويكون هذا أكثر وضوحاً في مقاومة الشتايكر للتحمل المستعرض بالرغم من التوصيات النظريه العديده في هذا المجال. لذلك فقد تم التركيز في هذا البحث على تحسين خواص منتوج الشتايكر من خلال تصميم خلطه خرسانيه مناسبه إضافةً إلى إقتراح إستخدام مشبكات سلكيه لضمان الحصول على شتايكر مقبول بالرغم من بعض هفوات العمال إثناء عملية الإنتاج والخزن والمناقله والتنفيذ في الموقع النهائي .

تشير بعض البحوث السابقه (Engel and Bakis – 2001 ,Netlon Ltd. – 1988 ,Shah and Key – 1972) إلى أن هناك إمكانيه لتحسين خواص البلاطات الخرسانيه المسبقة الصب وخاصةً مقاومتها للإنثناء والصدم من خلال إستخدام المشبكات سواء كانت من البوليمر أو الحديد او الياف أُخرى ، حيث أَنَ هذه المشبكات ستساهم في:

أ. تحسين متانة وديمومة البلاطات.

ب. تحسين الخواص الميكانيكيه العامه للبلاطات.

ج. زيادة قابلية البلاطات على إمتصاص الصدمات.

د. تقليل نسبة التلف إثناء المناقله أو الإرتطامات المُفاجئه.

ه. تقليل كمية التشققات الشعريه المُتوقع حدوثها إثناء الصب والمعالجه.

كما توصل باحثون آخرون (Brooks and Kenai – 1995 ,Mathews et al. – 1981,Shah and Key – 1972) إلى أن نوع المِشبَك وعدد الطبقات المستخدمه وشكل الفتحات وأبعادها يؤثر على سلوك البلاطات الخرسانيه المسبقة الصب من حيث المقاومه ودرجة التشقق ومسار التشققات وعرض وعمق التشقق وكيفية إنتشار وتشظي الضرر. ما يهمنا في هذا البحث هو إتخاذ إجراءات بسيطه وغير مكلفه لتلافي إخفاقات شائعه في منتوج الشتايكر العراقي ، وهذا ما سنتطرق له إثناء خطة البحث العمليه.

الجانب العملي:

المواد المستخدمه:

لجعل البحث قابل للتطبيق ، تم إستخدام نفس المواد المحليه الشائعة الإستخدام من قبل معامل إنتاج الشتايكر, الا أنه تم التأكيد على مطابقتها للمواصفات (وهذا ما لاتعتمده أغلب معامل إنتاج الشتايكر).

وعموماً تم إستخدام المواد التاليه :-

أ. الإسمنت: تم إستخدام الإسمنت البورتلاندي الإعتيادي المنتج في معمل إسمنت القائم ووجد بأنه مطابق للمواصفه العراقيه (م ق ع 5 – 1984).

ب. الركام الناعم : تم إستخدام الركام الناعم المُجَهَز من منطقة الأُخيضر وكان مطابق للمواصفه العراقيه (م ق ع 45 – 1980)، تدرجه ضمن المنطقه الثانيه (zone-2) ، ووزنه النوعي يبلغ 2.65 ، في حين بلغت نسبة الأملاح الكبريتيه 0.2 في المائة. وكان نظيفاً وخالياً من الشوائب العضويه.

ج- الركام الخشن :- تم إستخدام الحصى المكسر ، المُجَهَز من مقالع النباعي، ذو مقاس أقصى (14) ملم. وكان تدرجه مطابق للمواصفه العراقيه (م ق ع 45 – 1980)، ووزنه النوعي يبلغ 2.6 ، أما النسبة المئويه للأملاح الكبريتيه فتساوي 0.02 في المائة، وإن كثافته المرصوصة الجافة كانت بمقدار 1640 كغم/م^{3}. وكان نظيفاً وخالياً من الشوائب العضويه المنظوره.

د. الماء: تم إستخدام الماء الصالح للشرب لخلط ومعالجه الخرسانه في كافة أعمال البحث.

هـ. المشبك السلكي: تم إستخدام مشبك سلكي حديدي ذو فتحات سداسيه ذات مقاس 19ملم من النوع المنسوج، وكان قطر السلك المستخدم في هذا النسيج يبلغ 0.80 ملم ، وذو مقاومة شد قصوى مقدارها 275 نت/ ملم^{2} .

و. القوالب: تم إنتقاء قوالب غير متضرره ذات أبعاد قياسيه دقيقه لضمان إنتاج بلاطات بقياس (800×800× 42± 3) ملم. وروعي طلاء القوالب بالزيت لتسهيل عملية نزع الشتايكر بعد تصلبه منها.

الخلطات الخرسانية:

لضمان الحصول على خرسانه ذات مقاومه تؤدي إلى إكساب قطع الشتايكر قوة تحمل مستعرض أعلى من المطلوب في المواصفه العراقيه القياسيه رقم 1107 لسنة 1988 تم إعتماد الطريقه البريطانيه (Neville – 1995) لتصميم خلطه خرسانيه بحيث تؤمن مقاومة إنضغاط دنيا لاتقل عن 30 نت/ملم^{2} بعمر28 يوم ومقاومة إنثناء لاتقل عن 4 نت/ملم^{2} بعمر28 يوم . هذا بحد ذاته سيكون كافياً لزيادة الحمل المستعرض المطلوب لكسر قطعة الشتايكر إثناء الفحص عن القيمه القياسيه البالغه 5.4 كيلونيوتن حيث ان:

$$f_r = \frac{Mc}{I} \qquad (1)$$

أو:

$$f_r = \frac{\left(\frac{Pl}{4}\right)\left(\frac{h}{2}\right)}{\left(\frac{bh^3}{12}\right)} = 4N/mm^2$$

$$\therefore P = 5.4kN$$

بناءاً على ذلك وبعد إجراء خلطات تجريبيه موقعيه مُـصَـغَـرَه لمراعاة نوعية وظروف الركام المستعمل فعلياً في الخلط , وتصحيح النسب فقد كانت الخلطه الخرسانيه المقترحه ذات نسب خلط وزنيه بمقدار 1: 1.5 :2.85 ونسبة ماء/ إسمنت مقدارها 0.5 بذلك يكون محتوى الإسمنت المستخدم في هذه الخلطه يساوي 410 كغم/ م^3 (وهـذا أول جانب من الإخـتلاف بيـن التـصمـيم والواقع إذ أن المعامل لاتستعـمل هذه الكميات من الإسمنت لعوامل إقتصاديه معروفه لديهم). وقد تم تسمية هذه الخلطه بالخلطه الجديده M_{new}.

لإغراض المقارنه تم إستخدام نفس الخلطه الشائعه المستخدمه من قبل معامل إنتاج الشتايكر دون أي تدخل حيث كانت الخرسانه تُحضر بمقادير حجميه وقد تم تحويلها إلى نسبة خلط وزنيه تقريبيه تساوي 1 : 1.75 : 3.25 ونسبة ماء / أسمنت مقدارها 0.65 بذلك يكون محتوى الإسمنت المستخـدم في هذه الخلطه حوالي 360 كغم/ م^3 تقريباً. وكان غالبية الركام الخشـن المستعمل غـير مكسـر وبمقاس أقصى يبلغ 25 ملم تقريباً (على أي حال لم نلاحظ سيطره نوعيه معتمده على المواد الداخله في صناعة الخرسانه أصلاً). و تم تسمية هذه الخلطه بالخلطه القديمه M_{old}.

النماذج وفحوصاتها:

لغرض إستكمال جوانب البحث فقد تم تهيئة نماذج لإجراء فحوصات مرجعيه إضافةً إلى إنتاج نماذج شتايكر بالقياس الكامل ، و تم تحضير النماذج التاليه لإجراء الفحوصات المؤشره إزائها:

أ. مكعبات 150×150×150 ملم لفحص مقاومة الإنضغاط بعمر(7, 28, 60) يوم وبمعدل ثلاثة مكعبات لكل عمر.

ب. إسطوانات 150×300 ملم لفحص مقاومة الشد بالإنشطار بعمر (7, 28, 60) يوم وبمعدل ثلاثة إسطوانات لكل عمر.

ج. مواشيربأبعاد 100×100×500 ملم لفحص مقاومة الإنثناء بنفس الأعمار آنفة الذكر وبتسليط حملين مُـركَـزين يؤثران على نقاط تثليث الفضاء البالغ 450 ملم. وتم إعداد موشوران لكل عمر.

د. شتايكر بأبعاد { 800×800×3 ±42} ملم. لإجراء الفحوصات القياسيه بعمر 28 يوم. و تم إعداد ثلاثة عينات لكل نموذج.

هـ. شتايكر حاوي على مشبك سلكي موضوع بالطريقه الموضحه تفاصيلها في **الشكل(1)**. لإجراء الفحوصات القياسيه بعمر 28 يوم. و تم إعداد ثلاثة عينات لكل نموذج.

لإستكمال متطلبات المقارنه والإستنتاج الدقيق تم تهيئة كافة النماذج أعلاه بإستخدام الخلطه القديمه M_{old} وجرى تكرارها بإستعمال الخلطه الجديده M_{new}.

إعداد نماذج الشتايكر:

لإنتاج نماذج فحص الشتايكر بالقياس الكامل, وفق النسبه المصممه للخلط وبإستخدام نفس المواد ألأوليه والمكائن والمهارات المتيسره , تم إجراء ألآتي:-

أ. إستخدام الحصى المكسر الموجود موقعياً بعد غربلته بإستخدام غربال قياس 14ملم لإستبعاد الحصى ذو المقاسات الكبيره. أي بعباره أُخرى تم إستعمال حصى مكسر ذو مقاس إسمي أقصى مقداره (14) ملم. جرى غسل الحصى على أرضيه نظيفه لمنع إختلاطه بألأطيان. إن عملية الغسيل تزيل ذرات الغبار الملتصقه على سطوح حُبَيبات الحصى وتساعد على زيادة ترابطها مع المونه ألإسمنتيه. إن ترطيب الحصى بالماء قبل الخلط يجعله مُشَبَعاً بالماء فعندما يُخلَط مع بقية مكونات الخلطه الخرسانيه لايمتص أي كميه من الماء الضروري لتفاعل ألإسمنت, وإنما يُسهم في فرز الماء في اليوم ألأول من الصب بإتجاه المونه ألإسمنتيه بطريقه تشبه المعالجه الداخليه للخرسانه مما يزيد من ترابطها وبالتالي مقاومتها .

ب. تمت غربلة الرمل الموجود في الموقع بإستخدام غربال قياس 5 ملم على أرضيه نظيفه لتلافي إختلاطه بأتربه ألأرضيه. بذلك تم إستبعاد كُتَل الرمل المتوقع وجودها في الرمل , التي لاتتفتت خلال الخلط , والتي يُعتَقَد بأنها تُشَكِل نقاط ضعف في المنتوج النهائي.

ج. تم إختيار القوالب بأبعاد 800×800 ملم والتي لايقل إرتفاعها عن 40 ملم للحصول على السُمك القياسي المطلوب.

د. تم خلط الخرسانه وفقاً للنسبه التجريبيه الوزنيه التي جرى تصميمها والبالغه 1 : 1.5 : 2.85 مع نسبه ماء/ إسمنت بمقدار 0.5.

هـ. تم إستخدام الخلطه الجديده M_{new} لإنتاج نوعين من النماذج A و B . كل نموذج يتألف من ثلاثة عَينات بألقياس الكامل (800×800×42) ملم. النموذج ألأول A يُمَثِل الحاله ألإعتياديه بدون مشبك سلكي . أما النموذج B فَقَد جرى إنتاجه بإستخدام ألإسلوب المُبتَكَر التالي:

وُضِعَ خليط خرساني يُعادل ثلاثة أرباع الكميه المطلوبه لإنتاج قطعة شتايكر واحده في قالب الصب. بعد ألإهتزاز والتسويه أُوقِفَ الإهتزاز لوضع التَعزيز المؤلَف من قطعة نسيج سلكي مُشَبك مُرَبَعَه بأبعاد (50×50) سم , كما موضح في **الشكل (1)**, بطريقه تكون أضلاعها متعامده على أقطار قالب الصب . هذه الطريقه تضمن الحصول على أكبر مساحة تعزيز(تسليح) في المقاطع الوسطيه لقطعة الشتايكر بإستخدام أقل ما يمكن من المشبك السلكي. ثم أُضيفت الكميه المتبقيه من الخليط الخرساني البالغه حوالي ربع الكميه المطلوبه لإنتاج قطعة شتايكر واحده لتغطية المشبك السلكي بسُمك مقداره حوالي سنتمتر واحد . بعد ذلك جرى تسليط إهتزاز وعمل تسويه للسطح.

كما تم تكرار العمل ذاته بإستخدام الخلطه القديمه M_{old} لإنتاج نموذجين من الشتايكر. يتألف كل نموذج من ثلاثة عينات , هما النموذج C الإعتيادي ونموذج D الحاوي على مشبك سلكي.

تهيئة النماذج ومعالجتها:

تم إعتماد الآتي في تهيئة ومعالجة النماذج لغاية تاريخ الفحص:

أ. النماذج المرجعيه: تم معالجة العينات المرجعيه (المكعبات ، الأسطوانات، المواشير) بالماء حيث تم الخزن في أحواض ماء لغاية تاريخ الفحص.

ب. نماذج الشتايكر M_{new}: تمت معاملة النماذج وفق ألإسلوب التالي:

بعد مرور ساعتين من بدء الصب جرى ألإستمرار بالترطيب وذلك برش العينات بالماء لمدة 20 ساعه وهي داخل القوالب . بعد ذلك فُتِحَت القوالب وأُخرِجَت كافة العَينات وَوُضِعَت بصوره شبه عموديه. بَعدَ 10 ساعات من فَتح القوالب جَرى غَمرالعينات في حوض خرساني مملوء بالماء لمدة 27 يوماً , حيث أُخرِجَت قَبَل يوم واحد من تاريخ الفحص المختبري بعمر 28 يوم.

ج. نماذج الشتايكر M_{old}: تمت معاملة العينات وفقاً للطريقه الشائعه في المعامل العراقيه لغاية تاريخ الفحص.

النتائج ومناقشتها:

يوضح **الجدول (1)** معدل نتائج الفحوصات المرجعيه للخلطه الخرسانيه القديمه المعتمده من قبل المعامل M_{old} والخلطه الخرسانيه الجديده المقترحه إثناء البحث M_{new} . كما توضح **الاشكال (2, 3, 4)** مسار تطور المقاومات المختلفة مع الزمن.

بينما يوضح **الجدول (2)** نتائج فحوصات الشتايكر المنتج من الخلطتين وكذلك بإستخدام المشبكات السلكيه مع كل منهما. هذا ومن الجدير بالذكر بأنه تمت ألإستعانه بالمركز القومي للمختبرات ألإنشائيه لإجراء الفحوصات القياسيه لكافة نماذج الشتايكر.

تشير النتائج الموضحه في **الجدول (1)** إلى أن الخواص الميكانيكيه للخلطه الجديده M_{new} هي أعلى مما في الخلطه القديمه M_{old} , حيث إن نسبة الزياده في مقاومة ألإنضغاط بعمر 28 يوم تبلغ (45 %) , وإن نسبة الزياده في مقاومة الشد بألإنشطار تساوي (46 %) , وكذلك الحال بالنسبه إلى مقاومة ألإنثناء فقد كانت (3.30) نت/ملم^2 في الخلطه القديمه وأصبحت (5.11) نت/ملم^2 في الخلطه الجديده.

يتضح من **الشكل (2)** بأن هناك تطور جيد في مقاومة ألإنضغاط لكلا الخلطتين ، إلا أن معدل التطور في الخلطه M_{new} أفضل مما هو في الخلطه M_{old} ، ففي عمر 7 أيام كانت مقاومة ألإنضغاط للخلطتين M_{new} ، M_{old} هي (23.5) نت/ملم^2 و(16.8) نت/ملم^2 على التوالي. وقد إزدادت قيمتها بعمر 28 يوم إلى (38.4) نت/ملم^2 و(26.5) نت/ملم^2 ، وأصبحتا بعمر 60 يوم (45.9) نت/ملم^2 و(30.7) نت/ملم^2.

يوضح **الشكل (3)** معدل زيادة مقاومة الشد بالإنشطار مع الزمن للخلطتين ويتبين بأن المقاومة للخلطه M_{new} قد إزدادت بنسبة (53%) و(80%) بعمر 28 يوم و60 يوم على التوالي بالمقارنه مع المقاومه بعمر 7 أيام. في حين أن تلك الزياده قد كانت بنسبة (30%) و(48%) للخلطه M_{old}.

كذلك الحال بالنسبه لمقاومة الإنثناء وكما مبين في **الشكل (4)**. فقد إزدادت مقاومة الإنثناء للخلطه M_{new} بمقدار (1.36) نت/ملم^2 و(2.5) نت/ملم^2 بعمر 28 يوم و60 يوم على التوالي بالمقارنه مع المقاومه بعمر 7 أيام. في حين أن الخلطه M_{old} قد إزدادت مقاومتها للإنثناء بمقدار (0.93) نت/ملم^2 و(1.8) نت/ملم^2 بعمر 28 يوم و60 يوم على التوالي عند مقارنتها بمقاومة الإنثناء بعمر 7 أيام.

ومن الجدير بالذكر أن نسبة مقاومتي الشد بالإنشطار والإنثناء من مقاومة الإنضغاط هي الأُخرى قد تحسنت في الخلطه M_{new} بالمقارنه مع نتائج الخلطهM_{old}. إن نسبة مقاومة الشد بالإنشطارمن مقاومة الإنضغاط قد كانت (8.4%) في الخلطه M_{old} في حين (8.5%) في الخلطه M_{new} وبعمر 28 يوم. وأن نسبة مقاومة الإنثناء من مقاومة الإنضغاط قد كانت (12.5%) في الخلطه M_{old} وقد تحسنت إلى (13.3%) في الخلطه M_{new} وبعمر 28 يوم أيضاً.

إن تحسن جميع خواص الخلطه الخرسانيه المقترحه M_{new} بالمقارنه مع الخلطه الخرسانيه التقليديه M_{old} الشائعة الإستخدام في معامل إنتاج الشتايكر له أسباب عديده ومشخصه مسبقاً ولكن كان لابد لنا من إجراء الفحوصات لمعرفة النتائج بشكل دقيق. إن زيادة محتوى الإسمنت وتقليل نسبة الماء/الإسمنت وإختياراركام خشن مكسر ذو مقاس أقصى 14 ملم وإجراءات السيطره النوعيه على المواد الداخله في صناعة الخرسانه كل تلك العوامل قد ساهمت في تحسين خواص الخلطه الخرسانيه ، وكذلك أدت إلى زيادة نسبة مقاومتي الشد بالإنشطار والإنثناء كنسبه من مقاومة الإنضغاط وذلك لتحسن الترابط بين عجينة الإسمنت والركام الخشن في الخلطه الجديده.

كل ما ورد آنفاً من نتائج يشير إلى أن الشتايكر المنتج من الخلطه المقترحه الجديده M_{new} سيكون قطعاً أفضل بكثير من الشتايكر المنتج من الخلطه التقليديه القديمهM_{old} ، وهذا ما يبينه **الجدول (2)** حيث توضح النتائج بأن الشتايكر المنتج من الخلطه القديمه غير مطابق للمواصفات من ناحية المقاومه (الحمل المستعرض) والإمتصاص ، حيث كان معدل مقاومته للحمل المستعرض بمقدار (3.3) كيلو نيوتن ونسبة الإمتصاص (3.94 %) خلال 30 دقيقه و(7.90%) خلال 24 ساعه ،في حين أن تلك الخواص قد تحسنت في الشتايكر المنتج من الخلطه الجديده وأصبحت مقاومته للحمل المستعرض بمقدار (6.2) كيلونيوتن وبنسبة إمتصاص ذات معدل (3.10%) خلال 30 دقيقه و(4.20 %) خلال 24 ساعه.

إن إضافة المشبك السلكي بالطريقه التي تم ذكرها بالتفصيل في متن هذا البحث قد تدارك جزء من خلل الشتايكر المنتج من الخلطه القديمه حيث أصبح معدل مقاومة نماذج الشتايكر للحمل المستعرض بمقدار (4.40) كيلونيوتن أي إنها تحسنت بنسبة (33%) وإقتربت من الحد الأدنى المطلوب في المواصفه ، كذلك فقد تحسنت خواص الإمتصاص حين أصبحت ذات معدل (3.10%) خلال 30 دقيقه و(7.50 %) خلال 24 ساعه بدلاً من (3.94%) خلال 30 دقيقه و(7.90 %) خلال 24 ساعه.

أما إستخدام المشبك السلكي في إنتاج الشتايكر من الخلطه الجديده فقد حسن مرَةً أُخرى من المنتوج وأصبحت مقاومته للحمل المستعرض بمقدار (**7.5**) كيلونيوتن بدلاً من (6.2) كيلونيوتن ومعدل نسبة الإمتصاص (2.65%) خلال 30 دقيقه و(3.60%) خلال 24 ساعه بدلاً من (3.10%) خلال 30 دقيقه و(4.20%) خلال 24 ساعه. وهذا يعني أننا أصبحنا في مأمن بالمقارنه مع المواصفه القياسيه وهذا هو ما نتوخاه لملافات أي إخفاقات تنتج إثناء العمل من قبل كادر غير ماهر أحياناً أو بسبب عدم المراقبه الجيده والمستمره للمنتوج أو حدوث إخفاقات إثناء الخزن والمناقله.

الإستنتاجات:

من خلال النتائج التي تم الحصول عليها من هذا البحث وضمن المحددات المتعلقه به يمكن إستنتاج الآتي :

أ. لايمكن الحصول على شتايكر جيد ومقبول وفقاً للمواصفات بإتباع الأساليب الحاليه الشائعة الإستخدام في معظم المعامل المحليه التي لا تهتم بنوعية المواد الأوليه الداخله في صناعة الشتايكر ولا بدقة نسب خلطها ومن ثم معالجتها.

ب. إن إستخدام الخلطه الخرسانيه الوزنيه المقترحه البالغه 1 : 1.5 : 2.85 مع نسبة ماء /أسمنت مقدارها 0.5 مع ركام خشن مكسر ذو مقاس أقصى مقداره 14 ملم ، وإتباع السيطره النوعيه في العمل, بما فيها إجراء خلطات موقعيه تجريبيه عند حصول تغيير في مصدر تجهيز الركام او تغير محتواه الرطوبي خلال فصول السنه, سيؤدي إلى إنتاج شتايكر مستوفي لشروط المواصفه القياسيه العراقيه رقم 1107 لسنة 1988.

ج. إن إستخدام المشبكات السلكيه لتعزيز الشتايكر يؤدي إلى زيادة مقاومته لحمل الكسر بمقدار 21%+ مقارنةً مع الشتايكر الذي لايحتوي على مشبكات سلكيه.

المراجع:

Brooks, J.J. and Kenai, S.," Impact Properties of Polymer-grid Reinforced Cement Mortar." The International Journal of Cement Composites and Lightweight Concrete, Vol.11, No.3, 1995.

Engel, R. S. and Bakis, C.E.," Fiber Reinforced Polymer-grids for Reinforced Concrete." National Science Foundation Center, June, 2001.

Mathews, M.S., Rao, P.S., and Srinuasan. P., "Impact Studies on Ferrocement Slabs." International Symposium on Ferrocement, RILEM, 1981.

Netlon Ltd.," Tensor Grids in Concrete Applications." The Civil Engineering Division, Blackburn, December, 1988.

Neville, A.M., " Properties of Concrete. " Long man Group Ltd., 4th edition, 1995.

Neville, A.M., and Brooks, J.J.," Concrete Technology." Wiley & Sons Inc., New York, 1987.

Newman, J. and Choa, B. "Advanced Concrete Technology." Butterworth-Heine Main, First Published, 2003.

Shah, S.P. and Key, W. H." Impact Resistance of Ferrocement." ASCE Proceedings, Journal of Structural Division, January 1972.

المواصفه القياسيه العراقيه رقم 5 , " السمنت البورتلاندي " , وزارة التخطيط , الجهاز المركزي للتقييس والسيطره النوعيه , بغـــــــــداد , 1984 .

المواصفه القياسيه العراقيه رقم 45 , " ركام المصادر الطبيعـيه المستعمل في الخرسانه والبناء " , وزارة التخطيط , الجهاز المركزي للتـقـييس والســـيطره النوعيه , بغـــــــــداد , 1984 .

المواصفه القـياسـيه العـراقـيه رقم 1107 , " البلاطات الخرسانيه السابقة الصب" , وزارة التخطيط , الجهاز المركزي للتقييس والســـيطره النوعيه , بغـــــــــداد , 1988 .

الرموز:

f_r : مقاومة إنثناء الخرسانه (N/mm^2) .

M : العزم المطلوب لكسر النموذج بألإنثناء (kN.m).

c : نصف سُمك النموذج (mm).

P : قوة التحمل المستعرض (kN).

l : المسافه بين نقاط إسناد النموذج (mm).

I : عزم القصور الذاتي للمقطع العرضي للنموذج (mm^4).

b : عرض النموذج (mm).

h : إرتفاع النموذج (mm).

جدول (1): نتائج الفحوصات المرجعية للخلطات الخرسانية.

نوع الخلطه	معدل مقاومة ألإنضغاط N/mm^2			معدل مقاومةالشد بألإنشطار N/mm^2			معدل مقاومة ألإنثناء N/mm^2		
	7 يوم	28 يوم	60 يوم	7 يوم	28 يوم	60 يوم	7 يوم	28 يوم	60 يوم
M_{new}	23.5	38.4	45.9	2.12	3.25	3.82	3.75	5.11	6.25
M_{old}	16.8	26.5	30.7	1.72	2.23	2.55	2.37	3.30	4.16

جدول (2): نتائج فحص البلاطات الخرسانية.

نوع الخلطه	قوة التحمل المستعرض kN			ألإمتصاص %			
	نتيجة الفحص	المعدل	حدود المواصفه	نتيجة الفحص		حدود المواصفه	
				30 دقيقه	24 ساعه	30 دقيقه	24 ساعه
M_{new} بدون مشبك	5.6 6.4 6.6	6.2	5.4	3.20 3.00 3.10	4.30 4.05 4.20	4 حد أعلى	10 حد أعلى
M_{new} مع المشبك	8.5 7.2 7.0	7.5	كذلك	2.85 2.50 2.60	3.80 3.40 3.60	كذلك	كذلك
M_{old} بدون مشبك	3.7 3.3 2.8	3.3	كذلك	4.33 3.67 3.82	9.50 6.00 8.20	كذلك	كذلك
M_{old} مع المشبك	4.8 3.9 4.5	4.4	كذلك	3.50 3.00 2.80	7.20 7.50 7.80	كذلك	كذلك

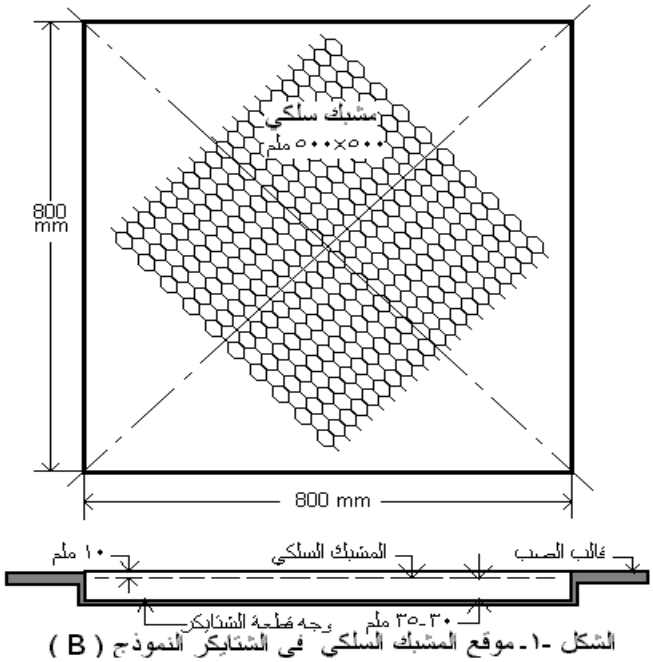

الشكل -١- موقع المشبك السلكي في الشتايكر النموذج (B)

الشكل (1): موقع المشبك السلكي في بلاطات النموذج B.

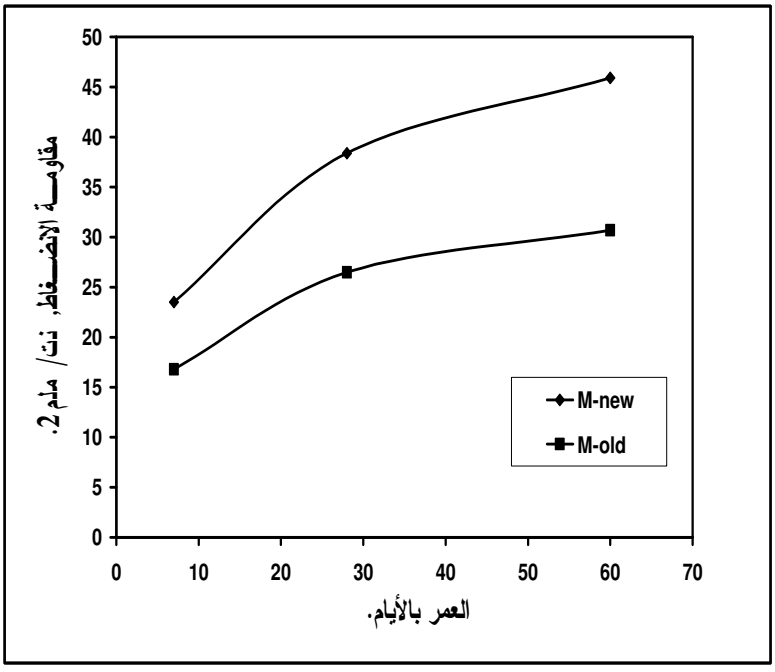

الشكل (2): تطور مقاومة الانضغاط مع العمر للخلطات الخرسانية.

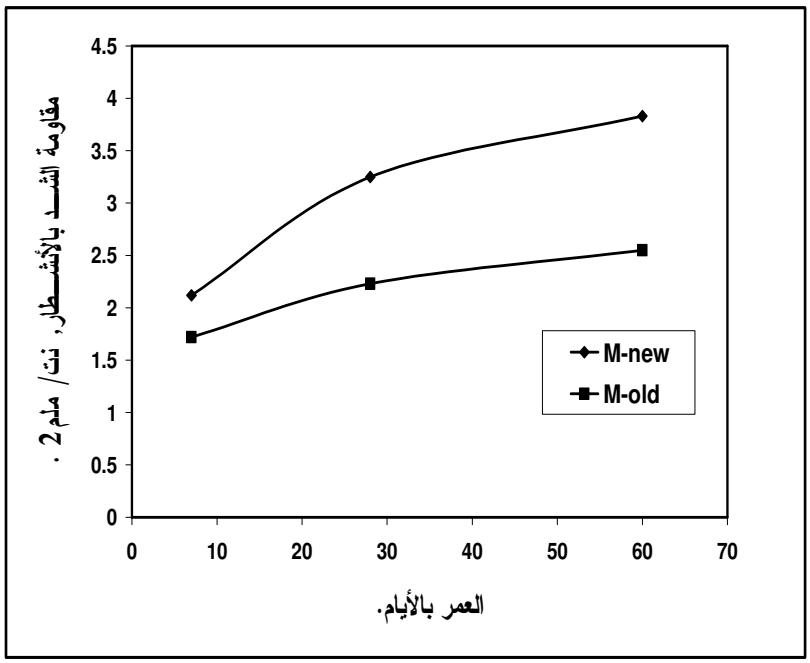

الشكل (3): تطور مقاومة الشد بالانشطار مع العمر للخلطات الخرسانية.

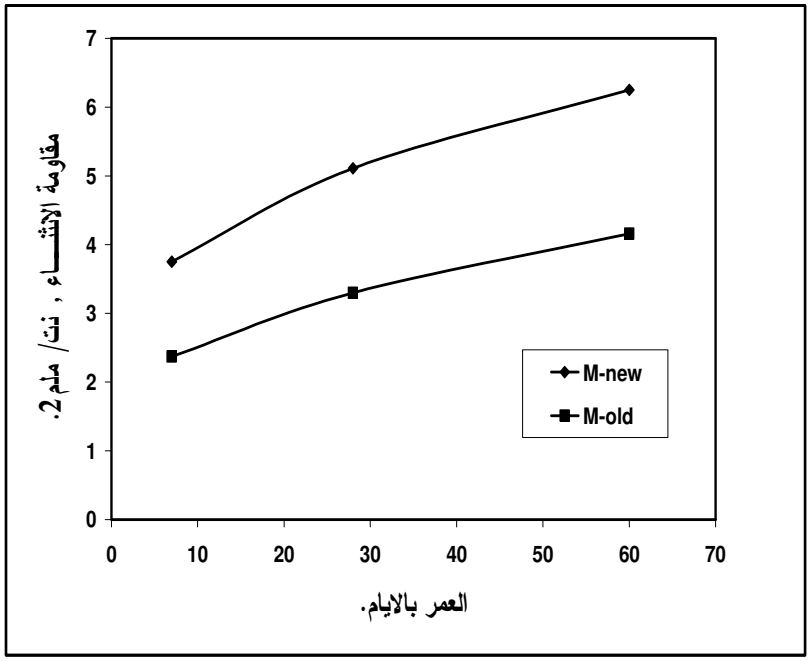

الشكل (4): تطور مقاومة الانثناء مع العمر للخلطات الخرسانية.

دراسة إمكانية إنتاج قطفة كيروسين من نفط اليمن كوقود نفاث عالي الجودة

د. حامد ناصر بن هرهره **د. سالمين سعد الشعملي**
قسم الهندسة الكيميائية – كلية الهندسة والبترول
جامعة حضرموت للعلوم والتكنولوجيا
E-mail: dr_hamedharhara@yahoo.com

الخلاصة

تم إجراء دراسة مخبرية للتركيب الكيميائي والخواص الفيزيائية لقطفات من الكيروسين المقطر من النفط اليمني وإجراء مقارنات بين تلك العينات المخبرية والتجارية ، بهدف البحث والتاكيد على أمكانية إنتاج وقود طائرات بمواصفات عالية الجودة. وقد تبين من أول نظرة للنتائج المستحصلة أن جميع الخواص الفيزيوكيميائية (Physico-Chemical Properties) لكل العينات تقع ضمن الحدود القياسية دولياً ASTM & IP. فالمحتوى الهيدروكربوني للعينات يتوزع حجماً في الحدود: 15% بارافين طبيعي؛ 50% بارافين متفرع، 2% نفثين أحادي الحلقة، 16% نفثين ثنائي الحلقة؛ 16% أروماتات أحادي الحلقة وتسودها التفرعات؛ 1% أروماتات ثنائي الحلقة. العينات غير شرهة للرطوبة ولم يتغير اللون لكثير من الوقت. الشعلة غير الداخنة في الحدود العليا القياسية (25 ملم). درجة التجمد في إدنى الحدود القياسية (-51 م^0). الموصلية الكهربائية في أوسط الحدود القياسة. كل هذا يؤكد بأن الكيروسين اليمني يمكن تصنيفه من أفضل الوقود لطيف من الطائرات النفاثة المدنية والعسكرية حيث سيسمح بالإرتفاعات القصوى لإنخفاض درجة تجمدة وكثافته كما سيسمح بالسرعة العالية للطيران لإرتفاع نسبة البارافين المتفرع والحلقي المتميزة بالطاقة الحرارية العالية (~ 44 ميقاجول\كلجم) دون الحاجة الملحة لإضافة محسِّنات كيميائية وإنما قد يستلزم إضافة جرعة من أيزومير بارفيني لتنخفض نسبة البارافين الطبيعي والاروماتات.

POSSIBILITY STUDY OF KEROSENE FRACTION PRODUCED FROM YEMEN CRUDE OIL AS JET FUEL WITH HIGH QUALITY SPECIFICATION

Dr. Hamed Nasser Bin Harharah **Dr. Salmin Saed Elshaamali**
Chemical Department-Faculty of Engineering & Petroleum
Hadramout University of Science & Technology
E-mail: dr_hamedharhara@yahoo.com

ABSTRACT
Laboratory investigation and many comparisons between laboratory and commercial samples of Yemeni kerosene distillates were carried out .The physico-chemical properties of the kerosene distillates were determined . The possibility of their utilization as an aviation turbine fuel with high quality specification " assisting the increase of flight height and velocity " was confirmed . At the first look to obtained results , it is shown that the physicochemical properties for all samples are in the international permissible limits. The carbon content is distributed as the following: 15% normal paraffin ; 50% branched paraffin ; 2% mono-cycloalkanes ; 16% bicycloalkanes ; 16% branched mono-cycloaromat with branches prevailing ; 1% bicycloaromat . The samples are not hygroscopic for long period of time . The smoke point is in higher limits standard . Where the freezing point is in lower limits standard .These points prove that the Yemeni kerosene might be prepared for a spectra of jet aircrafts. This Kerosen permit high flying height because it has lower density and freezing point and it permit high velocity of aviation because it has high percentage of branshed and cyclparaffins with high specific energy without needed for addition of chemical additives, but may be need for portion of isomers of paraffin.

المقدمة

من المعروف أن كيروسين الطائرات (Aviation Kerosine) عبارة عن قطفة بترولية مقطرة بدرجة غليان مابين 150 – 300 م^0 [Lucas,2000] أو 140– 180 إلى 260 – 300 م^0 [Bolshakov,1983] أو 160 – 260 م^0 [Jean,1995]. الزيادة في درجة الغليان النهائية لكيروسين الطائرات يؤدي إلى ارتفاع درجة التجمد وكمية العطريات وبالتالي تعمل على الحد من سرعة وارتفاع الطائرة [Bolshakov,1983]. تتكون قطفة الكيروسين من المركبات البارافينية المستقيمة والمتفرعة والنفثينات والعطريات وأحياناً كمية بسيطة جداً من الاولفين [Netshaev,1988,Ivanova,1974, Bolshakov,1983, Lucas,2000]. يتراوح العدد الكربوني للمركبات الهيدروكربونية في الحدود C_{14}-C_8 [Netshaev,1988]. وأن كل مركب له عدد من الايزمرات، يزداد كلما زاد العدد الكربوني [Netshaev,1988,Ivanova,1974] فقد تكون C_{10} لوحدها بالقطفة الكيروسينية في شكل عشرة أيزوميرات [Hirsch,1972]. وقد أقترح الباحث Chairtkov [1968] النسب الحجمية لتلك المركبات الهيدروكربونية الممكن وجودها في وقود الكيروسين على النحو التالي: 10–40 % بارافينات، 20–60 % نفثينات، 13–24 % عطريات أحادية الحلقة، 1–5 % عطريات ثنائية الحلقة. في حين أثبت Puskunov [1979] أن كمية المركبات الأروماتية في الكثير من أنواع وقود الكيروسين تتراوح مابين 10 – 22 % . أما Lucas [2000] حددالأرومات مابين 15 – 20% والبارافين الطبيعي 10 – 20 % والبارافين المتفرع مع الحلقي 60 – 75 % والالفين 0.1– 5 % حجماً. وكمية الكبريت لاتزيد عن 0.3 % وزناً. أن سبب الاهتمام في تحديد نسب العطريات هو انخفاض عددها السيتاني [Erikh,1988,Melncova,1981,Gureef,1986] وميولها نحو تكوين الرواسب الكربونية خاصة ثنائية الحلقة (النفثالين) عند الاحتراق، حيث تظهر في التيار الغازي جزيئا ت الكربون المتوهجة مما يودي إلى شدة إشعاع الشعلة وتلونها ونتيجة لذلك قصر عمر المحرك بسبب الاحتراق الموضعي على جدران غرفة

الاحتراق وكما ترفع كمية الملوثات المنبعثة [Erikh,1988,Melncova,1981]. أضف إلى ذلك ماتتميز به العطريات من شراهة في اكتساب الرطوبة مما تؤدي إلى ارتفاع نسبة الماء في الوقود [[Melncova,1981,Gureef,1986]. أما بالنسبة للمركبات الكبريتية في وقود الكيروسين فهي تغلب عليها مركبات التيوفين غير الحاوية على تفرعات حيث تصل نسبتها مابين 50–80 % [Melncova,1981] من الكمية الكلية القياسية، والتي يجب ان لاتزيد عن 0.3 % وزنا [James,1984, Lucas,2000] والمتوافق مع ASTM D1655.

تتزايد مطالب فحوصات الجودة للكيروسين المعد للطائرات وفق تطور تكنولوجيا الطائرات وظروف العمل. فإضافةً لخاصية الكثافة وكمية العطريات وكمية الكبريت وحرارة الاحتراق ودرجة التجمد يجب معرفة الثبات الحراري ونقاوة الوقود وارتفاع اللهب غير الباعث للدخان. يجب أن لاتزيد درجة التجمد عن ناقص 40 م^0 [Gureev,1986,Lastokina,1986,Wauquier,1995, Allison,1975] والسبب أن الوقود وسط خزان الطائرة يتعرض لتقلبات الطقس، فعند الطيران يحدث تبريد سريع ، حيث تنخفض درجة حرارته بمعدل 45 م^0 خلال ساعتين من أقلاع الطائرة [Bolshakov,1965]. ولدراسة التركيب الكيميائي تستخدم الكروماتوجرفيا الغازية أو الأمتزاز الكروماتوجرافي أو التشكل المعقد بالكاربامايد,[Proskuriakov,1981] [Hirsch,1972] أو طرق الجمعية الأمريكية لفحص المواد ASTM المتوافقة مع مقاييس معهد البترول البريطاني IP .

هدف البحث

بما أن اليمن من الدول المنتجة للنفط المتميز بقلة احتوائه على الكبريت وارتفاع كمية المقطرات الخفيفة. فكان لابد من البحث ودراسة التركيب الكيميائي والخواص الفيزيوكيميائية لقطفة الكيروسين المقطرة من النفط اليمني والتأكيد على إمكانية وكفاء استخدامها كوقود للطائرات النفاثة بمواصفات عالية الجودة .

طريقة البحث

مقارنة عينتان للكيروسين مقطرتان في فترتين مختلفتين من نفط يمني. عينة تجارية لشركة مصافي عدن وأخرى مخبرية . تم إجراء التجارب وفحوصات الخواص الفيزيو كيميائية مخبريا في مختبرات جامعة حضرموت وشركة النفط اليمنية فرع حضرموت والمختبر المركزي لمصافي عدن وفق الطرق القياسية العالمية ASTM & IP. الفحوصات الاساسية:

التقطير ASTM-86

جرت عملية التقطيرللنفط الخام الجاف عند الضغط الجوي بجهاز التقطير البسيط **شكل (1)** حسب المقياس العالمي. يسكب 125 ملل من العينة وسط دورق التقطير. يربط الدورق بمكثف. يسد الدورق بسدادة تحمل

محرار. موضع بصلة المحرارة أمام مخرج البخار من الدورق مباشرةً. يملئ حوض المكثف بالتلج والماء البارد. يفتح التسخين على العينة. خلال 7 دقائق تبدء نقطة الغليان. تسجل نقطة الغليان الإبتدائية لحظة سقوط أول قطرة من السائل المتكثف من الطرف السفلي للمكثف. معدل التكثيف وتجمع السائل داخل المستقبل منتظماً في حدود 4 – 5 ملل\دقيقة. عند درجة غليان 150 م^0 تستبدل اسطوانة المستقبل لتحتسب درجة الغليان الابتدائية لقطفة الكيروسين عند 151 م^0 حتى درجة غليان 260 م^0. ثم يستبدل المستقبل ويوقف التسخين عند 330 م^0. بنفس النظام تم إعادة تقطير العينات التجارية. خلال فترات التقطير تسجل الحجوم مع درجة الغليان الموافقة لها.

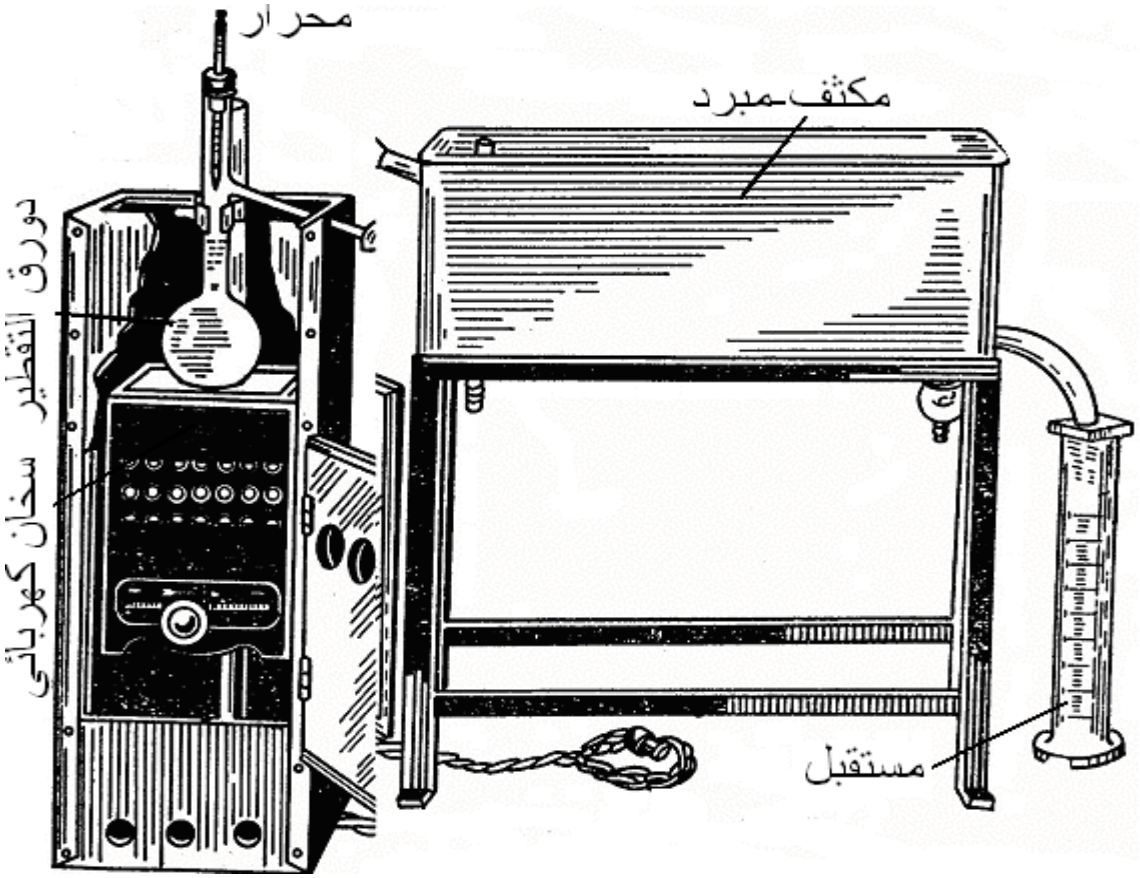

شكل (1) . جهاز التقطير المعياري

فحص الكثافة ASTM-1298

كثافة النفط الخام وقطفات الكيروسين تم قياسها بواسطة الهيدروميتر الزجاجي. توضع العينة في أسطوانة معيارية وتحفظ درجة الحرارة عند 15 م^0. يوضع الهيدروميتر المناسب وسط العينة. بعد أستقرار الهيدروميتر ودرجة الحرارة تؤخذ قراءة الهيدروميتر.

الامتزاز الكروماتوجرافي ASTM-1319

تم تحليل المحتوى الهيدروكربوني لقطفات الكيروسين بالإمتزاز الكروماتوجرافي. مادة الامتزاز هي جل السيليكا المنشط ((Silica gel (50-200 mesh). عمود الإمتزاز زجاجي، طوله 120 ملم وقطره 20 ملم. يعبأ

العمود بعامل الامتزاز مع الهز الخفيف بهدف التوزيع المتوازن لجل السيليكا. تسكب العينة في العمود. بعد أمتزاز العينة يقاس طول كل طبقة متألقة، ثم يضاف الكحول لمج العينة إلى أسفل العمود. ونحصل على بارافين، نفثين، أروماتية. تحسب نسبة كل مجموعة هيدروكربونية.

أختبار درجة التوهج (IP – 170)

تم تعيين درجة التوهج بجهاز آبل (Abel Apparatus) ذو الكوب المغلق. تسكب العينة في كوب الاختبار إلى العلامة المحدد. يعاد الكوب إلى موضعه في الجهاز بعد أن يغطاء بالغطاء الخاص الحامل لمحرار وخلاط . تسخن العينة بمعدل درجة مئوي لكل دقيقة مع إستمرار الخلط. عند العشر الدرجات المئوية السابقة لدرجة التوهج المتوقعة يبدأ توجيه لهب الاختبار ببطء إلى داخل الكوب. يكرر توجيه اللهب كلما إرتفعت الحرارة نصف درجة مئوي. يجب توقيف الخلاط لحظة وصول الهب إلى الكوب. تؤخذ درجة التوهج لحظة توهج بخار العينة بلون أزرق داخل الكوب وانطفاء لحظياً.

أختبار رد الفعل للماء ASTM-1094 (Water Reaction Test)

أستخدم محلول بفر الفوسفات Phosphate Buffer Solution المتعادل (pH=7) في تحديد قدرة العينة المخزونة شهراً على فصل الماء. يأخذ 20 ملل من محلول البفر عند درجة حرارة الغرفة في أسطوانة سعة 100 ملل محكمة الغطاء. يضاف إلية 80 ملل من العينة. تسد الاسطوانة وترج لمد دقيقتين دون تدوير. ثم تترك الأسطوانة لمدة 5 دقائق ليستقر الخليط فتظهر الطبقات. بدون تحريك الأسطوانة سجلت الحالة .

فحص نقطة الدخان ASTM- 1322

فحص نقطة الدخان لمقاطع الكيروسين تم تنفيذه في مصباح قياسي وسط ظروف الغرفة. بسكب 20 ملل من العينة وسط وعا السائل. وتُثبيت الفتيل المشبع مسبقا بالعينة على رأس الوعاء. وربط ذلك الوعاء الملئ بالعينة إلى الجهاز بإحكام. ثم يشعل الفتيل وينظم ليبقى طول اللهب 1 سم لفترة 5 دقائق. يرفع الفتيل تدريجيا بواسطة قرص التحريك حتى ينبعث الدخان. يخفض مستوى الفتيل ثانية حتى يختفي الدخان تماما. عندها يقاس إرتفاع اللهب بواسطة الخلفية المدرجة بالملميتر للمصباح وتسجل كنقطة الدخان.

قياس درجة التجمد IP-16

يوضع 25 ملل من العينة في الانبوب ثم تغطى بواسطة سدادة من المطاط تحمل عامود خلط (Stirrer) وثرموميتر مدرج من −80 إلى +20 م^0. بصلة الثرمومتر في وسط العينة. يوضع الأنبوب في الوسط المبرد بحيث يغطي الوسط مستوى العينة. تحرك العينة بأستمرار. تأخذ درجة الحرارة التي يظهر عندها

بلورات هيدروكربونية. تخرج الأنبوبة من الوسط البارد وترفع درجة الحرارة. تاخذ قراءة الترمومترلحظة إختفاء البلورات. نأخذ متوسط القرائتين كدرجة التجمد.

فحص شريط التآكل ASTM-130

الكشف عن تآكل شريط النحاس تم بواسطة إختبار اعتام لون الشريط. يغمر شريط النحاس المصقول في أنبوب الإختبار الحاوي على 30 ملل من العينة الخالية من الماء. يوضع انبوب الاختبار داخل أنبوب صلب ذا غطاء خاص. ثم يغمر الانبوب وسط حمام مائي عند 100 م^0 لمدة ساعتين. بعدها يرفع الشريط ويغسل بمذيب خفيف ثم ينشف بورقة ترشيح بالضغط دون المسح. يقارن لون الشريط بلوحة التآكل القياسية بحيث يكون الضوء الساقط عليها ينعكس بزاوية 45 ^{0} تقريبا .

تعيين محتوى الكبريت ASTM -1266

عيِّن محتوى الكبريت في العينة بواسطة طريقة المصباح. حيث تم إحراق 20 ملل من العينة في منظومة مغلقة باستخدام المصباح الخاص مع تكوين جوٍ إصطناعي مكون من 70 % ثاني أكسيد الكربون و 30 % أكسجين لمنع تكوين أكاسيد النيتروجين. أكاسيد الكبريت الممتصة والمؤكسدة إلى حمض الكبريتيك بواسطة محلول بيروكسيد الهيدروجين الذي يتدفق مع الهواء لفصل ثاني أكسيد الكربون المذاب. الكبريت المتحول إلى كبريتات في المادة الماصة، يتم تحديده بالمعايرة بواسطة محلول هيدروكسيد الصوديوم (0.05 N). والكاشف المستخدم هو 2 – 4 قطرات من ميثيل الأرجوان. بعد ذلك أتخدمت معادلة النسبة الكتلية:

$$S_{\%wt.} = 16.03M \times (A/10W)$$

حيث A – عدد المليترات من محلول هيدروكيد الصوديوم المستهلكة في المعايرة؛ M – المولالتي لمحلول هيدروكيد الصوديوم؛ W – عدد جرامات العينة المحروقة.

حساب حرارة الأحتراق الصافية ASTM-4529

حسبت الحرارة الصافية للإحتراق (Q`) وفق المعيار العالمي أعلاه المرتكز على العلاقتين التاليتين:

$$Q = 22.9596 - 0.0126587A + \frac{26640.9}{\rho} + \frac{32.622A}{\rho} - 6.69030 \times 10^{-5} A^2 - \frac{9217760}{\rho^2}$$

$$Q' = Q - 0.1163S$$

حيث Q` – كمية الحرارة الصافية في ضل وجود الكبريت بالعينة، ميقاجول\كيلوجرام؛ Q – كمية الحرارة الصافية في ضل عدم وجود كبريت في العينة، ميقاجول\كيلوجرام؛ ρ – كثافة العينة، كيلوجرام\متر مكعب؛ A – درجة الأنيلين، درجة مئوي؛ S – محتوى الكبريت،% وزناً .

فحص الموصلية الكهرائية IP-274

تم قياس الموصلية الكهربائية للعينات بواسطة غمرمسبار خلية الموصلية والذي يتكون من قطبين وسط لتر من العينة الموضوعة في أسطوانة . ثم تسليط جهد بين القطبين فينتج تياراً، يعبر التيار الناتج عن قيمة الموصلية ووحدته Picosiemens per meter (Ps/m) .

أختبار الثبات الحراري (ASTM-3241)

تم تقييم الثبات الحراري في جهاز JFTOT. تمر العينة المرشحة مسبقا وسط أنبوب مسخن إلى 260 م^0. يحكم على لون الانبوب بمساعدة لون ASTM المعياري.

هناك فحوصات أخرى إضافية قد تم أجراؤها حسب المقياس العالمي مثل: اللزوجة (IP-71)، درجة الانيلين (ASTM-611)، الحامضية الكلية (ASTM-3242)، النفثالين (ASTM-1840)، أستخلاص محتوى الماء (IP-74)، إضافةً إلى مراقبة مظهر Appearance العينة لمدة شهر كامل وهي في حالة خزن .

كما تم تجميع المركبات الهيدروكربونية المستقلة المتوقع وجودها في مدى غليان عينة الكيروسين. ووضعت في إطار مجموعات هيدروكربونية متناسقة مع درجتي غليان وتجمد كل مركب. لكي يتم أبراز تأثيركل مجموعة من تلك المجموعات الهيدروكربونية على جودة وقود الطائرات التوربينية وتأكيد نسبتها.

النتائج والمناقشة

نتائج فحص وتقطير النفط اليمني مدونة بالجدول (1).

توضح النتائج بهذا الجدول أن كمية الكبريت بالنفط اليمني منخفضة جداً في أدنى مستوياتها حيث لاتزيد عن 0.52 % وزناً، وكذلك أيضاً الكثافة في حدود 0.8658 جرام \ ملل، مما يدلل على الجودة العالية للنفط اليمني. كما لوحظ أن درجة الغليان الأبتدائية للنفط كانت 48.9 م^0. وعند درجة غليان 150 م^0 كانت نسبة المقطرالحجمية 12.8%. أعتبرهذا المقطع كجازولين خفيف. من درجة الغليان 151 م^0 إلى درجة غليان 260 م^0 كانت النسبة الحجمية 22 %. وأعتبرهذا المقطع كقطفة كيروسين.

Table (1). Physico-Chemical properties of Yemen crude oil (Masila region)

No.	property	unit	Test Method		Yemen crude Oil
			ASTM	IP	
1	***Composition***				
	Total Acidity	mgKOH/g	D3242		-
	Aromatic	% vol.	D1319	354	–
	Sulphur Content	% wt.	D1266	156	0.52
				336	
2	***Volatility***				
	Distillation:	^{0}C	D 86	123	
	I. B. Point				48.9
	10 %vol.				137
	12.8%				150
	15 %				161.5
	20 %				189
	25 %				216
	30 %				240.5
	35 %				264
	40 %				287
	50 %				330
	Flash Point	^{0}C	D3828	170	> 10
	Density at 15^{0}C	g/ml	D1298	160	o.8658
3	***Fluidity***				
	Freezing Point	Minus ^{0}C	D2386	16	6-18
	Viscosity at 20^{0}C	mm^2/s	D445	71	1.54
4	***Condutivity***				
	Elect.Conductivity,@ 28^{0}C	$_P$S/m	D2624	274	190

نتائج تقطير وفحوصات العينات المخبرية والتجارية لقطفات الكيروسين مدونة **بالجدول (2)**.

من أول نظرة للنتائج المدونة بهذا الجدول نلاحظ أن جميع الخواص الفيزيكو– كيميائية تقع ضمن الحدود المسموح بها دولياً. كما أن العينة المخبرية تشبة كثيراً العينة التجارية في نتائج الفحوصات وإن وجد اختلاف بسيط فهو قد يرجع إلى طريقة الإعداد ونظام العمل بالمختبر كما قد تكونا العينتين مأخوذتين من بئرين مختلفين في منطقة المسيلة.

حدد المقياس العالمي الكثافة لقطفات الكيروسين المعدة كوقود نفاث مابين 0.775–0.840 جرام\ملل. وقد وجدنا أن كثافة العينات المدروسة تقع ضمن ذلك النطاق. كما نجد أن كثافة كل عينة تتناسب مع حدود غليانها الابتدائية والنهائية، مثلا كثافة العينة التجارية هي 0.7976 جرام\ملل وحدود غليانها في المدى 154–266 م^0 في حين كثافة العينة المخبرية هي 0.7820 جرام \ ملل و بالتالي كانت درجة غليانها في المدى 151– 260 م^0. تؤكد ذلك كمية الكبريت حيث تقل عند العينة المخبرية بما يساوي 0.002 % وزنا عن تلك للعينة التجارية البالغ مقدار0.02 % وزنا أما المعيار العالمي فحده ≥ 0.3. مقدار المعايرة

للحامضية أقل عند العينة المخبرية بمقدار 0.001 ملج KOH\جرام عن تلك للعينة التجارية البـــالغ مقـــداره 0.004 ملج KOH \جرام في حين يسمح المقياس العالمي إلى 0.1 ملج KOH \جرام، وهكذا بالنسبة لدرجة التوهج حيث تصل 46 م^0 في حين لا تزيد عند العينة التجارية عن 43 م^0 أما المعيار العالمي فكان حـــده ≤ 38 م^0.

Table (2) Physico-Chemical properties of kerosene fractions ditilled from Yemen crude oil

No.	property	unit	Test Method		Kerosene		
			ASTM	IP	Standard limits, Jet A & A-1	Comm. Samples*	Lab. samples
	Composition						
1	Appearance	-	-	-	Clear bright no solid	Clear bright no solid	Clear bright no solid
2	Total Acidity	mgKOH/g	D3242	354	≤ 0.1	0.004	0.003
3	Aromatic	% vol.	D1319	156	≤ 25	17	17
4	Aniline Point	^{0}C	D611	2	-	60.5	62
5	Sulphur Content	% wt.	D1266	336	≤0.3	0.02	0.018
	Volatility						
6	Distillation:	^{0}C	D86	123			
	I. B. Point				Report	154	151
	10%vol.				205	168	171
	50%				Report	191	191
	90%				Report	232	223
	E. B. Point				300	266	260
7	Distil. Residue	% vol				1.5	1
8	Distil. Loss	% vol				1	0
9	Flash Point	^{0}C	D3828	170	≥38	43	46
10	Density at 15^{0}C	g/ml	D1298	160	0.775-0.84	0.7976	0.7820
	Fluidity						
11	Freezing Point	Minus ^{0}C	D2386	16	≤40**	50	51
12	Viscosity at 20^{0}C	mm^2/s	D445	71	≤8	1.55	1.56
	Combustion						
13	Smock Point	mm	D1322	57	≥19	23	25
14	Specific Energy	MJ/kg	D4529	381	≥42.8	43	43.5
15	Naphthalene	% vol	D1840		≤3	1.6	1
	Corrosion						
16	Copper Strip 2h@100^{0}C)		D130	154	≤1	1	Nil
	stability						
17	Tube Deposit Rating (visual)	Color standard	D3241	323	<3	1	1
	Contaminants						
18	Water reaction interface (Visual)		D1094	-	≤1b	1b	1
	Water content						
19		mg/100ml	-	-	-	1	Nil
	Condutivity						
20	Elect.Conductivity,@ 28^{0}C	$_p$S/m	D2624	274	50-450	250	200
	Additives						
21	Static Dissipator (Stadis450)	mg/l			Agrement	1	Nil

*- عينات شركة مصافي عدن ومختبرات منشأت المكلا

** - يتشابه Jet A-1 مع Jet A في جميع الخواص ماعدا درجة التجمد فأعلى درجة له ناقص 47 م^0

[JIG,2005,EAI Ltd,2000]

بينما يعطي المعيار العالمي كمية الأرومات في الوقود النفاث إلى 25 % حجما وطول الشعلة غير الداخنـــة بما لا يقل عن 19 ملم ودليل النفثالين إلى 3 % حجما، أظهر فحـــص الامتـــزاز الكرومـــاتوجرافي كميـــة

الأروماتات لدى العينات المخبرية والتجارية بما لا يزيد عن 17 %. ويؤكد ذلك كل من طول الشعلة غير الداخن (23–25 ملم) والثبات الحراري العالي ودليل النفثالين والذي لا يزيد عن 1% ، وبالتالي لا يسمح ظهور تلوّن للشعلة الخارجة من نفاث الطائرة. كما أن نسبة اكتساب الرطوبة المعدومة أو القليلة والتي لا تزيد عن 1 ملج\100 ملل تعمل على عدم نشوء بلورات ثلجية في خزان الوقود عند انخفاض درجة الحرارة لحظة الارتفاع أو على أنظمة نقل وبخ الوقود. وبالتالي فالكيروسين اليمني يعد كوقود توربيني عالي الجودة للطائرات النفاثة.

بما أن نسبة المجموعة العطرية في عينات الكيروسين في حدود 17% وبما أن ثنائية الحلقة منها تتميزبدرجة تجمد عالية تبلغ زايد 83 م^0 **جدول (3)** كما تتميز بطول قصير جداً للشعلة بدون دخان. إذن فلا يمكن أن تتواجد إلا بنسبة لا تزيد عن 1 % وهذا ما يؤكده فحص النفثالن الموضح بالجدول 2. وعلى هذا الأساس فإن نسبة الأروماتيات أحادية الحلقة ستكون 16% حجما، وهي ذات تفرعات. النسبة العظمى المتبقية وهي 83 % تشمل مجموعة البارافين الطبيعي والمتفرع وكذلك المجموعة النفثينية وهذا ما يؤكدة دليل التآكل والثبات الحراري العالي. وبما أن درجة التجمد للعينات تتراوح ما بين 50 – 51 م^0 بالناقص فمن المرجح أن نسبة البارافين الطبيعي في حدود لا تتجاوز 15% وهذا يتوافق مع رأي الباحث Chairtkov [1965] القائل إذا تم خفض نسبة البارافين الطبيعي إلى حدود 5–7 % تنخفض درجة الانسكاب إلى ناقص 60 م^0 (هذا ما يجب أن نعمل على تحقيقه). وعلى هذا الأساس نعتقد أن كمية البارافين المتفرع هي في حدود 50%، مع الاخذ بعين الأعتبار أن كل مركب بارافيني له العديد من الأيزوميرات [Mortier,1997,Hirsch,1972] والتي تتمتع بإنخفاض في درجات الغليان والكثافة والتجمد واللزوجة [Mortier,1997]، أما النسبة المتبقية (حوالي 18 %) فهي للمجموعة النفثينية. تتوزع إلى 2 % أحادي الحلقة C_8 و16 % ثنائي الحلقة C_{10}. هذا الرأي تؤكده معطيات الجدول 3 لمكونات تلك المجموعات الهيدروكربونية وكذا تأثير التوزيع الكربوني على درجات الغليان وبالتالي تحديد التركيبة الكيميائية لوقود الكيروسين النفاث. حيث نجد أن المركبات الهيدروكربونية السائدة في كيروسين الطائرات هي المركبات ذات العدد الكربوني C10 – C12 وهذا يتوافق مع [Mohammed,1997,Proskuriakov,1981, Hirsch,1972] .

Table (3). The Carbon Distribution accourding to Bioling and Freezing Points

No.	**Compound**	**B.P. , ^{0}C**	**F. P. , ^{0}C**

1	**Normal paraffin**		
	C_8	125.7	-59.6
	C_9	150.7	-56.4
	C_{10}	174	-32.5
	C_{11}	195	-28.4
	C_{12}	216	-11.8
	C_{13}	230	-8.8
	C_{14}	251	+8.3
2	**Naphthens**.		
	Mono-cyclic. C_7	117	-15.8
	C_8	147.5	-16.8
	bi-cyclic,		
	Decaline C_{10}	198.3	-47.8
3	**Aromatic**		
	mono-cyclic		
	Ethylbenzene	136	-95.8
	p - C_8	138	+15.8
	m- C_8	139	-56.8
	o - C_8	144	-30.8
	Pseudoumen	169	---
	Mesitylene	165	-59.8
	$(C_3H_7)-C_6$	159.5	Liquid
	i-$(C_3H_7)-C_6$	152	Liquid
	$(C_4H_9)-C_6$	180	Liquid
	i-$(C_4H_9)-C_6$	168	Liquid
	Durene,1,2,4,5 $(CH_3)_4$-C_6	195	+81.8
	Isodurene	196	-6.8
	$(CH_3)_5$-C_6	231	+55.8
	$(CH_3)_6$-C_6	265	+168.8
	$(C_2H_5)_3$-C_6	215	Liquid
	bi-cyclic		
	Naphthalene, C_{10}	218	+82.8
	Diphenyl , C_{12}	254	+72.3
	Diphenyl methane, C13	262	+29.8

الإستنتاجات:

نستنتج أن العينة المخبرية تشبة كثيراً العينة التجارية. وأن الخواص الفيزيكو- كيميائية للعينتين تقع ضمن أفضل الحدود القياسية دولياً. المحتوى الكربوني يتوزع في الحدود: 15 % بارافين طبيعي؛ 50 % بارافين متفرع؛ 2 % نفثين أحادي الحلقة؛ 16 % نفثين ثنائي الحلقة؛ 1 % أرومات ثنائي الحلقة؛ 16% أرومات أحادي الحلقة تسودها التفرعات. العينات غير شرهة للرطوبة ولم يتغير اللون لكثير من الوقت. الشعلة غير الداخنة في الحدود العليا القياسية (25 ملم). درجة التجمد في إدنى الحدود القياسية (-51 م^0). الموصلية الكهربائية في أوسط الحدود القياسية. كل هذا يؤكد بأن الكيروسين اليمني يمكن تصنيفه من أفضل الوقود لطيف من الطائرات النفاثة المدنية والعسكرية حيث سيسمح بالإرتفاعات القصوى لإنخفاض درجة تجمدة وكثافته كما سيسمح بالسرعة العالية للطيران لإرتفاع نسبة البارافين المتفرع والحلقي المتميزة بطاقة إحتراق

عالية (44 ميقاجول\كلجم) دون الحاجة الملحة لإضافة إضافات كيميائية وإنما قد يستلزم إضافة جرعة من أيزوميرات بارافينية لتنخفض نسبة البارافين والاروماتات.

المصادر

Alan G. Lucas , (2000), Modern Petroleum Technology, V. 2, 6th ed., John Wiley & Sons Ltd, England,. pp. 288 – 290.

Bolshakov G.F., (1983), Chemical & Technology of component's jet fuel, chemia, Linengrad, , pp. 268.

Jean – Pierre Wauquier, (1995), Petroleum Refining, , V. 1, pp. 332.

Ivanova, L. V., M. I. Korneev, V. N. Uzbashev, (1974), Technology of Petroleum and Gas Refiniry , Mir Publishers, Moscow, , pp. 12-13.

Netshaev, A.P., (1988), Organic Chemistry , Higher sSchool, Moscow., pp. 26.

Hirsch D. E., R. L. (1972), Hopkins & others, Analytical Chemistry, V. 44 , No. 6 , pp. 915-919 .

Chairtkov I. B., (1968), Modern and perspective hydrocarbons of diesel and jet fuel , Chemia , Moscow , pp. 123 .

Puskunov V. A., K. S. (1979), Chairnova & others , Chemistry and Technology of Fuel and Lubricant, , No. 10 , pp. 35 – 38 .

Gureef, A. A., (1986), Chimmotology, Chimia, Moscow, pp. 169.

Melncova L. A., (1981), Petrochemical , V.21, No.1, pp. 149 .

Erikh, V. N., M. G. Rasina and M. G. Rudin, (1988), The Chemistry and Technology of Petroleum and Gas, Mir Publishers, Moscow, , pp 92 -93.

James, H. G., E. H Glenn, (1984), Petroleu Refining Technologyand Ecconomics, 2ed edition, Marcel Dekker INC., New York, , pp. 12.

Allison J. P. , (1975), Criteria for quality of petroleum products, Applied Science Publishers Ltd., U.K., , pp. 66, 142.

Wauquier, J. –P. (1995), Petroleum Refining, Crude Oil, petroleum Products, process, Flowsheets, Editins Technip, Paris, , pp. 251.

Lastokina, G. A., E. D. (1986), Radtshiko, M. K. Rudina, Handbook of petroleum Refinig, Chemia, Linengrad, , pp. 433.

Gureev, A. A., I. G. Fux, V. L. (1986), Lashkhi, Chemmotology, Chemia, Moscow, , pp. 170.

Bolshakov, G. F., E. I. Gulin, N. N. Toritshnev, (1965), Phisico-chemical principles for motor, turbine and rocket fuel, Chemia, Moscow, ,pp. 26-40

Proskuriakov V. A., A. E. Drakina , (1981), Chemistry of Petroleum & Gas , Chemia , Linengrad , , pp.106 – 194.

ExxonMobil Aviation International Ltd, (2000), World Jet Fuel Specifications, , pp. 4-22.

Joint Inspection Group (JIG), (2005), Production Specifications, Bulletin No. 4. march. pp1-5.

Mortier, R. M., S. T. Orszulik, (1997), Chemistry and Technology of Lubricants, 2ed Edition, Blakie Academic & Profesional, Britain, , pp. 4.

Mohammed A., (1997), Thermal- stability and low-temperature properties of medium petroleum distillate, Sofia, , pp. 63.

دراسة تأثير بعض المتغيرات في لحام TIG SPOT لسبيكة (المنيوم–مغنيسيوم)

د. منى خضير عباس
استاذ مساعد

هيثم يحيى عبد المجيد
ماجستير معادن

قسم هندسة الأنتاج والمعادن / الجامعة التكنولوجية / بغداد–العراق

الخلاصة

يهدف البحث الى دراسة تأثير بعض المتغيرات في عملية لحام القوس الكهربائي النقطي بقطب التنكستن المحمي بالغاز الخامل (TIG Spot) لسبيكة (المنيوم–مغنيسيوم) نوع (5052-O) الغير قابلة للتعامل الحراري وذلك لأستخداماتها الصناعية الواسعة وتطبيقاتها الكثيرة في مجال تكنولوجيا اللحام. وأجريت عملية اللحام بأستخدام قطب تنكستن نوع($EWTh_2$) وقطر القطب (3.2mm) وتيار مستمر بقطبية مباشرة (DCSP) بعد تثبيت معدل انسياب الغاز (الأركون) 15litre/min. تم تحديد الظروف المثلى لمتغيرات عملية اللحام النقطي من تيار وزمن اللحام وطول القوس بالاعتماد على فحص قوة القص العظمى (مقاومة القص) لوصلات اللحام باستخدام جهاز أختبار الشد ، كذلك تم دراسة التغيرات الميتالورجية لمنطقة اللحام والمنطقة المتأثرة بالحرارة عند الظروف المثلى للحام.

توصل البحث الى ان قوة القص العظمى لوصلات اللحام النقطي تزداد مع زيادة تيار وزمن اللحام الى قيمةعظمى ثم تنخفض بعدها عند التيارات العالية والأزمنة الطويلة، حيث بلغت قيمة قوة القص العظمى الى (2.4KN) عند طول قوس (1.6mm) وتيار لحام(90Amp) وزمن لحام (7sec) ولسمك صفيحة (1mm). كما وجد ان اعلى صلادة للوصلة (53.5 HV) كانت عند مركز نقطة اللحام ثم أنخفضت تدريجياً بأتجاه المعدن الأساس .

A STUDY EFFECT OF SOME VARIABLES IN TIG SPOT WELDING FOR (ALUMINUM – MAGNESIUM) ALLOY

Dr. Muna K. Abbass
Ass.Prof.

Haitham Y. Abdul-Majid
M.Sc. Metallurgy

Dept. of Production Engineering and Metallurgy, University of Technology, Baghdad - Iraq

ABSTRACT
The present work investigates the effect of some of the variables in spot tungsten inert gas shielded welding (TIG Spot) for (Aluminum-Magnesium) alloy type (5052-O) which is non–heat treatable alloy for its wide industrial uses and applications in field of welding technology.
TIG Spot welding was performed by using tungsten electrode ($EWTh_2$)of diameter (3.2mm) and DC current with direct polarity (DCSP) at constant shielded gas flow rate (15litre/min).
The welded specimens were tested by using the Instron machine to determine the maximum shear force (shear strength) of spot welded and to define the optimum conditions of spot welding variables in relation to the weld current, weld time and arc length of welding to produce an acceptable weld. The metallurgical changes of the weld zone and heat affected zone were studied under optimum conditions of welding.
It has been shown that the increase in the welding current and welding time tends to increase the maximum shear force and it reaches maximum value and then decreases with high currents and long times. The maximum shear force was 2.4KN at welding current of (90) Amp , welding time (7)sec and arc length (1.6mm) for 1mm thickness.
It was also found that the highest value of hardness (53.5 Hv) was at the center of the spot welded and decreases gradually from the center of the weld spot towards the base metal.

المقدمة

نظراً لما تتميز به سبائك الألمنيوم– مغنيســـيوم من خفة وزن ومتانةعالية ومقاومة عالية للتآكل وكذلك قدرة على التشكيل واللحام فأن الواح الألمنيوم–مغنيسيوم تستخدم في صناعات عديدة في تصنيع السيارات والشاحنات والطائرات وفي مركبات الفضاء وصناعة السفن البحرية(Bolton, 1998).

توجد مشاكل كثيرة في لحام الألمنيوم وسبائكه منها قابليته العالية للتوصيل الحراري والكهربائي ووجود طبقة أوكسيد الالمنيوم (Al_2O_3) على سطح الالمنيوم دائما وهي ذات درجة أنصهار أعلى بكثير من معدن الألمنيوم مما تسبب بعض الصعوبات خلال اللحام الانصهاري. لذا تجرى عمليات التنظيف الميكانيكي والكيمياوي قبل عملية اللحام لأزالة طبقة الأوكسيد وتحسين خواص وصلات اللحام .(George, 2003-Khanna,1980)

يلحم الالمنيوم وسبائكه بطرق اللحام الانصهاري ولحام المقاومة الكهربائية ولحام الحالة الصلبة ولحام القصدبر ويفضل طريقتي لحام MIG وTIG في لحام سبائك الالمنيوم لامكانية تكوين الحرارة والتيار العاليين للحام (Stuart,1997) ويمكن استعمال لحام القوس الكهربائي النقطي بقطب التنكستن المحمي بالغاز الخامل (TIG Spot) بدلاً من لحام المقاومة الكهربائية أو أستعمال البراشيم لربط صفائح الألمنيوم الرقيقة لأن عملية اللحام تعطي لحاماً متينا ومترابطاً وخال من العيوب والاجهادات وتكون نوعية اللحام أفضل واكثر متانة من الربط بالبرشام لأن الثقب في حالة البرشام يعتبر منطقة تمركز الاجهادات مما يؤدي الى ضعف أوانخفاض خواص الصفائح المربوطة اوالمبرشمة (Riveted) (Konolovanov, 1986– Houldcroft,1977). ونظراً للسرعة العالية للحام وانتاج نوعية لحام جيدة وذات جودة ومتانة عالييتن جعلت طريقة اللحام بالقوس الكهربائي بقطب التنكستن المحمي بالغاز الخامل (TIG) من أكثر العمليات جاذبية في

لحام صفائح الألمنيوم وسبائكه علاوة على أمكانية لحامه بدون أستعمال معدن حشو(Filler Metal) أو قد يستخدم معدن حشو خلال عملية اللحام وهذا يعتمد علىسمك الشغلة، وتصميم الوصلة وخواص معدن اللحام. ويمكن أجراء عملية اللحام يدوياً أو أوتوماتيكياً (Brumpauph, 1973 –Gupta, 1995). لذا ظهرت الحاجة الى دراسة لحام TIG Spot النقطي في لحام سبائك الألمنيوم–معنيسيوم الغير قابلة للتعامل الحراري وهي من سبائك (سلسلة 5XXX) وذلك لأستخداماتها الصناعية الواسعة وتطبيقاتها المهمة في مجال تكنولوجيا اللحام مثل مصانع الطائرات وفي صناعة الاجهزة الكيمياوية وفي صناعة العدد والمستلزمات الغذائية وغيرها (http://www– Little, 1973) .

يهدف البحث الحالي الى دراسة تأثير بعض متغيرات لحام (TIG Spot) من تيار وزمن لحام وطول القوس على الخواص الميكانيكية (قوة القص العظمى والصلادة الدقيقة) للوصلات الملحومة لسبيكة المنيوم–مغنيسيوم نوع (5052-O) .

الجزء العملي

المواد المستخدمة

تم أستخدام صفائح من سبيكة (المنيوم– مغنيسيوم) نوع (5052-O) في حالة ملدنة (Annealed) وبسمك (1mm) وتم أجراء التركيب الكيمياوي للسبيكة بأستخدام جهاز التحليل الطيفي (Spectrometer ARL) وكذلك تم تحديد بعض الخواص الميكانيكية للسبيكة وكما موضح في **الجدولين (1) (2)** .

جدول (1) التركيب الكيمياوي لسبيكة(الالمنيوم–مغنيسيوم)(O- 5052)

Wt %	Mg	Mn	Si	Fe	Cu	Cr	Zn	Al
5052-O	2.26	0.0042	0.215	0.215	0.04	0.30	0.0025	96.9

جدول (2) بعض الخواص الميكانيكية لسبيكة (الالمنيوم–مغنيسيوم) (5052-O)

Alloy 5052-O	Yield point (Mpa)	Tensile strength (Mpa)	Elongation El%	Hardness (HB)
	88.6	190.5	23	33

تحضير عينات اللحام

تم تحضير عينات اللحام بتقطيع الصفائح المستلمة من سبيكة (5052-O) الى شرائح بطول 100mm وعرض 25mm وبسمك 1mm. **الشكل (1)** يبين أبعاد العينات لوصلة اللحام التراكبية. أجريت عملية التنظيف الكيمياوي للشرائح المحضرة بأستخدام خليط من الحوامض ($85\%H_2O + 10\%HNO_3 + 5\%HF$) (Metals H.B., 1985) ، حيث أغمرت هذه الشرائح (المنطقة المراد لحامها فقط) في هذا الخليط لمدة (2min) وذلك لازالة طبقة الأوكسيد الموجودة على سطح العينة بعد ذلك أخرجت الشرائح من خليط الحوامض وغسلت بالماء ثم جففت بالهواء .

عملية اللحام

أجريت عملية اللحام للشرائح المحضرة من سبيكة (5052-O)(بعد اجراء التنظيف الكيمياوي لها مباشرة) بأستخدام ماكنة لحام من نوع (G350-1)
(Messer Grieshiem Multiwig) حيث كانت ظروف عملية اللحام كما يلي:
معدل جريان غاز الأركون (15litre/min) ، قطر قطب التنكستن (3.2mm) من النوع(EWTh2) الحاوية على (2% ThO2) ، زاوية رأس القطب (60°) ، تيار مستمر بقطبية مباشرة (DCSP) بقيم تيار تراوحت من.Amp(50-140) لفترات زمنية من sec (1-8) وأطوال أقواس مختلفة
mm (4.8,3.2,1.6) لكل حالة.

الأختبارات الميكانيكية والفحوصات المجهرية

أولاً: أختبار قوة القص

تم أختبار جميع العينات الملحومة نقطياً بطريقة (TIG) (لحام نقطة واحدة في كل عينة) بأستخدام جهاز أختبار الشد (Instron Machine) وذلك لأختبار قوة القص (مقاومة القص) للعينات الملحومة. أعتمدت المواصفات العالمية (ISO R147) لأيجاد قوة القص العظمى لوصلات اللحام النقطي واستخدامها كمعيار في تحديد الظروف المثلى لمتغيرات عملية اللحام بطريقة لحام القوس الكهربائي بقطب التنكستن (TIG Spot) لصفيحة من سبيكة (Al-Mg).

ثانياً: أختبار الصلادة الدقيقة

تم أستخدام جهاز فيكرز (Vickers) لقياس الصلادة المجهرية الدقيقة لتحديد تأثير ظروف اللحام على منطقة اللحام والمنطقة المتأثرة بالحرارة (HAZ) .وتم اخذ المقطع العرضي لوصلة اللحام. تم تسليط حمل مقداره

(20) غرام وتم قياس معدل قطر الأثر الناتج وحساب الصلادة على طول الخط من نقطة اللحام الى المعدن الأساس وتم تطبيق القانون الآتي:

$HV = 1.8544\ P/d^2$, HV=(Kgf/mm²) الصلادة الدقيقة

معدل قطر الأثر d=(mm) , الحمل المسلط P=(Kgf)

ثالثاً: فحص البنية المجهرية

تم تحضير العينات الملحومة(TIG Spot) للفحص المجهري وذلك بأخذ المقطع العرضي لوصلة اللحام ومن ثم عمل لها أسناد على البارد (Cold mounting) ثم أجري لها عمليات التحضير من تنعيم بدرجات نعومة مختلفة(1200,1000,500,320) وصقل بأستخدام قماش صقل ومعجون ماس ذو حجم حبيبي (1µm) ثم غسلت العينات بالماء والكحول وجففت. وبعد ذلك أظهرت بأستعمال محلول أظهار من نوع (Keller solution)(25%HCL+15%HF+10%HNO3+50%H2O) حيث غمرت العينات في المحلول لفترة (20) ثانية ثم غسلت بالماء والكحول وجففت باستخدام مجفف هواء. وأستخدم الفحص لأظهار البنية المجهرية لمنطقة اللحام ومنطقة (HAZ) والمعدن الأساس.

النتائج والمناقشة

تأثير تيار وزمن اللحام

ان لتيار وزمن اللحام تأثيراً مباشراً على كمية الحرارة المتولدة من القوس الكهربائي النقطي بقطب التنكستن ولكن زمن اللحام اقل تأثيراً مقارنة بالتيار أذ يعتبر التيار من أهم العوامل المؤثرة على مقاومة اللحام لأن زيادة التيار يؤدي الى زيادة كمية الحرارة الداخلة (Heat Input) في منطقة اللحام مما يسرع من عملية أنصهار الجزء العلوي للصفيحة وحدوث عملية التغلغل(Abbass, 2001–Haddad, 1985). يلاحظ من الشكل(2) الذي يمثل العلاقة بين تيار اللحام وقوة القص العظمى لأزمنة مختلفة ولصفائح من سبيكة (5052-O) عند طول قوس (1.6mm)، ان زيادة تيار اللحام يؤدي الى زيادة قطر نقطة اللحام وبالتالي تزداد قوة القص وهذا يتوافق مع ما توصل اليه الباحثان (Aidun and Rennett, 1985) . وعندما يكون التيار قليلا فان أنصهار المعدن بين الصفيحتينً يكون غير كافي وبذلك تكون مساحة اللحام ذات مساحة صغيرة مما يجعل قوة القص لوصلة اللحام منخفضة .

يلاحظ من **الشكل(3)** ان قوة القص تصل الى قيمتها العظمى ثم تنخفض بسبب الأفراط في التسخين وتكوين حبيبات كبيرة وخشنة وكذلك زيادة زمن وتيار اللحام تؤدي الى حدوث ظاهرة التناثر (Splashing) وخروج وأندفاع المعدن المنصهر للصفيحة العلوية الى خارج منطقة اللحام وبالتالي فشل الوصلة عند قوة قص أقل

مع أستمرار زيادة قطر منطقة اللحام كما موضح في **الشكل(4)** الذي يبين العلاقة بين زمن اللحام وقطر منطقة اللحام لسبيكة (5052-O) ولطول قوس (1.6mm) عند تيارات لحام مختلفة .

ومن الأشكال السابقة نجد ان أفضل لحام الذي يعطي أعلى قيمة لقوة القص هي(2.4KN) عند تيار لحام (90Amp) وزمن لحام (7sec) ولطول قوس (1.6mm) وكان قطر منطقة اللحام(13.5mm) .

تأثير طول القوس

ان زيادة طول القوس تؤدي الى زيادة المسافة بين قطب التنكستن ووصلة اللحام مما يؤدي الى زيادة في قيم فولتية القوس وبالتالي سينخفض التيار وينخفض معه معدل أنصهارالمعدن بين الصفيحتين وبذلك تكون مساحة اللحام صغيرة مما يجعل قوة القص لوصلة اللحام منخفضة(Lancaster,1986). وكذلك فان نقصان طول القوس يؤدي الى انخفاص فولتية القوس وزيادة التيار وبالتالي زيادة كمية الحرارة المتولدة والداخلة الى وصلة اللحام. ولكن بسبب التوصيلية الحرارية العالية للالمنيوم وسبائكه فان فقدان وتشتيت الحرارة المتولدة من القوس الكهربئي يكون كبيرا لذا وجب زيادة تيار وزمن اللحام لغرض توليد الطاقة الحرارية الكافية والمناسبة لأنتاج وصلة لحام متينة وذات قوة قص عالية(George,2003- Lu, 1988).

والشكل (5) يوضح تأثير طول القوس على قوة القص العظمى لوصلات اللحام لسبيكة (5052-O)عند تيار (90Amp) ولأزمنة مختلفة وأطوال أقواس (4.8,3.2,1.6) ويلاحظ من الشكل السابق ان أفضل طول قوس كان (1.6mm) حيث أعطى أعلى قوة قص (2.4KN) عند زمن (7sec) .

الصلادة الدقيقة والبنية المجهرية

تم قياس الصلادة الدقيقة لكل من منطقة اللحام (W.M) والمنطقة المتأثرة بالحرارة (HAZ) عند الظروف المثلى لمتغيرات اللحام التي أعطت أعلى قوة قص لوصلة اللحام **والشكل(6)** يبين توزيع الصلادة الدقيقة عبر المقطع العرضي لوصلة اللحام لسبيكة (المنيوم- مغنيسيوم) (5052-O) وكانت قيمة الصلادة (HV53.5) عند مركز وصلة اللحام أعلى من صلادة المنطقة المتأثرة بالحرارة (HAZ) والسبب في ذلك يعود الى كمية الحرارة العالية في مركز منطقة اللحام وكذلك معدل التبريد السريع نتيجة لقابلية الألمنيوم العالية للتوصيل الحراري مما يؤدي الى تكوين حبيبات ناعمة بينما تعاني منطقة (HAZ) من نمو حبيبي مما يسبب أنخفاض الصلادة بصورة تدريجية عند الأبتعاد عن منطقة اللحام وصولاً الى المعدن ألأساس. أضافة الى ظهور الاطوار (Al_3Mg_2) و (FeSi) في وصلة اللحام كما بينت نتائج حيود الأشعة السينية. **والشكل (7)** يبين البنية المجهرية لوصلة اللحام لسبيكة (ألمنيوم – مغنيسيوم) نوع (5052-O) ومناطق اللحام المختلفة .

ألأستنتاجات

1- تمتاز السبيكة (5052-O) بقابلية لحام جيدة بطريقة (TIG Spot) .

2- ظروف اللحام المثلى لسبيكة (5052-O) كانت عند تيار (90Amp) وزمن (7sec) وطول قوس (1.6mm) لسمك (1 mm) اذ أعطت اعلى قوة قص لوصلة اللحام (2.4KN).

3- تزداد قيم قوة القص العظمى لوصلة اللحام مع أزدياد تيار وزمن اللحام الى قيمة عظمى ثم تنخفض بعدها عند التيارات العالية والأزمنة الطويلة .

4- تزداد قيم قوة القص العظمى عند نقصان طول القوس(المسافة بين قطب التنكستن والوصلة).

5- يزداد قطر منطقة اللحام مع زيادة تيار وزمن اللحام وتستمر بالزيادة لحين خروج المعدن المنصهر وأندفاعه خارج منطقة اللحام عند التيارات العالية وألأزمنة الطويلة.

6- تمتلك وصلة اللحام صلادة عالية بلغت (53.5HV) عند مركز نقطة اللحام ثم تقل الصلادة الدقيقة تدريجياً عند الأبتعاد عن منطقة اللحام بأتجاه المعدن الأساس .

المصادر

Abbass F. (2001), Study of TIG Spot in (Al-Mn) Alloy, MSC. Thesis , University of Technology ,.

Aidun D.K. (1985), Effect of Resistance Welding Variables On The Strength Of Spot Welded 6061-T4 Alloy, Welding Journal , Vol.64, No.12 , , PP.15-25.

Bolton W. (1998), Engineering Materials Technology, Butter Worth ,3rd ed. ,.

Brumpauph J.E. 1973" Welders Guide and Handbook " , Howard Wsas Co..

Filler Alloy Selection For aluminum welding, Google's cache of http://www.alcotec.com/atfas.htm.

George Rowe- Alcotec Wire Corporation (2003), Essential Variables For MIG Welding Aluminum ,Svetsaren ,The ESAB Welding and Cutting Journal ,Vol.58, No.2 , PP.12-13.

Gupta R.P. (1995), Welder,Tech. India Publications,.

Haddad G.N. (1985), Temperature Measurement in Gas Tungsten Arc Welding, Welding Journal , Vol.64, No.12 , ,PP.339S-342S.

Houldcroft P.T. (1977), Welding Process Technology, Cambridge University Press,.

Khanna O.P. (1980), Welding Technology, Dhawpatria Sans,.

Konolovanov U.A. (1986), Helium − Arc Spot Welding of Aluminum , Sheet Structure, Welding Production , No.4 , , PP.14-15.

Little R.L. (1973), Welding and Welding Technology " McGraw Hill ING ,.

Lancaster J.F. (1986), The Physical Of Welding, 2nd edition , Bergamon Press, London,.

Lu M .and Kou S. (1988) , Power and Current Distribution in Gas Tungsten Arcs , Welding Journal , Vol.67 , No.2 , PP.29S-34S.

Metals Handbook (1985), Aluminum , Cleaning and Finishing , Vol.5 9th ,.

Stuart W.G. (1997), Advanced Welding, Macmillan Press LDT ,1st Published, Printed in Hong Kong,.

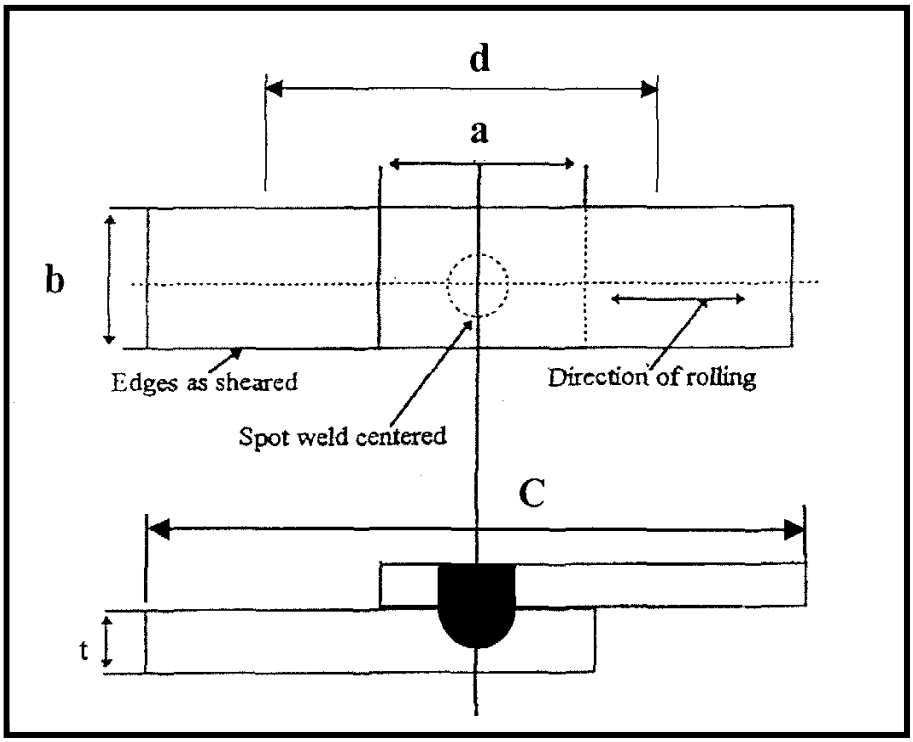

a=over lapping =25 mm, b= width=25mm, c=length=175mm
d=clamping distance=95mm, t=thickness=1mm

شكل (1) وصلة اللحام التراكبيـــة

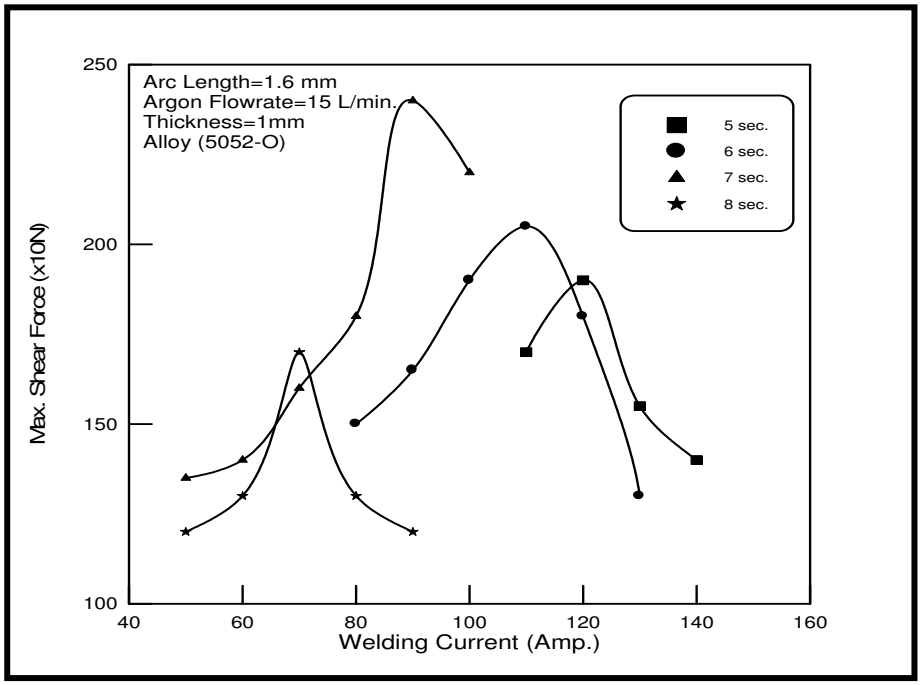

شكل (2) العلاقة بين تيار اللحام وقوة القص العظمى لوصلات لحام السبيكة (5052-O) لازمنة مختلفة ولطول قوس(1.6mm)

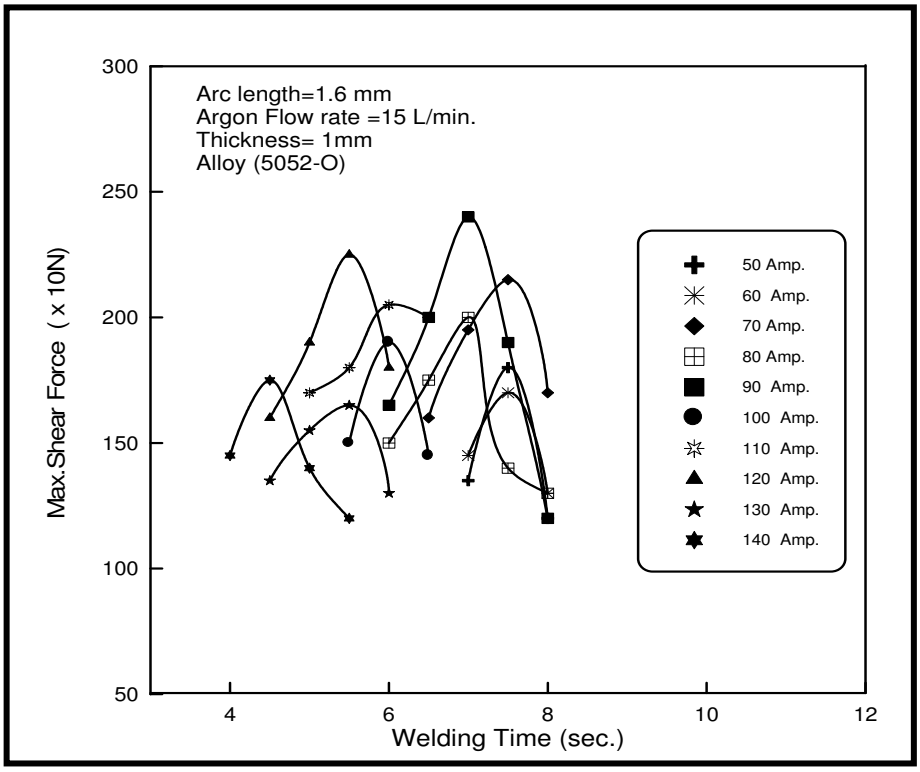

شكل (3) العلاقة بين زمن اللحام وقوة القص العظمى لوصلات لحام السبيكة (5052-O) ولطول قوس (1.6mm) عند تيارات لحام مختلفة

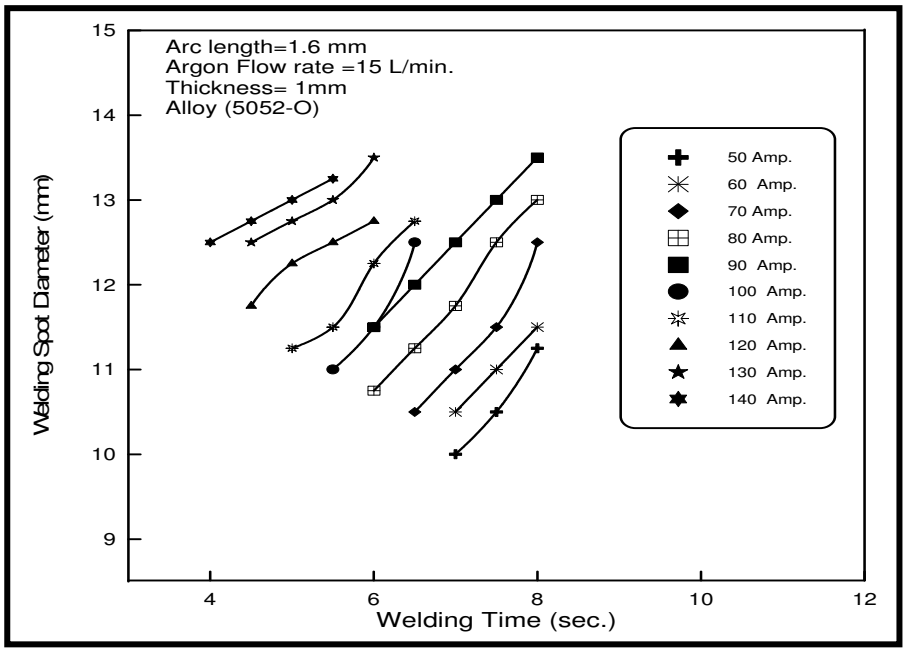

شكل (4) العلاقة بين زمن اللحام وقطر منطقة اللحام لوصلات لحام السبيكة (5052-O) ولطول قوس (1.6mm) عند تيارات لحام مختلفة

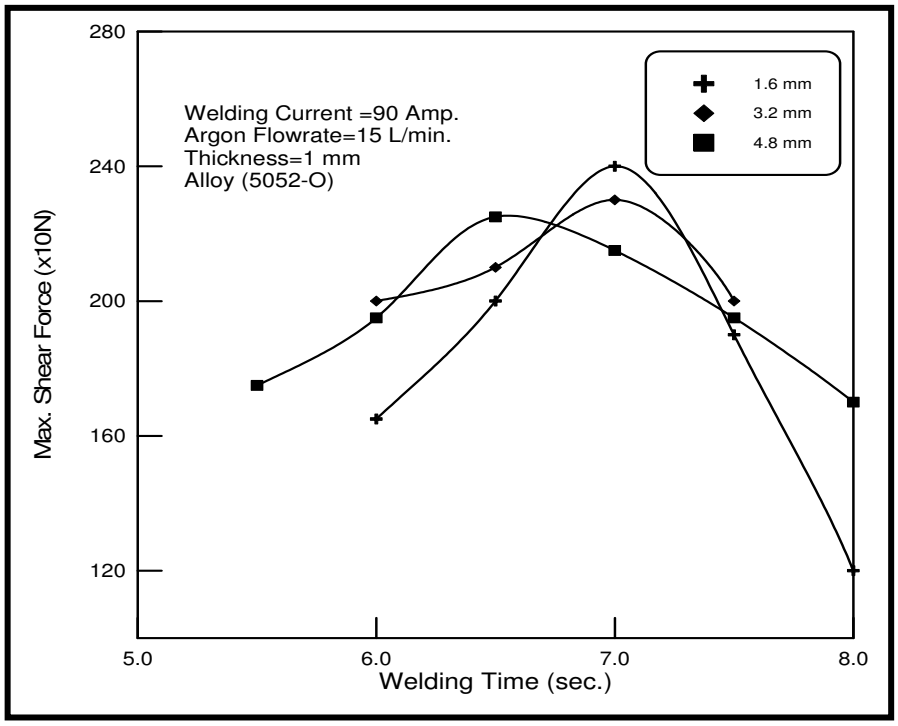

شكل (5) العلاقة بين زمن اللحام وقوة القص العظمى لوصلات لحام السبيكة (5052-O) ولاطوال اقواس مختلفة عند تيار لحام (90Amp.)

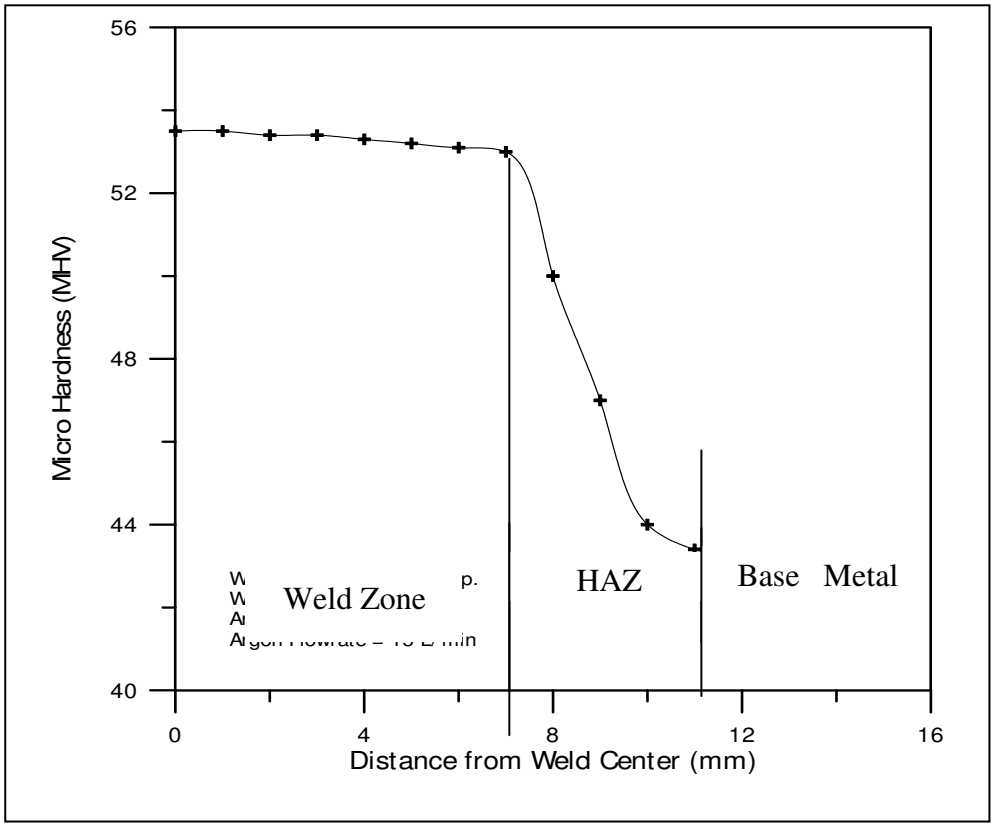

شكل (6) توزيع الصلادة الدقيقة لوصلة اللحام لصفيحة من سبيكة (5052-O)

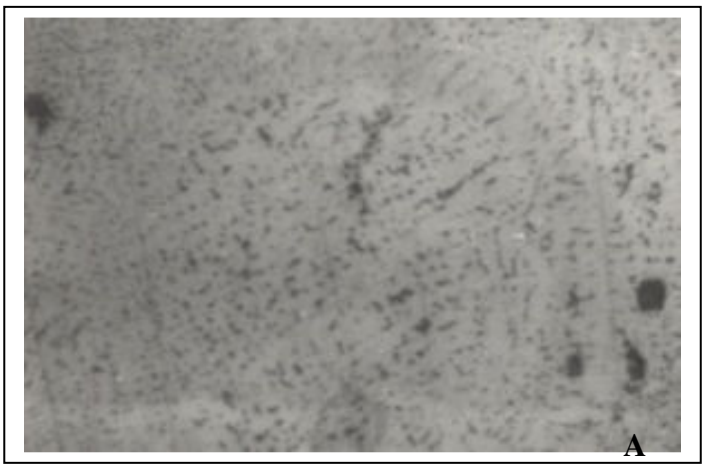

السبيكة الاساس
قوة التكبير X 380

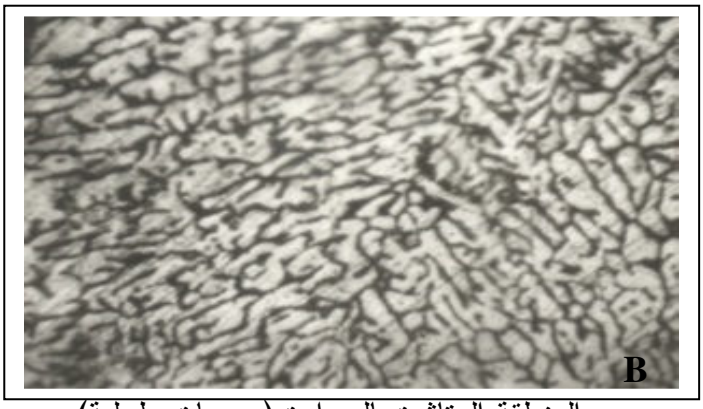

المنطقة المتاثرة بالحرارة (حبيبات طولية)

قوة التكبير X 380

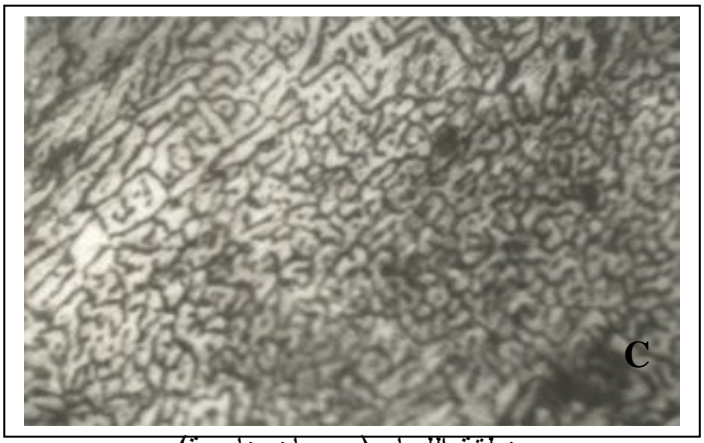

منطقة اللحام (حبيبات ناعمة)

قوة التكبير X 380

الشكل (7) البنية المجهرية لوصلة لحام السبيكة (5052-O)

محلول الاظهار نوع(Keller solution)

PREDICTION OF AERODYNAMIC COEFFICIENTS OF MISSILE USING PANEL METHOD

Prof. Kamil I. AL-Doulaimi College of Miltary
Asst. Prof Hussain Y. M. **Wisam Mohsin Jabur** College of Eng. / University of Baghdad

ABSTRACT
The low order panel method with Neumann boundary condition have been used to predict the normal force curve slope, the pitching moment curve slope, the center of pressure location and the aerodynamic load distribution for missile in compressible, steady flow. The wing-body-canard interference problem have been solved using two schemes (iterative method and internal singularity method) both are based on the panel method. The normal force curve slope, the pitching moment curve slope and the center of pressure location for a given missile has been predicted using the present numerical method and the DATCOM technique.

الخلاصة

تم استخدام طريقة الأواح ذات الدرجة الواطئة مع الظروف المحيطة لنيومان وذلك للتنبا بميل المنحني للقــوة العمودية ، عزم الطول، موقع مركز الضغط وتوزيع الأحمال الايروديناميكية لصاروخ في جريان انضغاطي مستقر، أن مشكلة تداخل الجناح مع الجسم ومع الزعنفة الجانبية تم حلها بواسطة طريقتين (طريقة التكــرار وطريقة الوحدة الداخلية) والطريقتان اساسها طريقة الألواح . أن ميل منحي القوة العمودية ، عزم الطول ، وموقع مركز الغضط للصاروخ المعتمد تم التنبأ به باستخدام الطريقة العددية الحالية وتقنية DATCOM

KEY WORDS
Missile aerodynamic, panel method, wing-body aerodynamic, prediction of aerodynamic coefficients, potential flow simulation.

INTRODUCTION

Preliminary design and aerodynamic assessment of missile configuration require a rapid and accurate method to predict the aerodynamic coefficients. Accurate calculation of flow field around complete missile is essential to provide aerodynamic data for the structural designer, the performance engineer and the designer of the control system. Three different methods can be employed to determine the missile aerodynamics: 1) wind tunnel tests, 2) Handbooks, 3) C.F.D techniques. Current trends in the design of missile emphasize renewed interest of industry in computational methods capable of supporting aerodynamic design. Within existing teehniques in this region, finite difference methods solving either the full potential or Euler's equators have made the most significant advances in recent years. However, the lack of efficient numerical procedures to generate the computational grid around arbitrary three-dimensional configurations is still a major

problem area for these methods. The Panel Method has been demonstrated to be the most efficient approach to the solution of inviscide flows around arbitrarily complex three-dimensional configurations, since it has the distinct advantage over the alternative C.F.D techniques (finite difference, finite element, etc.) in the fact that the unknowns are situated on the surface of the configuration and not throughout the external space. Therefore, the panel method is very attractive for routine use and amenable for use on medium or small computing facilities since it requires much less programming effort and computing time if compared with the other C.F.D techniques.
The purpose of the present work is to predict the normal force curve slope, pitching moment curve slope and the center of pressure location for a given missile configuration at steady, subsonic and compressible flow using the low order panel method with Numann boundary condition.

PANEL METHOD

The Panel Method is based on distributing singularity elements on the wetted surface of the body around whith the flow characteristics to be found This will reduce the solution to finding the strength of each singularity element that have been distributed.
The incompressible, irrational continuity equation, in terms of the total potential ϕ^* 0 is presented in Ref.[Joseph Katz, 1991] as:

$$\nabla^2\phi^* = 0 \qquad (1)$$

where the total potential 0 is described as ϕ^*

$$\phi^* = \phi + \phi_\infty \qquad (2)$$

Following Green's identity, the general solution to equation (1) can be constructed by sum of sources a and doublets μ:

$$\phi^*_{(x,y,z)} = \frac{1}{4\pi}\int_{body+wake} \mu n.^{\varpi}\nabla(\frac{1}{r})ds - \frac{1}{4\pi}\int_{body} \sigma(\frac{1}{r})ds + \phi_\infty \qquad (3)$$

The Neumann Boundary Condition has been employed with Eq.(3), where a zero normal velocity componen $\partial\phi^* l\partial n = 0$ is directly specified on the surface:

$$\nabla(\phi + \phi_\infty).n^{\varpi} = 0 \qquad (4)$$

Where ϕ^* is the perturbation potential consisting of the two integral terms in Eq.(3). Satisfying this boundary condition in Eq. (3) results in:

$$\frac{1}{4\pi}\int_{body+wake} \mu.^{\varpi}\nabla\left[\frac{\partial}{\partial n}(\frac{1}{r})ds - \frac{1}{4\pi}\int_{body} \sigma\nabla(\frac{1}{r})ds + \nabla\phi_\infty\right].n^{\varpi} = 0 \qquad (5)$$

By knowing the strength of the singularity elements that have been distributed, Eq. (5) will describe the velocity field every where. If we apply this integral equation to each surface panel, and further assume that the singularity strength on each panel is constant, then a system of relatively simple algebraic equations can be obtained in matrix form as:

$$[a_{ij}][k_j] = [-]Q^{\omega}_{\infty}.n^{\varpi}_i \qquad (6)$$

Where k is any singularity element, a_{ij} is the influence coefficient which its physical means The normal velocity induced by a unit strength singularity element at a point in the flow field

[Chun-Mo Lee, 1984]. The only unknown in this matrix equation is the N singularity element strength. The solution of this matrix by Gaussian elimination method results in these unknowns. Any other standard matrix method can be used Since these algebraic equations has a dominated diagonal because the influence of the singularity element on it self is the maximum.

COMPRESSIBILITY EFFECT

The Prundth, JIauert and Gothert rule [Herman Schlichting , 1979] is applied to treat the compressibility effect. This approach is transforming the real body in compressible flow filed to an equivalent body in incompressible flow field by multiplying the Y and Z dimensions of the body and the angle of attack by β:

X_{inc} $\alpha_{\text{inc}} = \beta\alpha$

$Y_{inc} = \beta Y$ $\cot\Lambda_{\text{inc}} = \beta \cot \Lambda$

$Z_{inc} = \beta Z$

Where $\beta = \sqrt{1 - M_{\infty}^{2}}$

After the incompressible flow solution due to this equivalent body is determined, the transmission is reversed to the compressible plane by dividing the resulting aerodynamic coefficients by β^2

NUMERICAL PROCEDURE

Each configuration (wing-body or wing-body-canard) is subdivided into a non-lifting component (body) and lifting components (wing and canard). The non-lifting component is simulated by a constant strength quadrilateral source elements, while the lifting component is simulated by either horseshoe vortex or a vortex ring singularity elements.

THE BODY

The method pioneered by Hess and Smith [Hess, J. L., 1967] forms the basic solution for the body in this work, where the body is replaced by a large number of flat panels, each one carrying a constant strength, quadrilateral source singularity element as in **Fig.(1)**. The body is assumed to be cylindrical with circular cross section and described by number of points on its surface. These points are organized in sections and meridians as shown in **Fig.(l),** short straight lines connecting these points forming quadrilateral panels with the exception of certain regions where the lines converge and the elements are triangular, each panel is a constant strength source singularity element and contains a collocation point placed in the centroid of the panel area.

After obtaining the strength of each source element have been distributed on the body surface the total perturbation velocity components that induced at any collocation point is obtained by summing the perturbation velocities that induced by every source element at this collocation point. The total velocity Q at any collocation point is obtained by summing the total perturbation velocity q and the free stream velocity Q_{∞} that acting on this panel and by using Bernoulli equation [Joseph Katz, 1991], the pressure coefficient at any panel is optioned as:

$$C_{pi} = \frac{P_i - P\infty}{0.5\rho Q_{\infty}^{2}} = 1 - \frac{Q_i^2}{Q_{\infty}^{2}} \qquad (\text{i} = 1 \text{ to NB}) \qquad (7)$$

where

$$Q_i = q_i + (Q_{\infty})_i \qquad (8)$$

The normal force coefficient, the pitching moment coefficient around the nose apex as shown in **Fig.(2)**, and the center of pressure are calculated as:

$$C_N = \frac{1}{S_{ref}} \sum_{i=1}^{NB} C_{Pi} A_i nz_i \qquad (9)$$

$$C_m = \frac{1}{S_{ref} L_{ref}} \sum_{i=1}^{NB} C_{pi} A_i \left[nx_i . (Z_C)_i + nz_i . (X_C)_i \right] \qquad (10)$$

$$\frac{X_{CP}}{L_{ref}} = -\frac{C_m}{C_N} \qquad (11)$$

THE WING AND THE CANARD

The wing and the canard are must be uncambered with zero thickness and simulated by distributing either horseshoe vortices or vortex rings on the surface. The main advantage of these singularity elements is in the simple programming effort required, in addition, they are capable of modeling the effect of wing planform shapes on the fluid dynamic load [Joseph Katz, 1991]. For wingbody configurations, the wing is simulated by distributing horseshoe vortices on the wing surface. While for wing-body-canard configurations, the lifting components (wing and canard) are simulated by distributing a vortex ring singularity elements, since the wake shape for this type of elements can be modeled, where this property is required to simulate the effect of the canard's wake on the wing behind.

HORSESHOE VORTEX

The wing planform is defined by the span, leading edge and trailing edge sweep angles, and divided into NW trapezoidal flat panels with side edges parallel to the global X-axes as shown in **Fig.(3).** Each panel is defined by the coordinates of it's four corners points, and approximated by a flat plate contain a horseshoe vortex. A typical horseshoe vortex element is shown in **Fig.(4)** where the bound vortex is placed at the panel quarter chord line and the collocation point at the center of the panel's , , three-quarter-chord line. The trailing vortices are placed parallel to the global X-axes. The vortex strestr is assumed to be constant for the horseshoe element and a positive circulation is defined as shown in **Fig.(4)**. The lift on each panel containing a horseshoe vortex element is obtained by using the Kutta-Jaukowski theorem [Jack Moran, 1984]:

$$L_i = \rho \nabla y_i Q_\infty \Gamma_i \qquad (\text{i} = 1 \text{ to NW}) \qquad (12)$$

Where ∇y_i is the span of each wing panel. The overall wing lift coefficient, moment coefficient around the wing root cord apex and the center of pressure location are:

$$C_L = \frac{1}{0.5 Q\infty S_w} \sum_{i=1}^{NW} \nabla y_i \Gamma_i \qquad (13)$$

$$C_m = \frac{1}{0.5 Q\infty S_w Cr} \sum_{i=1}^{NW} \nabla y_i \Gamma_i . (X_C)_i \qquad (14)$$

$$\frac{X_{C.P}}{Cr} = \frac{C_m}{C_L} \qquad (15)$$

Where $(XC)_i$ is the global X-coordinate of the center point of panel i.

VORTEX RING

As have been stated before, this singularity element has been employed with the wing-body-canard configurations. The canard planform is divided into NC trapezoidal flat panels in the same manner that have been employed with the horseshoe vortex singularity element, each panel contains a vortex ring singularity element as shown in **Fig.(5).** The leading segment of the vortex ring is placed on the panel's quarter chord line. The collocation point is placed at the center of the Three-quarter

chord line. The normal vector $\overset{\omega}{n}$ is defined at this point and positive circulation is defined as shown in **Fig.(5).**

The canard's wake is aligned in parallel with the free stream and divided into five panels in the stream wise, each wake panel contains a vortex ring with strength equals to the strength of the shading panel at the canard trailing edge as shown in **Fig.(5).** The overall length of the wake is twenty times the span. The wing planform have been divided into NW trapezoidal panels in the same manner that described above, with a deference that the span of each wing panel was made equal to the span of the shading canard panel, as shown in **Fig.(5)**. Also, the wing wake was treated in the same way that has been employed with the canard's wake. The Kutta condition is satisfied along the trailing edge by setting the strength of each wake vortex equal to the strength of the shading panel at the trailing edge, i.e.:

$$\Gamma_W = \Gamma_{T.E} \qquad (16)$$

The lift force that acting on each panel containing a vortex ring singularity element have been calculated by using another form ofKutta-Jaukowski theory [7]:

$$L_{ij} = \rho Q_\infty (\Gamma_{i,j} - \Gamma_{i-1,j}) \nabla y_{ij} \qquad (i > 1) \qquad (17)$$

Where j is a spanwise counter which have values from one to the number of the panels in the spanwise, and i is a cordwise counter which have values from one to the number of the panels in the cordwise as shown in **Fig.(7)**, this figure also shows the sequence of scanning for wing or canard panels to obtain the lift on each panel from Eq.(16). Eq.(16) is applied to the panels that placed after the leading edge panel (i.e. i>l), while for the leading edge panels (i.e. i=l), the lift is calculated as:

$$L_{ij} = \rho Q_\infty (\Gamma_{i,j} \nabla y_{ij} \qquad (i = 1) \qquad (18)$$

The total lift and moment acting on the wing are:

$$C_L = \frac{\sum_{K=1}^{NW} L_{ij}}{0.5 \rho Q_\infty^2 S_w} \qquad (19)$$

$$C_m = \frac{\sum_{K=1}^{NW} L_{ij} . (X_C)_{ij}}{0.5 \rho Q_\infty^2 S_w Cr} \qquad (20)$$

WING-BODY-CANARD INTERFERENCE

The interference between the canard and the body is similar in its physical nature to the wing-body interference. In addition, the influence of the downwash behind the canard on the wing lift has been

taken in account. Three different methods have been employed to describe the wing-body-canard interference:

ITERATIVE METHOD

The following steps can describe it:

1- In the free stream, calculate the strength of each source panel on the fuselage surface.
2- In the flow field interfered by the fuselage, calculate the strength of each vortex panel on the surface of the canard.
3- Using the vortex and source strength, which obtained from the steps (1) and (2), remodel the flow field by superposition and calculate the strength of each vortex on the wing.
4- Using the vortex strength of the canard and the wing, which obtained from step (2) and (3), remodel the flow field by superposition and recalculate the strength of each source panel on the fuselage surface.
5- Re-obtain the steps (2), (3) and (4) four times.

INTERNAL SINGULARITIES METHOD

A schematic view of this method is shown in **Fig.(8).** Vortex panels have been distributed inside the body in the wing-body junction region, and extended from the wing-body junction line to the body longitudinal axes. The strength of each internal panel vortex equals the strength of the neighboring wing root panel vortex. The same treatment is employed for the canard-body interference.

DATCOM SOLUTION

The DATCOM solution [DATCOM , 1972] is employed to solve the interference problem for the wing-body-canard configuration only. The aerodynamic forces acting on each isolated component of the configuration (wing, body and canard) are predicted from the numerical solution of the panel method. Therefore, the final solution that resulting from this technique is not depending solely on the DATCOM. The lift curve slope and the pitching moment curve slope around the center of gravity for a wingbody-canard configuration can be obtained according to this scheme as follows:

$$C_{La} = (C_{La})_e^{'}\left[K_N + K_{W(B)} + K_{B(W)}\right]\frac{S_e^{'}}{S^{'}} + (C_L)_e^{''}\left[K_N + K_{W(B)} + K_{B(W)}\right] \cdot \frac{q^{''}}{q_\infty}\frac{S^{''}}{S^{'}}\frac{S_e^{''}}{S^{''}} + (C_{La})_{W^{''}(V)} \qquad (21)$$

$$C_{ma} = -\frac{X_{c.g} - X^{'}}{\bar{C}^{'}}\left[K_N + K_{B(W)} + K_{W(B)}\right](C_{La})_e^{'}\frac{S_e^{'}}{S^{'}} - \frac{X_{e.g} - X^{''}}{\bar{C}^{''}}\left(\frac{\bar{C}^{''}}{\bar{C}^{'}}\right)\left\{\left[K_{B(W)} + K_{W(B)}\right]^{''}(C_{La})_e^{''}\frac{S_e^{''}}{S^{''}}\frac{S^{''}}{S^{'}}\frac{q^{''}}{q_\infty} + (C_{La})_{W^{*}(V)}\right\} \qquad (22)$$

The parameter $(CL_a)_{W^{*}(V)}$ represents the effect of canard voracity on the wing lift.

OVERALL LOAD CALCULATIONS

Since the strength of the singularity elements that have been distributed on each component (wing, body and canard) are obtained after solving the interference problem by either the iterative method or the internal singularity method, the aerodynamic loads acting on a wing-body-canard or a wingbody configuration can be calculated. For a wing-body-canard configuration, the total velocity Q at any collocation point on the body surface is obtained by summing the total perturbation

velocity components induced by the body source elements, the wing vortex elements and the canard vortex elements with the free stream velocity components in the local coordinates of the panel under consideration. By substituting this velocity in Eq.(6), the pressure coefficient (Cp) at the panel that containing this collocation point is obtained.
The normal force coefficient and the pitching moment coefficient are obtained from:

$$C_N = \frac{1}{0.5\rho Q_\infty^2 S_{ref} L_{ref}} \left[\left[\sum_{k=1}^{NB} 0.5\rho Q_\infty^2 (C_p)_k A_k .nz_k \right]_{body} + \left[\sum_{k=1}^{NW} L_k \right]_{wing} + \left[\sum_{k=1}^{NC} L_k \right]_{canard} \right] \quad (23)$$

$$C_m = \frac{1}{0.5\rho Q_\infty^2 S_{ref} L_{ref}} \left[\left[\sum_{k=1}^{NB} 0.5\rho Q_\infty^2 (C_p)_k A_k .(nx_k .(Z_C)_k + nz_k .(X_C)_k) \right]_{body} + \left[\sum_{k=1}^{NW} L_k .(X_C)_k \right]_{wing} + \left[\sum_{k=1}^{NC} L_k .(X_C)_k \right]_{canard} \right] \quad (24)$$

Where L_k is the lift force acting on the panel k (of the wing or the canard). Since vortex ring singularity elements have been distributed on the wing and canard panels of the wing-body-canard configuration, the lift L_k is obtained in The same manner that have been described in the Eq.(16) and Eq.(17).

RESULTS AND DISCUSSION

Fig.(9) shows the sketch and the dimensions of two different missiles stated in Ref.[3]. The normal force curve slope has been predicted for missile A, while for missiles B, the center of pressure location as a ratio of the wing root cord have been predicted. Good agreement exists between the experimental data and the present numerical solution. **Fig.(10)** illustrates the sketch and paneling of the configuration of.[Joseph Katz, 1991]. The wing is trapezoidal of aspect ratio 3.2 having a leading edge sweep angle of 29.3 . The canard is located in the plane of the wing and consisted of delta and swept rectilinear surfaces respectively. The lift coefficient of canard-wing combination at incompressible flow. based on the wing area for a configuration of delta canard, swept canard and canard off is predicted by using the internal singularity method as shown in **Fig. (11), (12)** and **(13)** respectively. For all these cases, the present numerical results agree well with the experimental data. The results of the internal singularity method for the three cases together are presented in **Fig.(14),** where the configuration with the swept canard has the greatest lift coefficient, while the configuration without canard (canard off) has the smallest lift coefficient.
Fig.(15) shows the dimensions and the paneling of a given missile, which has been named as the "Typical Canard Missile", it consists of an ogive nose with cylinder body, the body is divided into two cylinders, the first has a diameter of 15.2 cm. and the second has a diameter of 11 cm. The canard is trapezoidal with 40 deg. Leading edge sweep angle, the wing is also trapezoidal with 8.6 deg. Leading and trailing edge sweep angle, mounted in the same plane of the canard. The effect of Mach number on the normal force curve slope is presented in **Fig.(16)**, a slight difference can be observed between the result of iterative method and the internal singularity method, while larger difference was noticed between the result of DATCOM solution and the both techniques of the present numerical solutions (the iterative method and the internal singularity method). However, the same trend can be noticed between the results of these three solutions. **Fig.(17)** describe the effect of Mach number on the pitching moment curve slope around the nose. A slight difference can be noticed between the results of the two schemes of the panel method solution, while the results of the

DATCOM solution is greater with the same trend as the result of the panel method. The difference between the results of the panel method and the DATCOM solution is expected, since the DATCOM solution is based on empirical relations and parameters that driven from the slender body theory. **Fig.(18)** illustrates the center of pressure location and it's variation with the Mach number. The results of the both schemes of the panel method are in similar trend as the DATCOM results, where the center of pressure is shifted backward as the Mach number increased.

Fig.(19) presents the effect of increasing the exposed wing semispan on the aerodynamic characteristics of the typical canard missile. It can be noticed that the normal force and the pitching moment curve slope is increased by increasing the wing span, since the wing area and aspect ratio is increased. This may be attributed to the increasing in the lifting force that generated on the wing (since the wing area and aspect ratio is increased). As a result of this, the center of pressure was shifted in backward direction. The nonlinear relationship which can be noticed between the results of **Fig.(19)** and the wing's exposed semispan is expected, since increasing the wing span changes it's aerodynamic characteristics, and this will effects on the wing-body and the wing-canard interference. The effect of the wing longitudinal position (as a distance from the nose apex) is shown in **Fig.(20)**, the wing was shifted in the backward direction. A slight increasing in the normal force curve slope is noticed. This is believed to be due to reducing the canard's downwash strength that acting on the wing. Since the vertical distance between the wing's surface and the canard's wake is increasing by shifting the wing in backward direction, which leads to reducing the canard's downwash strength that acting on the wing. The pitching moment curve slope is also increased and the center of pressure is shifted in backward direction. The effect of decreasing the body maximum diameter on the aerodynamic characteristics of the Typical Canard Missile is presented in **Fig.(21).** Where the normal force curve slope and the pitching moment curve slope are increased by reducing the body maximum diameter. The center of pressure is shifted backward by decreasing the body maximum diameter. This can be attributed the decrement in the nose surface area and the increment in the nose fineness ratio that happens when the body maximum diameter is decreased, also, reducing the body diameter will reduces the body upwash that acting on the canard. As a result of all this, the normal force that generated from the canard and the nose will decreases. The non-linear relationship between the predicted aerodynamic characteristics and the body maximum diameter that can be noticed in **Fig.(21)** is attributed to the non-linear relationship which already exists between the diameter and the cross-sectional area (since the reference area is the body maximum cross-sectional area). Also, change the body maximum diameter effects the canard-body interference, and change the aerodynamic characteristics of the nose (since it's fineness ratio will changed).

CONCLUSIONS

The comparisons with the experimental data tend to the following conclusions:

1- The low order panel method can predict the aerodynamic characteristics and load distribution for the complex three-dimensional configurations in the linearized, steady, subsonic flow with good accuracy.
2- Since the low order panel method have low computing cost associated with less programming effort if compared with the other C.F.D technique, it is flexible and fast.

Depending on the results that describing the effect of some geometry changes on the aerodynamic characteristics of the typical canard missile, the following conclusions are obtained.

1- The center of pressure can be shifted backwards by either increasing the wing span or decreasing the body maximum diameter, or by shifting the wing backwards.
2- Increasing the wing span shifts the center of pressure backwards with a remarkable increase in normal force curve slope. While almost the same change in center of pressure location can be achieved by shifting the wing backwards, with a difference that the increment in normal force

curve slope in this case is small if compared with the increment that was achieved in the normal force curve slope when the wing span was increased.

3- The change in the center of pressure location, which can be accomplished by changing the body maximum diameter, is much less than the change that results from changing wing span or location.

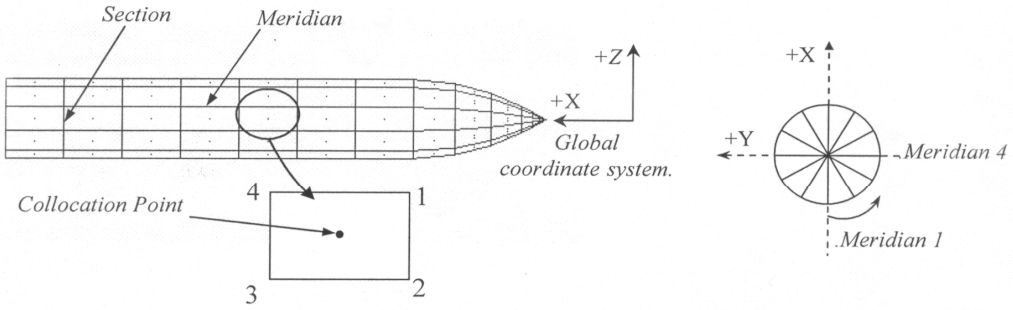

Fig.(1) Body Discretization.

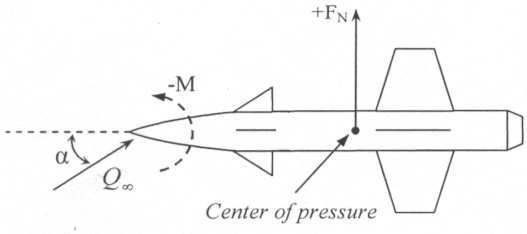

Fig.(2) Normal force and pitching moment around the center of gravity.

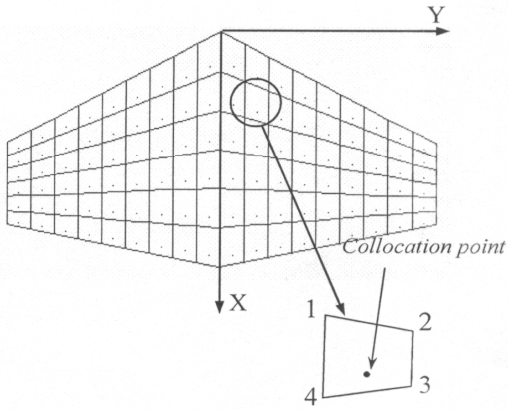

Fig.(3) Wing discretization

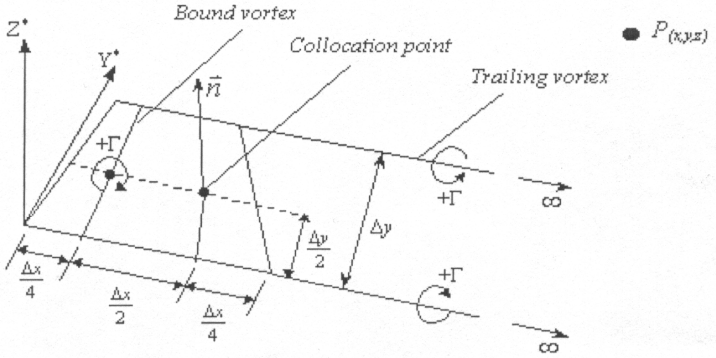

Fig.(4) A typical horseshoe vortex element.

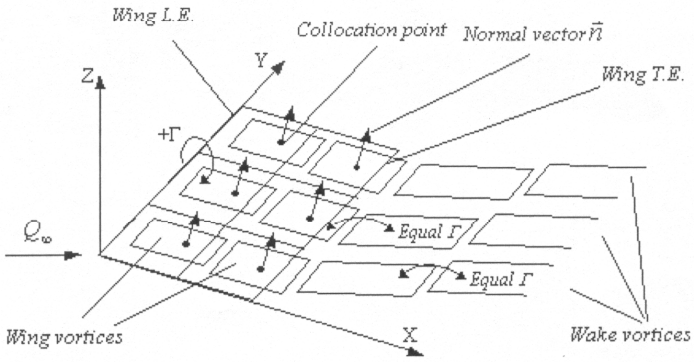

Fig.(5) Vortex ring model for a lifting surface (wing or canard).

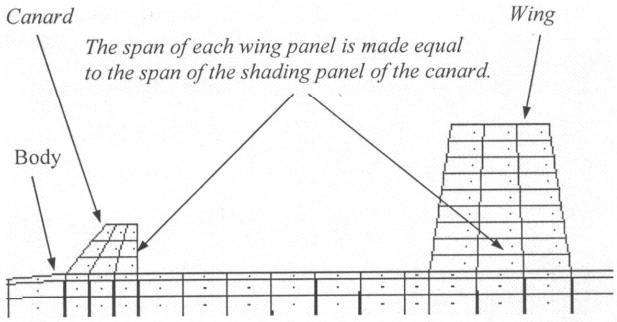

Fig.(6) Wing and canard discretization for wing-body-canard configuration.

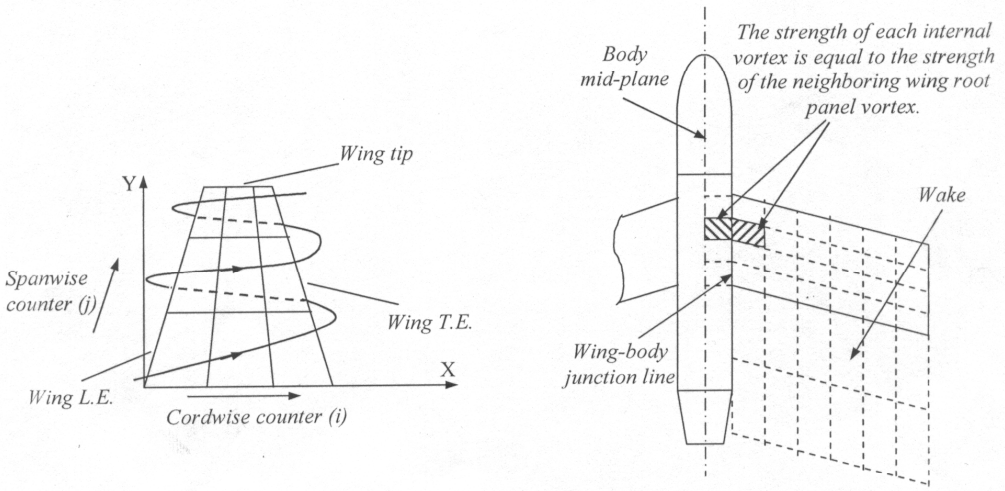

Fig.(7) Sequence of scanning the panels for the wing or the canard.

Fig.(8) Internal Singularities method.

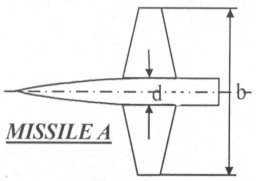

AR=3 AR_e=2.74
λ=0.4 λ_e=0.433
$\Lambda_{L.E}$=19.1° d/b=0.145
$M_\infty = 0.25$ S_e/S=.802

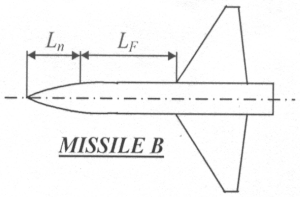

AR=3 AR_e=2.84
λ=0.143 λ_e=0.169
$\Lambda_{L.E}$=38.7° $(C_r)_e$=13.5 in.
d=5 in. b=27.4 in.
L_n=8.75 in. L_F=26.65 in.
$M_\infty = 0.6$ S_e/S=.705

MISSILE A	$C_{N\alpha}$
Experimental result [3]	66.99
Iterative method	68.273
Internal singularity method	67.96

MISSILE B	X_{CP} (inches from the nose apex).
Experimental result [3]	38.909
Iterative method	39.96
Internal singularity method	40.18

Fig.(9) Normal force curve slope and center of pressure position for two different missiles.

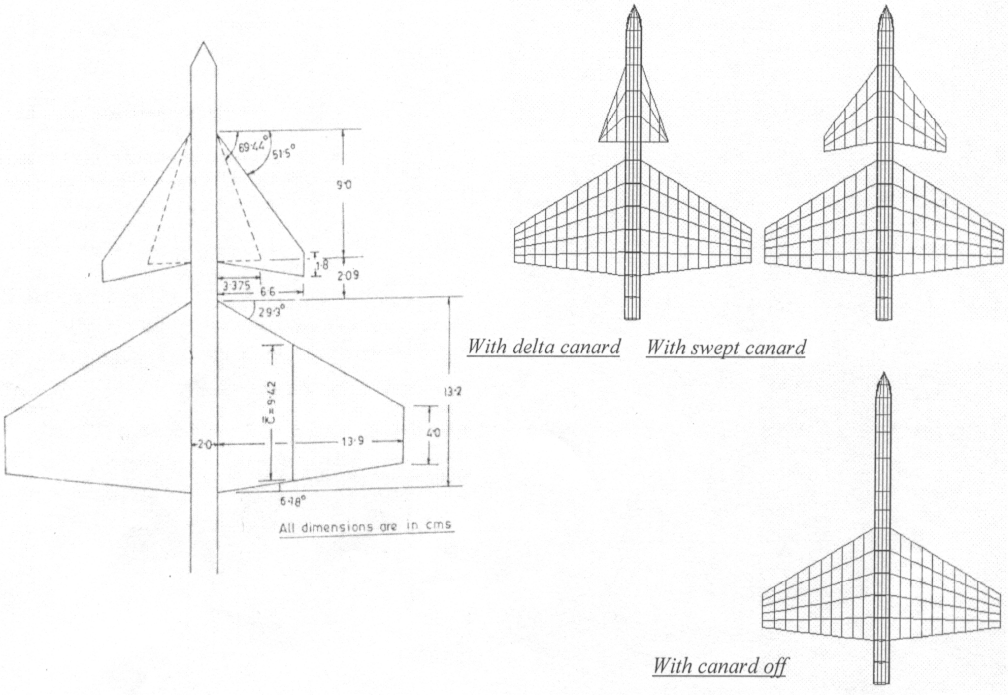

Fig.(10) Sketch and paneling of the configuration of Ref.[1].

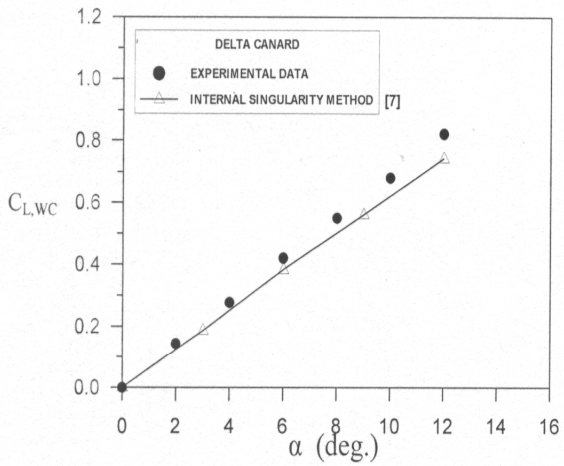

Fig.(11) Variation of lift with incidence for the configuration of Ref.[7] with delta canard.

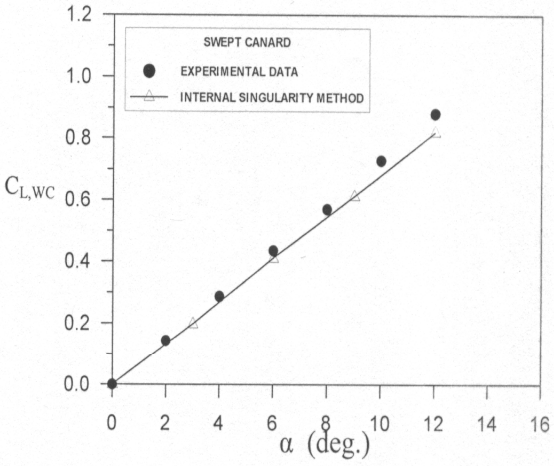

Fig.(12) Variation of lift with incidence for the configuration of Ref.[7] with swept canard.

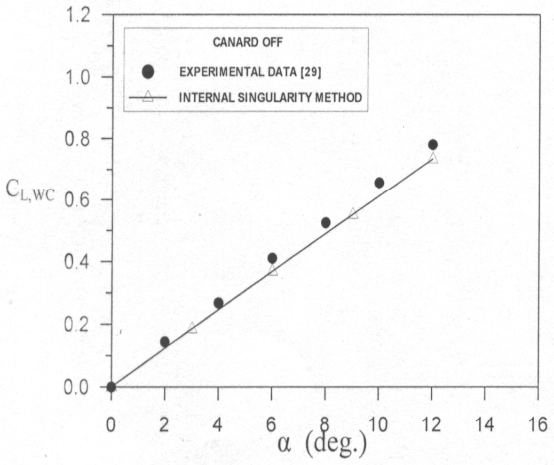

Fig.(13) Variation of lift with incidence for the configuration of Ref.[1] With canard off.

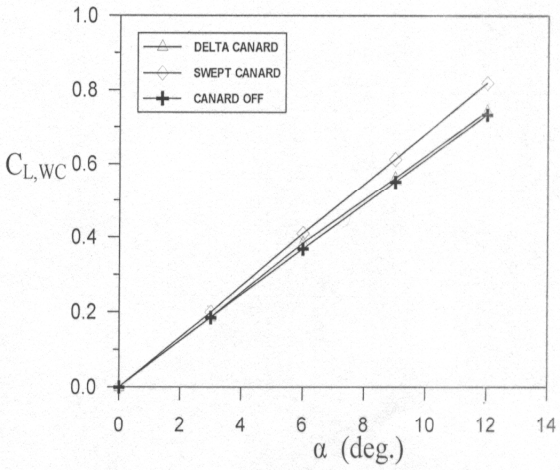

Fig.(14) Variation of lift with incidence for the configuration of Ref.[1].

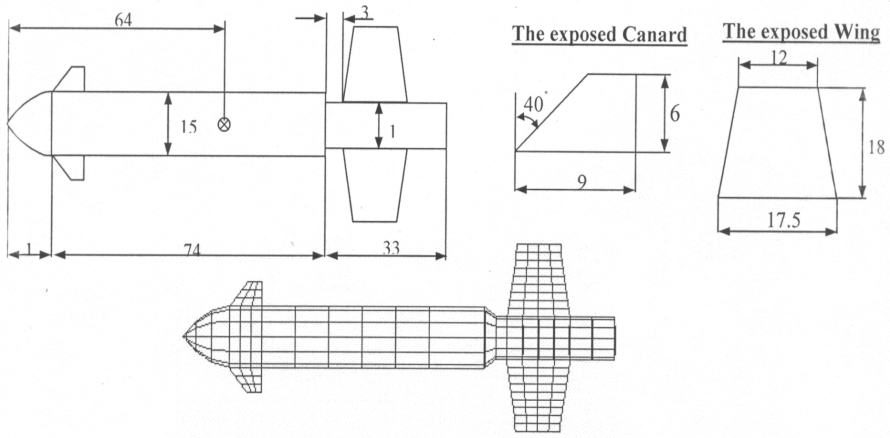

Fig.(15) Sketch and paneling of a typical canard missile,(all dimensions in cm.).

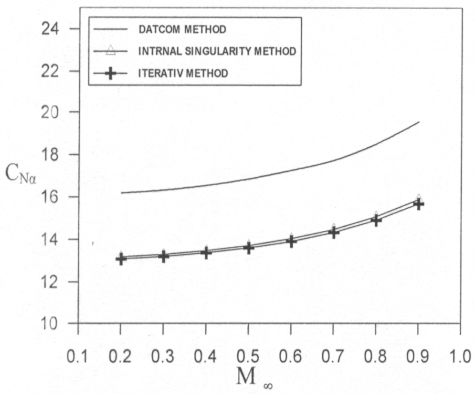

Fig.(16) Mach number effect on normal force curve slope for the Typical Canard Missile.

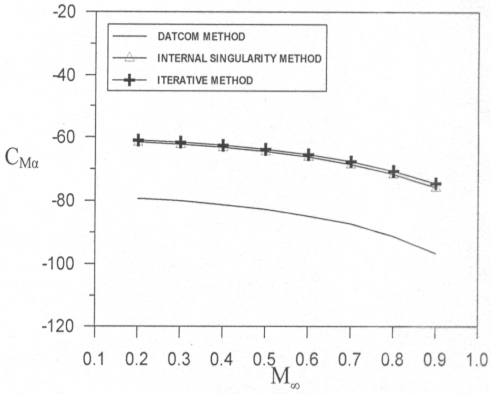

Fig.(17) Mach number effect on pitching moment curve slope for the Typical Canard Missile.

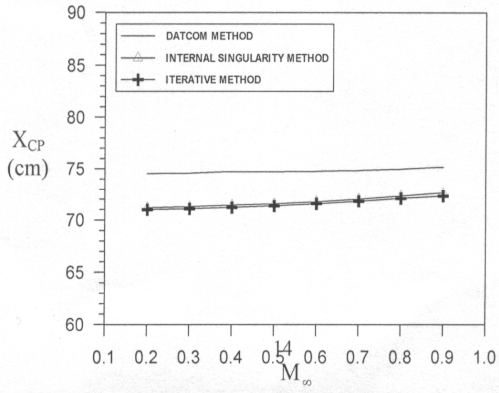

Fig. (18) Mach number effect on center of pressure location for the Typical Canard Missile

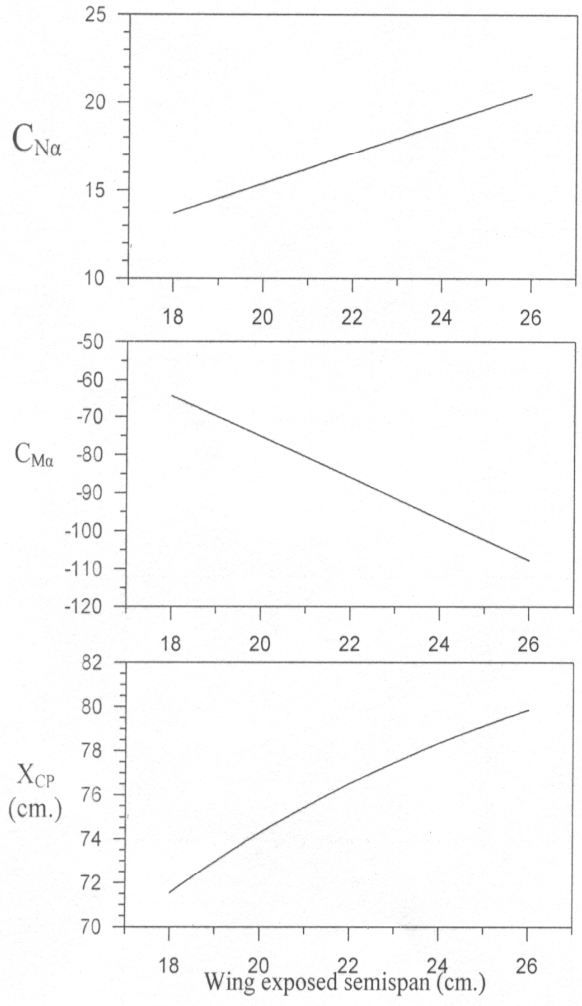

Fig.(19) Effect of increasing wing exposed semispan on the aerodynamic characteristics of the Typical Canard Missile at $M_\infty = 0.5$ using the internal singularity method.

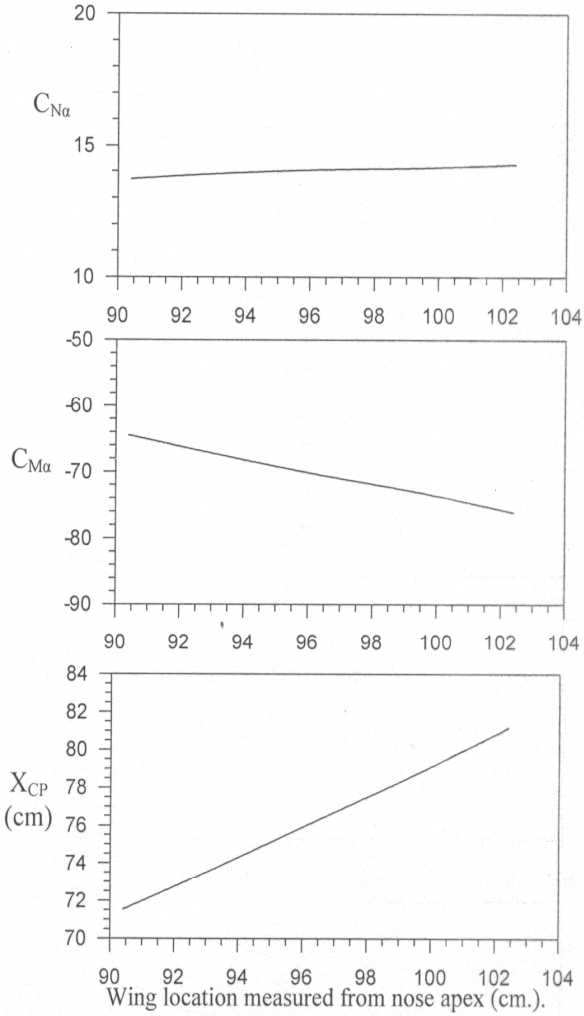

Fig.(20) Effect of wing location on the aerodynamic characteristics of the Typical Canard Missile at $M_\infty = 0.5$ using the internal singularity method.

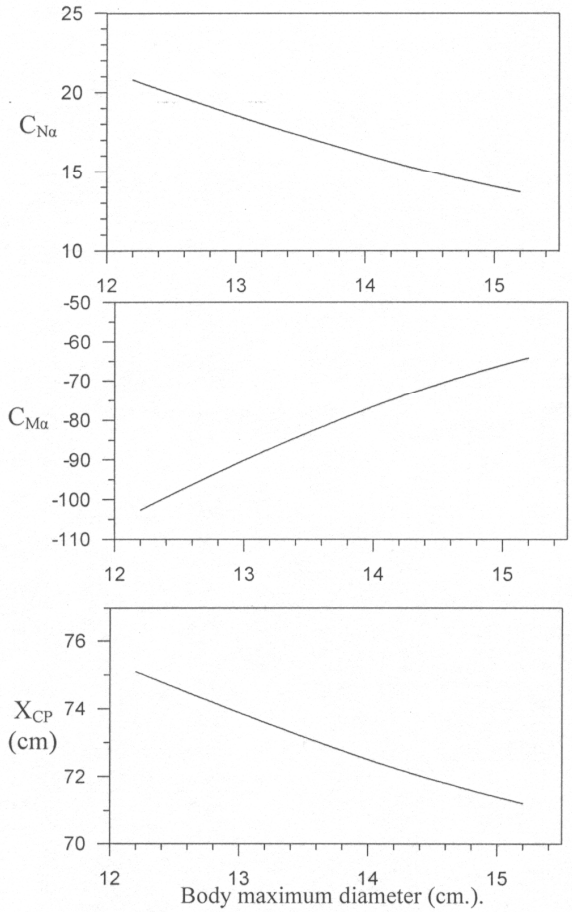

Fig.(21) Effect of body maximum diameter on the normal force, pitching moment curve slope and center of pressure location for the Typical Canard Missile at $M_\infty = 0.5$ using the internal singularity method.

REFERENCES

Bandyopadhyay G., (1989), Low Speed Aerodynamics of Canard Configurations, Aeronautical Journal, January.

Chun-Mo Lee and Sheng-Jil Hsieh, (1984), An Aerodynamic analysis and The Subsequent Motic of External Store, 4th International Conference on Applied Numerical Modeling, Dec. 27- 29Taiwan, R.O.C.

DATCOM, (1972), Douglas Aircraft Co., Inc.,.

Herman Schlichtmgetal (1979), Aerodynamics of the Airplane, McGraw-hill International Boo Company,.

Hess, J. L. and Smith, A. M. O, (1967), Calculation of Potential Flow About Arbitrary Bodies, Progress in Aeronautical Science Journal, Vol. 8, Pergamon Press,

Jack Moran (1984), An Introduction to Theoretical and Computational Aerodynamics, Job] Wiley and Sons,.

Joseph Katz and Alien Plotkin (1991), Low-Speed Aerodynamics, From Wing Theory to Pane Method". McGraw-Hill..

NOMENCLATURI

A	:Panel area
b	:Wing or canard span
$\overline{C}$	:Mean aerodynamic chord
C	:Local wing chord
c.g	:Center of gravity
$C_{L,WC}$	:Coefficient of canard and wing lift, referred to wing area
$C_{L\alpha}$	:Lift curve slope
C_m	:Pitching moment coefficient
$C_{m\alpha}$	:Pitching moment curve slope
C_N	:Normal force coefficient
$C_{N\alpha}$	:Normal force curve slope
Cr	:Wing or canard root chord
C_P	:Pressure coefficient
D	:Body diameter
d''	:Body diameter at the wing-body junction region
d'	:Body diameter at the canard-body junction region
K_N	:Ratio of nose lift
$K_{B(W)}$	:Ratio of body lift in the presence of wing
$K_{W(B)}$	:Ratio of wing lift in the presence of body
L_{ref}	:Reference length (body maximum diameter)
M_∞	:Free stream Mach number
$\vec{n}$	:Unit normal vector
NB	:Number of body panels
$\vec{Q}_\infty$	:Free stream velocity.
$\vec{Q}$	:Total velocity vector .
R	:Radius.
S_w	:Wing or canard planform area.
S_{ref}	:Reference area (body maximum cross-sectional area).
x, y, z	:Global coordinates.
X_c, Y_c, Z_c	:Global coordinates of the panel's center point.
$X_{C.P}$	:Center of pressure location.
$X_{c.g}$	:Center of gravity location.
Δx	:Panel length.
Δy	:Panel span.
α	:Angle of attack.
β	:Mach number prameter $\sqrt{1-M_\infty^2}$.
Γ	:Vortex strength.
$\Gamma_{T.E}$	:Trailing edge vortex strength.
Γ_W	:Wake vortex strength.
θ	:Meridian angle measured from the z-axes.
$\Lambda_{L.E}$	:Leading edge sweep angle.
$\Lambda_{T.E}$	:Trailing edge sweep angle.
ρ	:Air density (1.2 kg/m^3).
σ	:Source strength.
Φ^*	:Total potential.
Φ_∞	:Free stream potential.
Φ	:Perturbation velocity potential.

Superscripts

''	:Related to the wing .
'	:Related to the canard.

Subscripts

NC	:Number of canard panels
NW	:Number of wing panels
P	:Local pressure
P_∞	:Free stream pressure
$\vec{q}$	:Perturbation velocity vector
$\vec{Q}_\infty$	:Free steam velocity vector

DEVELOPMENT OF STATISTICAL MODEL FOR THE PREDICTION OF PERMANENT DEFORMATION IN PAVING MATERIALS

Hamed M. Alani
Prof. (Dept. of civil Eng.-Baghdad University)

Dr. Namir G. Ahmed
Lecturer (Dept. of HWY's & Transportation- University of Al-Mustansiriyah)

Abbas F. Jassim
Asst .lecturer (Dept. of HWY's & Transportation- University of Al-Mustansiriyah)

ABSTRACT

Permanent deformations (rutting) of asphalt pavements which appear in many roads in Iraq. have caused a major impact on pavement performance by reducing the useful service life of pavement and creating services hazards for highway users. Therefore, it is important to analyze and investigate this type of distress.

The objectives of the present paper include; the analysis of the main contributory factors influencing rutting, and development of statistical model for the prediction of permanent deformation in paving materials.

To achieved these objectives for the requirements of data collection. five types of gradation. (40-50) asphalt cement and different types of filler are used to prepare three hundred sixty asphalt concrete specimens throughout the work using Marshall method and Superpave system. Most of these specimens are tested by applying diametric creep under different temperatures and stress levels.

A statistical model has been developed for the prediction of rut depth in local asphalt paving materials as influencing by the factors of asphalt cement content, mineral filler type, air voids and environmental temperature.

الخلاصة

ان التشوهات الدائمية (التخدد) في التبليط الاسفلتي تظهر في العديد من طرق العراق،وتسبب تأثيرا رئيسيا على اداء التبليط و ذلك عن طريق تقليل العمر الخدمي للتبليط وجعل استخدام هذه الطرق محفوفة بالمخاطر،لذلك من المهم التحليل والتحري عن هذا النوع من الفشل.

ان اهداف الدراسة الحالية تتضمن تحليل العوامل الاساسية المؤثرة في التخدد،وتطوير نموذج احصائي للتنبؤ به في المواد الاسفلتية.

لتحقيق هذه الاهداف لمتطلبات جمع البيانات فقد تم استخدام خمسة انواع من تدرجات الركام واسفلت نوع(40-50) مع انواع مختلفه من المواد المالئة لتحضير ثلاثمائة وستون نموذج من الاسفلت الكونكريتي خلال فترة الدراسة مستخدمين طريقة مارشال ونظام التبليط الفائق (Superpave). وقد تم اجراء فحص الزحف على معظم هذه النماذج وضمن درجات الحراره ومستويات الاجهاد المختلفة.

وقد تم بناء نموذج احصائي للتنبؤ بمقدار التخدد في مواد التبليط المحلية والذي يتأثر ببعض العوامل الرئيسية المتمثلة بالفجوات الهوائية ونوعية المادة المالئة وكمية الاسفلت ودرجة الحرارة.

KEY WORDS

Permanent Deformation, Rutting P ediction, Rutting Statistical Model, Flexible Pavement Rutting. Factors Affecting Rutting.

INTRODUCTION

The asphaltic paving mixture is normally subjected to various detrimental types of distresses during its service life .These distresses are caused by load, weather, and construction practices, and /or deficient materials. Some of these serious distresses include rutting (permanent deformation). shoving, stripping, and fatigue (alligator cracking). which finally may lead to complete failure of

pavement at the same time. Such distresses will reduce the performance of asphalt pavements, which not only causes inferior ride quality to motorists but also yields higher life-cycle cost. Some of the mentioned distresses are associated with the asphalt cement binder and can be controlled significantly by modifying the material with chemical additives [Ramzi et al. (1998)].

Permanent deformation (rutting) of asphalt pavements has a major impact on pavement performance. Rutting reduces the useful service life of the pavement and, by affecting vehicle handling characteristics, creates serious hazards for highway users. Highway materials engineers have been handicapped in their efforts to provide rutting resistant materials in by the existing methods for testing and evaluating asphalt-aggregate mixes which are empirical and do not give a reliable indication of in-service performance [Huang et al. (1991)].

A variety of materials is currently available for use as modifiers to improve the performance of asphalt concrete pavements. Different efforts and techniques have been carried out to improve the ability of asphalt concrete to resist rutting; for example, many agencies around the United States have adopted specifications to address rutting distress in asphalt concrete pavements [Sousa et al. (1991)]

In Iraq, the severity of rutting has been increased in asphalt pavements possibility due to the increase in truck axle loads, tire pressure, and high pavement temperature in summer [Hussain 1985].

SOURSE OF DATA

The required data for the previously mentioned independent variables are gathered from the results of the experimental tests, while the dependent variable (rutting) is calculated according to the following statistical model, which is reported by Baladi (1988).

$$\text{Log(RD)} = -1.6 + (0.067)(AV) - (1.5)(\log(TAC)) + (0.07)(T) + (0.000434)(KV) + (0.15)(\log(ESAL)) - (0.4)(\log(MR_{SUB})) - (0.63)(\log(MR_{B})) + (0.1)(\log(SD)) + (0.01)(\log(CS)) \quad (1)$$

where:-

RD = *rut depth (inch),*
TAC = *thickness of AC course (inch),*
SD = *surface deflection (inch),*
AV = *the percent air voids of the AC mix (AV = 1, 2 . . . etc.),*
MR_b = *the resilient modulus of the base material (psi),*
MR_{sub} = *the resilient modulus of the roadbed soil (psi),*
TS = *the tensile strain at the bottom of the AC fiber,*
CS = *the compressive strain at the bottom of the AC layer,*
KV = *kinematic viscosity of the AC binder (centistokes),*
ESAL = *the number of equivalent single axle load at which the rut depth is being calculated, and*
T = average annual air temperature (°C).

STEPWISE REGRESSION PROCEDURE

This procedure begins by computing the simple regression model for each independent variable. It examines all such models to determine which is best and whether the F-statistic of the second variable (with the first variable already in the equation) is greater than F-to-enter. If two independent variables are highly correlated, only one of them will enter the equation. Once the first variable is included, the added explanatory power of the second variable will be minimal and its F-statistic will not be large enough to enter the model.

The procedure continues by deciding whether to add another independent variable at each step. The p-values of all variables are computed (at each step) and compared to the F-to-remove. If a variable F-statistic falls below this standard, it is removed from the equations.

These steps are repeated until no more variables are added or removed. The rutting model derived from the analysis is found to be:

$$RD=2.667283+0.061539*AC+0.001885*Temp.-0.160534*F+0.985539*AV \quad ...(2)$$

$$R=0.90 \quad R^2=0.813 \quad SEE=0.32958$$

where:-

RD = Rut depth in (mm)

AC=Asphalt content (AC from4.0 - 6.0)

Temp. = Temperature in °C

F= Filler type (1=Cement, 2=Hydrated lime and 3=Lime stone dust)

AV= the percent air voids of the AC mix (AV from 2.0 - 5.1)

By using STATISTICA software, the correlation coefficients between all of the variables are calculated and the correlation matrix is setup. This matrix and testing for (R) critical can be seen in **Table (1)**.

Table (1) Correlation Matrix for Rutting Model.

Correlations (New model.sta)					
	ASPHALT	TEMP	FILLER	AIR_VOID	RUTTING
ASPHALT	1	0.1764704	0.128907	-0.3033593	0.2495724
TEMP	0.1764704	1	0.3228478	-0.2466469	0.2288295
FILLER	0.128907	0.3228478	1	-0.1925076	-0.2912172
AIR_VOID	-0.3033593	-0.2466469	-0.1925076	1	0.8938356
RUTTING	0.2495724	0.2288295	-0.2912172	0.8938356	1

The summary of stepwise regression, regression summary and several possible models can be seen in **Tables (2), (3)**.

Table (2) Regression Summary and Summary of Step Wise Regression for Rutting Model.

Regression Summary for Dependent Variable: RUTTING						
R= .90295077 R^2= .81532009 Adjusted R^2= .81361797						
F(4,434)=479.00 p<0.0000 Std.Error of estimate: .32958						
		St. Err.		St. Err.		
	BETA	of BETA	B	of B	t(434)	p-level
Intercpt			2.6672835	0.2366708	11.270015	5.132E-26
ASPHALT	0.0311372	0.0218037	0.0615394	0.0430927	1.4280694	0.153991
TEMP	0.026925	0.0223344	0.0018855	0.001564	1.2055411	0.2286513
FILLER	-0.133712	0.0219855	-0.160534	0.0263957	-6.0818308	2.609E-09
AIR_VOID	0.8841817	0.0222487	0.9855385	0.0247992	39.740773	0

Table (3) Several Possible Models From the Stepwise Regression Analysis for the Selection of Rutting Model.

Case	Variable	Model	R^2	SEE
1	Av	RD=2.774+0.996Av	0.798	0.342
2	Av,F	RD=3.046+0.969Av-0.148F	0.812	0.330
3	Av,F,Ac	RD=2.708+0.98Av-0.151F+0.066Ac	0.812	0.329
4	Av,F,Ac,Temp	RD=2.667+0.98Av-.160F+0.061As+0.001Temp.	0.813	0.329

TESTING FOR THE MODEL

Testing for Normality

In addition to chi-square test for normality, the following two tests can be used. The first is called the Kolmogorov-smirnov (or K-S test).Whereas, the second is called the Lilliefors test .Both test work similarly by comparing the actual and normal cumulative probabilities. The difference between them is that K-S test assumed that the mean and the standard deviation of the population are known. While Lilliefors test requires to compute the mean and standard deviation from the data [Keller and Warrack (2000)].For this study and according to the available data Lilliefors test is suggested to be used.

Lilliefors Test

H_o =the data are normally distribution.

H1= the data are not normally distribution.

D= max [F(x)-S(x)]

Where

S(x): Sample cumulative distribution function (the proportion of sample value that are less than or equal to x).and,

F(x): Normal cumulative probabilities. (From normal distribution table).

$$P\left(Z \leq \frac{x_i - \bar{x}}{S}\right)$$

Where,

x_i =value of variable.

$\bar{x}$ =Sample mean.

S=Standard deviation of sample.

Lilliefors test result for the developed model can be seen in the following tables:

D-value for rutting model

Variable	(D) value
Temperature	0.035
Stress	0.042
Asphalt content	0.021
Filler type	0.039
Gradation type	0.035
Compaction methods	0.042
V.M.A.	0.031
Flow	0.015
Stiffness	0.040
Air voids	0.011
Rutting	0.018

For sample size >30 and significant level =0.05,

Then $D_{critical} = 0.886/(n)^{0.5}$

$D_{critical} = 0.0422$ for rutting model .The values of $D_{critical}$ are grater than the above tabulated for rutting model .Thus, D does not fall into the rejection region and there is no reason to reject the null hypothesis.

Checking for $R^{critical}$

Refer to the correlation matrix, most of the coefficients of correlation between each two variables $R_{calculated} > R_{tabulated}$ is equal to 0.095 (n=439, df= n-(1+1) =437).Thus, the null hypothesis that, there is no association between the variables is rejected at 95% confidence level.

The correlation coefficient of the final form of this model =0.90 > $R_{tabulated}$ =0.123, (n=439, df=n-(5+1) =433). Therefore, there is strong correlation between the rutting model and the independent variables in this model.

Goodness of Fit

To checking the goodness of fit for the predicted model. Chi-square test was carried out and the following results are expressed.

1- X^2-test

n=439, df=438, confidence level =95%

Case	variables	X^2-value	X_c^2-value
1	x=observed	91.77	233.99
	y=predicted rutting model		

For case 1 $X^2 < X_c^2$, there is no significant difference between the observed and the predicted values.

RESULTS OF THE ANALYSIS

The stepwise regression using STATISTICA software serves its purpose in drawing attention to dangerous inter-correlation and enables a selection of variables to be made on logical basis. The chosen variables are then entered in a regular multiple regression. The first model developed is shown at the end of the previous section as rutting model Equation (2).

The variables; air voids, filler type, temperature and asphalt content are chosen. The variables used in the model show that the rutting is strongly affected by air voids and asphalt content, while, filler type and temperature reflect lower effect on rutting. The model indicates that rutting increases with the increase in air voids, asphalt content and temperature, while it decreases with the filler type from cement to hydrated lime, which has low value of correlation with the rutting.

It was found that the linear forms of the variables result in best correlation between the independent variables and rutting.

A study of the correlation coefficient matrix and the variables selected for the regression analysis showed several variables correlated reasonably well with the dependent variable, but do not enter because of high order of inter-correlation with a variable already selected for the model. Accordingly, it was decided to reduce the number of variables, leaving as few as possible to describe the pavement.

DISCUSSION OF RESULTS

Regarding the rutting model; four variables are found to be common to the general picture of the model development; these were air voids, filler type, temperature, and asphalt content. The coefficient of determination is found to be 0.813, which means that this model can explain 81.3 percent of the rutting prediction.

There is no multicollinearity between the independent variables that affect the rutting model.

MODEL LIMITATION

As with all regression models, the model is only valid within the ranges of the variables developed .Some additional limitations can be mentioned, as in the follows;

1. Mix stiffness could be estimated by Heukelom method, and
2. The ranges of data for rutting model can be seen in Table (4).

Table (4) Range of Data in Rutting Model

Variables	Mean	Minimum	Maximum
ASPHALT CONTENT (%)	4.659	4.0	6.0
STRESS LEVEL (Mpa)	0.088	0.025	0.1
TEMPERATURE (°C)	31.93	20.0	60
COMPACTION TYPE (1and 2)	1.191	1.0	2.0
GRADATION TYPE (1,2,3,4and5)	3.387	1.0	5.0
FILLER TYPE (1,2,and 3)	1.293	1.0	3.0
STIFFNESS (Kg/cm^3)	4.479	3.0	101
FLOW (mm)	2.921	2.0	5.1
V.M.A (%)	12.54	8.79	100
AIR VOID (%)	2.997	2.0	5.1
RUTTING (mm)	5.760	3.866	8.420

VALIDATION OF THE DEVELOPTED MODEL

Introduction

The final step in the model building process is the validation of the developed models. The objective is to assess the ability of rutting prediction model to accurately predict the amount of rutting in the field using data not already used in developing the model.

Literature Review

A review of the statistical literature [Neter et al., 1990 and Snee 1977] suggests the following methods for validating a regression model:

- Check on Model Predictions and Coefficients
- Collection of New Data
- Comparison with Previously Developed Models
- Data Splitting
- Prediction Sum of Squares (PRESS)

Selection of Validation Methods

The literature suggests that all available methods of validation could be used. However, in this case, it is not possible to use all the methods of validation. Therefore, the applicability of each method in terms of the validation of the rutting model will be discussed and the most appropriate methods of validation will be selected.

The first method (Check on Model Predictions and Coefficients) attempts to make sure that the selected model agrees with the physical theory. This essentially has been already checked during the development process.

The second method (Collection of New Data) suggests that a new data set should be collected. Unfortunately, the collection of the new data is not possible due to time constraints.

The third method (Comparison with previously developed models) compares the results of a newly developed model with a previously developed model or with a theoretical model.

The fourth method (data splitting) has recommended that one may not consider data splitting unless $N > 2P+25$, where N is the sample size and P is number of estimated parameters.

The last method (Prediction Sum of Squares) is a form of data splitting and it is not feasible because of the available large sample size.

For the above mentioned discussion, because of the nature of the available data and minimization of the error of mean for the accuracy requirements, the third method (Comparison with previously developed models) is selected to assess the predictive ability of the rutting model.

COMPARISION WITH PREVIOUSLY DEVELOPTED MODELS

Shell design method (Manually calculated), shell pavement design software SPDM 3.0 and new rutting model have been applied to show the effect of variable variations on the permanent deformation values of asphalt concrete surface layer .The following default values are used in this process;

1-80 mm asphalt concrete mixture as surface layer with stiffness modulus varying according to the type of mixture

2- The above mentioned layer is supported by 200 mm asphalt concrete base layer with stiffness modulus of 1×10^9 N/m^2

3- Silty clay subgrade with a resilience modulus of 2.5×10^5 N/m^2 modulus

4- The MMAT (Mean Monthly Air Temperature), are (18.3, 21.4, 25.3, 31.8, 39.1, 42.7, 44.5, 46, 40.4, 34.9, 24.3, and18) [Iraqi Meteorological Organization, 2002].

5- Design life =15 year

6-The total number of axles per lane per day is equal to 2000, and it is anticipated that traffic will increase at the rate of 2 percent

Table (5) shows the rut depth calculation by using shell method (manual calculation), SPDM 3.0 software, and new rutting model for each mix variable.

Table (5) Rut Depth Calculation by Using Shell and New Developed Model

Mix No.	i	h_i (mm)	$T_{\bar{y}}$	$\eta_{\bar{y}}$ E+4	q	W E+6	$S_{bit,VSC}$ N/m^2	S_{mix} N/m^2 E+6	Z_i	C_{av}	Δh_i (mm)	Shell method		Developted rutting model
												Manually By charts (mm)	SPDM Software (mm)	
1	1	40	39	2	0.379	3.79	0.79	6.5	0.6	1.2	2.65	4.98	6.02	6.84
	2	40	36	4	0.382	3.76	1.59	7.4	0.6	1.2	2.33			
2	1	40	39	2	0.381	3.80	0.78	6.6	0.6	1.2	2.61	5.15	4.74	5.58
	2	40	36	4	0.381	3.80	1.57	6.8	0.6	1.2	2.54			
3	1	40	39	2	0.279	3.85	0.77	7.6	0.6	1.2	2.27	4.4	4.67	5.5
	2	40	36	4	0.381	3.8	1.57	8.1	0.6	1.2	2.13			
4	1	40	39	2	0.380	3.79	0.79	5.3	0.6	1.2	3.26	5.87	4.66	5.51
	2	40	36	4	0.380	3.79	1.58	6.6	0.6	1.2	2.61			
5	1	40	39	2	0.382	3.76	0.79	5.92	0.6	1.2	2.91	5.42	4.50	5.35
	2	40	36	4	0.382	3.76	1.59	6.87	0.6	1.2	2.51			
6	1	40	39	2	0.371	3.90	0.76	5.21	0.6	1.2	3.31	6.06	8.64	9.43
	2	40	36	4	0.371	3.90	1.53	6.27	0.6	1.2	2.75			
7	1	40	39	2	0.378	3.80	0.78	5.02	0.6	1.2	3.44	6.61	4.51	5.36
	2	40	36	4	0.378	3.80	1.57	5.44	0.6	1.2	3.17			
8	1	40	39	2	0.372	3.89	0.77	7.9	0.6	1.2	2.18	4.11	4.18	5.03
	2	40	36	4	0.372	3.89	1.54	8.95	0.6	1.2	1.93			
9	1	40	39	2	0.410	3.75	0.80	7.42	0.6	1.2	2.32	4.34	4.33	5.16
	2	40	36	4	0.410	3.75	1.60	8.52	0.6	1.2	2.02			
10	1	40	39	2	0.379	3.79	0.79	5.7	0.6	1.2	3.03	5.67	4.19	5.01
	2	40	36	4	0.379	3.79	1.58	6.54	0.6	1.2	2.64			
11	1	40	39	2	0.371	3.9	0.76	6.5	0.6	1.2	2.65	5.15	4.88	5.72
	2	40	36	4	0.371	3.9	1.53	6.9	0.6	1.2	2.50			
12	1	40	39	2	0.384	3.77	0.79	5.82	0.6	1.2	2.96	5.54	4.81	5.66
	2	40	36	4	0.384	3.77	1.59	6.68	0.6	1.2	2.58			
13	1	40	39	2	0.380	3.79	0.79	6.9	0.6	1.2	2.50	4.83	4.68	5.53
	2	40	36	4	0.380	3.79	1.58	7.4	0.6	1.2	2.33			
14	1	40	39	2	0.381	3.80	0.78	1.9	0.6	1.2	9.09	6.5	4.32	5.17
	2	40	36	4	0.381	3.80	1.57	2.33	0.6	1.2	7.41			
15	1	40	39	2	0.379	3.79	0.79	3.88	0.6	1.2	4.45	8.29	4.75	5.6
	2	40	36	4	0.379	3.79	1.58	4.5	0.6	1.2	3.84			
16	1	40	39	2	0.279	3.79	0.79	8.73	0.6	1.2	1.97	3.69	4.63	5.48
	2	40	36	4	0.279	3.79	1.58	10.02	0.6	1.2	1.72			
17	1	40	39	2	0.371	3.90	0.76	8.83	0.6	1.2	1.95	3.64	4.67	5.52
	2	40	36	4	0.371	3.90	1.53	10.22	0.6	1.2	1.69			
18	1	40	39	2	0.380	3.79	0.79	6.4	0.6	1.2	2.7	5.13	4.88	5.72
	2	40	36	4	0.380	3.79	1.58	7.1	0.6	1.2	2.43			
19	1	40	39	2	0.371	3.90	0.76	5.9	0.6	1.2	2.92	5.57	4.47	5.32
	2	40	36	4	0.371	3.90	1.53	6.5	0.6	1.2	2.65			
20	1	40	39	2	0.279	3.79	0.79	5.31	0.6	1.2	3.25	6.32	4.43	6.28
	2	40	36	4	0.279	3.79	1.58	5.62	0.6	1.2	3.07			
21	1	40	39	2	0.372	3.89	0.77	7.83	0.6	1.2	2.20	4.13	5.48	6.32
	2	40	36	4	0.372	3.89	1.54	8.92	0.6	1.2	1.93			

VALIDATION RESULTS

The rutting values resulted from SPDM software are plotted against those estimated by the new rutting model. This relation is shown in **Fig. (1)**.

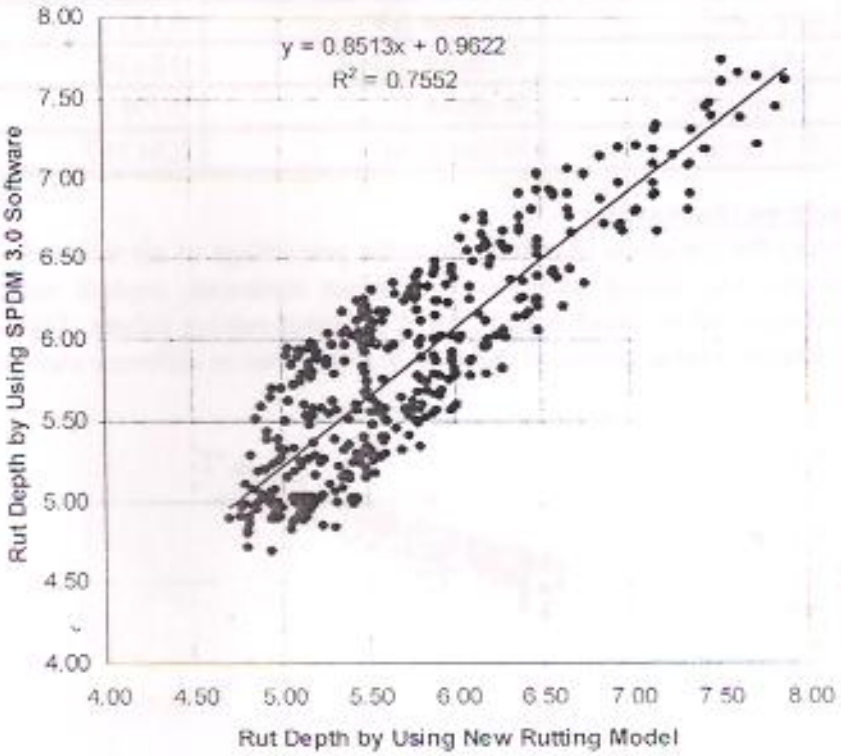

Fig. (1). SPDM 3.0 Software versus New Rutting Model Rut Depth

The best fit of the relation between the rutting value of SPDM 3.0 software and new rutting model can be found in the following form;

$$RD(SPDM\ 3.0\ Software) = 0.8513 * RD(New\ Rutting\ Model) + 0.962 \quad (3)$$
$$R^2 = 0.7552$$

where:-

RD (SPDM 3.0 Software) = Rut Depth Calculated Using SPDM 3.0 Software
RD (New Rutting Model) = Rut Depth Calculated Using New Rutting Model

These findings seem to have good agreement with the relation y = x.

Thus and for the local materials characteristics and environmental condition, the developed model can be recognized for the prediction of the rutting in Iraq within the mentioned limitations of this model.

SENSITIVITY ANALYSIS

Sensitivity analysis has been made to illustrate the effect of various parameters on rutting prediction model. Analysis is conducted to evaluate the effect of air void, filler type, asphalt content, and temperature on the rutting model of asphalt mixtures.

A parametric study is performed to select the suitable variables in the presented model. **Table (6)** shows the results of the parametric study. Based on the highest coefficient of determination (R^2), rut depth (*RD*), temperature (Temp.), filler type (F), and the air void (AV) are selected for the prediction model.

Table (6) Selection of Model Parameters

Model Parameter	Condition	R^2
RD, AV, F, Temp. ,AC	With all Parameter	0.8136
RD, F, Temp., AC	Without AV	0.1373
RD,AV,F, AC	Without Temp.	0.8234
RD, AV, Temp., AC	Without F	0.7981
RD, AV, F, Temp.	Without AC	0.81317

Effects of Air Voids on the Rutting

Fig. (2) Presents the variation of rutting with the percentage of air voids. In general, as the air void content increases the rutting increases. In certain instances, asphalt mixtures with similar gradation characteristics and air void content yield different rutting values. This difference may be attributed to the different arrangements of the void distributions in different samples.

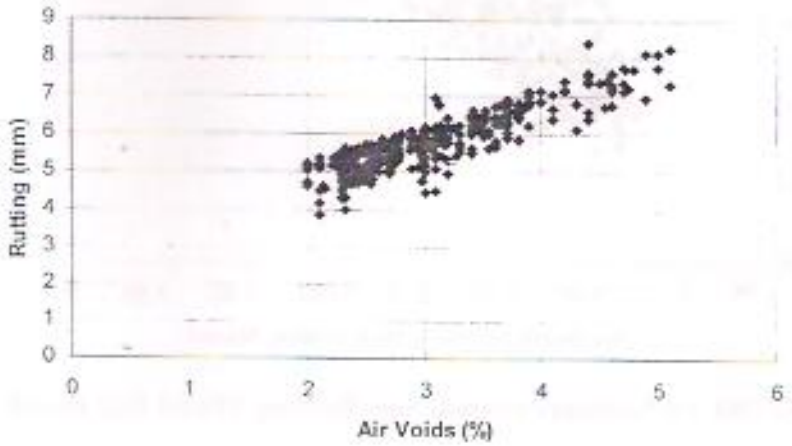

Fig. (2) Variation of Rutting with Air Voids

Effects of Asphalt Content on the Rutting

Fig. (3) Presents the variation of the rutting with the asphalt content. In general, as the asphalt content increases the rutting increases.

In certain instances, asphalt mixtures with similar gradation characteristics and asphalt content yield different rutting values. This difference may be attributed to the different asphalt distributions in different samples.

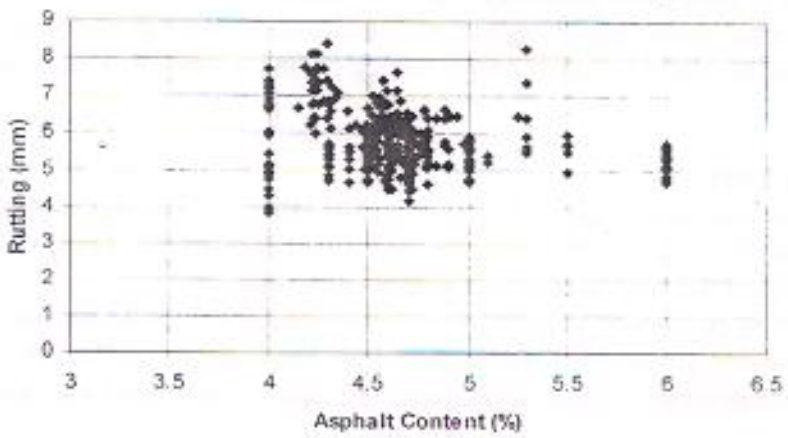

Fig. (3) Variation of Rutting with Asphalt Content

Effects of Filler Type on the Rutting

Fig. (4) Shows the effects of the variation of filler type on the rutting of HMA mixtures. No conclusions could be drawn since the filler type does not varies significantly in the considered mixtures.

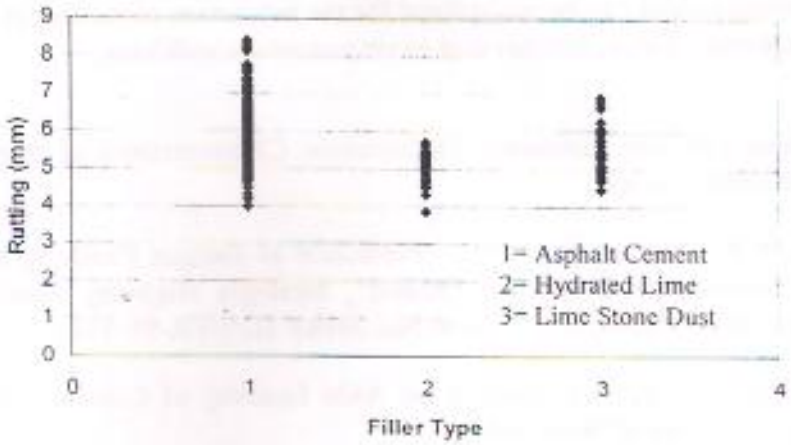

Fig. (4) Variation of Rutting with Filler Type

Effects of Temperature on the Rutting

Fig. (5) Shows the effects of the variation of temperature on the rutting of HMA mixtures. No conclusions could be drawn since the temperature does not varies significantly in the considered mixtures.

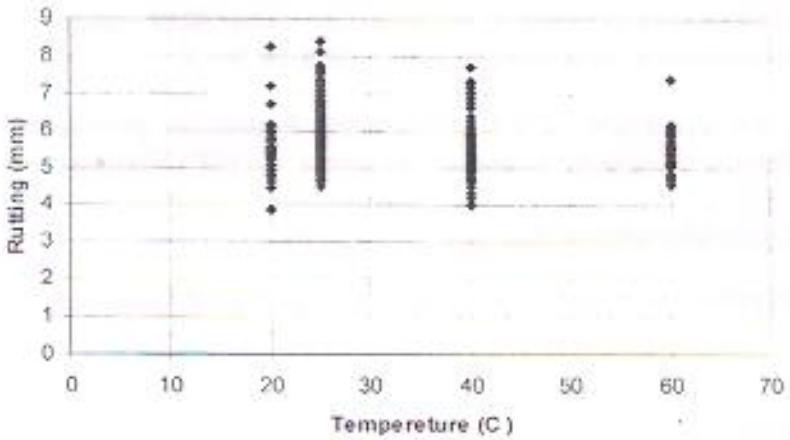

Fig. (5) Variation of Rutting with Temperature

CONCLUSIONS

1- As a result of the statistical analysis, the following model is developed to predict rutting in asphalt concrete mixture;

RD=2.667283+0.061539*AC+0.001885*Temp.-0.160534*F+0.985539*AV

where:-

RD= Rut depth in (mm)

AC=Asphalt content (AC from4.0 - 6.0%)

Temp. = Temperature in °C

F= Filler type (1=Cement, 2=Hydrated lime and 3=Lime stone dust)

AV= the percent air voids of the AC mix (AV from 2.0 - 5.1%)

2- As compared with the sensitivity analysis results, the air voids and asphalt content have a pivot role to influence the mixture ability to resist permanent deformation. While ,lower influence on the permanent deformation appear by other variables.

RECOMMENDATIONS

The developed rutting model can be recognized for the prediction of rutting in Iraq within its limitation and local materials characteristics and environmental conditions.

REFERENCES

Baladi,G.Y.,(1988),"Fatigue Life and Permanent Deformation Characteristics of Asphalt Concrete Mixes", Transportation Research Board.

Huang, Y. H., Drnevich, V.P., Roghani,H.,(1991)," Prediction of Fatigue Cracking and Rutting in Asphalt Pavements by Small-Scale Centrifuge Models", Strategic Highway Research Program National Research Council Washington, D.C. Report No. SHRP-ID/UFR-91-516

Hussain, S.F. (1985),"Effect of Type of Loading on Axle Loading of Commercial Vehicles in Baghdad," M.Sc. Thesis, University of Baghdad.

Keller, G., and Warrack, B. [2000], "STATISTICS for Management and Economies."5th Edition, USA.

Neter, J., Wassermann, W., and Kutner, M.H. [1990]. "Applied Linear Statistical Models: Regression, Analysis Of Variance, and Experimental Designs, 3rd Edition, Richard D.Irwin, Inc., Homewood. IL, 1181.

Ramizi,T.,Galal,A.and,Murshed,D. (1998),"Evaluation of coke dust modified Asphalt using Superpave ",Journal Transportation Engineering ,ASCE ,Vol.10 ,No.3.

Sousa,J.B., Joseph,C., and ,Carl,L.M. ,(1991),"Summery Report on permanent deformation in asphalt concrete ,",Strategic Highway Research Program (SHRP),National Research Council, Washaington ,D.C.
URL: http://gulliver.trb.org/publications/shrp/SHRP-A-318.pdf

Snee, R.D. [1977], "Experiments in Industry," American Society of Quality Control, Milwaukee, WI.

NOMENELATURE

RD = Rut depth in (mm)
AC = Asphalt content (AC from4.0 - 6.0%)
Temp. = Temperature in °C
F = Filler type (1=Cement, 2=Hydrated lime and 3=Lime stone dust)
AV = Air Voids of the AC mix (AV from 2.0 - 5.1%)
PRESS = Prediction Sum of Squares.
R = Coefficient of Correlation.
R^2 = Coefficient of Determination.
R_C = Critical Coefficient of Correlation
χ^2 = Chi-square.
χ_c^2 = Critical Chi-square.

STATIC ANALYSIS OF THIN-WALLED CURVED BEAM ELEMENT INCLUDING WARPING EFFECTS

Dr. Adnan Falih Ali
Assistant Professor
Dept. of civil
Eng.-Baghdad University)

Dr. Abdul Muttalib A. Almusawi
Assistant Professor
Dept. of civil
Eng.-Baghdad University)

Ann Nafi' Aussi
Chief Engineer in Mayorality of
Baghdad / Design Department

ABSTRA

A new mathematical model for three-dimensional thin-walled curved beam element of closed section with seven degree-of-freedom per node is derived using the finite element procedure. The seventh degree-of-freedom is to account for warping restraint effects in thin-walled closed sections. These effects may become significant and should be fully considered in such sections for which warping deformations are relatively large. This model considers the coupled action due to the curved geometry of the element using its exact static behavior in the derivation of the displacement field. Also, the model considers the non-uniform torsional behavior of closed thin-walled sections in cases where additional axial direct stresses and complementary shear stresses are formed. The developed warping function of this model considers the interaction between the normal warping stresses and the accompanying warping shear stresses as well as the coupled action between the torsion and bending.

In addition to the ordinary axial and flexural deformations, the strain energy, which is used to obtain the stiffness matrix of the developed curved beam element fully, considers the additional axial, primary and secondary shear deformations due to warping restraint. The validity of this element is investigated by comparing the developed program analysis results with some available analytical solutions.

الخلاصة

تم اشتقاق نموذج رياضي جديد لعنصر ذو مقطع نحيف الجدران من النوع المغلق ثلاثي الأبعاد ذو عقدتين وسبعة درجات حرية لكل عقدة باستخدام طريقة العناصر المحددة. تم استحداث درجة الحرية السابعة لإدخال تأثير التشوه الألتوائي للمقاطع المغلقة نحيفة الجدران. هذا التأثير يكون واضحا ويجب أن يؤخذ بنظر الاعتبار في مثل هذه المقاطع التي يكون تشوه الالتواء فيها كبير. استنادا الى التصرف الستاتيكي للعنصر عند اشتقاق مجال الإزاحة، يأخذ النموذج المقترح بنظر الاعتبار التأثير المزدوج الناتج عن شكل العنصر المنحني. إضافة الى ذلك يأخذ هذا النموذج بنظر الاعتبار التصرف الالتوائي غير المنتظم للمقاطع المغلقة عند تقييد ذلك التأثير مسببا" اجهادات محورية وقصية اضافية. دالة التشوه الالتوائي المشتقة لذلك العنصر تأخذ بنظر الاعتبار الترابط بين الاجهادات المحورية الناتجة عن ذلك التشوه واجهادات القص المصاحبة لها اضافة الى التأثير المزدوج بين عزم اللي وعزم الانحناء.

ان طاقة الانفعال المستخدمة في اشتقاق مصفوفة الجساءة للعنصر تتضمن، اضافة الى تأثير التشوه المحوري والانحناء الاعتيادي، تأثير التشوه المحوري والقص الأولى و الثانوي الناتج عن التشوه الالتوائي. تم تطـوير برنامج حاسوبي ولغرض التحقق من ملائمة دقة التصرف الساكن لهذا العنصر تم تقديم عدد مـن المـسائل ومقارنة نتائج البرنامج المعد مع الحلول التحليلية المتوفرة.

KEY WORDS
Closed thin-walled, Curved beam element, Warping.

INTRODUCTION

Thin-walled sections are often used in bridges, highways and some other important structures. One of the most distinctive features of thin-walled sections is their response to torsional loading. If warping is restrained or non-uniform torsion is applied, out of plane warping will occur and additional normal shear stress will arise, therefore considering warping in the analysis of thin-walled structures is very important.

Some previous works consider the curvature of curved beam elements of closed sections when warping restraint effects are included (Yoo 1987& 1979). Castigliano's theorem is used to obtain the stiffness matrix by inverting the flexibility matrix. In the present work the finite element procedure is used to derive the natural shape functions of the new model which considers the coupled action due to the curved geometry of the element using the exact static behavior as well as the non-uniform torsional behavior of closed thin-walled sections when warping is taken as an explicit degree-of-freedom. Such a model will be useful in obtaining the stiffness as well as the consistent mass matrices, which can be used in the dynamic analysis of curved structures.

NON-UNIFORM TORSION IN BOX GIRDERS

When warping displacements vary along the length causing non-uniform distribution of torsion along it, because of restraints of warping displacement at a cross section or a varying applied torque, an additional normal stress and an accompanying shear stress develop. In thin-walled section there is an interaction between this additional normal stress and the warping shear deformation given by the second term of the following warping displacement equation:

$$u_w = u_{wo} + \int_0^s \frac{T}{G\delta}\,ds - \tau' \int_0^s h ds \qquad (1)$$

u_{wo} is the displacement at $s = 0$.

Therefore the distribution of warping displacement u_w and warping normal stress σ_w at the cross-section is indeed affined to $\bar{\omega}$, but the relationship is not defined by τ' and τ'' , respectively as in the case of open sections, but instead by the first and second derivatives of a dimensionless warping function $f = f(x)$ (Dabrowski 1968).

$$u_w = -f'\bar{\omega} \qquad (2)$$

$$\sigma_w = Eu'_w = -Ef''\bar{\omega} \qquad (3)$$

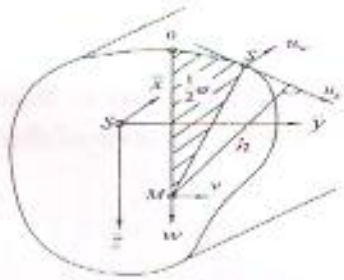

Figure(3-9): The components of displacement due to torsional shear deformation

Fig. (1) The components displacement due to torsional shear deformatio

Thus the bimoment (BM), which is a system of self-balancing components, is created as a resultant of warping restraint stresses:

$$BM = \int_A \sigma_w \, \hat{\omega} \, dA \tag{4}$$

which can be written as:

$$BM = -Ef''I_{\hat{\omega}} \tag{5}$$

in which

$$I_{\hat{\omega}} = \int_A \hat{\omega}^2 dA \tag{6}$$

$I_{\hat{\omega}}$ is the warping moment of inertia.

In dealing with closed sections, the shear deformation in the median surface of the wall will be taken into consideration by the following expression (Dabrowski 1968):

$$\gamma_{s\bar{x}} = \frac{\partial u_w}{\partial s} + \frac{\partial u_s}{\partial \bar{x}} - \frac{T}{G\delta} \tag{7}$$

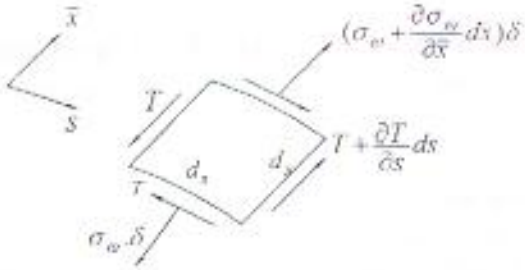

Fig. (2) A differential wall element

The total shear T can be determined from equilibrium conditions for a differential wall element shown in **Fig. (2)**, subjected to loading by normal forces $(\sigma_w \delta)$ and shear forces T, as:

$$T = \frac{H}{\Omega} - \frac{BM'}{I_{\hat{\omega}}}\left(S_{\hat{\omega}} - \frac{1}{\Omega}\int_A S_{\hat{\omega}} \, h \, ds\right) \tag{8}$$

This expression of the shear flow consists of two parts, a constant part known as the primary shear flow, which occurs only in the closed part of the section, and the secondary shear flow.

Where:

$$S_{\hat{\omega}} = \int_0^s \hat{\omega} \, \delta \, ds = \int_A \hat{\omega} \, dA \tag{9}$$

$$\bar{S}_{\bar{\omega}} = S_{\bar{\omega}} - \frac{1}{\Omega}\int S_{\bar{\omega}}\, h\, ds \tag{10}$$

The relationship between the functions f and τ may be determined from another description for the total shear T which can be obtained from the equation of shear strain $\gamma_{s\bar{x}}$ Eq. (7):

$$T = G\,\delta\,(-f'\frac{\partial\bar{\omega}}{\partial s} + h\tau') \tag{11}$$

$$\tau' = \mu\, f' + \frac{H}{GI_c} \tag{12}$$

or

$$\tau' = f' - \frac{E\,I_{\bar{\omega}}}{G\,\mu\,I_c} f''' \tag{13}$$

Integrating this equation with respect to x results:

$$\tau = f - \frac{E\,I_{\bar{\omega}}}{G\,\mu\,I_c} f'' + C \tag{14}$$

where:

C : is the constant of integration.

μ : is the warping shear parameter, which determined by the following expression.

$$\mu = 1 - \frac{J}{I_c} \tag{15}$$

$$Ic = \int h^2 \delta ds \tag{16}$$

$$J = \frac{\Omega^2}{\oint ds/\delta} \tag{17}$$

FORMULATION OF A CURVED BEAM ELEMENT WITH WARPING

The basic assumptions utilized in the formulation of the curved beam element are (Yoo 1987), (Dabrowski 1968):

1- The element is prismatic.
2- The loads are applied statically and constitute a conservative force system.
3- The cross-section maintains its original shape.
4- The deformations are small with respect to the dimensions of the cross-section (linearized problem).
5- The material is homogeneous, isotropic and obeys Hook's law.
6- The cross-sectional dimensions are small relative to the radius of curvature.
7- The cross-sectional shape is preserved under all loads, or thin-walled beams of a non-deformable cross-section.
8- The projection of the cross-section on a plane normal to the tangential axis does not distort during deformation.

The three dimensional formulation of curved beam elements can be divided into two separate groups:

1- Group-1: an in-plane group considering only displacement in the $\bar{x}, \bar{y}$ plane as an arch.
2- Group-2: a normal-to-plane group considering only displacements in the $\bar{x}, \bar{z}$ plane as a horizontally curved beam.

where x, y, z are the local curvilinear coordinates of the curved beam element as shown in **Fig. (3)**. The forces and displacements are positive if their vectors point in the direction of the positive coordinates. Right hand rule is used for the sign of moments and rotations.

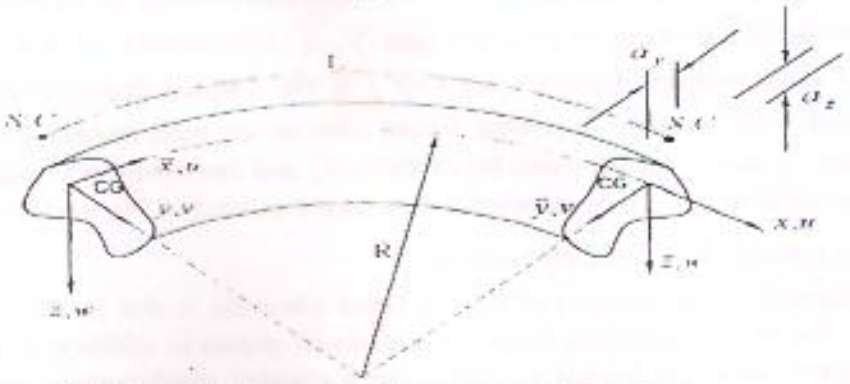

Thin-walled curved beam coordinates

Fig. (3) Thin-walled curved beam element in local curvilinear coordinates

Fig. (4) shows the generalized forces and displacements for the curved beam element with warping.

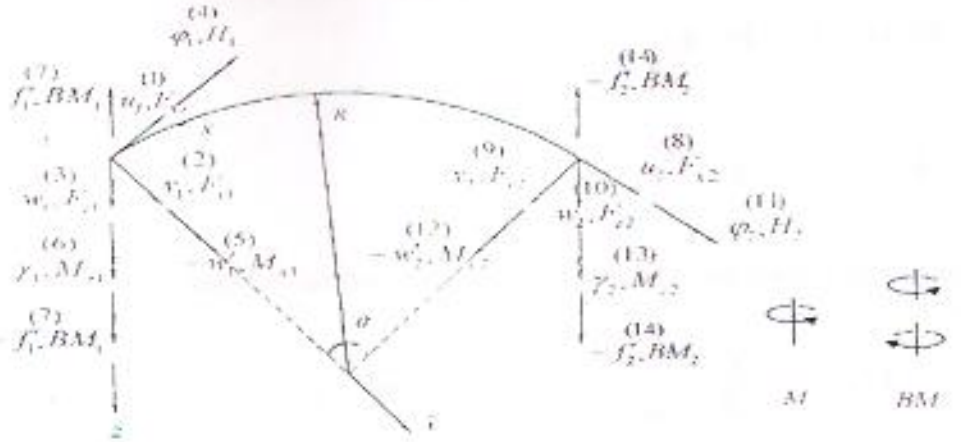

Generalized Forces and Displacements for curved beam with warping

The relationship between internal forces and the displacements at a point on the middle surface of the member are mentioned in (Dabrowski 1968), (Yoo 1987 & 1979):

$$
\left.
\begin{aligned}
F_{\bar{x}} &= EA(u' - v/R) \\
M_{\bar{z}} &= EI_{\bar{z}}(v'' + v/R^2) \\
M_{\bar{y}} &= -EI_{\bar{y}}(w'' - \varphi/R) \\
M_{S.V.} &= GJ(\varphi' + w'/R) \\
M_w &= -EI_{\hat{\omega}} f''' \\
H &= M_{S.V.} + M_w \\
BM &= -EI_{\hat{\omega}} f'' \\
F_{\bar{y}} &= -M'_{\bar{z}} \\
F_{\bar{z}} &= M'_{\bar{y}} + H/R
\end{aligned}
\right\} \qquad (18)
$$

in which $F_{\bar{x}}$ is the axial force; $M_{\bar{y}}$ and $M_{\bar{z}}$ are the bending moments about $\bar{y}$ and $\bar{z}$-axes (using the right-hand rule); H is the total torque, being a vector sum of St.Venant torque $M_{S.V.}$ and warping torque M_w; BM is the bimoment; u is the axial deformation in the direction of $\bar{x}$; v, w are displacements in the directions of principal axes $\bar{y}$, $\bar{z}$, respectively; φ is the angle of rotation about $\bar{x}$-axis; f is the warping function and $(-f')$ is the warping degree-of-freedom for closed sections associated with bimoment, primes denote derivatives with respect to $\bar{x}$-axis; R is the radius of curvature; E and G are the modulus of elasticity and the modulus of rigidity respectively; A is the cross-sectional area; $I_{\bar{y}}$, $I_{\bar{z}}$ are principal moments of inertia; J is the torsional constant and $I_{\bar{\omega}}$ is the warping constant for closed thin-walled.

The primary difficulty in the analysis of curved beam elements is due to the coupling action of bending, torsion (in curved members loaded normal-to-its plane) in addition to bending and axial extension (in curved members loaded in-plane). So a coupled displacement field is derived and developed using the equations of equilibrium in terms of component deformation for the linear static problem projected on coordinate axes.

Equilibrium Equations of Curved Beams

The equilibrium equations of a curved beam loaded in-plane are:-

$$-\frac{EA}{R}\left(u'-\frac{v}{R}\right)+EI_{\bar{z}}\left(v^{iv}+\frac{v''}{R^2}\right)=-q_{\bar{y}}+m'_{\bar{z}} \tag{19-a}$$

$$\frac{EI_{\bar{z}}}{R}\left(v''+\frac{v'}{R^2}\right)+EA\left(u''-\frac{v'}{R}\right)=q_{\bar{x}}+\frac{m_{\bar{z}}}{R} \tag{19-b}$$

While the equilibrium equations for a curved beam loaded normal-to-plane while warping effects are considered are:

$$-EI_{\bar{y}}\left(w^{iv}+\frac{w''}{R^2}\right)+\left(EI_{\bar{y}}+GJ\right)\frac{f''}{R}-\frac{EI_{\bar{\omega}}}{\mu R}\left(1+\frac{EI_{\bar{y}}}{GI_c}\right)f^{iv}=m'_{\bar{y}}+q_{\bar{z}} \tag{20-a}$$

and

$$-\frac{EI_{\bar{y}}}{R}\left(w''+\frac{w}{R^2}\right)+\frac{EI_{\bar{y}}}{R^2}f-\frac{E^2I_{\bar{\omega}}I_{\bar{y}}}{G\mu I_c R^2}f''-GJf''+\frac{EI_{\bar{\omega}}}{\mu}f^{iv}=-m_{\bar{x}}-\frac{EI_{\bar{y}}C}{R^2} \tag{20-b}$$

Some forces in eqs. (18), (19) and (20) refer to the line of centroids others refer to shear center. The shear center with coordinates $a_{\bar{y}}$ and $a_{\bar{z}}$, measured from the centroid, is called the principal sectorial pole, or simply, principal pole. Using the same radius of curvature, R, in these equations for gravity center and shear center can be acceptable since in most practical beams the quantity $a_{\bar{y}}/R$ as compared to unity can be neglected without inducing a significant error. Thus the derived displacement field does not have to be limited to curved beams of doubly or singly symmetric sections with the axis of symmetry being in the plane of bending.

General Displacement Fields and Displacement Functions

The generalized displacements and force vectors for a curved beam, as shown in **Fig. (4)**, are:

$$\{\Delta_w\}=[u_1,\ v_1\ \ w_1\ \ \varphi_1\ \ -w_1'\ \ \gamma_1\ \ -f_1'\ \ u_2\ \ v_2\ \ w_2\ \ \varphi_2\ \ -w_2'\ \ \gamma_2\ \ -f_2']^T \tag{21}$$

and

$$\{F_w\}=\left[F_{\bar{x}1}\ F_{\bar{y}1}\ F_{\bar{z}1}\ H_1\ M_{\bar{y}1}\ M_{\bar{z}1}\ BM_1\ F_{\bar{x}2}\ F_{\bar{y}2}\ F_{\bar{z}2}\ H_2\ M_{\bar{y}2}\ M_{\bar{z}2}\ BM_2\right]^T \quad (22)$$

The subscript w refers to a curved beam with warping. While the subscripts (1) and (2) refer to nodes 1 and 2, respectively, which are the end nodes of the element. The positive direction of the generalized displacements and forces point to the positive local coordinate system as shown in **Fig. (4)**.

A coupled boundary condition is introduced for the first group, curved beam loaded in plane, which is defined in references (Yoo 1979) and (Yoo 1987) as:

$$\gamma = v' + \frac{u}{R} \quad (23)$$

The subdivided generalized displacement vectors are:

$$\{\Delta_{w1}\}=\left[u_1\ v_1\ 0\ 0\ 0\ \gamma_1\ 0\ u_2\ v_2\ 0\ 0\ 0\ \gamma_2\ 0\right]^T \quad (24\text{-a})$$

$$\{\Delta_{w2}\}=\left[0\ 0\ w_1\ \varphi_1\ -w_1'\ 0\ -f_1'\ 0\ 0\ w_2\ \varphi_2\ -w_2'\ 0\ -f_2\right]^T \quad (24\text{-b})$$

$\{\Delta_{w1}\}$ and $\{\Delta_{w2}\}$ are for group-1 and 2 respectively. Also, the subdivided generalized force vectors are:

$$\{F_{w1}\}=\left[F_{\bar{x}1}\ F_{\bar{y}1}\ 0\ 0\ 0\ M_{\bar{z}1}\ 0\ F_{\bar{x}2}\ F_{\bar{y}2}\ 0\ 0\ 0\ M_{\bar{z}2}\ 0\right]^T \quad (25\text{-a})$$

and

$$\{F_{w2}\}=\left[0\ 0\ F_{\bar{z}1}\ H_1\ M_{\bar{y}1}\ 0\ BM_1\ 0\ 0\ F_{\bar{z}2}\ H_2\ M_{\bar{y}2}\ 0\ BM_2\right]^T \quad (25\text{-b})$$

$\{F_{w1}\}$ and $\{F_{w2}\}$ are for group-1 and 2 respectively.

In-Plane Displacement Field and Displacement Functions

For group-1, the homogeneous case of equilibrium eqs. (19-a, b) can be rewritten as:

$$L_1 v + L_2 u = 0 \quad (26\text{-a})$$

$$L_3 v + L_4 u = 0 \quad (26\text{-b})$$

where:

$$L_1 = -I_{\bar{z}}\frac{d^4}{d\bar{x}^4} - \frac{I_{\bar{z}}}{R^2}\frac{d^2}{d\bar{x}^2} - \frac{A}{R^2} \quad (27\text{-a})$$

$$L_2 = \frac{A}{R}\frac{d}{d\bar{x}} \quad (27\text{-b})$$

$$L_3 = \frac{I_{\bar{z}}}{R}\frac{d^3}{d\bar{x}^3} + \left(\frac{I_{\bar{z}}}{R^3} - \frac{A}{R}\right)\frac{d}{d\bar{x}} \quad (27\text{-c})$$

$$L_4 = A\frac{d^2}{d\bar{x}^2} \quad (27\text{-d})$$

Since the operators are linear and are commutative, the following equation can be applied to v or u:

$$(L_1 L_4 - L_3 L_2) = 0 \quad (28)$$

or

$$\frac{d^6}{d\bar{x}^6} + \frac{2}{R^2}\frac{d^4}{d\bar{x}^4} + \frac{1}{R^4}\frac{d^2}{d\bar{x}^2} = 0 \quad (29)$$

The coupled displacement field of the curved beam element loaded in plane can be obtained from the solution of these differential equations as:

$$v(\bar{x}) = A_1 + A_2 \cos\frac{\bar{x}}{R} + A_6 \sin\frac{\bar{x}}{R} + A_7 \frac{\bar{x}}{R}\cos\frac{\bar{x}}{R} + A_8 \frac{\bar{x}}{R}\sin\frac{\bar{x}}{R} \tag{30-a}$$

$$u(\bar{x}) = A_1 \frac{\bar{x}}{R} + A_2 \sin\frac{\bar{x}}{R} - A_6 \cos\frac{\bar{x}}{R} + A_7\left[F_A \cos\frac{\bar{x}}{R} + \frac{\bar{x}}{R}\sin\frac{\bar{x}}{R}\right] + A_8\left[F_A \sin\frac{\bar{x}}{R} - \frac{\bar{x}}{R}\cos\frac{\bar{x}}{R}\right] + A_{12} \tag{30-b}$$

$\gamma(\bar{x})$ can be obtained from eq. (23)

$$\gamma(\bar{x}) = A_1 \frac{\bar{x}}{R^2} + A_7 \frac{1+F_A}{R}\cos\frac{\bar{x}}{R} + A_8 \frac{1+F_A}{R}\sin\frac{\bar{x}}{R} + \frac{A_{12}}{R} \tag{30-c}$$

where:

$$F_A = 1 - \frac{2I_{\bar{y}}}{AR^2} \tag{31}$$

which may be called the Winkler's constant (Yoo 1979) and (Yoo 1987).

Normal-to-Plane Displacement Field and Displacement Functions With Warping

A coupled model of a curved beam element loaded normal-to-plane with warping, as an explicit degree-of-freedom, is derived. In addition to the coupling action between bending and torsion, this model considers the total shear deformation (primary and secondary shear deformation), which is caused by warping; the coupled displacement field is derived from the homogeneous case of equilibrium equations (20-a, b):

$$L_5 w + L_6 f = 0 \tag{32-a}$$

$$L_7 w + L_8 f = 0 \tag{32-b}$$

where:

$$L_5 = -EI_{\bar{y}}\frac{d^4}{dx^4} - \frac{EI_{\bar{y}}}{R^2}\frac{d^2}{d\bar{x}^2} \tag{33-a}$$

$$L_6 = -\frac{EI_{\hat{\omega}}}{\mu R}\left(1+\frac{EI_{\bar{y}}}{GI_c}\right)\frac{d^4}{d\bar{x}^4} + \frac{(EI_y + GJ)}{R}\frac{d^2}{dx^2} \tag{33-b}$$

$$L_7 = -\frac{EI_y}{R}\frac{d^2}{d\bar{x}^2} - \frac{EI_{\bar{y}}}{R^3} \tag{33-c}$$

$$L_8 = \frac{EI_{\hat{\omega}}}{\mu}\frac{d^4}{dx^4} - \left(\frac{E^2 I_{\hat{\omega}} I_y}{GR^2 \mu I_c} + GJ\right)\frac{d^2}{d\bar{x}^2} + \frac{EI_y}{R^2} \tag{33-d}$$

Also these operators are linear and are commutative, therefore the following equation can be applied to w or f:

$$(L_5 L_8 - L_6 L_7) = 0 \tag{34}$$

or

$$R^2\frac{d^8}{dx^8} + \left(2 - \frac{R^2 \mu GJ}{EI_{\hat{\omega}}}\right)\frac{d^6}{d\bar{x}^6} + \left(\frac{1}{R^2} - \frac{2\mu GJ}{EI_{\hat{\omega}}}\right)\frac{d^4}{dx^4} - \frac{\mu GJ}{R^2 EI_{\hat{\omega}}}\frac{d^2}{d\bar{x}^2} = 0 \tag{35}$$

Solving these differential equations results the coupled displacement field of the curved beam element loaded normal-to-plane while warping effects are considered:

$$w(\bar{x}) = A_3 + A_4\frac{\bar{x}}{R} + A_5\cosh\frac{\hat{\alpha}\,\bar{x}}{R} + A_7\sinh\frac{\hat{\alpha}\,\bar{x}}{R} + A_{10}\cos\frac{\bar{x}}{R} + A_{11}\sin\frac{\bar{x}}{R} + A_{12}\frac{\bar{x}}{R}\cos\frac{\bar{x}}{R} + A_{14}\frac{\bar{x}}{R}\sin\frac{\bar{x}}{R} \quad (36\text{-a})$$

and

$$f(\bar{x}) = \frac{A_3}{R} + A_4\frac{\bar{x}}{R^2} + A_5\frac{(1+\hat{\alpha}^2)}{R\mu}\cosh\frac{\hat{\alpha}\,\bar{x}}{R} + A_7\frac{(1+\hat{\alpha}^2)}{R\mu}\sinh\frac{\hat{\alpha}\,\bar{x}}{R} - A_{12}\frac{ABIC}{R}\sin\frac{\bar{x}}{R} + A_{14}\frac{ABIC}{R}\cos\frac{\bar{x}}{R} \quad (36\text{-b})$$

while φ can be obtained from this equation $\varphi = -\frac{w}{R} + f - \frac{EI_{\hat{\omega}}}{G\mu I_c}f'' + C$

$$\varphi(\bar{x}) = A_5\frac{\hat{\alpha}^2}{R}\cosh\frac{\hat{\alpha}\,\bar{x}}{R} + A_7\frac{\hat{\alpha}^2}{R}\sinh\frac{\hat{\alpha}\,\bar{x}}{R} - \frac{A_{10}}{R}\cos\frac{x}{R} - \frac{A_{11}}{R}\sin\frac{\bar{x}}{R} - \frac{A_{12}}{R}\left[ABICW\sin\frac{\bar{x}}{R} + \frac{\bar{x}}{R}\cos\frac{\bar{x}}{R}\right] + \frac{A_{14}}{R}\left[ABICW\cos\frac{\bar{x}}{R} - \frac{\bar{x}}{R}\sin\frac{\bar{x}}{R}\right] \quad (36\text{-c})$$

in which:

$$ABIC = \frac{2\hat{\beta}^2}{1+\hat{\alpha}^2+\hat{\beta}^2+\bar{\xi}^2} \quad (37)$$

$$ABICW = \frac{2(\hat{\beta}^2+\bar{\xi}^2)}{1+\hat{\alpha}^2+\hat{\beta}^2+\bar{\xi}^2} \quad (38)$$

$$\hat{\alpha} = \sqrt{R^2\frac{\mu GJ}{EI_{\hat{\omega}}}} \quad (39)$$

$$\hat{\beta} = \sqrt{R^2\frac{\mu I_{\bar{y}}}{I_{\hat{\omega}}}} \quad (40)$$

and

$$\bar{\xi} = \sqrt{\frac{EI_{\bar{y}}}{GI_c}} \quad (41)$$

Strain Energy of The Curved Beam Element

In addition to the normal stresses due to bending and axial force, which are developed in a curved beam, an additional axial direct stress (or normal warping stress) and both primary and secondary shear stresses due to the total torque and the bimoment, respectively will be formed in the horizontally curved beam when restrained warping effects are included. As the cross-sectional dimensions are small compared to the radius of curvature, the shear stresses due to bending can be neglected.

The relationship between forces and normal or shear stresses of thin-walled curved beam elements are:

$$\sigma_{\bar{x}} = \sigma_{\bar{x}1} + \sigma_{\bar{x}2} \quad (42)$$

in which $\sigma_{\bar{x}1}$ and $\sigma_{\bar{x}2}$ are the normal stresses of groups-1 and 2, respectively.

$$\sigma_{x1} = \frac{F_x}{A} - \frac{M_{\bar{z}} \cdot \bar{y}}{I_{\bar{z}}} \tag{43}$$

$$\sigma_{x2} = \frac{M_{\bar{y}} \cdot \bar{z}}{I_{\bar{y}}} + \frac{BM \cdot \hat{\omega}}{I_{\hat{\omega}}} \tag{44}$$

$$\tau_{sx} = G[\frac{\Omega \tau'}{\oint ds} + (\frac{\Omega}{\oint ds} - h)(f' - \tau')] \tag{45}$$

The strain energy is:

$$U = U_1 + U_2 \tag{46}$$

where U_1 and U_2 are strain energies of groups-1 and 2, respectively.

$$U_1 = \frac{E}{2} \int_{\bar{x}} [A(u' - \frac{v}{R})^2 + I_{\bar{z}}(v'' + \frac{v}{R^2})^2] d\bar{x} \tag{47}$$

The strain energy of group-2 comprises strain energies due to normal and shears deformations

$$U_2 = U_{2n} + U_{2s} \tag{48}$$

The strain energy due to normal stress for group-2 is:

$$U_{2n} = \frac{E}{2} \int_{\bar{x}} [I_{\bar{v}}(w'' - \frac{\varphi}{R})^2 + I_{\hat{\omega}} f''^2] dx \tag{49}$$

While the strain energy due to the primary and secondary shear deformations that will be appeared when restrained warping effects are included, U_{2s}, can be expressed as:

$$U_{2s} = \frac{GJ}{2} \int_{\bar{x}} \tau'^2 d\bar{x} + \frac{G}{2} \int_{\bar{x}} (I_c - J)(f' - \tau')^2 d\bar{x} \tag{50}$$

Stiffness Matrix of Curved Beams With Warping

A stiffness of order (14x14) is derived by minimizing the potential energy. Due to the complication of $[B]$ matrix expressions, the numerical integration technique is used to produce the stiffness matrix elements.

$$[K_t] = [K1] + [K2] \tag{51}$$

in which

$[K_t]$: is the total stiffness matrix for the curved beam element with warping in the local coordinate.

$[K1]$: is the stiffness matrix of order (6x6) for the curved beam loaded in plane (group-1)

[K2]: is the stiffness matrix of order (8x8) for the curved beam loaded normal-to-plane (group-2) when warping effects being included.

In-Plane Stiffness Matrix

The stiffness matrix of this group consists of axial and bending stiffness matrices, as:

$$[K1] = [KA] + [KB1] \tag{52}$$

in which $[KB1]$ denotes bending stiffness matrix for group-1:

$$[KA]=EA\int_0^L[BA]^T[BA]d\bar{x} \quad (53\text{-a})$$

and

$$[KBI]=EI_z\int_0^L[BBI]^T[BBI]d\bar{x} \quad (53\text{-b})$$

in which $[BA]$ and $[BBI]$ are row vectors relating the joint displacements to strain field for group-1 ($\varepsilon=[B]\{\Delta\}$)

$$[BA]=[N_u'-N_v/R] \quad (54\text{-a})$$

and

$$[BBI]=[N_v''+N_v/R^2] \quad (54\text{-b})$$

The individual element for $[KA]$ and $[KBI]$ can be expressed as:

$$KA_{ij}=EA\int_0^L(N_u'-\frac{N_v}{R})i.(N_u'-\frac{N_v}{R})j\,d\bar{x} \quad (55\text{-a})$$

and

$$KB1_{ij}=EI_z\int_0^L(N_v''+\frac{N_v}{R^2})i.(N_v''+\frac{N_v}{R^2})j\,d\bar{x} \quad (55\text{-b})$$

where i or j = (1, 2, 6, 8, 9, 13)

$$(N_u'-\frac{N_v}{R})i=A_{(7,i)}\frac{(1-F_A)}{R}\sin\frac{\bar{x}}{R}-A_{(8,i)}\frac{(1-F_A)}{R}\cos\frac{\bar{x}}{R} \quad (56\text{-a})$$

$$(N_v''+\frac{N_v}{R^2})i=\frac{A_{(1,i)}}{R^2}-A_{(7,i)}\frac{2}{R^2}\sin\frac{\bar{x}}{R}+A_{(8,i)}\frac{2}{R^2}\cos\frac{\bar{x}}{R} \quad (56\text{-b})$$

Normal-to-Plane Stiffness Matrix

The stiffness matrix of this group comprises of four subdivided stiffness matrices, as in the following:

$$[K2]=[KB2]+[KBM]+[KT1]+[KT2] \quad (57)$$

where:

$[KB2]$: is the bending stiffness matrix for group-2 when warping is considered.

$[KBM]$: is the stiffness matrix resulting from the warping normal stress and strain caused by the bimoment.

$[KT1]$ and $[KT2]$: are torsional stiffness matrices resulting from the total shear deformation, which comprises the primary and secondary shear deformations.

$$[KB2]=EI_y\int_0^L[BB2]^T[BB2]d\bar{x} \quad (58\text{-a})$$

$$[KBM]=EI_\omega\int_0^L[BBM]^T[BBM]dx \quad (58\text{-b})$$

$$[KT1]=GJ\int_0^L[BT1]^T[BT1]dx \quad (58\text{-c})$$

$$[KT2]=G(I_c-J)\int_0^L[BT2]^T[BT2]d\bar{x} \quad (58\text{-d})$$

in which $[BB]$, $[BBM]$, $[BT1]$, and $[BT2]$ are row vectors relating the joint degrees-of-freedom to strain field for group-2 with warping.

$$[BB2]=\left[N''_w-\frac{N_\varphi}{R}\right] \tag{59-a}$$

$$[BBM]=[N''_f] \tag{59-b}$$

$$[BT1]=[N'_\tau] \tag{59-c}$$

$$[BT2]=[N'_f-N'_\tau] \tag{59-d}$$

in which

$$N_\tau=N_\varphi+\frac{N_w}{R} \tag{60}$$

The expressions for the individual element of the subdivided stiffness matrices are:

$$KB2_{ij}=E\,I_{\bar{y}}\int_0^L\left(N''_w-\frac{N_\varphi}{R}\right)i\left(N''_w-\frac{N_\varphi}{R}\right)j\,d\bar{x} \tag{61-a}$$

$$KBM_{ij}=E\,I_{\hat{\omega}}\int_0^L(N''_f)i(N''_f)j\,d\bar{x} \tag{61-b}$$

$$KT1_{ij}=GJ\int_0^L(N'_\tau)i(N'_\tau)j\,d\bar{x} \tag{61-c}$$

$$KT2_{ij}=G(I_c-J)\int_0^L(N'_f-N'_\tau)i(N'_f-N'_\tau)j\,d\bar{x} \tag{61-d}$$

where $i, j = (3, 4, 5, 7, 10, 11, 12, 14)$.

The individual elements of the $[B]$ vectors in eqs. (59) are:

$$\left(N''_w-\frac{N_\varphi}{R}\right)_i=\frac{A_{(12,i)}}{R^2}(ABICW-2)\sin\frac{\bar{x}}{R}-\frac{A_{(14,i)}}{R^2}(ABICW-2)\cos\frac{\bar{x}}{R} \tag{62-a}$$

$$(N''_f)_i=\frac{A_{(5,i)}}{R^3\mu}\hat{\alpha}^2(1+\hat{\alpha}^2)\cosh\frac{\hat{\alpha}\,\bar{x}}{R}+\frac{A_{(7,i)}}{R^3\mu}\hat{\alpha}^2(1+\hat{\alpha}^2)\sinh\frac{\hat{\alpha}\,\bar{x}}{R}+\frac{A_{(12,i)}}{R^3}ABIC\sin\frac{\bar{x}}{R}-\frac{A_{(14,i)}}{R^3}ABIC\cos\frac{\bar{x}}{R} \tag{62-b}$$

$$(N'_\tau)_i=-\frac{A_{(4,i)}}{R^2}+\frac{A_{(5,i)}}{R^2}\hat{\alpha}(1+\hat{\alpha}^2)\sinh\frac{\hat{\alpha}\,\bar{x}}{R}+\frac{A_{(7,i)}}{R^2}\hat{\alpha}(1+\hat{\alpha}^2)\cosh\frac{\hat{\alpha}\,\bar{x}}{R}-\frac{A_{(12,i)}}{R^2}ABICW\cos\frac{\bar{x}}{R}-\frac{A_{(14,i)}}{R^2}ABICW\sin\frac{\bar{x}}{R} \tag{62-c}$$

$$(N'_f-N'_\tau)_i=A_{(5,i)}\frac{J}{R^2\mu I_c}\hat{\alpha}(1+\hat{\alpha}^2)\sinh\frac{\hat{\alpha}\,\bar{x}}{R}+A_{(7,i)}\frac{J}{R^2\mu I_c}\hat{\alpha}(1+\hat{\alpha}^2)\cosh\frac{\hat{\alpha}\,\bar{x}}{R}+A_{(12,i)}\frac{EI_{\hat{\omega}}}{R^4G\mu I_c}ABIC\cos\frac{\bar{x}}{R}++A_{(14,i)}\frac{EI_{\hat{\omega}}}{R^4G\mu I_c}ABIC\sin\frac{\bar{x}}{R} \tag{62-d}$$

TRANSFORMATION INTO SYSTEM CORDINATES

The stiffness matrices of the three-dimensional curved beam elements refer to the element local axes $\bar{x}, \bar{y}, \bar{z}$. The total transformation of the stiffness matrices of curved beam elements from local coordinates can be expressed as:

$$[K_G]=[T]^T[T']^T[K_L][T'][T] \tag{63}$$

where

$[K_C]$: is the global stiffness matrix of a curved beam element.

$[K_L]$: is the stiffness matrix of curved beam element in the local coordinate system.

On the other hand, $[T']$ is the transformation matrix used for the first stage of transformation from the local curvilinear coordinates $\bar{x}, \bar{y}, \bar{z}$ to the local straight coordinates x, y, z **(Fig. (5).** The elements of this matrix are the direction cosines between the two systems $(\bar{x}, \bar{y}, \bar{z})$ and (x, y, z). For curved beams with warping, the $[T']$ matrix will be of order of (14x14), which can be expressed as:

$$[T'] = \begin{bmatrix}
c & -s & 0 & & & & & & & & & & & \\
s & c & 0 & & & & & & & & & & & \\
0 & 0 & 1 & & & & & & & & & & & \\
0 & 0 & 0 & c & -s & 0 & & & & & & & & \\
0 & 0 & 0 & s & c & 0 & & & & & & & & \\
0 & 0 & 0 & 0 & 0 & 1 & & & & & & & & \\
0 & 0 & 0 & 0 & 0 & 0 & 1 & & & & & & & \\
0 & 0 & 0 & 0 & 0 & 0 & 0 & c & s & 0 & & & & \\
0 & 0 & 0 & 0 & 0 & 0 & 0 & -s & c & 0 & & & & \\
0 & 0 & 0 & 0 & 0 & 0 & 0 & 0 & 0 & 1 & & & & \\
0 & 0 & 0 & 0 & 0 & 0 & 0 & 0 & 0 & 0 & c & s & & \\
0 & 0 & 0 & 0 & 0 & 0 & 0 & 0 & 0 & 0 & -s & c & & \\
0 & 0 & 0 & 0 & 0 & 0 & 0 & 0 & 0 & 0 & 0 & 0 & 1 & \\
0 & 0 & 0 & 0 & 0 & 0 & 0 & 0 & 0 & 0 & 0 & 0 & 0 & 1
\end{bmatrix} \quad \text{SYMM.} \qquad (64)$$

where $s = \sin(\theta/2)$, and $c = \cos(\theta/2)$.

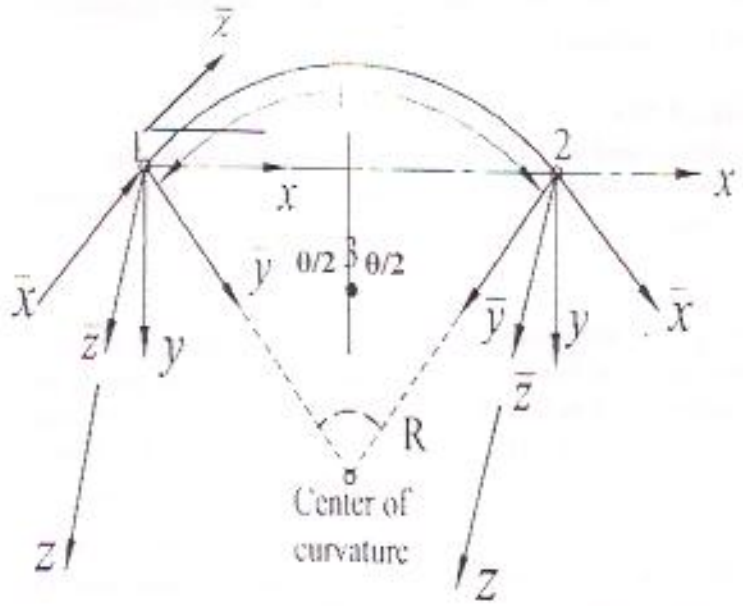

Fig. (5) Curvilinear coordinates $\bar{x}, \bar{y}, \bar{z}$ and straight coordinates x, y, z

$[T']$ Matrix in Eq. (63) is for the second stage of transformation to convert the stiffness matrix from local straight coordinates to the global coordinate system. For curved beams with warping, [T] can be expressed as:

$$[T]=\begin{bmatrix} [T^n] & 0 & 0 & 0 & 0 & 0 \\ & [T^n] & 0 & 0 & 0 & 0 \\ & & 1 & 0 & 0 & 0 \\ & & & [T^n] & 0 & 0 \\ & \text{SYMM.} & & & [T^n] & 0 \\ & & & & & 1 \end{bmatrix} \quad (65)$$

where $[T^n]$ is the (3x3) transformation matrix as described by reference (Dabrowski 1968)and can be expressed as (Azar 1972 & Krishnamoorthy 1988):

$$[T^n]=\begin{bmatrix} \cos\alpha.\cos\beta & \sin\beta & \sin\alpha.\cos\beta \\ -\cos\alpha.\sin\beta.\cos\gamma - \sin\alpha.\sin\gamma & \cos\gamma.\cos\beta & -\sin\alpha.\sin\beta.\cos\gamma + \cos\alpha.\sin\gamma \\ \cos\alpha.\sin\beta.\sin\gamma - \sin\alpha.\cos\gamma & -\sin\gamma.\cos\beta & \sin\alpha.\sin\beta.\sin\gamma + \cos\alpha.\cos\gamma \end{bmatrix} \quad (66)$$

where α, β, γ are rotations about Y, Z, X, respectively.

The value (1) in $[T]$and $[T']$, in rows 7 and 14 is the direction cosines of the member for the seventh degree-of -freedom (warping).

VERIFICATION PROBLEMS

A computer program is developed for static analysis to demonstrate the accuracy of the developed curved beam element. Two problems are analyzed. The results of the present study analysis are compared with exact solutions.

Problem (1)

A single span curved box girder subjected to truck eccentric loading is analyzed. Effects of warping are considered in the analysis. The loading and geometry of the box girder of this problem with its sectional properties are shown in **Table. (1)** and **Fig. (6)**. The modulus of elasticity E and Poisson's ratio υ are 30000 k / in^2 (206832.41 MPa) and (0.2931), respectively. Both supports of the girder are pinned in bending and torsion $(M_y = 0,\ \varphi = 0,\ BM = 0)$. Four elements are used in the analysis of this girder. **Table. (2)** shows a comparison between the present study analysis results, when curved beam elements with warping are used and reference (Heins and Oleinik 1976) analysis results. This reference analyzed the same problem and presented results where 200 curved beam elements that he developed were used. Also, this comparison includes the results of the closed-form solution from reference (Dabrowski 1968). The closed-form solution equations are presented in Appendix (A). The results of the present study analysis show an excellent agreement with the closed-form solution results and the maximum difference is ($3.232\text{x}10^{-5}$%) from these results. On the other hand, the present study analysis results show a maximum difference of (.174 %) from the displacements and rotations results of reference (Heins and Oleinik 1976). The values of the

bimoment in reference (Heins and Oleinik 1976) are found to be far from the closed form solution values, while the present analysis bimoment values are very close to those of the exact solution.

Table.(1) Problem (1) applied loads

Node	Location	Vertical concentrated load (k)	Concentrated torsion (k.in)
2	0.22L	6	-288
3	0.50L	32	-1152
4	0.78L	32	-1152

Table.(2) Results of problem (1)

Item	Location	Exact solution Ref. (Dabrowski 1968)	Ref. (Heins and Oleinik-1976) analysis results	Present study results
Vertical displacement w (in)	0.05L		0.53808172 E-1	0.53804271 E-1
	0.15L		0.15688980	0.15687833
	0.22L		0.22150741	0.22149105
Rotation φ (rad)	0.05L		-0.14346389 E-3	-0.14332976 E-3
	0.15L		-0.42225950 E-3	-0.42172726 E-3
	0.22L		-0.60145488 E-3	-0.60250367 E-3
Shear force F_z (k)	0		29.28	29.28
Bending moment M_y (k.in)	0.05L	0.93261162E+3	0.93261258E+3	0.93261151 E+3
	0.15L	0.27955038E+4	0.27955067E+4	0.27955037 E+4
	0.22L	0.40956474E+4	0.40956516E+4	0.40956472 E+4
Total torque H (k.in)	0	-0.21723501E+4	-0.21725838E+4	-0.21723502E+4
	0.05L	-0.21606918E+4	-0.21606924E+4	-0.21606920E+4
	0.15L	-0.20674695E+4	-0.20674700E+4	-0.20674697E+4
T_{sv} (k.in)	0	-0.21653588E+4	-0.21680428E+4	-0.21653590E+4
	0.05L	-0.21532267E+4	-0.21563426E+4	-0.21532268E+4
	0.15L	-0.20536354E+4	-0.20576431E+4	-0.20536356E+4
T_w (k.in)	0	-0.69912562E+1	-0.43073081E+1	-0.69912557E+1
	0.05L	-0.74651696E+1	-0.43497252E+1	-0.74651694E+1
	0.15L	-0.13834114E+2	-0.98269119E+1	-0.13834115E+2
BM (k.in^2)	0.05L	-0.21436112E+3	-0.12958343E+3	-0.21436111E+3
	0.15L	-0.79732544E+3	-0.45730444E+3	-0.79732543E+3
	0.22L	-0.16957586E+4	-0.24010951E+4	-0.16957586E+4

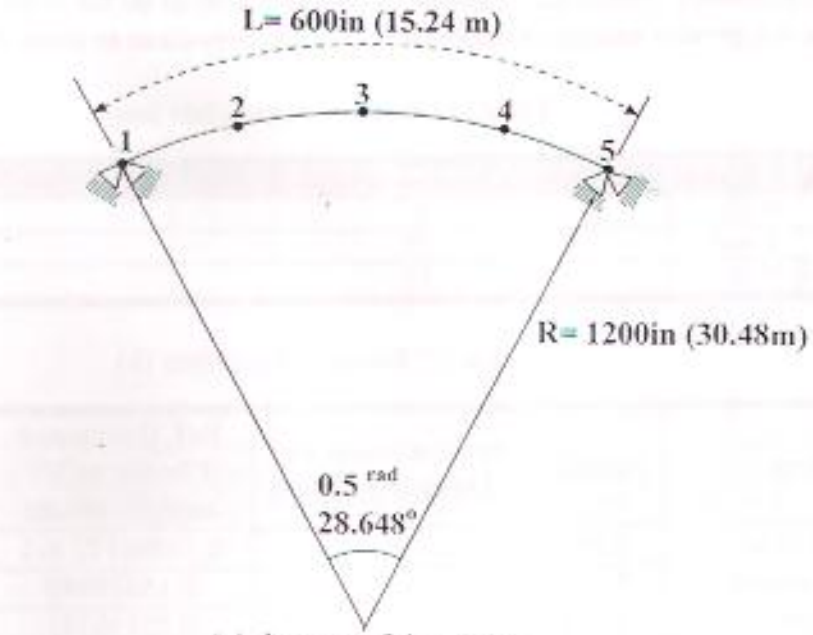

(a): Layout of the girder

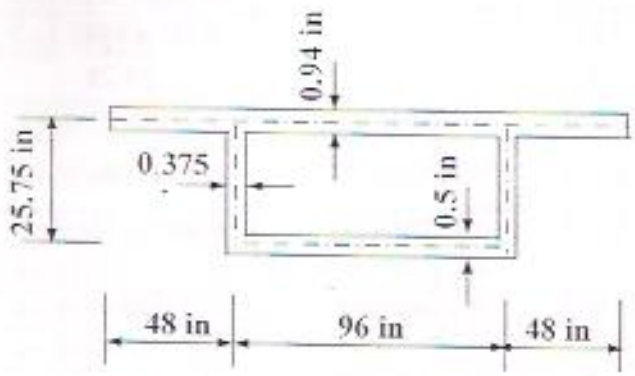

(b): Cross section

Section properties:

J = 0.567513128 E+5 in^4 (2.3621679 E -2 m^4) $I_{\bar{y}}$ =0.2724672458 E +5 in^4 (1.1340943 E -2 m^4),

$I_{\bar{\omega}}$ =4.914587775 E +6 in^6 (1.319743 E -3 m^6), I_c = 0.6975613917 E +5 in^4 (2.9034697 E -2 m^4)

Fig. 6 : Curved box girder of problem (1)

Problem (2)

A semicircular fixed ended arch of radius (R=1.5 m) is analyzed. The sectional properties are (J= 6.4E-3, I_z = 1.6E-3 m^4). The modulus of elasticity is (E = 200000 MPa) and Poisson's ratio is (υ =0.3). To assess the validity of both in-plane action of the developed curved beam element; the arch is loaded by a concentrated load of (250 kN) at the crown in the plane of the arch.. The analyzed arch consists of two elements. The results of this analysis are compared with the exact solutions of reference (Martin 1966). The comparison, which is given in **Table (3)**, shows an excellent agreement with the exact solution and the maximum difference is (.187 %).

Table (3) Results of problem (2)

Item	Exact solution results from Reference (Martin 1966)	Present study results
Vertical displacement under the load (cm)	$PR^3/85.802E\,I_z$ =0.3073E-2	0.3074890E-2
Bending moment at supports M_z (kN.cm)	0.1104 PR=0.4140E+4	0.414774E+4
Bending moment under the load (kN.cm)	0.1514PR=0.56775E+4	0.568005E+4

CONCLUSIONS

1- Since the new displacement field is derived from the homogeneous part of the equilibirum equations that control the static behavior of a thin-walled curved beam element of a closed section :vhen warping effects are included, the element's stiffness matrix that derived using this displacement field gives very closed results compared with the closed form solution results and can be said it is an exact solution therefore there is no added advantage or increase in the accuracy when implying finer mesh.

2- Considering the non-uniform torsional behavior of a closed thin-walled section of the curved beam element in the derivation of its warping function makes the results very close to the closed form solution.

REFERENCES

Azar, J. J., (1972), Matrix Structural Analysis, Pergramon Press Inc., New York, pp. 97-105.

Dabrowski, R., (1968), Curved Thin-Walled Girders, Cement and Concrete Association, London, England Translation No.144,.

Heins, C. P., and Oleinik, J. C. (1976), Curved Box Beam Bridge Analysis, Computers & Structures, Vol. 6, pp. 65-73.

Krishnamoorthy, C. S., (1988), Finite Element Analysis: Theory and Programming, TATA McGraw-Hill, New Delhi.

Martin, H. C., (1966), Introduction to Matrix Methods of Structural Analysis, McGraw-Hill, New York, pp. 144-152.

Yoo, C. H. (1979), Matrix Formulation of Curved Girders, Journal of Structural Division, ASCE, Vol. 105, No. EM6, pp. 971-988.

Yoo C. H. (1987), A Consistent Discrete Elements Technique for Curved Members, Computers & Structures, Vol. 25, No.1, pp. 137-146.

Appendix A

Table (A.1): Stress resultants in the basic system for a loading system comprising a concentrated load P and a separate twisting moment M Ref. (Dabrowski 1968).

Quantity	Rang.	Expression
M_y	I	$(PR-M)\frac{\sin\beta'}{\sin\theta}\sin\varphi$
	II	$(PR-M)\frac{\sin\beta}{\sin\theta}\sin\varphi'$
H	I	$(M-PR)\frac{\sin\beta'}{\sin\theta}\cos\varphi+PR\frac{\beta'}{\theta}$
	II	$-(M-PR)\frac{\sin\beta}{\sin\theta}\cos\varphi'-PR\frac{\beta}{\theta}$
$\frac{M_w}{\mu}$	I	$\frac{M(1-\eta)+PR\eta}{k}\frac{\sinh kb}{\sinh kL}\sinh kx+(MR-PR^2)\eta\frac{\sin\beta'}{\sin\theta}\sin\varphi$
	II	$\frac{M(1-\eta)+PR\eta}{k}\frac{\sinh ka}{\sinh kL}\sinh kx'+(MR-PR^2)\eta\frac{\sin\beta}{\sin\theta}\sin\varphi'$
$\frac{BM}{\mu}$	I	$[M(1-\eta)+PR\eta]\frac{\sinh kb}{\sinh kL}\cosh kx+(M-PR)\eta\frac{\sin\beta'}{\sin\theta}\sin\varphi$
	II	$-[M(1-\eta)+PR\eta]\frac{\sinh ka}{\sinh kL}\cosh kx'-(M-PR)\eta\frac{\sin\beta}{\sin\theta}\sin\varphi'$
k		$\sqrt{\frac{\mu GJ}{EI_\omega}}$
η		$\frac{1}{1+(kR)^2}$

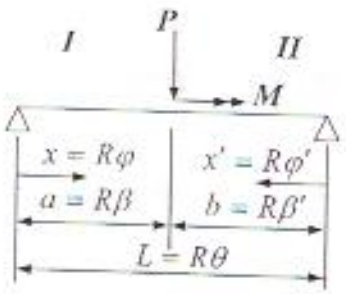

LIST OF SYMBOLS

a_y, a_z : Coordinates of shear center measured from centroid.
A : Cross-sectional area.
$ABIC, ABICW$: Dimensionless parameters defining cross-sectional rigidities.
A_i : Displacement field unknowns.
$[BA]$, $[BBI]$: Row vectors relating the joint degree-of-freedom to strain field of group

–1.

$[BB2]$, $[BT]$	:	Row vectors relating the joint degree-of-freedom to strain field of group – 2 without warping.
$[BB_W]$, $[BBM_W]$, $[BT_{W1}]$, $[BT_{W2}]$	:	Row vectors relating the joint degree-of-freedom to strain field of group – 2 with warping.
BM	:	Bimoment.
$\{D_1\}$	:	Generalized displacement field for groups –1.
$\{D_{w2}\}$	:	Generalized displacement field for group –2 when warping is considered.
E	:	Modulus of elasticity.
$F_{\bar{x}}, F_{\bar{y}}, F_{\bar{z}}$	:	Axial and shear forces.
f	:	**Dimensionless warping function.**
$\{F_w\}, \{\Delta_w\}$	:	Generalized force and displacement vectors for the curved beam element with warping.
F_A	:	Dimensionless parameters.
G	:	Shear modulus.
h	:	The distance of contour from the shear center.
H	:	Total torque.
$I_{\bar{y}}, I_{\bar{z}}$	:	Principal moments of inertia.
$I_{\bar{\omega}}$	:	Warping moment of inertia for closed and open-closed sections.
I_c	:	Central second moment of area.
J	:	St. Venant's torsional constant.
$[K_1]$	:	Stiffness matrix for a curved beam element loaded in plane.
$[K_2]$	:	Stiffness matrix for a curved beam element normal to plane.
$[K_A]$	:	Axial stiffness matrix of group –1.
$[KB_1]$, $[KB_2]$	:	Bending stiffness matrices of groups –1 and –2.
$[K_{W2}]$	:	Stiffness matrix for a curved beam element normal to plane when warping is considered.
$[KBM_W]$	:	Stiffness matrix results from warping normal stress and strain caused by bimoment.
$[KB_W]$	:	Bending stiffness matrices of group–2 when warping is considered.
$[KT_{W1}]$, $[KT_{W2}]$	:	Torsional stiffness matrices from result primary and secondary shear deformation.
$[K_G]$	:	Global stiffness matrix of curved beam elements.
$[K_L]$,	:	Total stiffness matrix for curved beam elements without warping in the local coordinate.
$[K_{LW}]$	:	Total stiffness matrix for curved beam elements with warping in the local coordinate.
L	:	Element length.
$L_1, L_2, \ldots L_{11}$	:	Differential operators.
$M_{\bar{x}v}, M_w$	:	St. Venant's and warping torques.
$M_{\bar{y}}, M_{\bar{z}}$	:	Bending moments.
$[N_1]$	:	Shape function matrices for groups –1.
$[N_{w2}]$	:	Shape function matrices for group –2 when warping are considered.
R	:	Radius of curvature.
r	:	The polar radius of gyration.
s	:	The contour ordinate measured from a selected point on the median line of the section.
$S_{\bar{\omega}\bar{i}}$	:	The principal sectorial static moment.

T	:	Shear flow.
$[T]$	:	Transformation matrix.
U	:	Strain energy.
u, v, w	:	Displacements in direction of $\bar{x}, \bar{y}, \bar{z}$.
u_w, u_s	:	Axial and tangential components of the median surface displacement of the plate wall.
$\bar{x}, \bar{y}, z$	:	Local curvilinear coordinates.
x, y, z	:	Local straight coordinates.
X, Y, Z	:	Global coordinates.
$\hat{\alpha}$	:	Decay coefficient for non-uniform torsion of closed and open-closed sections.
$\hat{\beta}, \hat{\xi}$	:	Dimensionless parameters.
γ	:	Kinematic degree-of-freedom.
δ	:	Wall thickness in general.
θ	:	Subtended angle of the curved beam element.
μ	:	Warping shear parameter for closed and open-closed sections.
υ	:	Poisson's ratio.
σ_{x1}, σ_{x2}	:	Normal stresses of groups –1 and –2.
σ_w	:	Warping normal stress.
τ_{sx2}	:	Shear stress of group –2.
τ	:	Total angle twist ($\tau = \varphi + w/R$).
φ	:	Angle of twist.
ω	:	Sectorial area.
$\hat{\omega}$	:	Unit warping for closed and open-closed sections.
Ω	:	Twice the area of closed part of a section enclosed by the median line of the wall.

OPTIMIZATION OF THE OPERATION OF A COMPLEX WATER RESOURCES SYSTEM

PART -I : ANALYSIS OF THE CONVERGENCE CRITERION IN A SOLUTION BY THE DISCRETE DIFFERENTIAL DYNAMIC PROGRAMMING

Abdulhadi Ahmed Al-Delewy
Asst. Prof. , Department of Civil Engineering, College of Engineering, University of Babylon.

Numa Hamad Imara
Prof., Department of Building and Construction , University of Technology .

ABSTRUCT

An iterative – solution procedure necessarily involves pre – specified convergence criteria to stop iteration. The Discrete Differential Dynamic Programming procedure to solve optimization problems formulated by the Dynamic Programming is an iterative – solution procedure which, in its traditional form, involves two convergence criteria, namely, (α) and (β).

The research used the optimum operation of an existing complex water – resources system as a case study. The objective function was formulated as the maximum real monetary return. The formulated optimization model was run for a total of (194) different operation cases. Beside the traditional (α) and (β), seven new styles for a unique convergence criterion were examined in the solution.

Considering the monetary return and the number of performed iterations as the bases of comparison, the research showed that the new (γ) convergence criterion was the favorite among the tested convergence criteria.

الخلاصة

إن طريقة الحل التكراري تتضمن بالضرورة معايير تقارب محددة مسبقاً لإيقاف التكرار. إن طريقة البرمجة الدينامية التفاضلية المتقطعة هي طريقة حل تكراري، وهي بصيغتها التقليدية تتضمن معيارين للتقارب هما (α) و(β).

استخدم البحث التشغيل الأمثل لنظام موارد مائية مركب حقيقي كحالة تطبيقية، وصيغت دالة الهدف كأعلى عائد مالي حقيقي. تم تشغيل نموذج الأمثلية لما مجموعه (194) حالة تشغيلية مختلفة. وبالإضافة الى (α) و(β) التقليديتين، فقد اختبرت في الحل سبعة أشكال جديدة من معيار وحيد للتقارب.

وباعتماد مقدار العائد المالي وعدد دورات الحل التكراري كأساس للمقارنة، فقد بيّن البحث بأن معيار التقارب الجديد (γ) كان الأفضل بين معايير التقارب المختبرة.

KEY WORDS
Reservoir Operation; Dynamic Programming; Discrete Differential Dynamic Programming; The Convergence Criterion.

INTRODUCTION

The mathematical model which simulates the optimal operation of a single reservoir, (j = 1), or a set of jointly - operated reservoirs, (j = 1,2,..., J), is called a reservoir - operation problem, ROP. The solution of such a problem implies establishing the optimal inflow - storage - outflow relationship, i.e., finding the appropriate operation policy and, consequently, the respective trajectory, that yields the optimal outcome. The operation policy, $\{\hat{R}(j, t)\}$, is the set of feasible reservoirs releases, R(j , t), during the consecutive time stages, (t = 1,2, ... , T). The trajectory, $\{\hat{S}(j, t)\}$, is the set of feasible reservoirs storages, S(j , t), at the beginning of the considered stages. The obtained solution corresponds solely to the specified inputs and constraints.
A complex water - resources system denotes a multi - objective, multi - reservoir system. The complexity of the system comes from the complexity of the solution of its ROP.
In [AL-DELEWY: 1995], the discrete deterministic model has been identified as the appropriate practical general formulation for ROPs of the same style as the one under consideration in this research. Moreover, after reviewing several currently - used methodologies for formulating such ROP, particularly the Linear Programming [DANTZIG: 1963], the Linear Decision Rule [REVELLE et al.: 1969], and the Dynamic Programming [BELLMAN: 1957], the forward algorithm of a Dynamic - Programming formulation was identified as the most appropriate one. Furthermore, after reviewing several currently - applied procedures for solving the aforementioned formulation, particularly the Discrete Dynamic Programming [BELLMAN and DREYFUS: 1962], Bellman's successive approximations [BELLMAN: 1961], the Incremental Dynamic Programming [BERNHOLTZ and GRAHAM: 1960], (quoted in TURGEON: 1982]), the Discrete Differential Dynamic Programming, DDDP, [HEIDARI et al.: 1971], and the Multi - Level Incremental Dynamic Programming [NOPMONGCOL and ASKEW: 1976], the DDDP was identified as the most appropriate procedure of solution.

THE CONVERGENCE CRITERIA :

The DDDP is an iterative computation procedure. The measure of success of an iterative solution is how quick it converges to a certain target. In DDDP, the target is the global maximum return. Iteration is terminated when a certain pre-specified measure (criterion) of the aimed success is reached, or when a pre-specified total number of interations (K) has been performed.
For a total objective function, F[.], expressed in monetary terms (discounted return), then, {F[k] - F[k-1]} shows the improvement in the return of iteration step (k-1) due to iteration step (k). Similar to other iterative procedures, the DDDP involves a certain convergence criterion, CC , for the aforesaid improvement. The one commonly used is the duple CC of [CHOW and RIVERA: 1974], namely:

For computation cycles other than the last one, i. e., Cy < CY.

$$\frac{F[k] - F[k-1]}{F[1] - F[0]} \leq \alpha \qquad [1]$$

For the last computation cycle, i. e., Cy = CY:

$$\frac{F[k] - F[k-1]}{F[k-1]} \leq \beta \qquad [2]$$

The values used by [CHOW and RIVERA: 1974] are: $\alpha = 0.1$; $\beta = 0.001$. This CC has been used by [ALI: 1978], and others.

The objective of this research is to analyze the CC which is used in the DDDP solution of the formulated ROP, aiming at obtaining an improved CC as compared to the one traditionally used. The analysis will be based on the results of a case study that reflects a real operation process.

THE CASE STUDY

The case study is shown schematically in **Fig.(1).** It involves two, serially - connected reservoirs, denoted as RS1 and RS2. The system serves two distinct areas, denoted as MA and LA.

According to the considerations set forth in [AL-DELEWY: 1995], the following has been adopted in the research:

1- Stages, (t), are calendar months ; the operation horizon is one year, i.e., (t = 1, 2 , … , 12).

2- The objectives considered in the objective function, the constraints imposed on the system, and the values for inflow, demands, losses, and schedule of prices, are as given in [AL-DELEWY: 1995].

3- The dynamics of the system are as follows:

$$\text{For RS1: } S(1,t+1) = S(1 , t) + I(1 , t) - R(1 , t) - Ev(1 , t) \quad [3]$$

$$\text{For RS2: } S(2,t+1) = S(2 , t) + U(2 , t) - R(2 , t) - Ev(2 , t) \quad [4]$$

$$\text{where: } U(2,t) = R(1,t) + IC(1,t) - OC(1,t) \quad [5]$$

4- The overall single - stage objective function, representing the net return of the system, is given by [AL-DELEWY: 1995] as :

$$Z[t] = \sum_{j-1}^{2} [ZI(j , t) + ZP(j , t)] \quad [6]$$

$$\text{where: } ZI(j , t) = ZIM(j , t) - LSpI(j , t) - LEvI(j , t) \quad [7]$$

$$\text{and } ZP(j , t) = ZPM(j , t) - LSpP(j , t) - LEvP(j , t) \quad [8]$$

RUNNING THE MODEL

The general designation for the operation scenarios is "X a b c d e f g"; (X) denotes the basic group,where (X=A) denotes operating RS1 assuming non-existence of RS2; (X=B) denotes the reverse of (X=A); (X=C) denotes the operating of the complex system, i.e., operating RS1 and RS2 conjointly. The parameters (a) through (f) stand for the following: (a) denotes specified sub-group of (X=C), (b) denotes flood-control criteria; (c) for inflow data; (d) for the initial trial trajectory; (e) for the state of the ends of the trajectory; and (f) for the selected values of (K), (CY), and (Cw(Cy)). The parameter (g) denotes the applied convergence criteria. Eight styles of convergence criteria were used, namely:

g = 1 ⟹CC involves both (α) and (β) [as given in Eqs. (1) and (2), respectively];

g = 2 ⟹CC involves (β) only;

g = 3 ⟹CC is the new (γ) criterion (proposed in the research), where:

$$F^*[k] - F^*[k-1] \leq \gamma \quad [9]$$

$$\gamma = 0.00001 \times FO \times CY^2 / Cy^2 \quad [10]$$

g = 4 ⇦ 1) but (α) is replaced by ($\alpha 1 = 2\alpha$);
g = 5 ⇦ 1) but (α) is replaced by ($\alpha 2 = 0.5\alpha$);
g = 6 ⇦ 3) but (γ) is replaced by ($\gamma 1 = 2\gamma$);
g = 7 ⇦ 3) but (γ) is replaced by ($\gamma 2 = 0.5\gamma$);
g = 8 ⇦ 3) but (γ) is replaced by ($\gamma 3$), where:

$$\gamma 3 = 0.00002 \times FO \times CY / Cy \qquad [11]$$

A total of (194) operation scenarios were run, covering a variety of operation cases. In respect to the convergence criterion, the numbers of the run scenarios are as given in **Table (1)**.

RESULTS AND ANALYSES :

Results of running the aforementioned operating scenarios showed the following:

The (α) and (β) Criteria:

1- With all scenarios involving the (α) and (β) criteria together, i.e., scenarios (g=1) , (g=4) and (g=5), the (β) criterion is satisfied in one iteration step only.
2- When (α) criterion is used alone, i.e., without (β) criterion for the last computation cycle, the results were mostly the same as if (β) criterion was in use.

The Comparative Analyses

Comparative analyses based on ranking have been performed. The ranking was based mainly on the magnitude of the global optimal return (F*), with a consideration to the total number of executed iteration steps (TK). The results are summarized in **Table (2)**

Moreover:

1- Analysis (1) indicates that the results of (g=2) are the poorest as compared to those of (g=1) and (g=3). Sample comparison of the results is illustrated in **Fig. (2)**.
2- In Analysis (2), the improvement in the results by (g=4) as compared to those of (g=2) is almost insignificant.
3- In Analysis (3), the improvement over (g=3) by both (g=6) and (g=7) was mainly a slight reduction in (TK).
4- In Analysis (4), the results of seven scenarios from (g=3) and (g=8) were identical.
5- In Analysis (5), the differences between the results of the respective scenarios of sub-groups (g=1) and (g=3) of group (X=C) ranged from [equal (F*) and a difference of one iteration in (TK)] to [(F*=3,264,205 th. ID; TK=64) and (F*=3,267,254 th. ID; TK=58)], respectively, which is in favour of (g=3).
6- The global optimal solution for the basic C - scenarios is F**=3,240,714 th. ID; TK=30), given by a scenario from the sub-group (g=3).

CONCLUSION

Analysis of the results, as given hereinbefore , indicates that the (γ) criterion is the favorite among the applied convergence criteria, including that of [CHOW and RIVERA: 1974]. Consequently, rather than the duple convergence criterion, (α) and (β), the established single criterion (γ) is recommended.

RFERENCES

ALI, A. A. S. [1978], Development of reservoir operating rules with particular reference to the River Tees system". Ph. D. thesis, University of Newcastle Upon Tyne, UK.

Bellman, R. E. [1957], Dynamic Programming, Princeton University Press, Princeton, N. J., U.S.A.

Bellman, R. E. [1961], Adaptive control processes, Princeton University Press, Princeton, N. J., U.S.A.

Bellman, R. E. and S. E. Dreyfus [1962, 1971], Applied dynamic programming, Princeton University Press, Princeton, N. J., U.S.A.

CHOW, V. T. and G. C. RIVERA [1974], Application of DDDP in water resources planning". Water Resources Center; Research Report No. 78, University of Illinois, U.S.A.

Dantzig, G. B. [1963], Linear programming and extensions". Princeton University Press, Princeton, N. J., U.S.A.

Al-Delewy, Abdulhadi Ahmed[1995], Optimization of the operation of a complex water resources system with application to the Diyala River system". Ph. D. dissertation, University of Technology, Baghdad.

Heidari, M. , V. T. Chow, P. V. Kokotovic and D. D. Meredith [1971], Discrete differential dynamic programming approach to water resources systems optimization, WRR, 7(2), pp. 273-282.

Nopmongcol, P. and A. ASKEW [1976], Multilevel incremental dynamic programming,. WRR, 12(6), pp. 1291-1297.

Revelle, C., E. Joeres and W. Kirby [1969], The linear decision rule in reservoir management and design. 1 : Development of the stochastic model". WRR, 5(4), pp. 767-777.

Turgeon, A. [1982], Incremental dynamic programming may yield non optimal solutions, WRR, 18(6), pp. 1599-1604.

NOMENELATURE :

Cy : counter for performed computation cycles; its limiting value is CY.
Ev(j,t) : evaporation loss from the j-th reservoir during stage (t).
F[k] : total discounted return (thousand Iraqi Dinars) from the system as a result of performing the k-th iteration step; however, F0= F[0] = 0.
I(j,t) : total inflow to the j-th reservoir during (t).
IC(j,t) : natural inflow to the j-th channel during (t).
LEvI(j,t) : loss (th. ID) due to evaporation, evaluated as if it is (SpI).
LEvP(j,t) : ditto, evaluated as if it is (SpP).
LSpI(j,t) : loss (th. ID) due to spilling beyond irrigation demand.
LSpP(j,t) : ditto, beyond hydropower generation.
OC(j,t) : water consumption taken directly from the channel.
U(j,t) : additional inflow to a reservoir from an artificial source.
Z[t] : single - stage objective function.
ZI(j,t) : single - stage discounted return from irrigation.
ZIM(j,t) : ditto, of a sub - system.
ZP(j,t) : single - stage discounted return from hydropower generation.
ZPM(j,t) : ditto, of a sub - system.

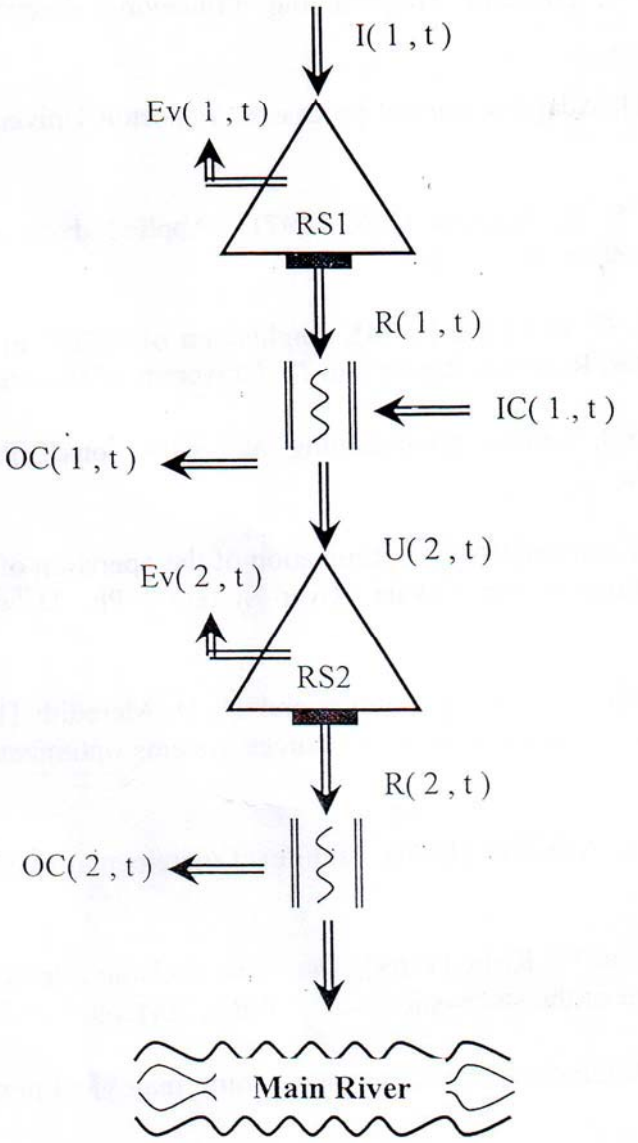

Fig. (1) : Schematic representation of the case study.

Table (1) Categories of the applied operation scenarios .

Parametric Category	Sub - group	No. in the basic group			Total No.
		A	B	C	
$\alpha + \beta$	g = 1	14	14	36	64
β	g = 2	8	8	4	20
γ	g = 3	14	14	38	66
$\alpha 1 + \beta$	g = 4	2	2	2	6
$\alpha 2 + \beta$	g = 5	2	2	2	6
$\gamma 1$	g = 6	2	2	2	6
$\gamma 2$	g = 7	2	2	2	6
$\gamma 3$	g = 8	8	8	4	20

Table(2) Summary of the comparative analyses .

ANALYSIS No.		1			2			3				4		5	
SUB-GROUP		g1	g2	g3	g1	g4	g5	g3	g6	g7	g8	g3	g8	g1	g3
NUMBER OF SCENARIOS	NUMBER USABLE IN THE ANALYSIS	20	20	20	6	6	6	6	6	6	6	20	20	64	64
	FIRST RANK	9	---	11	2	4	1	1	3	3	1	9	4	29	35
	SECOND RANK	11	---	9											
	THIRD RANK	---	20	---											

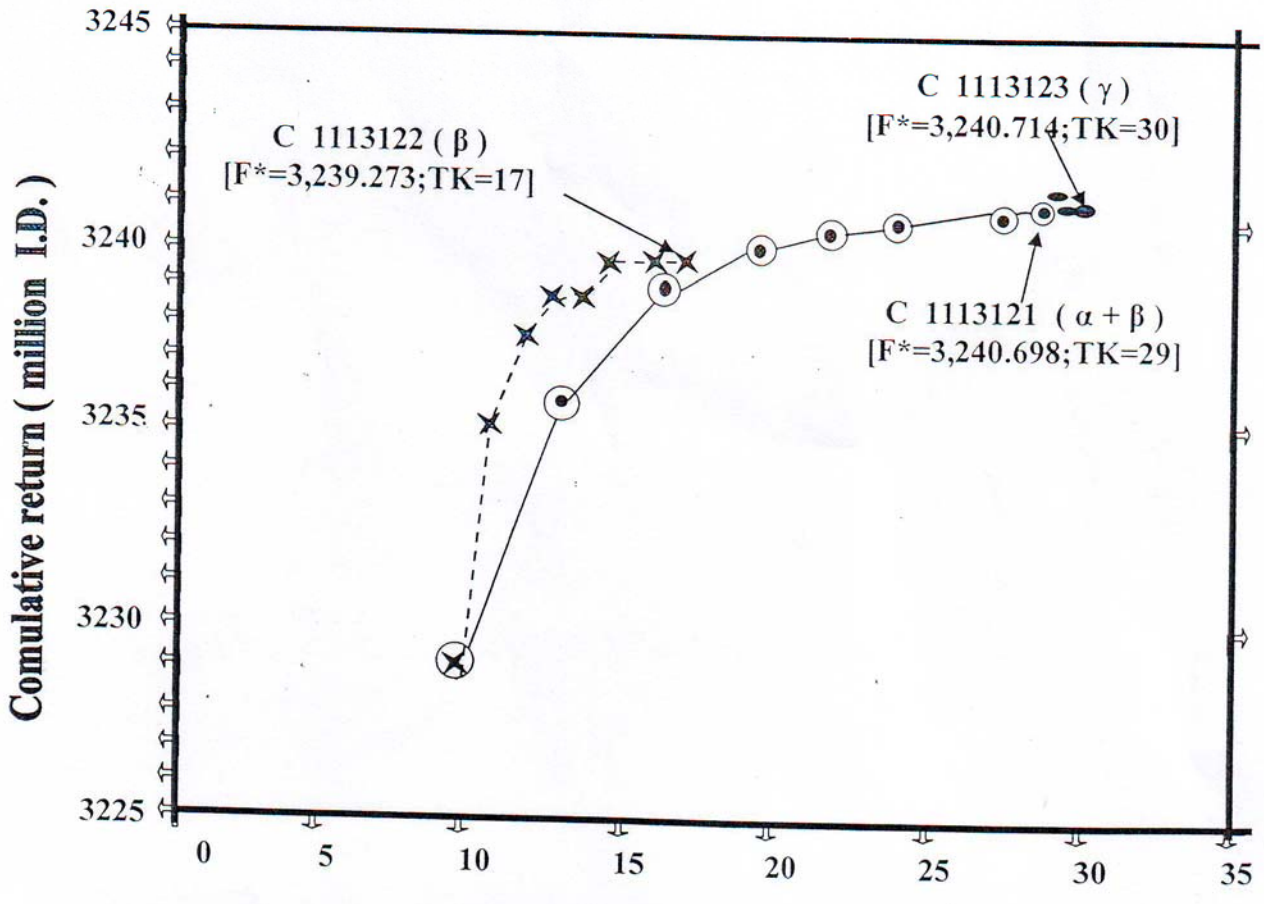

Fig. (2) Comparative results of applying the convergence criteria (α + β) , (β), and (γ).